



Università degli Studi di Napoli *Federico II*

DOTTORATO DI RICERCA IN FISICA

Ciclo XXXIV

Coordinatore: prof. Salvatore Capozziello

Cosmic messengers as a tool to investigate astroparticle physics

Settore Scientifico Disciplinare FIS/02

Dottorando

Damiano Francesco Giuseppe Fiorillo

Tutore

Prof. Gennaro Miele
Prof. Stefano Morisi

Anni 2019/2021

List of papers

This thesis is based on a list of projects realized during my PhD. Most of the results in Chaps. 5 to 9 are based on the following papers, on which most of the presentation is based (in the order in which they are discussed here):

1. "Starburst galaxies strike back: a multi-messenger analysis with Fermi-LAT and IceCube data", with A. Ambrosone, M. Chianese, A. Marinelli, G. Miele, O. Pisanti, published in *Mon.Not.Roy.Astron.Soc.* 503 (2021) 3, 4032-4049, arXiv:2011.02483
2. "Unified thermal model for photohadronic neutrino production in astrophysical sources", with S. Morisi, A. Van Vliet, W. Winter, published in *JCAP* 07 (2021) 028, arXiv:2103.16577
3. "Decaying dark matter at IceCube and its signature on High Energy gamma experiments", with M. Chianese, G. Miele, S. Morisi, O. Pisanti, published in *JCAP* 11 (2019) 046, arXiv:1907.11222
4. "Heavy decaying dark matter at future neutrino radio telescopes", with M. Chianese, R. Hajjar, G. Miele, S. Morisi, N. Saviano, published in *JCAP* 05 (2021) 074, arXiv:2103.03254
5. "Cosmogenic neutrino fluxes under the effect of active-sterile secret interactions", with G. Miele, S. Morisi, N. Saviano, published in *Phys.Rev.D* 101 (2020) 8, 083024, arXiv:2002.10125
6. "Observable features in ultrahigh energy neutrinos due to active-sterile secret interactions", with G. Miele, S. Morisi, N. Saviano, published in *Phys.Rev.D* 102 (2020) 8, 083014, arXiv:2007.07866
7. "IceCube constraints on violation of equivalence principle", with G. Mangano, S. Morisi, O. Pisanti, published in *JCAP* 04 (2021) 079, arXiv:2012.07867.

A number of further projects are connected with the same subjects, but they are not discussed at length in the thesis, and their results are only mentioned in the text (in chronological order):

1. "Constraints on heavy decaying dark matter with current gamma-ray measurements", with M. Chianese, R. Hajjar, G. Miele, N. Saviano, submitted for review to *JCAP*, arXiv:2108.01678
2. "Sensitivity of KM3NeT to Violation of Equivalence Principle", with M. Chianese, G. Mangano, G. Miele, S. Morisi, O. Pisanti, published in *Symmetry* 13 (2021) 1353, arXiv:2107.13013
3. "Could nearby star-forming galaxies light up the point-like neutrino sky?", with A. Ambrosone, M. Chianese, A. Marinelli, G. Miele, to be published in *ApJ Letters*, arXiv:2106.13248.

Further projects have been carried out between my master thesis and my PhD which have resulted in papers not discussed in this thesis (in chronological order):

1. "Direct Detection of Light Dark Matter from Evaporating Primordial Black Holes", with R. Calabrese, M. Chianese, N. Saviano, submitted for review in *Phys. Rev. Lett.*, arXiv:2107.13001
2. "Absorption from Primordial Black Holes as source of baryon asymmetry", with A. Ambrosone, R. Calabrese, G. Miele, S. Morisi, arXiv:2106.11980
3. "Primordial Black Hole Dark Matter evaporating on the Neutrino Floor", with R. Calabrese, G. Miele, S. Morisi, A. Palazzo, submitted for review in *Phys. Rev. D*, arXiv:2106.02492
4. "A test of the hadronic origin of γ -rays from blazars with up to month-later follow-up of IceCube Alerts with Imaging Air Cherenkov Telescopes", with K. Satalecka, I. Taboada, C. F. Tung, to be published in *ApJ*, arXiv:2105.14043
5. "Top-flavor scheme in the context of W' searches at LHC", with R. Calabrese, A. De Iorio, A. Iorio, G. Miele, S. Morisi, published in *Phys.Rev.D* 104 (2021) 5, 055006, arXiv:2104.06720
6. "Tau Neutrinos with Cherenkov Telescope Array", with G. Miele, O. Pisanti, arXiv:2007.13423
7. "Investigating two heavy neutral leptons neutrino seesaw mechanism at SHiP", with M. Chianese, G. Miele, S. Morisi, published in *Int.J.Mod.Phys.A* 34 (2019) 08, 1950047, arXiv:1812.01994
8. "Neutrino phenomenology from leptogenesis", with F. Buccella, G. Miele, S. Morisi, O. Pisanti, P. Santorelli, published in *Eur.Phys.J.C* 78 (2018) 10, 817, arXiv:1806.07615.

Contents

Preface	7
I Theoretical background	13
1 Multi-messenger production	15
1.1 Cosmic-rays: acceleration processes	15
1.1.1 Diffusive shock acceleration	16
1.1.2 Maximal energy	19
1.2 Gamma-ray production	21
1.2.1 Leptonic gamma-ray production	22
1.2.2 pp processes	24
1.2.3 $p\gamma$ processes	26
1.3 Neutrino production	27
1.3.1 pp processes	28
1.3.2 $p\gamma$ processes	29
2 Multi-messenger propagation	33
2.1 Cosmic-ray propagation	33
2.2 Gamma-ray propagation	37
2.3 Neutrino propagation	40
3 Detection of gamma-rays and neutrinos	43
3.1 Gamma-ray detectors	43
3.1.1 Space-based detectors	43
3.1.2 Ground-based detectors	45
3.2 Neutrino detectors	46
3.2.1 Neutrino telescopes	47
3.2.2 Neutrino radio arrays	51
4 Gamma-ray and neutrino astrophysical sources	53
4.1 Cosmic accelerators	53
4.1.1 Supernova remnants	58
4.1.2 Active galactic nuclei	60
4.1.3 Gamma-ray bursts	62
4.1.4 Tidal disruption events	63
4.2 Cosmic reservoirs	64

4.2.1	Starburst galaxies	64
4.2.2	Galaxy clusters	65
4.2.3	Galactic production	66
4.3	Cosmogenic neutrinos	67
II Investigating the sources of neutrinos and gamma-rays		69
5	Neutrino and gamma-ray production in starburst galaxies	71
5.1	Neutrino and gamma-ray fluxes from individual SBGs	72
5.2	Diffuse neutrino and gamma-ray fluxes	76
5.3	Multi-messenger analysis	79
5.4	Results	81
5.5	Discussion	86
6	Unified model of photohadronic neutrino production	87
6.1	Thermal model	88
6.1.1	Temperature mapping	88
6.1.2	Cosmic-ray spectrum	90
6.1.3	Benchmark examples	91
6.2	Sensitivity of neutrino detectors	94
6.3	Flavor composition	97
6.4	Conclusions	99
III Beyond Standard Model physics		101
7	Decaying Dark Matter at neutrino and gamma-ray telescopes	103
7.1	Neutrinos and gamma-rays from dark matter decay	104
7.1.1	Particle spectrum from dark matter decay	106
7.1.2	Neutrino fluxes	107
7.1.3	Gamma-ray fluxes	108
7.2	Neutrinos from dark matter decay at IceCube	110
7.2.1	Methods	111
7.2.2	Results	114
7.2.3	Gamma-ray fluxes: comparison with the experiments	115
7.3	Neutrinos from dark matter decay at radio telescopes	116
7.3.1	Dark matter detectability	117
7.3.2	Dark matter constraints	118
7.4	Discussion	123
8	Active-sterile secret interactions at neutrino telescopes	125
8.1	The model	126
8.2	Constraints	127
8.2.1	Laboratory constraints	127
8.2.2	Cosmological bounds	130
8.2.3	Astrophysical bounds	132
8.3	Neutrino fluxes	133
8.3.1	Standard astrophysical sources	133

8.3.2	Secret interaction	134
8.4	Results	136
8.4.1	TeV-PeV range: power-law model	136
8.4.2	EeV range: cosmogenic	138
8.5	Discussion	139
9	Testing Violation of Equivalence Principle with neutrinos	141
9.1	Neutrino propagation in a gravitational field	142
9.2	VEP effects on atmospheric neutrinos	144
9.2.1	Propagation of atmospheric neutrinos under VEP	145
9.2.2	Statistical analysis	146
9.3	VEP effects on astrophysical neutrinos	148
9.4	Discussion	151
	Conclusions	151
	Appendix A Second-order Fermi mechanism	155
	Appendix B Analytical solutions for cosmic-ray acceleration	159
	Appendix C Formal treatment of cosmic-ray propagation	163
	Appendix D Derivation of the thermal model	167
	Appendix E Cross sections for active-sterile interactions	173
	Appendix F Secret interactions with sterile neutrino decay	177
	Acknowledgments	179

Preface

Physics at the highest energy scales is notoriously hard to test. With the advent of the Large Hadron Collider it has been possible to probe particle physics up to an energy of 13 TeV. However, an order-of-magnitude increase in this energy scale is not feasible in the near future. Beside the accelerators built by human technology, the most energetic particles we are aware of are powered by electromagnetic processes within astrophysical sources. These particles, namely the cosmic-rays, are ideal for studying high-energy processes and possibly for testing Beyond Standard Model (BSM) physics. Indeed, the origin of particle physics is strongly intertwined with cosmic-ray observations.

However, a difficulty to deal with is the uncertainty on their origin. Even though the discovery of cosmic-rays dates back to 1912, it is at present unknown which astrophysical sources are responsible for their production. Various acceleration mechanisms have been proposed in the context of different astrophysical sources, but there is no agreement on what are the dominant sources. Beside its importance as a theoretical question, this lack of knowledge necessarily limits the extraction of information on BSM physics.

Determining the sources of cosmic-rays is hard mainly because they propagate in galactic and intergalactic magnetic fields, which are typically turbulent. For this reason, the trajectories of cosmic-rays are not predictable and do not point back to their sources. A step toward a deeper understanding of the cosmic-ray production was done with the construction of gamma-ray experiments. High-energy gamma-rays are produced by cosmic-rays via different mechanisms which will be reviewed in this thesis. Differently from cosmic-rays, however, gamma-rays are neutral and are therefore not deflected by magnetic fields. For this reason, they point back to the source they came from. The observation of high energy gamma rays allows the identification of sources potentially connected with cosmic-ray production and acceleration.

The final step so far in the quest for the cosmic-ray origin has been the construction of neutrino observatories. In fact, compared to gamma rays, neutrinos are expected to be produced only when cosmic rays interact hadronically. Furthermore, due to their weak interactions, high energy neutrinos arrive at Earth with no attenuation, whereas photons with energies larger than about 1 TeV suffer a strong attenuation from collisions with the Extragalactic Background Light. Therefore, the observation of neutrinos of astrophysical origin made by IceCube, a Gton neutrino telescope in the South Pole, is a marker of hadronic interactions of cosmic-rays within their sources. At the same time it allows to observe the products of cosmic-ray interactions at energies above 100 TeV, much higher than the ones testable by gamma rays.

The first part of this thesis is dedicated to a review of the physics of cosmic-rays, astrophysical gamma-rays, and astrophysical neutrinos. The combined observation of these particles is the focus of multi-messenger astronomy, which is the main strategy followed in most of the works of this thesis. We divide the discussion of this first part in four subjects: the acceleration of cosmic-rays and the processes of production of high-energy gamma-rays and neutrinos (Chapter [1](#)), the processes which influence the propagation of these particles in the interstellar and intergalactic space (Chapter [2](#)),

the experiments aiming at the detection of astrophysical gamma-rays and neutrinos and the results obtained so far (Chapter 3), and finally a review of the main sources believed to be responsible for the production of the astrophysical neutrinos observed so far (Chapter 4).

The identification of point-like sources of these astrophysical neutrinos has been so far limited. IceCube has detected a diffuse flux of astrophysical neutrinos, but most of these have no temporal or spatial correlation with known sources. Some noticeable exceptions include the blazar TXS 0506+056, the tidal disruption event AT2019dsg, and the starburst galaxy with an active galactic nucleus NGC1068. However, the analysis of correlations with astrophysical sources has not yet provided a definite answer to the question of where these neutrinos come from. Such a definite answer will shed light on the question of what are the most significant sources of cosmic-rays.

A first group of works discussed in this thesis deals with this question. In Chapter 5, we consider a specific class of sources which are expected to produce high-energy gamma-rays and neutrinos, namely starburst galaxies. We revise the estimates of the gamma-ray and neutrino fluxes produced in starburst galaxies, emphasizing the effect of the intrinsic variability of the cosmic-ray populations within each starburst galaxy. In Chapter 6, we consider a compact model of neutrino production in collisions between protons and soft photons, which is believed to be a dominant mechanism of neutrino production in the so-called photohadronic sources. We show that a limited number of parameters is able to describe quite accurately the properties of high-energy neutrinos produced in these sources, proposing a model which can be helpful in systematic studies of many different classes of astrophysical sources at once.

Despite the many uncertainties on the sources of the high-energy neutrinos and gamma-rays observed by the current experiments, they can still provide a powerful source of information on high-energy physics and BSM physics. This is the subject of a second group of works presented in this thesis, in which we analyze a number of extensions of the Standard Model.

Indeed, some of the questions left open by the Standard Model may receive answers by high-energy neutrino observations. Among these, a central one is the nature of dark matter, namely the dark component of matter suggested by astrophysical and cosmological observations. Dark matter has been only observed through its gravitational effects, for example on the velocities of rotation of stars in galaxies or on the formation of structures in the primordial universe. However, most of the dedicated searches for a dark matter particle interacting with visible matter have so far failed in finding any. Neutrino astronomy opens a new possibility of dark matter detection, by looking for neutrinos produced in the decay of dark matter particles at the galactic and extragalactic scale. We study this possibility in Chapter 7, in which we show that even weakly interacting dark matter, with lifetimes ten orders of magnitude longer than the lifetime of the universe, can be tested at neutrino experiments.

A sector of BSM physics for which high-energy neutrino observations are naturally suited is the study of the neutrino properties. In the Standard Model, neutrinos are assumed to come in three flavors, and to be interacting only through the weak interactions. Both these assumptions may no longer hold true in a more complete theory, and indeed many extensions of the Standard Model including a fourth sterile (i.e. not interacting through the weak interaction) neutrino have been proposed. Furthermore, the presence of non-weak interactions among neutrinos (often dubbed neutrino secret interactions) is constantly tested either in the study of meson decays, or by looking at dense neutrino environments such as supernovae or the primordial universe. In Chapter 8, we exemplify the potential of high-energy neutrinos to probe new neutrino physics with a specific model of secret interaction between active neutrinos and an additional sterile neutrino. We show that, due to the scattering of active neutrinos on the low-energy cosmic neutrino background, the spectrum of astrophysical neutrinos could exhibit observable absorption features and slight changes in the flavor composition.

Finally, a well-known open question of the Standard Model is how to describe consistently gravity in an ultraviolet-complete quantum theory. For this reason, a great work is devoted to testing the founding assumptions of general relativity, the current classical theory of gravitation. In Chapter [9](#) we follow this path and test the possible presence of a violation of the equivalence principle (VEP), leading to a different gravitational coupling for different combinations of neutrino flavor states. We show that the energy and angular distribution of high-energy atmospheric neutrinos is sensitive enough to VEP to significantly constrain its magnitude. Furthermore, we show that the flavor composition of astrophysical neutrinos is also a promising sensitive probe of VEP, which may become able in 10 to 20 years to exclude most of the parameter space of this BSM extension.

Part I

Theoretical background

Chapter 1

Multi-messenger production

In the first part of this thesis, we summarize the theoretical background on gamma-ray and neutrino observations, as well as their connection with high energy astrophysics. The first step is a discussion of how these very energetic particles are produced in astrophysical sources, and this first chapter is devoted to this topic. Even though cosmic-rays are not the primary subject of this thesis, they are the progenitors of high energy gamma-rays and neutrinos: for this reason, we start our discussion in Sec. [1.1](#) by describing the diffusive shock acceleration mechanism, by which cosmic-rays are believed to be accelerated. This discussion is necessary to justify the common assumption of power-law spectra for the high-energy particles produced in astrophysical sources, as well as to introduce the important concept of the maximal energy to which particles can be accelerated. In the following Secs. [1.2](#) and [1.3](#) we describe the leptonic and hadronic processes causing the production of high-energy gamma-rays and neutrinos. The two sections are necessarily intertwined, since the hadronic processes are responsible for both neutrino and gamma-ray production: we therefore split the discussion among those features that are more relevant for gamma-rays and neutrinos.

1.1 Cosmic-rays: acceleration processes

Cosmic-rays are the primary particles whose collisions produce gamma-rays and neutrinos. A discussion of how cosmic-rays are accelerated to the high energies at which we observe them is therefore a necessary basis for all the rest of this work. Since it is not the primary aim of this thesis, in this section we limit ourselves to a short discussion of shock acceleration in supernova remnants (SNRs): however, it should be mentioned that other processes have been proposed as candidates acceleration mechanisms, including magnetic reconnection and unipolar induction, e.g., in pulsars.

The observation of cosmic-rays shows in a definite way that charged particles can have a non-thermal, typically power-law, distribution as a function of the energy. This statement is confirmed by the observation of power-law photon spectra from many astrophysical sources, which are believed to be generated by cosmic-rays, inheriting their power-law spectra. The problem is then to explain how a distribution of particles initially at thermal equilibrium can be accelerated to non-thermal spectra with very high energies¹. A standard solution to the problem is given by the diffusive shock acceleration mechanism, originally proposed independently in Refs. [1-4](#). This is generally known as Fermi first order mechanism, since it was inspired by a previous candidate mechanism proposed by

¹In fact a related problem is the injection, namely how a group of particles are selected among the initially thermal one to be accelerated.

Fermi [5] generally known as the Fermi second order mechanism (the reason for the different names will be more clear below). In this section, after a short description of the original Fermi second order mechanism, we describe the diffusive shock acceleration process, and the properties of cosmic-rays accelerated by this mechanism.

1.1.1 Diffusive shock acceleration

The idea behind the mechanism is that charged particles require electric fields to be accelerated. Due to the high conductivity of the cosmic plasma, electric fields are hard to maintain in astrophysical environments. They can however be generated by moving magnetic fields, according to the law of induction. This was the original motivation behind the mechanism proposed by Fermi, in which cosmic-rays collide with moving magnetic clouds. Even without a detailed calculation, we can understand the physical reason why this mechanism fails. Let us assume that the magnetic cloud moves with a non-relativistic velocity V , colliding with a relativistic particle with energy E and with angle θ compared to the cloud velocity. Since the cloud is macroscopic, it behaves as a rigid wall, imparting to the particle a velocity $2V \cos \theta$. The impulse of the particle, and therefore its energy (which are equal for a relativistic particle), increases by an amount

$$\delta E = 2EV \cos \theta. \quad (1.1)$$

Here and throughout this thesis we adopt natural units in which $\hbar = c = 1$. If we average over all possible directions², this vanishes. The physical meaning is that, to first order in V/c , there is no increase on average in the particle energy because there are as many forward as backward collisions. The average relative energy increase will be of second order in V/c , as confirmed by a more detailed calculation: this is the reason why this is named a second order mechanism. The energy increase in each collision is therefore very small, and many collisions are required to accelerate the particles to the highest energies observed. We leave for App. A a more detailed discussion of Fermi second order mechanism.

The scenario of diffusive shock acceleration, on the other hand, is based on the observation that cosmic-rays do collide with magnetic inhomogeneities which are maintained by turbulence in the interstellar space (the mechanism of collision will be discussed in more detail in Chap. 2). The main type of inhomogeneities are Alfvén waves [6], which collide with cosmic-rays causing them to diffuse in the interstellar space. However, the velocity propagation of these waves is much smaller than the speed of light, meaning that they are practically static with respect to the relativistic particles: a static magnetic field, as well known, cannot do work on a particle and increase its energy. The solution proposed in Refs. [1-4] involves the presence of a shock wave, such as the ones produced in SNRs. The shock waves heats the gas that it sweeps up, and particles passing through the shock wave are accelerated in a similar way by colliding with the Alfvén waves. Let us discuss more quantitatively how this process works.

In a shock wave the velocity, temperature, pressure, and magnetic field in the interstellar medium jump discontinuously; for simplicity, we neglect the magnetic field in this treatment. The values of the quantities on the two sides of the shock are connected by the conservation of the flux of particles, momentum, and energy passing through the shock; the corresponding relations, namely the Rankine-Hugoniot conditions [7], are most simply expressed in the shock rest frame. We denote by a suffix 1 (2) the quantities upstream (downstream) of the shock: then the relation between the

²Here we assume isotropy of the particle direction in the laboratory frame: in the cloud comoving frame deviations from isotropy are only of second order in V/c , because the particles move close to the speed of light and the cloud is practically at rest compared to them.

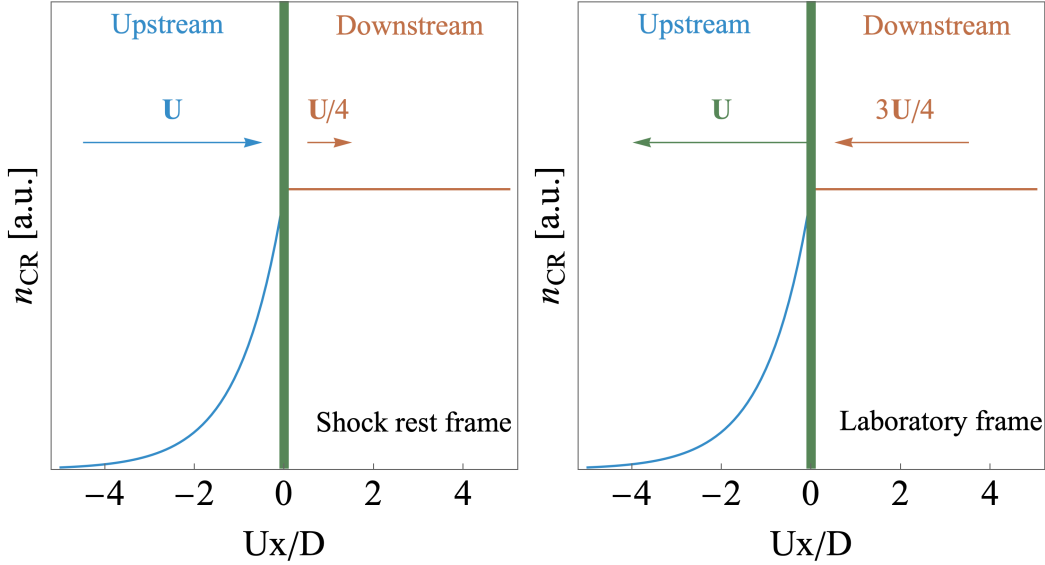


Figure 1.1: Cosmic-ray density near a shock in the shock rest (laboratory) frame. The quantities referring to the upstream gas, the shock, and the downstream gas are shown in blue, green, and orange respectively.

gas velocities, denoted by u , and the gas density, denoted by ρ , on each side of the shock is³

$$\frac{u_1}{u_2} = \frac{\rho_2}{\rho_1} = \frac{(\gamma + 1)M_1^2}{(\gamma - 1)M_1^2 + 2}, \quad (1.2)$$

where M_1 is the Mach number of the shock wave with respect to the sound speed upstream of the shock and γ is the polytropic index of the gas (we remind that in a polytropic gas density and pressure are connected by the relation $p \propto \rho^\gamma$). In the limit of a strong shock, moving with a very large Mach number, this fraction tends to a definite value, which, for a monoatomic gas ($\gamma = 5/3$), is $\frac{u_1}{u_2} = 4$. The two velocities can be simply connected to the velocity of the shock in the laboratory frame: in this frame the upstream gas is at rest, so the shock moves with velocity $U = u_1$. It follows that $u_1 = U$, $u_2 = U/4$. The geometrical structure of the shock wave and the velocities both in the shock rest frame and in the laboratory frame (namely the rest frame of the upstream gas) are summarized in Fig. 1.1.

The acceleration process can be now described as follows: when a cosmic-ray in the upstream region is advected by the shock, it enters the downstream region. Relative to the upstream region, the downstream gas is moving with a velocity $v_1 - v_2 = 3V/4$. Therefore, when the particle collides with the Alfvén waves in the downstream region, the latter are moving with respect to the particle and can therefore do work on it, increasing its energy. A symmetrical situation is found when the particle pass from the downstream to the upstream region: also in this case the gas from the upstream region is moving toward the particle with a velocity $3V/4$, and therefore the particle gains again energy from collision with the moving magnetic waves. The efficiency of this acceleration mechanism is based in fact on the observation that the particle gains energy each time it collides with the shock.

³We assume non-relativistic shocks, for which $u_1, u_2 \ll c$, where c is the speed of light: however, we will later comment on how the results change in the case of relativistic shocks.

To describe in mathematical terms this situation, let us introduce the distribution of cosmic rays in phase space $f(\mathbf{r}, \mathbf{p}, t)$. In the laboratory frame the phase space distribution obeys the Vlasov equation (we will later introduce the diffusion on magnetic fields)

$$\frac{\partial f}{\partial t} + \frac{\mathbf{p}}{E} \cdot \frac{\partial f}{\partial \mathbf{r}} = 0. \quad (1.3)$$

If the gas in which the particles are moving is not at rest, but moves with a space-dependent velocity $\mathbf{u}(\mathbf{r})$, the momentum of the particle from the gas rest frame to the laboratory frame changes as $\mathbf{p} \rightarrow \mathbf{p} + E\mathbf{u}(\mathbf{r})$. This amounts to a change of variables in Eq. 1.3, so in terms of the momentum in the frame comoving with the gas the equation becomes

$$\frac{\partial f}{\partial t} + \frac{p_i + Eu_i}{E} \frac{\partial f}{\partial r_i} - (p_i + Eu_i) \frac{\partial u_j}{\partial r_i} \frac{\partial f}{\partial p_j} = \nabla \cdot (D\nabla f), \quad (1.4)$$

where we have also added a term on the right-hand side describing the diffusive collision of cosmic-rays on the magnetic waves (see Sec. 2.1 for the diffusion coefficient D). To simplify further this equation, we assume a plane, normal shock orthogonal to the z direction. In the shock rest frame the problem is stationary⁴ and the distribution depends only on z and \mathbf{p} ; furthermore, assuming that the momenta are distributed isotropically, we can average over the direction of \mathbf{p} and obtain the final form of the equation⁵

$$u \frac{\partial f}{\partial z} - \frac{1}{3} \nabla \cdot \mathbf{u} p \frac{\partial f}{\partial p} = \frac{\partial}{\partial z} \left(D \frac{\partial f}{\partial z} \right), \quad (1.5)$$

where $\nabla \cdot \mathbf{u} = (u_2 - u_1)\delta(z)$ if the shock is placed at $z = 0$; also, we take the upstream region at $z < 0$ and the downstream region at $z > 0$. We omit the intermediate passages and report directly the solution of this equation, which is derived in App. B

$$f(z, p) = \begin{cases} f_u(p) + \left[\frac{3u_1}{u_1 - u_2} \int_0^p \frac{dp'}{p'} f_u(p') \left(\frac{p'}{p} \right)^{\frac{3u_1}{u_1 - u_2}} - f_u(p) \right] e^{\frac{u_1 z}{D}} & z < 0, \\ \frac{3u_1}{u_1 - u_2} \int_0^p \frac{dp'}{p'} f_u(p') \left(\frac{p'}{p} \right)^{\frac{3u_1}{u_1 - u_2}} & z > 0. \end{cases} \quad (1.6)$$

This solution depends on an arbitrary function $f_u(p)$, which is the distribution of the particles infinitely far from the shock in the upstream region: these are the particles that have not been accelerated yet, and therefore $f_u(p)$ has support only at low energies. As a simple choice we take $f_u(p) = \frac{n}{4\pi p_0^2} \delta(p - p_0)$, where n is the spatial density upstream and p_0 is a low energy value. By substitution we see that both upstream and downstream there is a component, coming from the integral, behaving as a power law in momentum $p^{-3u_1/(u_1 - u_2)}$. Substituting $u_2 = u_1/4$ the behavior of the spectrum is $f(z, p) \propto p^{-4}$. Since for relativistic particles $p \simeq E$, and the phase-space volume is $4\pi p^2 dp$, we find that the distribution in terms of the energy is proportional to $E^{-2} dE$, recovering the well-known result that for diffusive shock acceleration the cosmic-rays are distributed as a power law in energy. The spectral index of the power law attains a constant value equal to 2 (throughout

⁴The assumption of stationarity is a subtle one, and its validity will be discussed in more detail below.

⁵The derivation of this equation skips over a subtlety, due to the fact that the diffusion term will be derived in Sec. 2.1 in a frame in which the magnetic waves are at rest, whereas in the shock rest frame this is not anymore true. However, since the Alfvén waves are non-relativistic both in the laboratory and in the shock frame, the term we are neglecting is only of order $(v_A/c)^2$, where v_A is the Alfvén velocity; this correction accounts for the stochastic acceleration of cosmic-rays from the randomly moving waves, which might be relevant to explain the low energy part of the spectrum, but does not influence the high energy behavior we are interested in here.

this work, wherever it is not explicitly stated, we refer by spectral index to the power of the energy), independent of the details of the precise velocity of the shock and the diffusion coefficient. This was indeed one of the reason behind the relevance of diffusive shock acceleration, since this value is quite close to the observed value for the cosmic-rays at Earth⁶.

Let us discuss in physical terms the solution that we have just found. In the upstream region there is a spatially uniform component of cosmic-rays ($f_u(p)$) which is not accelerated, constituted by the particles who have never interacted with the shock wave, and a term decreasing far from the shock. This term describes the particles who have already passed through the shock back and forth several times and therefore are accelerated with the power law spectrum. On the other hand, in the downstream region the accelerated particles are not suppressed and extend down to $z \rightarrow \infty$. They give rise to a particle flux $j = f(z, p)u_2$ escaping from the shock to downstream infinity, which is caused by the advection of the particles: in other words, these are the particles that have been overcome by the propagating shocks and are escaping from behind it. This spatial distribution of the particles already accelerated by the shock is shown graphically in Fig. 1.1

The result has been derived under several assumptions: let us discuss some of them and what is their effect:

- we have assumed that the shock waves behaves as an external field, feeling no influence from the cosmic-rays. In reality cosmic-rays moving back and forth through the shock cause a pressure, whose effect is to smooth the discontinuity in the velocity and pressure at the shock. Therefore the majority of the cosmic-rays experience the passage through a weaker shock with a smaller compression ratio, leading to a softer spectrum at lower energies; only the higher energy cosmic-rays experience an increased compression ratio, making the spectrum harder at harder energies. The spectra obtained taking into account the non-linear effects of cosmic-rays on the shock have therefore a characteristic concave shape, with spectral index larger than 2 at low energies and smaller than 2 at high energies [9][12];
- we have assumed that the shock waves were non-relativistic. Relativistic shocks can be important for acceleration of cosmic-rays near very energetic astrophysical events, such as active galactic nuclei and gamma-ray bursts (see Chap. 4). A full discussion of relativistic shock acceleration is beyond the aims of this work: here we only report the result of numerical and analytical studies [13-17], which have shown that near relativistic shocks cosmic-rays attain a power-law spectrum⁷ in energy, with a spectral index around 2.2. This result is also in agreement with the spectral index of cosmic-ray electrons near gamma-ray bursts, as estimated from gamma-ray observations [18].

1.1.2 Maximal energy

The stationary solution that we have found possesses some surprising aspects: first of all, the spectrum behaves as a power law in energy, so there are particles with energies which can be infinitely large. Furthermore, even though the diffusion on magnetic waves is the primary mechanism by which particles gain energy, the diffusion constant does not appear in the energy spectrum. Finally, the total number of cosmic-rays integrated over all space diverges. All these aspects are connected with the limited validity of a stationary solution: in reality if the shock is active for a finite time particles can only be accelerated up to a maximum energy, determined by how many times they can cross the

⁶The observed spectral index of the cosmic-rays at Earth is about 2.7; however, the spectrum is somewhat softened by the energy-dependent escape of cosmic-rays from the Galaxy. Taking this into account, the spectral index of accelerated cosmic-rays is estimated to be close to 2.4 [8].

⁷This is expected due to the lack of any characteristic scale of momentum.

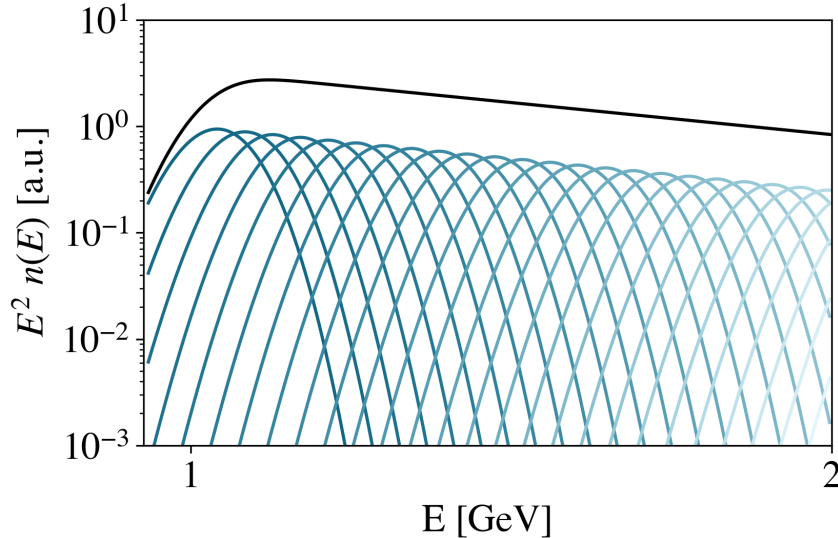


Figure 1.2: Cosmic-ray spectrum after 24 crossings through the shock wave; the progressive crossings are shown in decreasing order of color intensity. The superposition is shown in black.

shock, and they cannot reach the spatial infinity. We discuss in App. [B](#) the time-dependent solution to the transport equation: here we adopt simpler arguments to determine the qualitative features of the solution.

In a time-dependent solution, cosmic-rays are progressively accelerated each time they cross the shock. At each crossing back and forth of the shock (which is generally called a cycle of acceleration), the particle will experience an energy gain: to determine it, we observe that in a single passing through the shock the particle collides with magnetic waves coming toward it with a velocity $u_1 - u_2$. Following the same reasoning that led to Eq. [1.1](#), we see that when the particle enters the other region its energy gain is $\delta E = E \frac{u_1 - u_2}{c} \cos \theta$. When we average over the angle θ , the probability of collision is proportional to $2 \sin \theta \cos \theta$, where the factor $\cos \theta$ accounts for the relative velocity between the particle and the shock. After averaging, we find that the energy gain in a single passing through the shock is $\delta E = \frac{2(u_1 - u_2)}{3c} E$. In a total cycle, the energy gain is twice this value $\Delta E = \frac{4(u_1 - u_2)}{3c} E$, because the particle gains energy in both the passages through the shock.

On the other hand, the cycle has a finite duration, which we can estimate as follows. When the particle is released from the shock in the upstream or downstream region, it is diffused by a characteristic length which can be estimated by the transport equation as $l_{1,2} \sim \frac{D}{u_{1,2}}$, where the suffix refers to the region. Since cosmic-rays move with relativistic speeds, the time they take to go back to the shock is then $t_{1,2} \sim \frac{D}{u_{1,2}c}$. The duration for a complete cycle is therefore of the order of $T_{\text{acc}} = f \frac{D}{c} \left(\frac{1}{u_1} + \frac{1}{u_2} \right)$, where f is a numerical factor: a more precise determination (see App. [B](#)) gives $f = 4$. Substituting the shock velocity, we find that on average the particle energy increases with a rate

$$\frac{dE}{dt} = \frac{\Delta E}{T_{\text{acc}}} = E \frac{V^2}{20D}. \quad (1.7)$$

This is the rate of energy increase of the particles which keep crossing and recrossing the shock. On the other hand, a fraction of the particles will escape the shock in the downstream region: to estimate the probability that a particle escapes the shock, we simply notice that its motion is a superposition of the relativistic motion with the speed of light (which in our units is 1) in random directions, and the hydrodynamic advection with velocity u_2 which makes it escape from the shock. The relativistic isotropic motion causes a flux of particles to run back to the shock: since their velocity is 1, the flux is $n/4$, where n is the cosmic-ray density downstream (in fact only half of the particles have a velocity directed toward the shock, and the component of the velocity toward the shock is uniformly distributed between 0 and 1: therefore the mean velocity is $1/2$). On the other hand, the flux of particles escaping downstream is simply nu_2 . Therefore the probability of escape is

$$P_{\text{escape}} = \frac{nu_2}{n/4} = 4u_2. \quad (1.8)$$

The stationary power-law spectrum we have derived above can be regarded as the superposition of the original low-energy spectrum passing through the shocks N times: at each crossing the energy increases by a factor $\frac{4(u_1-u_2)}{3c}$, but the probability of doing N crossings without escaping downstream rapidly decreases as $e^{-NP_{\text{escape}}}$. A graphical representation of the power-law spectrum in this interpretation is given in Fig. 1.2

If the shock has a finite duration T , and the particles had originally an energy E_0 , they can only attain a maximum energy E_{max} given by the condition

$$T = \frac{20}{V^2} \int_{E_0}^{E_{\text{max}}} \frac{dE}{E} D(E), \quad (1.9)$$

where for generality we have assumed that the diffusion coefficient is a function of the energy. This diffusion coefficient will be discussed in more detail in Sec. 2.1: a simple argument that we can use here is that for strong turbulence the particle mean free path cannot be smaller than their Larmor radius. From kinetic theory the diffusion coefficient must therefore be larger than the Bohm coefficient $D = \frac{1}{3}R_Lc = \frac{E}{3qB}$, where R_L is the Larmor radius, q is the charge and B is the magnetic field. Substituting this form of the diffusion coefficient, we find that the maximal proton energy is

$$E_{\text{max}} = \frac{3}{20}ZeBV^2T, \quad (1.10)$$

where $q = Ze$ for a nucleus with atomic number Z . Therefore, for a finite duration of the event accelerating cosmic-rays, only a maximum energy can be attained which is proportional to the duration of the event. The condition that the source lasts sufficiently long as to accelerate the cosmic-rays to the highest observed energy will be used in Chap. 4 to determine which sources are best candidates for cosmic-ray production.

As a final comment, Eq. 1.10 seems to suggest that large magnetic fields are connected with cosmic-rays accelerated to high energies. However, if the magnetic field becomes too large, first the high-energy electrons and then the high-energy protons start losing energy by emission of synchrotron radiation (introduced in Sec. 1.2): in this case the maximal proton energy is significantly lower. This subject will be discussed quantitatively in Chap. 4

1.2 Gamma-ray production

The existence of non-thermal charged particles is a natural explanation for the observed astrophysical gamma-rays. The processes by which gamma-rays are produced by cosmic-rays is the subject of the

present section. This is not meant to be a complete overview, and we will only limit to those processes which will be needed in this work.

The production of secondary gamma-rays from cosmic-rays can be broadly divided into leptonic and hadronic mechanisms. In leptonic mechanisms gamma rays are produced via radiative processes, which include bremsstrahlung, synchrotron and inverse Compton radiation. The production is named leptonic since electrons are mainly responsible for it, due to their smaller masses compared to hadrons. In hadronic mechanisms both gamma rays and neutrinos can be produced by the decay of mesons originating from proton collisions. The target of these collisions can either be nuclei at rest, typically from interstellar gas, or low energy photons. These two cases are separately identified as pp and $p\gamma$ interactions respectively. In the next subsections we will discuss each of these production mechanisms separately.

1.2.1 Leptonic gamma-ray production

A first source of high-energy gamma-rays are accelerating charged particles. As known from classical physics, in a given force field the acceleration of a particle is inversely proportional to its mass, so that lighter particles have larger accelerations and consequently emit more radiation. For this reason radiative processes are generally associated with electrons, which are lighter than protons. These electrons can accelerate due to either their Coulomb interaction with nuclei, or their interaction with a magnetic field, or because of scattering with a target radiation field. Accordingly there are three distinct radiative processes, respectively bremsstrahlung, synchrotron and curvature radiation (we will focus on synchrotron radiation only), and Inverse Compton (IC) processes. In this section we will collect the information which will be most useful in this work.

Bremsstrahlung radiation originates from Coulomb scattering between electrons and ions (the ion-ion collision involve particles with larger masses which therefore emit less radiation, whereas in the electron-electron collision the dipole moment of the system, proportional to the center of mass position, does not move because of momentum conservation, so there is no dipole radiation). The cross section for bremsstrahlung is a classic result of both classical and quantum electrodynamics (see, e.g., Refs. [19,20]). The emitted photon spectrum has a characteristic dependence E_γ^{-1} on the photon energy at low energies: this is a universal property in the emission of soft particles. This behavior changes at energies so large that the emitted quanta cannot be considered soft, namely such that $E_\gamma \simeq E$, where E is the characteristic energy of the colliding particles.

Bremsstrahlung can appear in multiple contexts in high energy astrophysics: for example, it can arise from a thermal population of ions and electrons. However, for the purpose of this work, we are mainly interested in the bremsstrahlung radiation originating from relativistic electrons colliding with a target of fixed protons, such as those in the interstellar medium. For this process, the cross section can be approximated as [21]

$$\frac{d\sigma}{dE_\gamma} = \frac{\sigma_{\text{brem}}}{E_\gamma} \theta(E_e - E_\gamma), \quad (1.11)$$

where $\sigma_{\text{brem}} \simeq 3.4 \times 10^{-26} \text{ cm}^2$, and E_e and E_γ are respectively the electron and photon energy^[8]. Hence we see that the differential cross section for photon production approximately does not depend on the electron energy, and produces a spectrum of soft photons with the characteristic dependence E_γ^{-1} .

A second radiative process involving relativistic electrons is synchrotron radiation. This originates when electrons move in a magnetic field: the latter causes the electrons to spiral around the

⁸For collisions off nuclei with charge Z , the cross section approximately increases by a factor Z^2 ; this is only approximately true because of the presence of screening in the collision on atoms.

magnetic field lines, imparting the electrons a centripetal acceleration which makes them radiate. In principle one would expect the electrons, which are rotating with the Larmor frequency $\omega_L = qB/E$ (where B is the external magnetic field), to emit radiation peaked at the same frequency: however, due to relativistic beaming, the radiation is actually peaked at a much higher frequency. In fact the observer only receives radiation when the particle is moving towards them within an angle of order $1/\gamma$. Since the period of the particle is of order $T_L = E/qB$, the portion of the period in which radiation is effectively conveyed to the observer is T_L/γ . The observer measures an even shorter period due to the Doppler effect, equal to $T = T_L(1 - v)/\gamma \simeq T_L/2\gamma^3$. Therefore we finally find that the frequency perceived by the observer is of order $\omega_s \sim 1/T \sim (E/m)^3\omega_L$, where we neglected a factor 2, and m is the electron mass. While this argument is sufficient to determine the peak frequency of synchrotron spectrum, it does not provide the frequency dependence. The spectrum of the emitted photons can be computed in the dipole approximation by decomposing the particle (centripetal) acceleration in its Fourier components [19]: we refer the reader to the literature for the exact formulas in terms of the MacDonald functions. It is found that the spectrum is indeed peaked at a frequency of the order of ω_s , and that the emitted power per unit frequency behaves approximately as $(\omega/\omega_s)^{1/3}e^{-16\omega/3\omega_s}$ [22].

A final radiative process that we will need to consider is Inverse Compton, namely the scattering of a very energetic electron on a low-energy radiation field. Regarded from the rest frame of the electron, this process is simply the scattering of radiation on a fixed particle, so we will start our discussion from this reference frame: we use the prime for quantities in this frame. If the photon frequency ω' (in the electron rest frame) is much smaller than the electron mass, the scattering is just the classical Thomson scattering, for which the cross section $\sigma_T = 8\pi e^2/3m^2$. When the frequency of the incident photon becomes comparable with the electron mass, the classical theory is not applicable anymore (indeed, restoring for a moment the Planck constant, this condition is written $\hbar\omega' \sim m$): this is the Klein-Nishina regime in which the cross section decreases as $\sigma(\omega') \simeq \frac{3}{8}\sigma_T \frac{m}{\omega'} (\log \frac{2m}{\omega'} + \frac{1}{2})$.

Let us discuss the passage from the laboratory frame to the electron rest frame. Assume that ω is the initial photon frequency in the laboratory frame. Then by Lorentz transformations $\omega' = \gamma\omega(1 - \cos\theta)$, where θ is the angle between the photon and electron directions and we have assumed an ultrarelativistic electron. After the collision, the frequency in the electron frame of the final photon ω'_f differs from ω' by terms of order ω'/m , which are relevant only for center-of-mass energies near the Klein-Nishina threshold, when Inverse Compton is suppressed. Therefore, we neglect them and assume $\omega'_f = \omega'$. Translating back to the laboratory frame, we find $\omega_f = \gamma^2\omega(1 - \cos\theta)(1 + \cos\phi)$, where ϕ is the angle between the final photon direction in the electron rest frame and the original electron direction. To obtain a precise estimate, we should average this relation over the angular distribution of the initial and final photons: however, this relation is sufficient to show that the scattered photon frequency is larger than the initial photon one by a factor $\gamma^2 = (E/m)^2$. We will now obtain a more precise estimate by a different argument.

We consider an electron moving with velocity \mathbf{v} in an isotropic bath of photons, which we regard as a fluctuating ensemble of electric and magnetic fields [23]. For a relativistically moving particle the energy radiated per unit time in the field is [19]

$$\left(\frac{dE}{dt}\right)_{\text{rad}} = \frac{2e^4}{3m^2}\gamma^2 \left[(\mathbf{E} + \mathbf{v} \times \mathbf{B})^2 - (\mathbf{E} \cdot \mathbf{v})^2 \right]. \quad (1.12)$$

By averaging this expression over the isotropic ensemble of electromagnetic fields we obtain the mean energy loss

$$\left(\frac{dE}{dt}\right)_{\text{rad}} = \sigma_T U \gamma^2 \left(1 + \frac{v^2}{3}\right). \quad (1.13)$$

This is the total energy radiated by the charge; U is the energy density of the electromagnetic waves. However, a part of this energy is not extracted from the charge itself, but rather is diffused from the photon bath through which the charge is moving. This is just the energy that is diffuse by Thomson scattering, and it corresponds to the emitted energy for $v = 0$. By subtracting this component, we obtain the energy loss of the charge

$$\frac{dE}{dt} = \frac{4}{3}\sigma_T U \gamma^2 v^2. \quad (1.14)$$

For a particle moving through a bath of photons with frequency ω , $U = n\omega$, with n being the photon number density. Therefore, the mean frequency of the photons emitted by Inverse Compton is

$$\omega_f = \frac{4}{3}\omega\gamma^2. \quad (1.15)$$

1.2.2 pp processes

Differently from leptonic processes, pp processes involve the strong interaction of two protons colliding with one another. The proton-proton collision leads to the production of mesons, which ultimately decay into lighter stable particles, namely electrons (and positrons), photons, and neutrinos. In astrophysical environments, pp collisions typically involve a very energetic proton from the cosmic-rays and a non-relativistic proton from the ISM. In this section we will discuss the production of mesons from the pp collision and the subsequent decay of mesons into photons: the decay into neutrinos will be discussed in Sec. [1.3.1](#)

Since we are interested in meson production, we will refer only to the inelastic pp collisions. The cross section for inelastic pp collisions has a threshold at a cosmic proton energy which, in the laboratory frame (assuming the target proton is at rest), is about 1 GeV. After this threshold, the cross section exhibits a logarithmic growth with the energy. Since pp collisions are intrinsically hadronic processes, they cannot be described from first principles, due to the non-perturbative character of strong interactions. The cross sections for these collisions are typically obtained from Monte Carlo generators based on phenomenological models of the strong interaction. The main numerical codes available for this task include PYTHIA [\[24\]](#), QGSJETII-04 [\[25\]](#), SIBYLL [\[26\]](#). These codes are based on different techniques for modeling strong interactions at different energy scales: for example, PYTHIA describes both hard quantum chromodynamics (QCD) processes, based on the leading order parton distribution functions, and soft QCD processes, using phenomenological Regge parametrizations of the data. On the other hand, SIBYLL describes the hard interactions by means of the minijet model, whereas the soft interactions are described with the dual parton model. A recent comparison between the results of these codes can be found in Ref. [\[27\]](#).

From a practical standpoint, the use of numerical codes for the description of pp processes would be rather involved. Therefore, analytical parametrizations are available [\[28\]](#) for the total cross section for pp interaction, $\sigma_{pp}(E_p)$, and the energy spectra of the particles produced in the interaction. The latter are typically expressed in terms of the functions $F_i(x, E_p)$, defined so that

$$dN_i = F_i\left(\frac{E_i}{E_p}, E_p\right) \frac{dE_i}{E_p}, \quad (1.16)$$

where dN_i is the differential number of the i -th species particles with energy E_i , and E_p is the proton energy. The functions F_π and F_η , for the production of π and η mesons, are reported in Ref. [\[28\]](#). Due to isospin symmetry, π^+ , π^- and π^0 are all produced in the same amounts. In terms of these functions, the number of secondary particles injected per unit energy, volume and time is

$$\frac{dN_i}{dE dt dV} = \int_{1 \text{ GeV}}^{+\infty} \frac{dE_p}{E_p} \sigma_{pp}(E_p) n_{\text{ISM}} n_p(E_p) F_i\left(\frac{E_i}{E_p}, E_p\right), \quad (1.17)$$

where n_{ISM} is the ISM density, acting as a target for pp interaction, and $n_p(E_p)$ is the stationary distribution of cosmic-ray protons per unit volume and energy; the lower limit at approximately 1 GeV takes into account the threshold for pp collision.

Gamma-ray production in pp collision happens via the process $\pi^0 \rightarrow \gamma\gamma$. Since this is a two-body decay, in the center-of-mass frame of the pion the two photons carry an energy equal to half the pion mass, and their common line of motion will be distributed isotropically. Converting to the laboratory frame, in which the pion has an energy E_{π^0} , we find that the photon energy is distributed uniformly between the two values $E_\gamma^\pm = \frac{E_{\pi^0}}{2} \left(1 \pm \sqrt{1 - m_\pi^2/E_{\pi^0}^2}\right)$. The distribution for the photons from π^0 decay can then be written as (the factor of 2 comes from the two photons produced in the decay)

$$\frac{dn_{\pi^0 \rightarrow \gamma}}{dE_\gamma} = \frac{2}{\sqrt{E_{\pi^0}^2 - m_\pi^2}} \Theta \left[E_\gamma - \frac{E_{\pi^0}}{2} \left(1 - \sqrt{1 - m_\pi^2/E_{\pi^0}^2}\right) \right] \Theta \left[-E_\gamma + \frac{E_{\pi^0}}{2} \left(1 + \sqrt{1 - m_\pi^2/E_{\pi^0}^2}\right) \right]. \quad (1.18)$$

For relativistic pions, this expression can be simplified to

$$\frac{dn_{\pi^0 \rightarrow \gamma}}{dE_\gamma} = \frac{1}{E_{\pi^0}} F_{\pi^0 \rightarrow \gamma} \left(\frac{E_\gamma}{E_{\pi^0}} \right), \quad (1.19)$$

where we have introduced the notation of Ref. [29] for the decay function, which will be used throughout this work, and

$$F_{\pi^0 \rightarrow \gamma}(x) = 2\Theta(1 - x). \quad (1.20)$$

A smaller contribution comes from the η decay, for which the main decay channels are (in order of decreasing branching) $\eta \rightarrow \gamma\gamma$, $\eta \rightarrow \pi^0\pi^0\pi^0$, $\eta \rightarrow \pi^+\pi^-\pi^0$, $\eta \rightarrow \pi^+\pi^-\gamma$, all of which produce either γ , or π^0 decaying into γ , in the final state. The two-body decay channels can be easily treated like the $\pi^0 \rightarrow \gamma\gamma$ decay above; the three-body decay channels are more complicated because of the higher number of variables. However, as mentioned in Ref. [28], the specific shape of the decay function influences only weakly the results, and furthermore the photons from η decay are secondary anyway.

Even though the analytical parametrizations are sufficiently easy to allow a rapid computation of the secondary spectra in most cases, it is still useful to have an approximate idea of the shape of the secondary spectra. Due to the approximate Feynman scaling in hadronic interactions, the functions $F_i(x, E_p)$ mostly depend on x , and only weakly on E_p . For this reason, there is an approximate scaling in the production of secondary pions: in particular, if the number of protons per unit volume and energy in a source has a power-law spectrum, one similarly expects a power-law injection spectrum for the pions. This conclusion is only approximately true, due to the logarithmic dependence of the pp cross section on the energy, which causes a slight spectral hardening in the pion spectrum compared to a simple power law⁹.

Since scaling is approximately verified in this context, a typical approximation that is used in the literature is that the pion energy is on average $E_\pi = E_p/5$. On the other hand, we have seen that in the pion decay photons have a flat energy distribution between 0 and E_π , so on average they carry an energy $E_\gamma = E_\pi/2$. Therefore, in this approximation photons carry an average energy

⁹Here we have assumed that the stationary distribution of protons was a power law. In more realistic situations, protons are injected with a power-law spectrum, but then suffer energy losses and energy-dependent depletion processes (such as escape from astrophysical sources), so their stationary distribution may be different from a power law. A special situation is the so-called calorimetric one, in which protons mainly lose their energy via the same pp interactions which also produce gamma-rays and neutrinos. In this case, the produced photon spectrum will be a power law with no spectral hardening, because the increase of the pp cross section with the proton energy is balanced by a corresponding increase in the proton energy losses.

$E_\gamma = E_p/10$. For a power-law proton spectrum with a maximal proton energy $E_{p,\max}$, protons with energies above 1 GeV will participate to pp interactions: the resulting gamma-ray spectrum will be approximately a power law between the energies of $1\text{GeV}/10 \simeq 0.1$ GeV and $E_{p,\max}/10$.

1.2.3 $p\gamma$ processes

The second hadronic process of interest in gamma-ray and neutrino production is the collision of high energy protons with low energy photons, or photohadronic collision. Soft photon targets are a common feature of astrophysical environments, and therefore $p\gamma$ processes can be significant in this context.

The threshold for $p\gamma$ interaction is at a center-of-mass energy of about 0.2 GeV. Let us denote by ε_γ and E_p the photon and proton energy respectively. Furthermore, we introduce the angle θ between the proton and photon momenta. The condition for $p\gamma$ interaction therefore can be written¹⁰ as $E_p\varepsilon_\gamma(1 - \cos\theta) \gtrsim 0.04 \text{ GeV}^2$, which depends on the angle between proton and photon. In Ref. [30], it is shown that by averaging the cross section over the angle, under the assumption of an isotropic photon target, the condition can be written as

$$E_p\varepsilon_\gamma \gtrsim \frac{m_p\varepsilon_{\text{th}}}{2}, \quad (1.21)$$

with m_p the proton mass and $\varepsilon_{\text{th}} \simeq 150$ MeV. Whereas for pp interactions the proton energy had to be larger than 1 GeV, from this condition we see that, for typical photon temperatures below the keV, the proton needs energies of the order of 100 TeV to participate to $p\gamma$ interactions. For this reason, $p\gamma$ processes are mainly connected with cosmic accelerators, namely sources where cosmic-rays are accelerated to ultra-high energies: we will detail this point in Chap. 4.

Just like pp processes, photohadronic processes too are generally described by means of numerical codes: the main tool for this task is the Monte Carlo code SOPHIA [31,32]. In this code three main contributions are accounted for in the $p\gamma$ collision: at low energies the cross section is dominated by a number of resonances, the most prominent of which is the Δ -resonance

$$p + \gamma \rightarrow \Delta^+ \rightarrow \begin{cases} n + \pi^+ & 1/3 \text{ of cases} \\ p + \pi^0 & 2/3 \text{ of cases.} \end{cases} \quad (1.22)$$

The branching ratios of the Δ resonance can be obtained by the Clebsch-Gordon coefficients of the isospin state 1/2 (the intermediate Δ resonance) in the two final states.

A second contribution taken into account is the direct production of pions, which are mediated by the t -channel exchange of mesons. This is implemented in SOPHIA using phenomenological fits to the data for the total cross sections. Finally, at higher energies the dominant contribution can be described by means of the exchange of quasiparticles originating from Regge resonances, namely the reggeon and the pomeron. This channel is also generally known as multi-pion production, because of the large number of pions in the final states: the multi-particle production is described in SOPHIA by means of QCD-fragmentation of color strings.

The use of SOPHIA for the simulation of $p\gamma$ interactions can be time-consuming, just as in the pp case. For this reason, simpler analytical approaches are worthy of attention. A commonly used approximation is the use of the Δ -resonance contribution alone, assuming that each secondary carries a fixed fraction of the initial proton energy. For example, for pion production it is assumed that an energy $E_\pi \simeq 0.22E_p$ is carried by the daughter pion [30]. Correspondingly, photons carry

¹⁰Assuming $\varepsilon_\gamma \ll E_p$.

on average an energy $E_\gamma = E_\pi/2 \simeq 0.11E_p$. The neglect of the multi-pion contribution in this approach, however, is not always justified, as emphasized, e.g., in Refs. [22,30,33–35].

Another approximate way of describing neutrino and gamma-ray production is the use of the analytical parametrizations provided in Ref. [36]. Here the spectra of secondary photons and neutrinos from monochromatic protons and photons are provided as analytical fits to the numerical results by SOPHIA. In this approach, the intermediate distributions of secondary pions, neutrons and kaons are not available, so that only the final result for neutrinos and gamma-rays can be used. This approach is simple and complete for the gamma-ray production: on the other hand, in the case of neutrinos, which originate from the decay of charged particles, this information may be incomplete in sources with strong magnetic fields. In this case synchrotron losses may significantly distort the distribution of the intermediate mesons, so that the result of Ref. [36] are not applicable anymore.

The intermediate meson and neutron production in $p\gamma$ interaction can be described using the result of Ref. [30]. Here each of the contribution accounted for in SOPHIA (resonance, direct production and multi-pion production) is parameterized by a collection of interaction types. For each interaction type the secondary particle is assumed to carry a fixed fraction of the proton energy, with an interaction rate depending on the center-of-mass energy. The parameters of each interaction type, namely the fraction of energy carried by the secondary and the interaction rate, are determined. In this way the spectrum of pions, kaons and neutrons injected by $p\gamma$ interactions can be determined. Finally, the gamma-ray spectrum can be obtained from the pion spectrum using the decay function introduced in Eq. [1.20].

The behavior of the pion spectra from $p\gamma$ interactions will be the main subject of Chap. [6], where we will discuss it in quantitative terms. Here we will limit ourselves to some qualitative remarks on the gamma-ray spectra. First of all, if the target photons are at an energy ε_γ , only protons with energy higher than $E_p \gtrsim 70 \text{ TeV}/\varepsilon_\gamma$ [keV] can interact. Since the gamma-rays produced have an average energy $E_\gamma = E_\pi/2$, and the pions have an average energy $E_\pi = 0.22E_p$, the average gamma-ray energy is $E_\gamma = 0.11E_p$, and therefore the minimum energy at which $p\gamma$ photons are produced is of the order of $7 \text{ TeV}/\varepsilon_\gamma$ [keV]. Thus $p\gamma$ photons typically are produced at a much higher energy scale than pp photons. The shape of the spectrum in this region will be discussed^[11] in Chap. [6], where we show that typically it is not a simple power law, as in the case of pp processes, but it depends significantly on the shape of the target photon spectrum.

1.3 Neutrino production

The third component of the multi-messenger framework (neglecting gravitational waves) is the neutrino. Neutrinos are expected to be produced only in the hadronic pp and $p\gamma$ interactions that we have discussed in the previous section. For this reason, they are a fundamental part of the multi-messenger approach: whereas the leptonic or hadronic nature of high-energy gamma-rays is difficult to probe, the observation of neutrinos is a definite signature of hadronic interactions. In this section we discuss the pp and the $p\gamma$ processes, that have been described in the previous section, from the viewpoint of neutrino interaction: more specifically, we will introduce the decay processes of secondary particles which lead to neutrino production.

¹¹The discussion in Chap. [6] is focused on neutrinos: however, the discussion can be extended in a similar way to gamma-rays as well.

1.3.1 pp processes

pp interactions lead to the production of pions in the final state. As was already discussed in the previous sections, neutral pions can subsequently decay into photons. On the other hand, the main decay channel of charged pions^[12] is $\pi^+ \rightarrow \mu^+ \nu_\mu$ and the charge conjugated process for π^- . The muons produced in this way can themselves decay into electrons $\mu^+ \rightarrow e^+ \nu_e \bar{\nu}_\mu$. The full pion decay chain, therefore, ends up in the production of ν_e , ν_μ and $\bar{\nu}_\mu$.

The pion decay is a two-body process, and therefore the energy spectrum of the resulting muon and neutrino can be determined in the same way as the spectrum of the photons in Sec. 1.2.2 with the only complication that the muon is not massless and therefore limits the final available phase-space. The result for the neutrino decay function is

$$F_{\pi^+ \rightarrow \nu_\mu}(x) = \frac{1}{1 - r_\pi} \Theta(1 - r_\pi - x), \quad (1.23)$$

with the definition of decay function as in Sec. 1.2.2 and $r_\pi = (m_\mu/m_\pi)^2$. For the muon decay function one generally needs separately the spectrum of left-handed and right-handed muons, which should be obtained by computing the relevant Feynman diagrams. The result is

$$F_{\pi^+ \rightarrow \mu_R^+}(x) = \frac{r_\pi(1-x)}{(1-r_\pi)^2 x} \Theta(x-r_\pi), \quad F_{\pi^+ \rightarrow \mu_L^+}(x) = \frac{x-r_\pi}{(1-r_\pi)^2 x} \Theta(x-r_\pi). \quad (1.24)$$

In the limit $r_\pi \rightarrow 0$, the pion decays only to left-handed muons, as it should because of the helicity structure of the interaction^[13]. Finally, the decay functions for the two helicity states of the muon to decay into electron and muon neutrinos are

$$F_{\mu^+ \rightarrow \bar{\nu}_\mu} = \left(\frac{5}{3} - 3x^2 + \frac{4x^3}{3} \right) + h \left(-\frac{1}{3} + 3x^2 - \frac{8x^3}{3} \right) \quad (1.25)$$

and

$$F_{\mu^+ \rightarrow \nu_e} = (2 - 6x^2 + 4x^3) + h(2 - 12x + 18x^2 - 8x^3), \quad (1.26)$$

where h is the helicity of the muon. All these decay functions are collected in Ref. [29]. The average fraction of the pion energy carried by the neutrino can be obtained by these probability distributions. The result is that each neutrino carries on average an energy $E_\nu = E_\pi/4$: we observe that this is half of the energy carried by each photon in the corresponding π^0 decay. Since in turn each pion carries on average about 1/5 of the parent proton energy, this leads to the often-used approximation that neutrinos carries a fraction 1/20 of the parent proton energy.

The convolution of these decay functions with the analytical parametrizations for the pion spectra from pp interactions in Ref. [28] leads to the neutrino spectrum: in fact, as also mentioned in Sec. 1.2.2, the same Ref. [28] performs directly this computation and provides the gamma-ray and neutrino spectra from pp collisions. The simple connection between the pion and neutrino spectra we have just described cannot be used in strongly magnetized environments, where, before decaying, pions are subject to strong synchrotron losses.

As in the case of gamma-rays, also for neutrinos a power-law spectrum for protons translates into a power-law spectrum for neutrinos. Therefore, if we have protons with a power-law spectrum, interacting in an energy range between 1 GeV (the lower threshold for pp interactions) and $E_{p,\max}$ (the maximal proton energy), we expect a neutrino power-law flux between 50 MeV and $E'_{p,\max}/20$ with the same spectral index as the proton flux.

¹²The decay into electrons is helicity-suppressed.

¹³In the same limit the decay rate would vanish by helicity suppression.

We now discuss the connection between the gamma-ray and neutrino spectra. This connection arises naturally from the observation that they come from the same process. In pp collisions neutral and charged pions are produced roughly with the same multiplicity, due to isospin symmetry: if we call $Q_i(E_i)$ the number of particles injected per unit energy, volume and time by the interaction, we have $Q_{\pi^+}(E) = Q_{\pi^-}(E) = Q_{\pi^0}(E) = Q_{\pi}(E)$. We make the simplifying assumption, descending from the considerations above, that gamma-rays and neutrinos carry a fixed fraction of the parent pion, specifically $E_{\gamma} = E_{\pi}/2$, $E_{\nu} = E_{\pi}/4$. Since all pions eventually decay into gamma-rays and neutrinos, the final spectra can be written as $E_{\gamma}Q_{\gamma}(E_{\gamma}) = 2[E_{\pi}Q_{\pi}(E_{\pi})]_{E_{\pi}=2E_{\gamma}}$ for photons and $\sum_{\alpha} E_{\nu}Q_{\nu_{\alpha}}(E_{\nu}) = 6[E_{\pi}Q_{\pi}(E_{\pi})]_{E_{\pi}=4E_{\nu}}$, where $\alpha = e, \mu, \tau, \bar{e}, \bar{\mu}, \bar{\tau}$, for neutrinos. By equating the pion spectrum from the two expressions, we find the connection (we multiply by an additional factor of energy to give the expression as typically reported in the literature [37–39])

$$\frac{1}{3} \sum_{\alpha} E_{\nu}^2 Q_{\nu_{\alpha}}(E_{\nu}) = \frac{1}{2} [E_{\gamma}^2 Q_{\gamma}(E_{\gamma})]_{E_{\gamma}=2E_{\nu}}. \quad (1.27)$$

This expression relates the neutrino and gamma-ray spectrum at their source. The condition translates to a condition on the observed fluxes, provided that the gamma-ray fluxes reach the Earth without any distortion: this is not generally true, because gamma-rays undergo scattering processes during their propagation to the Earth. Furthermore, they might be partially absorbed within the source itself, if there are low-energy photons on which they can scatter: in this case the source becomes opaque. The question of gamma-ray propagation is discussed in more detail in Chap. 2.

Finally, let us comment on the flavor composition of neutrinos produced in pp interactions. In the scenario described above, in each pp interaction we have the production of an equal number of π^+ and π^- : the former produces in its decay the particles ν_e, ν_{μ} and $\bar{\nu}_{\mu}$, and the latter produces the charge-conjugate particles. Therefore one expects a fraction of muon neutrinos (and antineutrinos) equal to twice the fraction of electron neutrinos (and antineutrinos); of course no tau neutrinos are expected, since the tau lepton is too massive. The fraction of neutrinos and antineutrinos are equal in this mechanism. The information on flavor composition is generally given in terms of the flavor ratio, namely the fraction of the flux in each of the three flavors: in our case the flavor ratio is (1:2:0). Since the origin of these neutrinos is the full decay chain of pions, this flavor composition is known as pion beam. Strong magnetic fields can modify this conclusion: however, they are rare in pp sources.

1.3.2 $p\gamma$ processes

For $p\gamma$ collisions the main process determining the neutrino production is again pion decay. The convolution of the decay functions given in the previous section with the pion injection spectrum, obtained as described in Sec. 1.2.3, allows to determine the neutrino spectra from pion decay in $p\gamma$ interaction. Neutrinos are also produced from neutron decay $n \rightarrow p + e^{-} + \bar{\nu}_e$, which leads to electron antineutrinos only, and kaon decay $K^+ \rightarrow \mu^+ \nu_{\mu}$. Both these contributions are generally smaller, and are mainly important in strong magnetic fields, which we will discuss below. Neutrinos carry on average an energy $E_{\nu} = E_{\pi}/4$: since in turn pions carry an average energy $E_{\pi} = 0.22E_p$ for Δ -resonance interaction, the average neutrino energy can be written as $E_{\nu} = 0.05E_p$.

As we also mentioned in Sec. 1.2.3, photohadronic production of neutrinos will be discussed mainly in Chap. 6. In the same way as for gamma-rays, also neutrinos from $p\gamma$ interactions are expected at the highest energies: repeating the same derivation made at the end of Sec. 1.2.3, and taking into account that neutrinos carry on average only 1/4 of the pion energy, we find that $p\gamma$ neutrinos are produced in a range between $3.5 \text{ TeV}/\varepsilon_{\gamma} [\text{keV}]$ and $0.05E_{p,\text{max}}$.

Let us determine the multi-messenger connection between the gamma-rays and neutrinos from pion decay in the case of $p\gamma$ processes. The relation among the average energies is still the same as in pp processes, namely $E_\gamma = E_\pi/2$, $E_\nu = E_\pi/4$. However, the ratio between the number of charged pions and neutral pions is not the same as in pp processes, and is harder to predict in a general way. The two main contributions to pion production in this case are the Δ -resonance and the multi-pion production. Δ -resonance, according to Eq. [1.22](#), gives rise approximately only to π^+ and π^0 , with the latter being produced with twice the probability of the former. Multi-pion production, on the other hand, produces all three pions. A reasonable average, typically used in the literature, is that the cumulative production of Δ -resonance and multi-pion leads to a fraction of π^0 roughly equal to that of charged pions, so that $E_\pi Q_{\pi^0}(E_\pi) \simeq E_\pi Q_{\pi^+}(E_\pi) + E_\pi Q_{\pi^-}(E_\pi)$. In this case the multi-messenger connection in Eq. [1.27](#) changes to

$$\frac{1}{3} \sum_{\alpha} E_\nu^2 Q_{\nu_\alpha}(E_\nu) = \frac{1}{4} [E_\gamma^2 Q_\gamma(E_\gamma)]_{E_\gamma=2E_\nu}. \quad (1.28)$$

The two conditions for pp (Eq. [1.27](#)) and $p\gamma$ (Eq. [1.28](#)) can be written compactly in terms of the parameter $K_\pi = \frac{E_\pi Q_{\pi^+}(E_\pi) + E_\pi Q_{\pi^-}(E_\pi)}{E_\pi Q_{\pi^0}(E_\pi)}$. For pp interactions $K_\pi \simeq 2$, and for $p\gamma$ interactions $K_\pi \simeq 1$; in general

$$\frac{1}{3} \sum_{\alpha} E_\nu^2 Q_{\nu_\alpha}(E_\nu) = \frac{K_\pi}{4} [E_\gamma^2 Q_\gamma(E_\gamma)]_{E_\gamma=2E_\nu}. \quad (1.29)$$

Regarding the flavor composition of $p\gamma$ neutrinos, in the scenario depicted above it is still pions that give rise to neutrinos, and therefore the flavor ratio is still (1:2:0). However, since the ratio of π^+ to π^- is changed, the corresponding neutrino to antineutrino ratio can be different: for the ideal Δ -resonance, for example, the neutrino to antineutrino ratio would be 2:1.

Another important component of neutrinos from $p\gamma$ interaction is originated from neutron decay. In fact neutrons produced in the Δ -resonance $p\gamma \rightarrow \pi^+ n$ typically carry 4/5 of the parent proton energy, and in turn in the decay of a neutron $n \rightarrow p e \bar{\nu}_e$ the neutrino carries an average fraction of the neutron energy equal to 5.1×10^{-4} (see, e.g., [30](#)). Since this fraction is so low, neutrinos coming from neutron decay may dominate over the neutrinos from pion decay in the low energy part of the spectrum. In this case the production is dominated by electron antineutrinos, so the flavor composition is (1:0:0): this flavor regime is known as neutron beam.

These conclusions on the flavor composition are only valid in the absence of strong magnetic fields. If this condition is violated, then charged mesons may be subject to severe energy losses due to synchrotron radiation. These synchrotron losses for a particle with mass m can be obtained by integrating the synchrotron spectrum given in Sec. [1.2.1](#), or, more easily, by using the Larmor formula for dipole radiation [19](#) with the acceleration produced by the Lorentz force. The result, for a magnetic field B and for ultra-relativistic particles of mass m and charge e , is

$$b(E) = \frac{dE}{dt} = \frac{4e^4 B^2 E^2}{9m^4}. \quad (1.30)$$

From this relation we see that lighter particles with high energies lose their energy more rapidly. In the decay chain leading to neutrino production $\pi^+ \rightarrow \mu^+ \nu_\mu$, $\mu^+ \rightarrow e^+ \nu_e \bar{\nu}_\mu$ (we do not write the charge-conjugated processes), the muons are lighter than pions and may be subject to synchrotron losses before them. Their decay may then be inhibited because they are moved to lower energies. In this case only π decay producing ν_μ , and the flavor composition becomes (0:1:0), the so-called muon-damped regime [40,41](#). The neutrino to antineutrino ratio does not change from our previous discussion. The condition for this to happen can be formulated in terms of the timescales for the

Composition	Flavor ratio at source	Process
Pion beam	(1:2:0)	$\pi \rightarrow \mu + \bar{\nu}_\mu,$ $\mu \rightarrow e + \bar{\nu}_e + \nu_\mu$
Muon-damped regime	(0:1:0)	$\pi \rightarrow \mu + \bar{\nu}_\mu$
Muon beam	(1:1:0)	$\mu \rightarrow e + \bar{\nu}_e + \nu_\mu$
Neutron beam	(1:0:0)	$n \rightarrow p + e + \bar{\nu}_e$
Kaon beam	(0:1:0)	$K^+ \rightarrow \mu^+ + \nu_\mu$

Table 1.1: Summary of the flavor compositions discussed in the text.

processes: the timescale of synchrotron radiation can be defined as $\tau_{\text{synch}} = E/b(E)$. If muons decay slower than this timescale, then they are damped by the losses. Since the decay lifetime is $\tau_{\text{decay}} = \tau_\mu E/m_\mu$, where τ_μ is the lifetime in the center of mass frame, the condition for muon-damped regime is

$$E \geq \sqrt{\frac{9m_\mu^5}{4e^4 B^2 \tau_\mu}}. \quad (1.31)$$

Above this critical energy, neutrinos from muon decay become suppressed.

The muons damped by the synchrotron losses are moved at lower energies, and may produce a pile-up of neutrinos in this energy range, as shown in Ref. [22]. If these neutrinos dominate over the ones produce by pion decay, the resulting flavor composition is known as muon beam. In this case, muon decay produces a flavor composition (1:1:0). The muon-beam regime was originally proposed at very high energies from decays of heavy charmed mesons [42].

At the very highest energies, pion decay can be inhibited too by synchrotron losses: this happens if the condition, analogous to Eq. [1.31],

$$E \geq \sqrt{\frac{9m_\pi^5}{4e^4 B^2 \tau_\pi}} \quad (1.32)$$

is verified. In this case also pions will be damped to lower energies by the synchrotron losses. The steepening of the spectrum can be described by means of the Fokker-Planck equation taking into account synchrotron losses and decay lifetime; see, e.g., Ref. [22].

Finally, above the critical energy [1.32], a component which might become relevant are neutrinos from kaon decay. These are produced in less quantities in $p\gamma$ collisions, but their larger masses make them less sensitive to synchrotron losses. If neutrinos from kaon decay dominate, the flavor composition is (0:1:0).

We summarize the flavor compositions typically expected in astrophysical sources in Table [1.1], collecting the processes which originate neutrinos in each case. We emphasize that an astrophysical source is expected to produce an energy-dependent flavor ratio, with different flavor compositions dominating at different energies depending on the interplay among synchrotron losses and the decay lifetimes of the different mesons [29, 43, 44].

Chapter 2

Multi-messenger propagation

2.1 Cosmic-ray propagation

It was already mentioned in Sec. [1.1](#) that cosmic-rays propagating in galactic and intergalactic magnetic fields are deflected by the Lorentz force. Due to the turbulent nature of these magnetic fields, the trajectory of the particles has a diffusive character, analogous to the trajectories of Brownian motion. In this section we will describe qualitatively the character of this propagation, and we will obtain order of magnitude estimates for the diffusion coefficient describing it: we refer to Appendix [C](#) for a more rigorous mathematical treatment of this problem.

Let us assume the presence of a strong regular magnetic field B directed along the z axis and a weaker turbulent component $\delta\mathbf{B}(\mathbf{r})$. The unperturbed trajectory of the particle, without the turbulent field, would be a spiral orbit along the axis z of the regular field; the radius of the spiral is the Larmor radius. If the turbulent field varies over length scales much larger than the Larmor radius, then the magnetic field is changing adiabatically. In this case the particle will simply follow the direction of the magnetic field lines without being deflected much from its unperturbed trajectory [19](#). On the other hand, if the turbulent field varies over length scales much smaller than the Larmor radius, the particle will be deflected on microscopic length scales (compared to the Larmor radius), but will feel on average no effect. These observations suggest that the particle will be mainly diffused by magnetic fields changing on the scale of the Larmor radius, so the scattering by magnetic fields has a resonant character. This resonance can also be looked upon from another point of view. In a frame in which the particle is not moving along the axis z , the spatial variation of the turbulent field is felt as a temporal variation with a frequency $\omega = k_z v_z$, where k_z is the wave number and v_z is the particle velocity along the z axis. The particle is at the same time orbiting around the axis z with the Larmor frequency $\Omega = \frac{qB}{E}$, with q being the particle charge and E its energy. If the two frequencies are equal, the particle exhibits a cyclotron resonance [45](#), absorbing energy resonantly from the varying (in the frame defined above) magnetic field.

The order of magnitude of the deflection suffered by cosmic-rays can be estimated by physical arguments. The process can in fact be regarded as the collision of cosmic-rays on turbulent magnetic waves of a fixed wavelength, which by the resonance condition must be of the order of the Larmor radius. If we denote by δu_k the fraction of the magnetic energy density that is in the form of magnetic waves with this wavelength, the scattering rate will be proportional to δu_k . Since the only parameter with the dimensions of time entering the problem is the (reciprocal) Larmor frequency,

the scattering rate is expected to be of the order of $\Gamma \sim \Omega \delta u_k$ ¹. Therefore, similarly to a gas of colliding particles, cosmic-rays will diffuse with a diffusion coefficient of order

$$D \sim \frac{1}{3} v^2 \Gamma^{-1} \sim \frac{v^2}{3\Omega \delta u_k}. \quad (2.1)$$

A rigorous treatment for the case of the turbulent field much weaker than the regular one (the so-called quasi-linear theory, see, e.g., Ref. [46]) shows that this simple formula gives the correct order of magnitude and dependence on the parameters, even though it skips over the important difference between diffusion parallel and transverse to the regular magnetic field.

Let us estimate the energy dependence of the diffusion coefficient. The particle energy enters Eq. 2.1 both in the Larmor frequency and in δu_k , which should be evaluated at the resonance wavenumber $k \simeq \frac{\Omega}{v} = \frac{qB}{Ev}$. δu_k measures the fraction of energy contained in the turbulent magnetic field, and its dependence on the wavenumber is determined therefore by the nature of the turbulent motions originating the magnetic field. Although a quantitative theory of turbulence has yet to be formulated, simple arguments are sufficient to obtain this dependence for the case of fully developed turbulence of a non-magnetic fluid: these lead to the so-called Kolmogorov model of turbulence (see, e.g., Ref. [7]). The idea is that turbulence can be regarded as the flow of energy from large vortices to small vortices, down to the smallest scale motions which are dissipated by viscosity. Therefore, if v_k is the velocity of the vortices with wavenumber of order k , there is a net flux of energy per unit mass of the order of $q \sim \frac{v_k^2}{k^{-1}/v_k}$. This flux should be independent of the wavelength, in the typical fashion of cascade processes, and therefore $v_k \propto k^{-1/3}$. The energy contained at this wavenumber is therefore $E_k \propto v_k^2 \propto k^{-2/3}$. If there is a rough equipartition between the kinetic energy of the fluid and the energy contained in the turbulent magnetic perturbations, then we expect the same behavior for δu_k . Following this argument, we write

$$\delta u_k \simeq \delta u_{k_0} \left(\frac{k}{k_0} \right)^{-2/3}. \quad (2.2)$$

By substituting this result in Eq. 2.1, we find that $D \propto E^{1/3}$. This dependence is reflected in the energy dependence of the time that the cosmic-rays spend inside a Galaxy like our own, namely the escape time: this time is of order $\tau_{\text{diff}} \simeq l^2/D \propto E^{-1/3}$, where l is a characteristic length of the Galaxy. A different prediction would be obtained if the ISM were a strongly magnetized fluid: in this case there would still be a net flux of energy per unit mass q flowing from large-scale to small-scale perturbations. However, the mechanism with which the perturbations are dissipated is not anymore viscosity, but rather the interaction among magnetic waves. The rate of energy dissipation must then be proportional to the rate of collision of random magnetic waves, which depends on the fourth power of v_k . By dimensional arguments it must be $q \sim \frac{v_k^4}{u_A k^{-1}}$. Since the energy is $E_k \propto v_k^2$, we find $E_k \propto k^{-1/2}$, which is indeed the result of the Kraichnan model for turbulence in magnetized fluids [6]. In this case the escape time would decrease as $E^{-1/2}$.

A way to verify these predictions is through the ratio between the concentration of carbon and boron in the cosmic-rays. The reason is that boron is not a primary component of cosmic-rays and is instead produced when carbon nuclei collide with the nuclei from the ISM. Therefore, the concentration of boron must be proportional to the time that the carbon nuclei spend in the Galaxy. Indeed, the measurement of the boron to carbon ratio shows an energy dependence as $E^{-\delta}$, with δ

¹The dimensional argument is not sufficient to exclude powers of the dimensionless ratio m/E . However, since the equations of motion in a static magnetic field involve only the energy of the particle, and not its rest mass, these factors can be excluded a priori.

close to 0.3 [47], in very good agreement with the prediction of the Kolmogorov model for turbulence. The order of magnitude that is deduced for the diffusion coefficient at around 10 GeV is $D \simeq 10^{28} \text{ cm}^2 \text{ s}^{-1}$ [8].

Finally, let us comment on the diffusion coefficient in the case of strong turbulence, for which we obtained by simple arguments the Bohm form in Sec. 1.1. The quasi-linear theory developed here and in App. C does not rigorously apply to the case of strong turbulence. However, we see that the relations which we have derived indeed reproduce the Bohm result if we take $\delta u_k \simeq 1$. Therefore, even though this result is beyond the limits of validity of quasi-linear theory, it suggests that the Bohm form for the diffusion coefficient is generally motivated in the case of strong turbulence.

The diffusion by turbulent hydromagnetic waves described here is only one of the processes affecting the propagation of cosmic-rays. Its effect is to add a term to the right-hand side of the transport equation of the form

$$\left(\frac{\partial f}{\partial t}\right)_{\text{diff}} = \nabla \cdot (D \nabla f). \quad (2.3)$$

Here f is the phase space distribution² of the cosmic-rays. Let us give a general overview of other processes which can be relevant, and their effect on the transport equation:

- when one is interested in the nuclear composition of the cosmic-rays, a fundamental process is spallation, namely the collision of cosmic-ray nuclei on the hydrogen nuclei of the ISM. As a result of this collision, heavy nuclei split up into lighter nuclei. The description of spallation requires the introduction of distribution functions f_i for each species of nuclei; the production of lighter nuclei can then be described by an effective interaction rate $\frac{d\Gamma_{i \rightarrow j}}{dE}$ representing the probability per unit time of production of the species j with energy E from the collision of a nucleus i . We do not investigate this subject further, since it will not appear in the works discussed in this thesis, and instead refer the reader to the literature (e.g. [8]). For extragalactic propagation of cosmic-rays, a similar process to account for is photodisintegration of heavy nuclei on low-energy photons, in particular the photons from the Cosmic Microwave Background and the Extragalactic Background Light (see Sec. 2.2), through the reaction ${}^A X \gamma \rightarrow {}^{A-1} X N \gamma$. The energy threshold for this process is at around 10^{10} GeV;
- in the discussion above we have always assumed the magnetic perturbations to be static, so that they cannot do work on charged particles. In reality these perturbations move with a velocity which is reasonably distributed isotropically and of the order of the Alfvén velocity v_A . The correction coming from the motion of the Alfvén waves, of order v_A^2/c^2 , can be obtained by changing the diffusion equation derived in App. C to a moving reference frame. However, the result can be guessed even without doing the calculation: since the velocity of the waves is isotropically distributed, particles will gain an energy of the order of $E \frac{v_A}{c}$ in head-on collisions and lose the same energy in the opposite case. On average they will suffer a quadratic stochastic gain of energy $E^2 \frac{v_A^2}{c^2}$ for each collision. Since the collision rate is of order Γ as estimated above, we expect a stochastic increase of energy per unit time of order $\frac{\langle \delta E^2 \rangle}{\delta t} \simeq \Gamma E^2 \frac{v_A^2}{c^2}$. Indeed the results of a more detailed treatment [48] shows that a Fokker-Planck term is added to the right-hand side of the transport equation

$$\left(\frac{\partial f}{\partial t}\right)_{\text{reacc}} = \frac{1}{p^2} \frac{\partial}{\partial p} \left(p^2 \frac{\langle \delta v^2 \rangle}{c^2} E^2 \left[\int_{-1}^{+1} \frac{d\mu}{2} D_{\mu\mu} \right] \frac{\partial f}{\partial p} \right), \quad (2.4)$$

²We actually refer to the distribution already averaged over the direction of the particle momentum.

where $D_{\mu\mu}$ is the pitch-angle diffusion coefficient defined in App. C and $\langle\delta v^2\rangle$ is the velocity dispersion of the magnetic waves, which is indeed of the order of v_A^2 . This is generally known as the reacceleration term; its main effects are felt at low energies, below the GeV;

- if the medium in which cosmic-rays move has a macroscopic motion with velocity $\mathbf{u}(\mathbf{r})$ (such as in the presence of strong galactic winds, as will be the case in Chap. 5), we have seen in Sec. 1.1.1 that the transport equation is changed by two terms in the right-hand side, which we write separately for clarity

$$\left(\frac{\partial f}{\partial t}\right)_{\text{adv}} = -\mathbf{u} \cdot \nabla f, \quad (2.5)$$

and

$$\left(\frac{\partial f}{\partial t}\right)_{\text{ad}} = \frac{1}{3} \nabla \cdot \mathbf{u} p \frac{\partial f}{\partial p}. \quad (2.6)$$

The first term here represents the advection of cosmic-rays, which are transported by the wind; the second term represents the adiabatic energy losses, due to the effective expansion of the medium in which cosmic-rays are moving³;

- for the hadronic component of the cosmic-rays there are a number of processes which lead to energy losses. These include: the Bethe-Heitler collision on low-energy photons $p\gamma \rightarrow pe^+e^-$, which is the dominant energy loss mechanism between 10^9 GeV and 10^{10} GeV, the pp collision with interstellar and intergalactic gas (this is the main energy loss process within our galaxy: we will consider it again in Chap. 4 since it is an expected source of gamma-rays and neutrinos), and the $p\gamma$ collision with low-energy photons. The latter is the most important process above 10^{10} GeV, and is expected to make the extragalactic sky opaque to ultra-high energy cosmic-rays: this threshold energy is generally known as the Greisen-Zatsepin-Kuzmin [49, 50] (GZK) cutoff. We will consider it in more detail in Chap. 4 since this process is expected to be an important source of ultra-high energy of neutrinos, named cosmogenic neutrinos;
- for the leptonic component of cosmic-rays the relevant processes for energy loss are of course different. At low energies the dominant process is ionization loss by Coulomb interactions with the atoms; at higher energies the radiative processes described in Sec. 1.2.1 namely the emission of photons by bremsstrahlung, synchrotron and Inverse Compton processes, are the most important sources of energy loss. Leptonic energy losses are of diffusive character, meaning that in each elementary event they lead only to a small fraction of the lepton energy to be lost: therefore they can be dealt with by adding a Fokker-Planck term to the right-hand side of the transport equation

$$\left(\frac{\partial f}{\partial t}\right)_{\text{loss}} = \frac{\partial}{\partial E} (b(E)f), \quad (2.7)$$

where $b(E) = \langle -\frac{dE}{dt} \rangle$ is the average energy loss, written as the sum of the contributions from all the relevant processes. All the leptonic processes mentioned here are also active for hadrons interacting electromagnetically. However, due to their larger masses, they are generally less relevant. These radiative processes can influence, for example, the propagation of light mesons: we have seen an example in Sec. 1.3.2 where synchrotron losses were responsible for the steepening of the pion spectrum at high energies.

³In fact this term can be accommodated to effectively account for the cosmological redshifting of energy of extragalactic cosmic-rays simply by assuming the classical Hubble law $\mathbf{u}(\mathbf{r}) = H(t)\mathbf{r}$ with $H(t)$ the Hubble parameter: this is of course a phenomenological way of describing the energy redshifting.

Collecting the terms corresponding all these processes one obtain the complete diffusion-loss equation describing the propagation of cosmic-rays in the Galaxy. A common approximation adopted in practical calculation is to use the momentum distribution $n(p, t) = \frac{1}{V} \int d^3\mathbf{r} f$ averaged over the spatial coordinates (here V is the total volume of the galaxy in which cosmic-rays are contained). In doing the integral of the transport equation, the diffusion and the advection term are integrated over the volume to give

$$\left(\frac{\partial n}{\partial t}\right)_{\text{adv}} + \left(\frac{\partial n}{\partial t}\right)_{\text{diff}} = \frac{1}{V} \int d^3\mathbf{r} \left[\left(\frac{\partial f}{\partial t}\right)_{\text{adv}} + \left(\frac{\partial f}{\partial t}\right)_{\text{diff}} \right] = -\frac{1}{V} \int d\Sigma \cdot (\mathbf{u}f - D\nabla f), \quad (2.8)$$

where we have converted the volume integral into an integral over the boundary of the region in which the cosmic-rays are confined (which typically is a galaxy). In this form it is clear that the effect of diffusion and advection on the number of particles per unit momentum is that of depleting the particles via their escape flow from the boundaries of the galaxy. In a phenomenological way this term is often written as

$$\left(\frac{\partial n}{\partial t}\right)_{\text{adv}} + \left(\frac{\partial n}{\partial t}\right)_{\text{diff}} = -\frac{n}{\tau_{\text{adv}}} - \frac{n}{\tau_{\text{diff}}}, \quad (2.9)$$

where $\tau_{\text{adv}} \sim l/u$, $\tau_{\text{diff}} \sim l^2/D$, and l is a characteristic dimension of the galaxy. This approach is generally known as the leaky-box model for cosmic-rays.

The approach to the cosmic-ray propagation outlined in this section is of course a simplified one, which however suits our purposes for this thesis: in particular, we will refer to this approach in Chap. 5 for the cosmic-ray protons propagation in starburst galaxies, and in Chap. 7 for the electron propagation in extragalactic and galactic environments.

2.2 Gamma-ray propagation

Gamma-ray propagation is considerably simpler than the cosmic-ray one, by virtue of the neutrality of photons. Because of this, gamma-rays are not deflected by cosmic magnetic fields and move straightforwardly from their sources to the Earth. Nevertheless, their propagation is not completely trivial because of their possible interaction with the low-energy photons they encounter on their way. This is the main subject of this section.

For definiteness, we start our discussion with extragalactic propagation. The existence of low-energy radiation in extragalactic environments is an established one. A well-known component of this radiation is the Cosmic Microwave Background (CMB), namely the relic radiation left over from the primordial plasma after the Universe became neutral. CMB has a blackbody spectrum, since it originated from a strongly coupled plasma of photons and electrons, and its present temperature is about 2.73 K, or 0.2 meV. Furthermore its redshift evolution is easy to describe at least until recombination, at $z \sim 1100$, since the number density simply scales as $n(z) \propto (1+z)^3$. The second most important component of radiation is Extragalactic Background Light (EBL), which has a double bump structure where the first bump (cosmic optical background) originates from stellar nucleosynthesis, and the second bump (cosmic infrared background) originates from optical and ultraviolet radiation absorbed by dust and reradiated as infrared. Since its formation is strongly intertwined with the formation history of galaxies, the knowledge of EBL is much more uncertain than CMB. Recent parametrizations and fit to the EBL energy and redshift dependence are given in Refs. 51, 52.

The propagation of high-energy gamma-rays in cosmic environments is significantly affected by these low-energy photons. The reason is that two photons can interact in a pair production reaction

$\gamma\gamma \rightarrow e^+e^-$. The minimum squared center-of-mass energy required for the reaction is evidently $(2m_e)^2$, where m_e is the electron mass. If the energetic gamma-ray has energy E_γ and the soft photon has energy ϵ_γ , their squared center-of-mass energy is $E_\gamma\epsilon_\gamma(1 - \cos\theta)$, where θ is their relative angle. Therefore in order of magnitude, if ϵ_γ is the typical energy of EBL photons⁴, gamma-rays will be affected which have an energy

$$E_\gamma \gtrsim \frac{m_e^2}{\epsilon_\gamma}. \quad (2.10)$$

For an EBL energy around $\epsilon_\gamma \simeq 1$ eV we find a minimum energy at which absorption begins of about $E_\gamma \simeq 250$ GeV. Therefore, in terms of the density of low-energy photons per unit energy $n(\epsilon_\gamma, z)$, a photon with energy E_γ at the Earth, produced at a redshift z_i , will experience an optical depth

$$\tau(E_\gamma) = \int_0^{z_i} \frac{dz}{H(z)(1+z)} \int d\epsilon_\gamma \int_0^\pi \frac{\sin\theta d\theta}{2} \sigma_{\gamma\gamma}[E_\gamma(1+z), \epsilon_\gamma, \theta] n(\epsilon_\gamma, z). \quad (2.11)$$

Here $\sigma_{\gamma\gamma}$ is the cross-section for pair production [20] as a function of the energies of the two photons and the angle θ between their directions. This optical depth leads to an effective absorption of the high-energy photons, and the absorption coefficient is $e^{-\tau(E_\gamma)}$: because of this, the extragalactic sky is essentially opaque to photons with energies much larger than 100 GeV.

Even though photons with sufficiently high energy cannot reach the Earth, their energy is not lost in the process $\gamma\gamma \rightarrow e^+e^-$, but rather it is transferred to the secondary electrons. These electrons can themselves collide with the ambient photons in Inverse Compton interaction $e\gamma \rightarrow e\gamma$, producing new gamma-rays. Therefore the initial collision gives rise to a cascade of particles which reprocesses the original photon energy into a new photon spectrum at lower energies. A precise description of this cascade requires the numerical solution of the transport equations for the electron and photon distribution: this is implemented, e.g., in the code γ -CASCADE [53].

The cascade produced in the interaction has a shape which can be understood qualitatively at least in the case of large propagation lengths (see, e.g., [54]). In this case the cascade has the time to develop and reach a universal shape which we now describe. Let us take the simplest case of a monochromatic soft photon target with energy ϵ_γ :

- at high energies, $E_\gamma > \frac{m_e^2}{\epsilon_\gamma}$, in the limit of very large propagation lengths all the photons interact and we expect the photon flux to be completely attenuated;
- at intermediate energies, $\frac{m_e^2}{3\epsilon_\gamma} < E_\gamma < \frac{m_e^2}{\epsilon_\gamma}$, the gamma-rays attenuated by the $\gamma\gamma$ collision are continuously replenished by the Inverse Compton photons. In this region each particle approximately transfers half of its energy to both the secondaries, and therefore the process has all the features of a multiplicative cascade. Such cascades are well-known in the theory of extensive air showers [8], and they are known to lead to a spectrum of the form $n_\gamma(E_\gamma) \propto E_\gamma^{-2}$. This universal form of the spectrum can be understood by observing that it contains exactly the same amount of energy in each decade of energy of the particle, as is typical of scale-invariant problems. A simple way of obtaining this result is the following: we call P_γ the probability (per unit length) of interaction of a photon, and P_e the corresponding probability for electrons. After the cascade has propagated for a long time, an equilibrium is established in which the production of each particle is balanced by its absorption. Then the following

⁴We take the EBL photons because they have higher typical energies than the CMB ones, and therefore can affect even lower energy gamma-rays.

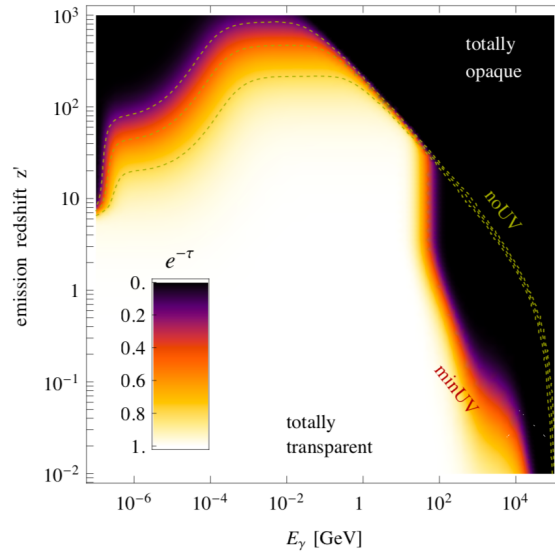


Figure 2.1: Attenuation factor due to $\gamma\gamma$ collisions as a function of photon energy and redshift. Figure taken from Ref. [55].

equations must be satisfied

$$\begin{aligned} n_\gamma(E_\gamma)P_\gamma &= n_e(2E_\gamma)P_e, \\ n_e(E_e)P_e &= n_e(2E_e)P_e + 2n_\gamma(2E_e)P_\gamma. \end{aligned} \quad (2.12)$$

This equation admits indeed the solution $n_e(E_e) \propto E_e^{-2}$, $n_\gamma(E_\gamma) \propto E_\gamma^{-2}$;

- at low energies, $E_\gamma < \frac{m_e^2}{3\epsilon_\gamma}$, gamma-rays cannot anymore interact with the soft photons, because of the low energy. On the other hand, electrons can still interact: in each interaction they produce a photon which has on average the typical Inverse Compton energy $4E_e^2\epsilon_\gamma/3m_e^2$ (see Sec. 1.2.1). In this regime electrons are not produced, and they only continuously lose their energy with a constant energy flux $n_e(E_e)dE_e/dt \simeq \sigma_T n_T n_e(E_e)4E_e^2\epsilon_\gamma/3m_e^2$, where σ_T is the Thomson cross section and n_T is the number density of the target soft photons. Since this flux must be constant, it must be $n_e(E_e) \propto E_e^{-2}$. By integrating over the Inverse Compton emissivity, this implies a photon spectrum $n_\gamma(E_\gamma) \propto E_\gamma^{-3/2}$.

Therefore we reach the result that the gamma-ray flux is attenuated and reprocessed by the cascading process into a lower energy flux. This flux has a universal structure of a broken power law, with a low-energy phase dominated by Inverse Compton emission and a higher energy phase with the typical shower structure. The total energy of the reprocessed cascade flux is approximately equal to the initial energy of the absorbed photons. Since this energy is reprocessed in a flux with a behavior E^{-2} , one typically expects the cascade contribution to be significant if the original photon spectrum is harder than E^{-2} .

A graphical representation of the impact of $\gamma\gamma$ collisions on EBL and CMB is provided in Fig. 2.1 where we show the attenuation factor (without accounting for cascades) due to $\gamma\gamma$ collisions. The Universe becomes essentially opaque to gamma-rays even at very low redshifts at energies of about 10 TeV.

2.3 Neutrino propagation

Compared to gamma-rays and cosmic-rays, the propagation of neutrinos from their sources to the Earth is much simpler, at least in the Standard Model. Neutrinos are in fact weakly interacting particles which propagate freely, so that the source emissivity determines in a simple way the neutrino flux at the Earth. Non-standard physics may change this simple statement: in fact, Chaps. 8 and 9 are devoted to such non-standard effects in neutrino propagation.

The only complication to the simple standard scenario is the presence of flavor oscillations during neutrino propagation, which we now discuss. The reason behind neutrino oscillations is the difference between flavor and mass eigenstates. In the Standard Model, the weak interaction Lagrangian selects three neutrino states, namely the electron, muon and tau neutrino, interacting diagonally with their respective lepton SU(2) partner. Here and throughout this thesis we denote these flavor eigenstates by Greek indices: thus ν_α are flavor eigenstates, with $\alpha = e, \mu, \tau$.

The mass term of the neutrinos, on the other hand, has an origin which is still unclear: by similarity with the mass terms for the other particles, it likely originates from the Yukawa interaction of neutrinos with a scalar field acquiring a vacuum expectation value. The precise mechanism however is still not known: it may involve additional heavy neutrinos, leading to the so-called seesaw mechanism [56–58], or non-standard right-handed counterparts to neutrinos providing a Dirac mass, or it may involve no additional species, with a Majorana mass term for the standard neutrinos. Here we adopt an effective mass term independent of the high-energy physics which originated it⁵

$$\mathcal{L}_{\text{mass}} = - \sum_i m_i \bar{\nu}_i \nu_i. \quad (2.13)$$

The Latin indices are used here to refer to a new set of states, which are generally linear combination of the flavor eigenstates, and which we call mass eigenstates. The dispersion relation for the i -th mass eigenstate is $E(p) = \sqrt{m_i^2 + p^2}$. The inequality between mass and flavor eigenstates is responsible for the phenomenon of neutrino oscillations: in fact, an electron produced by weak interaction in the α -th flavor eigenstate will propagate freely as a superposition of mass eigenstates. Each mass eigenstate acquires a different phase during the propagation, due to the different dispersion relations, generating a finite amplitude for the original neutrino to evolve to a different flavor. The oscillation probabilities depend on the connection between the mass and the flavor eigenstates: the general convention is

$$|\nu_\alpha\rangle = U_{\alpha i} |\nu_i\rangle, \quad (2.14)$$

where U is the unitary Pontecorvo-Maki-Nakagawa-Sakata (PMNS) matrix [59,60]. As a general 3×3 unitary matrix, U is parametrized by 9 real numbers in general, three of which are mixing angles of a real orthogonal matrix; the remaining six are phases. However, we have 5 free parameters corresponding to the five independent phase redefinition of the lepton and neutrino fields⁶. Therefore, 5 of the 9 parameters can be absorbed in these 5 transformations. For Majorana neutrinos the situation is slightly different, in that the neutrinos phases cannot be redefined: therefore only 3 phases can be eliminated by redefining lepton fields. In summary we are left with a unitary matrix parametrized by 3 mixing angles and 1 (3) phase for Dirac (Majorana) neutrinos. The updated values for these best-fit parameters from oscillation experiments are reported in Refs. [61]

Let us now apply this formalism to neutrinos originated in astrophysical sources. The weak decay of hadrons produces a neutrino, say, in the flavor eigenstate α . In its propagation to Earth,

⁵However, we do assume Dirac mass term for simplicity.

⁶For the 6 fields of neutrinos and leptons one would expect 6 independent phases: however, a redefinition of all lepton and neutrino fields by a global phase leaves the Lagrangian unchanged, and thus does not change the PMNS matrix.

its different component in mass eigenstates, with amplitude $U_{\alpha i}$, acquire a dephasing

$$\Phi_i = p_i l = \sqrt{E^2 - m_i^2} l \simeq El - \frac{m_i^2}{2E} l, \quad (2.15)$$

where p_i is the momentum of the i -th mass eigenstate, E is its energy and l is the propagation length (this procedure is discussed in greater detail in Chap. 9, where we will apply it to the propagation in a gravitational field). The different amplitude for mass eigenstates will therefore acquire a relative dephasing. According to the standard rules of quantum mechanics, the probability of detecting the neutrino at Earth with flavor β is

$$P_{\alpha \rightarrow \beta} = \left| \sum_i U_{\alpha i} U_{\beta i}^* \exp \left[i \frac{m_j^2 - m_i^2}{2E} l \right] \right|^2. \quad (2.16)$$

In principle Eq. 2.16 provides an exact relation for the probability of flavor conversion. However, the detection of neutrinos always involves a finite energy resolution, meaning that the neutrino energy should be averaged over some probability distribution depending on the observed energy. Another source of uncertainty comes from the propagation length, since naturally the precise position of the neutrino in the astrophysical source is not known. The uncertainties on the energy and on the position of the neutrino are so large, compared with the oscillation lengths defined by $2E/(m_j^2 - m_i^2)$, that the oscillating factors vanish after the average. Therefore, the average equation should be used in place of Eq. 2.16

$$\bar{P}_{\alpha \rightarrow \beta} = \sum_i |U_{\alpha i}|^2 |U_{\beta i}|^2. \quad (2.17)$$

Due to mixing, the flavor composition of astrophysical neutrinos observed at the Earth is generally different from that with which the neutrinos are produced: in $f_{\alpha}^{\text{source}}$ is the fraction of neutrinos in the α flavor at the source, the corresponding fraction at Earth is

$$f_{\beta}^{\text{Earth}} = \sum_{\alpha} P_{\alpha \rightarrow \beta} f_{\alpha}^{\text{source}}. \quad (2.18)$$

Chapter 3

Detection of gamma-rays and neutrinos

The detection of the high-energy messengers from astrophysical sources is of course a key subject of this dissertation. This chapter is devoted to this question. We focus on gamma-rays and neutrinos, namely the secondary messengers of the cosmic-ray production in astrophysical sources. In particular, we review the main experiments, both current and planned, aimed at detecting high-energy gamma-rays (Sec. [3.1](#)) and neutrinos (Sec. [3.2](#)).

3.1 Gamma-ray detectors

The detection of high-energy gamma-rays requires dedicated instrumentation. Astrophysical gamma-rays do not reach the surface of the Earth, due to absorption in the atmosphere. When a gamma-ray enters the atmosphere, it rapidly loses its energy in a cascade of particles induced by the pair production and bremsstrahlung processes. In order to overcome this difficulty, two complementary approaches have been proposed: space-based and ground-based detectors.

3.1.1 Space-based detectors

Space-based detectors naturally overcome the difficulty of atmosphere absorption, whereas they have to face many technical challenges. These detectors are typically sensitive between 300 keV and 300 GeV. Since we will mainly be interested in ultra-high energy gamma-rays, these detectors are less relevant for this dissertation. However, as we will see (see Chap. [4](#)), the observations of diffuse gamma-rays can significantly constrain some scenarios of high-energy neutrino production.

The detection of gamma-rays in space-based telescopes is based on two main processes, namely Compton scattering and pair production: the latter is more relevant above 10 – 20 MeV. The Fermi Large Area Telescope (Fermi-LAT) is based on the process of pair production, and is therefore sensitive mainly from 20 MeV up to hundreds of GeV (we do not discuss here the Fermi Gamma Burst Monitor). The LAT is composed of a tracker, made of active material which can track the products of pair conversions, a calorimeter, and an anti-coincidence detector. We do not enter the detail of the experiment, for which we refer the reader to the literature [\[64\]](#).

For the purposes of this thesis, we are mainly interested in the LAT measurements of the extragalactic gamma-ray background (EGB) [\[62, 63\]](#). The EGB is the superposition of gamma-rays

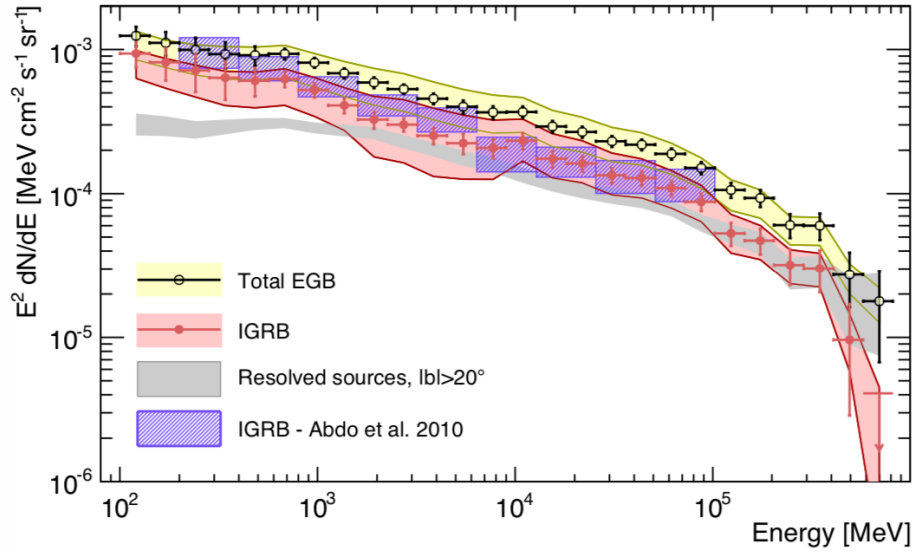


Figure 3.1: IGRB and EGB intensities measured by Fermi-LAT [62] as a function of the energy. The EGB measurements are shown in black (yellow uncertainty band), the IGRB are shown in red, the resolved sources are shown as a gray band. The original measurements of the IGRB in Ref. [63] are shown in blue. Figure taken from Ref. [62].

from extragalactic sources, which include most of the sources discussed in Chap. 4, such as Active Galactic Nuclei, Gamma-Ray Bursts, and starburst galaxies. For each population, the contributions from resolved and unresolved sources are superposed. The relative magnitude of these contributions depend on the typical luminosities of the source class. For example, blazars are sufficiently bright that even at cosmological distances they can be individually resolved, allowing for robust estimates of the relative contribution of resolved and unresolved sources. On the other hand, Active Galactic Nuclei with misaligned jets and starburst galaxies are more rarely detected as individual sources. Therefore, they are believed to mainly contribute to the unresolved emission, even though this can only be determined on the basis of some physical model for their luminosity evolution. The separation between resolved and unresolved component has been performed originally by the EGRET Collaboration [65, 66] and later by the Fermi-LAT Collaboration [62]. The contribution from unresolved sources is generally known as Isotropic diffuse Gamma-Ray Background (IGRB). The total EGB is then by definition the sum of the IGRB and the resolved sources intensity. We emphasize that, while the EGB is a well-defined quantity independently of the measurement instrument, the IGRB necessarily depends upon the potential of the instrument in resolving individual sources. As a final comment, the measurements of the IGRB may in principle be affected by contamination from diffuse Galactic emission.

While the first measurements of the EGB have been provided by the SAS-2 satellite [67] and EGRET [68], the LAT has improved the limits on the EGB by a factor of about 10, based on 50 months of data taking. A large portion of the EGB has been identified by Fermi-LAT with known point-like and extended sources within the many catalogs released by the Fermi-LAT Collaboration. The largest fraction of these sources has been identified with AGN, which therefore are believed to constitute the dominant contribution to the gamma-ray sky. We show in Fig. 3.1 the IGRB measured by Fermi-LAT, as well as the total EGB. The abrupt decrease at the energies around

100 GeV is due to the opacity of the Universe to gamma-rays via $\gamma\gamma$ collisions, described in Chap. 2. As shown in Ref. [69], the EGB spectrum is well explained by a dominant blazar component, with a component from radio-galaxies which becomes comparable at energies below ~ 1 GeV. Star-forming galaxies are shown to contribute only a small amount to the total EGB. In Chap. 5 we will revisit these estimates in light of a more detailed determination of the diffuse gamma-rays from starburst galaxies.

3.1.2 Ground-based detectors

Ground-based detectors can only detect gamma-rays through the products of the cascades generated in atmosphere. This is typically done by targeting either the Cherenkov radiation produced by the secondary particles in the cascade (Imaging Air Cherenkov technique), or the charged particles in the cascade reaching the ground (Extensive Air Shower technique). We discuss these two techniques in turn.

Cherenkov radiation is naturally emitted by the ultra-relativistic particles in the showers formed by gamma-rays in the atmosphere. Given the refractive index in air, a shower forming at an altitude of about 2 km originates a Cherenkov cone which reaches the ground in a ring with a radius of about 120 m. In order to detect this radiation, Imaging Air Cherenkov Telescopes (IACTs) are placed in arrays with spacings of the order of a hundred meters. The Cherenkov radiation, which is mainly in the optical range, is focused by the wide mirrors of each IACT into a camera formed by a densely packed array of photomultiplier tubes.

One of the main challenges of IACTs is the discrimination of signal over the background. IACTs typically operate in moonless nights, to minimize contamination from optical sources. Furthermore, the short duration of the Cherenkov signal of a shower (of the order of tens of ns) allows to distinguish the signal over the Poisson fluctuations in the night sky background. Even so, a fundamental source of background is constituted by showers originating from ultra-high energy cosmic-rays. Imaging of the Cherenkov light produced from the shower is the key tool for discriminating gamma-ray from cosmic-ray induced showers: indeed, in these two cases different lateral distributions are obtained for the light emitted from the shower.

The state of the art of the IACTs is represented by three main arrays: the High Energy Stereoscopic System (HESS) Observatory [70] and the Very Energetic Radiation Imaging Telescope Array System (VERITAS) [71] in the Northern hemisphere, and the Major Atmospheric Gamma-ray Imaging Cherenkov (MAGIC) [72] in the Southern hemisphere. A promising advance in the IACTs technology is expected with the future Cherenkov Telescope Array (CTA) [73]. While current IACTs typically host from two to five telescopes, CTA will be composed of two arrays of more than 100 telescopes disposed over two sites, in the Northern and Southern hemisphere. This will allow a sensitivity ten times larger than the present instrumentation, as well as a larger collection area spanning both hemispheres.

A second class of ground-based detectors is constituted by Extensive Air Shower (EAS) arrays, namely instruments that detect the charged radiation from EASs reaching the ground. Because of this requirement, typically EAS arrays are placed at higher altitudes than IACTs and their target are higher energy gamma-rays and cosmic-rays. The array may be composed either of Resistive Plate Chambers or of water Cherenkov tanks, which work on the calorimetric principle detecting the Cherenkov light from charged particles passing through the detector. Because of their working principle, water Cherenkov detectors have generally a worse angular resolution than IACTs, but they have a wider field of view, since they do not need to be pointed to a specific source, and they do not require night-sky observations, therefore having a much higher duty cycle. The last two properties make water Cherenkov detectors particularly suited for transient high-energy observations.

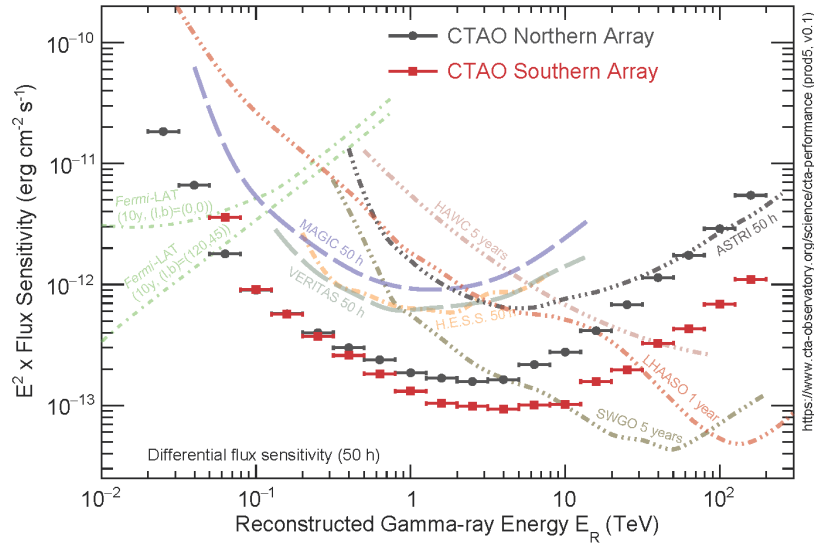


Figure 3.2: Differential flux sensitivity of different classes of gamma-ray detectors. Figure taken from <https://www.cta-observatory.org>.

Among the present EAS arrays we mention High-Altitude Water Cherenkov Observatory (HAWC), consisting of 300 water tanks at an altitude of about 4 km. Due to its feasibility for transient source detection, HAWC has been able to detect 19 previously undetected TeV gamma-ray sources [74]. A future improvement in EAS arrays is constituted by LHAASO, which will reach an unprecedented sensitivity in the high-energy region. LHAASO will be constituted by an array of electromagnetic particle detectors (LHAASO-KM2A), spanning an area of 1.3 km²; a water Cherenkov detector facility, with a sensitive area of about 42000 m²; a 1 km² underground water Cherenkov array for muon detection; an array of 18 air Cherenkov telescopes.

As a comparison of the properties of space-based and ground-based detectors, we show in Fig. 3.2 the 5 σ differential sensitivity of the main experiments mentioned above. The comparison among different classes of experiments can only be performed roughly, due to the different criteria for sensitivity estimation and the different field of view, which, as we remarked above, is much wider for EAS arrays than for IACTs. However, the improvement in the CTA sensitivity compared to previous IACTs installments such as MAGIC and VERITAS is clearly seen. At energies larger than 10 TeV, larger sensitivities are reached by EAS experiments such as LHAASO.

3.2 Neutrino detectors

The detection of neutrinos with energy larger than 100 TeV has been a notoriously hard task for experimental physics, which culminated with IceCube’s discovery of an extraterrestrial flux of neutrinos in 2010. In this section, we will briefly discuss the challenges posed by high-energy neutrino detection, and the strategy to overcome them in the so-called neutrino telescopes. Afterwards, we will describe the complementary strategy of neutrino radio detection, on which various planned detectors will be based.

3.2.1 Neutrino telescopes

The detection of high-energy neutrinos requires a rather large instrumentation. A simple way to understand this requirement is to start from the Waxman-Bahcall estimate of the diffuse neutrino flux presented in Chap. 4. While this was proposed as an upper limit, it is a reasonable estimate of the neutrino flux which has been effectively observed by IceCube. Thus we use $\frac{d\Phi}{dE_\nu} \simeq 2 \times 10^{-7} E_\nu^{-2}$ GeV cm⁻² s⁻¹. We will use a very simplified representation of a neutrino detector as a volume V of instrumented material with density $\rho \simeq 0.9$ g cm⁻³. Taking the charged current cross-section for neutrino-nucleon interaction of the order of $\sigma \simeq 5 \times 10^{-39} E_\nu$ cm² GeV⁻¹ [61], we find for the order of magnitude of the event rate at around 100 TeV

$$\frac{dN}{dt} = 18 \text{ yr}^{-1} \frac{V}{1 \text{ km}^3}. \quad (3.1)$$

This is a very simplified and optimistic estimate, which does not account for the absorption of neutrinos in their propagation through the Earth, as well as the efficiency of detection: for a more realistic estimate, see, e.g., Ref. [75]. Even in this simplified framework, this estimate shows that a sizable number of neutrinos detected per year requires a km³-scale detector. The realistic estimate decreases the expected number of events to about 1.5 per year.

The principle of detection of neutrinos in neutrino telescopes is to look for the products of a neutrino interaction within or immediately outside of the detector. Neutrinos interact either via charged-current interactions

$$\nu_\alpha + N \rightarrow \ell_\alpha + X, \quad (3.2)$$

with N nucleon, X a generic final state, and ℓ_α the corresponding lepton, or via neutral-current interactions

$$\nu_\alpha + N \rightarrow \nu_\alpha + X. \quad (3.3)$$

In both cases, the final state is characterized by the presence of relativistic charged particles, which can be detected via their Cherenkov emission. Therefore, present neutrino telescopes are generally based on an array of digital optical modules (DOMs) detecting the Cherenkov emission from particles in the final state. The timing of the different DOMs in the array, as well as the number of photons detected by each of them, can be used to reconstruct the initial position of interaction of the neutrino, its energy, its arrival time, and its direction. Therefore, for a good detection the target medium in which the secondary particles propagate must be transparent.

The requirement of a large amount of transparent target material for neutrino detection led in 1993 to the construction of the first Antarctic Muon And Neutrino Detector Array (AMANDA) [76]. This was realized by deploying strings of optical sensors within the ice. AMANDA was able in this way to detect atmospheric neutrinos. The experiment was later incorporated into IceCube [77].

IceCube uses as target material a cube of ice with a volume of 1 km³, endowed with 86 strings of optical sensors, for a total of 5160 DOMs. Near the center of the detector, a denser subarray of photomultiplier tubes, named DeepCore [78], allows a larger sensitivity to low-energy neutrinos (below 100 GeV). Finally, on top of the cube of ice there is a surface detector, named IceTop, aimed at the detection of cosmic-rays.

A number of other telescopes have been constructed or are under construction to complement IceCube. At present, ANTARES [79] is located in the Mediterranean sea, in the Northern hemisphere. Since it is located in the opposite hemisphere than IceCube, it complements the latter in terms of angular sensitivity. A future experiment also located in the Mediterranean sea is KM3NeT [80],

¹At energies higher than about 100 TeV the proportionality to the energy is expected to change, but this estimate is realistic at 100 TeV.

which will be composed of the two experiments ARCA and ORCA. ARCA will be a neutrino telescope similar to IceCube, instrumented over a volume slightly larger than 1 km^3 . On the other hand, ORCA will be mainly devoted to observations of low-energy neutrinos. A final experiment under construction is the neutrino telescope under Lake Baikal in Russia [81]. Finally, IceCube itself is expected to be upgraded to IceCube-Gen2 [82], which will have an instrumented volume of 10 km^3 , allowing for an order of magnitude increase in the rate of detected neutrinos.

Topologies of neutrino events

Depending on the properties of the final state of the neutrino-nucleon interaction, two main categories, or topologies, of neutrino events are distinguished, namely tracks and showers.

When the final state of the interaction contains a muon, namely in the case of charged-current interactions of muon neutrinos (Eq. 3.2 with $\alpha = \mu$), such a muon produces a track-like signature while propagating in the detector. For this reason, these events are known as tracks. The corresponding electron and tau neutrino charged-current interaction do not produce tracks, because the electron is subject to large energy losses by bremsstrahlung, and the tau has a much shorter decay length. Therefore, both electron and tau neutrinos would not produce a track, because the corresponding lepton would release its energy nearly immediately after the production (however, at the highest energies the tau neutrino can decay over larger lengths, see below). Track events allow a neutrino detection that is close to common astronomy. In fact, the array of DOMs can reconstruct the trajectory of the muon passing through the detector. Due to relativistic beaming, the trajectory of the muon is very close to the one of the incident neutrino. For this reason, the direction of the neutrino can be reconstructed for track events to within an accuracy of about 1° (for water Cherenkov detectors, such as ANTARES and KM3NeT, this can be as low as 0.5° ; this is due to the smaller scattering length of ice compared to water, which can partially degrade the resolution in ice). On the other hand, the energy of the incident neutrino can be reconstructed only with partial accuracy, since the muon escapes the detector and therefore carries a fraction of the original energy which is not recovered.

For electron and tau neutrino charged-current interactions, the original neutrino energy is completely released either in bremsstrahlung radiation in the case of the electron, or in the lepton decay in the case of the tau. Therefore, the signature in this case is a shower which contains most or all of the original neutrino energy. This allows for a more accurate energy reconstruction compared to track events. On the other hand, the length of the shower is typically small compared with the distances between the DOMs. Therefore, the shower appears nearly as point-like, making the reconstruction of the original neutrino direction difficult. The typical angular resolution which can be achieved is of the order of 15° .

While track events are quite unambiguously identified with muon neutrinos, shower events from charged-current interactions could come both from electron and tau neutrinos, and flavor reconstruction would require discriminating between the showers from the two flavors. A strategy for discrimination at energy below 1 PeV has been proposed in Ref. [83], based on the different signature in the collective light emitted in muon decays and in neutron captures on the hydrogen nuclei. At higher energies, however, the most promising strategy is based on the observation that the tau lepton decay length can become larger than the distances between the DOMs, due to relativistic time dilation. When this happens, the original vertex of neutrino interaction could be resolved from the point at which the tau lepton decays. Therefore, the event would appear not as a point-like shower, but rather as a first shower, corresponding to the neutrino vertex interaction; a track, corresponding to the propagation of the tau lepton; a second shower, corresponding to the decay of the tau lepton. This additional topology is known as double bang, and has been recently confirmed by IceCube

observation of two candidate double bang events [84]. This observation provides an unambiguous confirmation that the astrophysical neutrino flux also contains tau neutrino².

For neutral-current interactions of any flavor neutrinos, the final state is characterized by a neutrino escaping the detector and a hadronic shower, originating from the energy released to the nuclei. Since the neutrino escapes, this shower allows only partial energy reconstruction. Furthermore, since the cascade is hadronic, it releases most of its energy in mesons, and a part of it in muons, which can escape the detector too. Neutral-current showers could also be partially discriminated on the basis of the technique of Ref. [83].

IceCube observations of astrophysical neutrinos

Arguably the greatest breakthrough in neutrino astronomy was the discovery in 2013 by IceCube of a diffuse high-energy neutrino flux of astrophysical origin [85]. In order to distinguish these extraterrestrial neutrinos from the atmospheric neutrinos generated by cosmic-ray interactions in the atmosphere, IceCube has adopted different strategies, resulting in complementary data samples published by the collaboration. Here we focus on three of these data samples, namely the High-Energy Starting Events, the throughgoing muons, and the high-energy cascades.

The High-Energy Starting Events (HESE) are selected as only those events which have their interaction vertex completely contained within the detector. This is done by defining a veto region surrounding the volume of the detector, and excluding the events which trigger the DOMs in this veto region. In this way, downgoing atmospheric muons are rejected, since they would enter the detector from above and pass through the veto region. The veto procedure also allows to partially reject downgoing atmospheric neutrinos, which should be accompanied with high probability by a downgoing muon. With Monte Carlo simulations, the relation between the neutrino energy and the energy deposited in the detector, as well as the residual rate of background atmospheric events, has been estimated by the IceCube Collaboration. IceCube has detected a statistically significant excess over the predicted rate from atmospheric neutrinos, which can therefore be identified with astrophysical ones.

The most recent update of the HESE data has been released in Refs. [84, 86]. We report in Fig. 3.3 the energy and zenith angle distribution of the neutrinos observed by IceCube. The histogram columns represent the fraction of events corresponding to atmospheric muons, atmospheric neutrinos, and astrophysical neutrinos. These fractions of events are obtained by fitting the expected angular and spectral distribution of the three components to the observed data (for the unknown astrophysical component IceCube studies typically use an isotropic power-law spectrum, even though they have shown that the results do not change significantly for different choices, e.g., broken power law). At energies above 60 TeV (above the cyan region), the data are dominated by astrophysical neutrinos, and the atmospheric background becomes negligible. The small decline for negative $\cos(\theta_z)$ is due to Earth absorption, which as expected is completely efficient for the charged muons, and only marginally affects the lower energy neutrinos. The best-fit astrophysical energy spectrum obtained is

$$\frac{d\Phi_{6\nu}}{dE} = \Phi_{\text{astro}} \left(\frac{E_\nu}{100\text{TeV}} \right)^{-\gamma_{\text{astro}}} \cdot 10^{-18} \text{ GeV}^{-1} \text{ cm}^{-2} \text{ s}^{-1} \text{ sr}^{-1}, \quad (3.4)$$

with best-fit values $\Phi_{\text{astro}} = 6.37^{+3.46}_{-1.62}$ and $\gamma_{\text{astro}} = 2.87^{+0.21}_{-0.19}$.

²Among other consequences, this could be regarded as a strong confirmation of the validity of the neutrino oscillation framework. Indeed, tau neutrinos are not expected to be produced in standard astrophysical processes, and thus they could be detected at Earth due to oscillations during their propagation. This feature will be discussed also in Chap. 9.

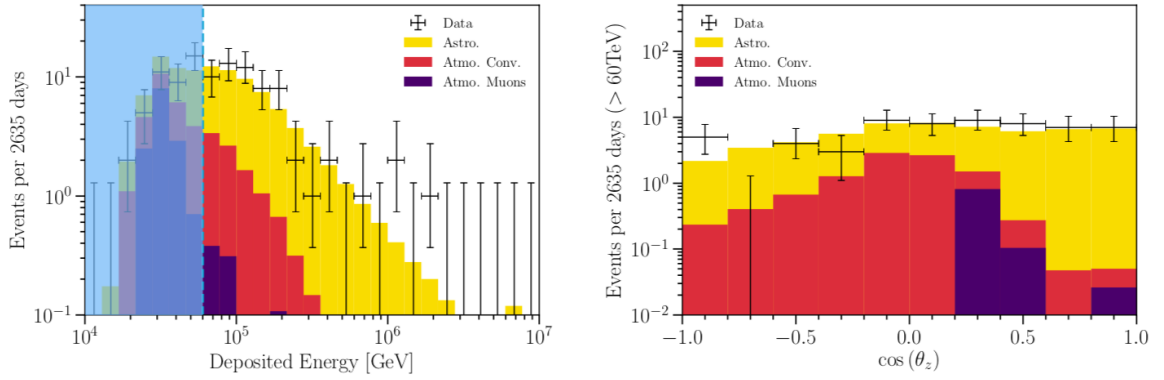


Figure 3.3: Energy (left panel) and zenith (right panel) distribution of HESE. The observed number of events in each bin are reported as black points; the expected number of astrophysical neutrinos (yellow), atmospheric neutrinos (red), and atmospheric muons (purple), obtained by statistical fit, are reported as histograms. The cyan region below 60 TeV are not considered for the statistical analysis of Ref. [86]. Figure taken from Ref. [86].

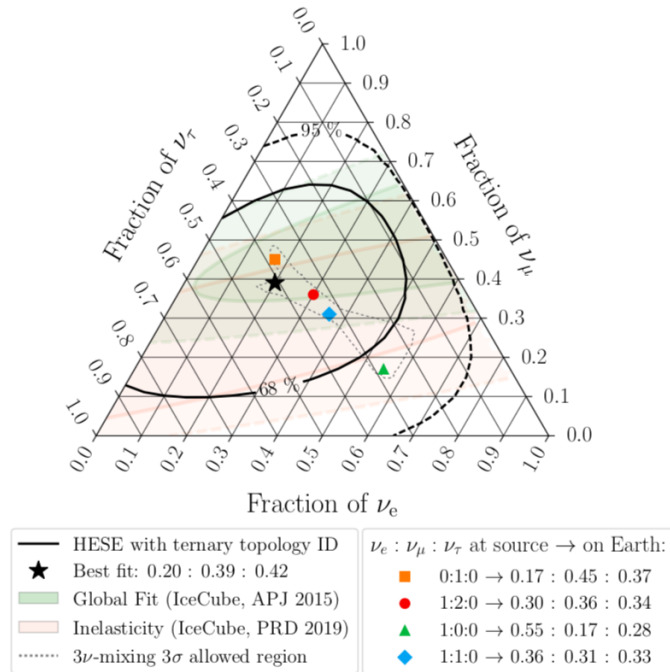


Figure 3.4: Flavor composition of astrophysical neutrinos inferred from HESE data. Contours inferred from previous data samples [87,88] are shown as shaded regions. Figure taken from Ref. [84].

The best-fit flavor composition of the astrophysical flux inferred from the HESE data is shown in Fig. 3.4 in the flavor triangle. The data are consistent at 68% confidence level with pion-beam (red point), muon-damped (orange point), and muon-beam (cyan point) flavor composition. Due to the identification of two candidates for double bang events, a flavor composition with no tau neutrinos at the Earth is excluded at 95% confidence level. The case with no muon neutrinos at the Earth is also excluded, since track/shower discrimination allows to definitely test the presence of muon neutrinos in the flux.

The discrimination between neutrinos and antineutrinos is more difficult to perform, due to the similar properties of the final states of interaction. One possibility is offered by the resonant charged-current scattering $\bar{\nu}_e + e \rightarrow W^- \rightarrow X$, where the final state X can be either leptonic or hadronic. The resonance of this interaction is known as Glashow resonance, and for electrons at rest it arises at an antineutrino energy of 6.3 PeV. Therefore, one expects an increase in the event rate at around this energy depending on the fraction of electron antineutrinos. The IceCube Collaboration has recently reported [89] the observation of an event with properties consistent with a Glashow resonance event. As emphasized in this paper, with more statistic it will be possible to discriminate among different scenarios based both on flavor composition and on the neutrino/antineutrino ratio.

A second data sample provided by the IceCube Collaboration is that of the throughgoing muons, which is based on a complementary approach to background rejection. For this sample only upgoing track events, namely upgoing charged-current muon neutrino events. Due to Earth absorption, there is little to no contamination due to atmospheric muons. The updated release of this data sample has been given in preliminary form in Ref. [90]. The throughgoing muons data sample has also been analyzed to determine the best-fit astrophysical muon neutrino spectrum, leading to the result

$$\frac{d\Phi_{\nu_\mu+\bar{\nu}_\mu}}{dE} = (1.44_{-0.24}^{+0.25}) \left(\frac{E}{100\text{TeV}} \right)^{-2.28_{-0.09}^{+0.08}} \cdot 10^{-18} \text{GeV}^{-1} \text{cm}^{-2} \text{s}^{-1} \text{sr}^{-1}. \quad (3.5)$$

Comparing Eq. 3.4 and Eq. 3.5, we find a near-2- σ tension between the spectral indices estimated by the two data samples. The origin of this discrepancy is at present unknown: possible proposed explanations involve either a purely statistical fluctuation, or the presence of different components. Indeed, the throughgoing muons data sample is mainly composed of upgoing neutrinos from the Northern hemisphere, and therefore is less sensitive to neutrinos from the Galactic centre, whereas the HESE data sample is mainly sensitive to neutrinos from the Southern hemisphere. Therefore, a galactic component with a softer spectral index could possibly explain the HESE/throughgoing muons tension. In Chap. 7 we will explore this possibility in the framework of a model of decaying dark matter producing neutrinos, leading to an anisotropic production toward the Galactic centre.

The final data sample we discuss in this work is the sample of cascade events released in Ref. [91]. These data are mostly sensitive to electron and tau neutrino fluxes, which produce mainly showers, and have only a $\sim 10\%$ fraction of muon neutrinos. Since the sample consists only of cascades, which have a good energy reconstruction, it is particularly suited for the determination of the spectral shape of the flux. Indeed, the best-fit spectral index for this data sample has the lowest uncertainty $\gamma = 2.53 \pm 0.07$ (using the same notations as above), and is somewhat intermediate between the results of HESE and throughgoing muons.

3.2.2 Neutrino radio arrays

At energies higher than 10 PeV, due to the power-law decrease of the neutrino flux, even a 1 km³ detector would lead to negligibly small event rates over a year timescale. Therefore, different approaches must be followed for ultra-high energy neutrino detection.

In order to increase the effective volume of the detectors, an approach that has been pursued is that of enlarging the interaction volume to the entire atmosphere of the Earth. This is the strategy followed by the so-called radio arrays. The main principle of detection of these detectors is the extensive air shower which develops after a neutrino interacts in the atmosphere. An electromagnetic shower emits radio waves coherently, partially due to the magnetic field of the Earth, which separates electrons from positrons. A second radio emission is due to the progressive production of an excess of electrons over positrons in the shower, due both to the Compton production of electrons and to the annihilation of positrons with the electrons in the medium. This excess negative charge behaves like a current, producing coherent radio emission. This effect was first predicted by Askaryan in Refs. [92,93], and is therefore known as Askaryan effect. The radio emission from the shower can propagate practically with no attenuation and can therefore be detected even at large distances from the shower. This makes it possible to detect ultra-high energy neutrinos, cosmic-rays, and gamma-rays, using as target material large volumes of material, which typically is chosen as ice, air, or water. Among the planned radio detectors, we mention RNO-G [94], which will consist of 35 stations with tens of antennas per each, aimed at the detection of in-ice generated showers; IceCube-Gen2 Radio Array [95,96], which will complete IceCube-Gen2 with an array of station devoted to observations of ultra-high energy showers, and will improve the RNO-G sensitivity by about an order of magnitude; GRAND [97], which is a planned array of radio telescopes using as target material large volumes of atmosphere. While the final stage of GRAND, referred to as GRAND200k, will be composed of 200000 antennas, an intermediate stage of construction known as GRAND10k will be composed by 10000 antennas.

A second principle of detection, on which also GRAND is based, is the detection of Earth-skimming tau neutrinos [98-112]. When a tau neutrino enters the Earth with ultra-high energy, it eventually collides with the nuclei in the rocks via charged-current interaction, producing an outgoing tau lepton. Since at the highest energies the tau lepton has a relatively large lifetime (the decay length is about $\ell \simeq 50 \text{ m}(E/\text{PeV})$) and relatively small energy losses in Earth, it can escape the Earth and enter the atmosphere from below. Its subsequent decay produces a shower³ which is either hadronic or electromagnetic, depending on the decay channel of the tau lepton. The electromagnetic light emitted by the particles in the shower allows then to identify the event. This detection principle is adopted, for example, by GRAND, and it allows to detect neutrinos passing through the Earth at small angles with the surface. For vertical neutrinos, with large angles to the surface, absorption typically makes the Earth opaque to the propagation of neutrinos. Searches for Earth-skimming tau neutrinos have already been performed by the ultra-high energy cosmic-ray detectors Pierre Auger Observatory (PAO) [110,113] and by MAGIC [114]. The non-observation of such events has allowed to constrain the magnitude of the diffuse neutrino flux at ultra-high energies.

³This is actually the same mechanism of the double bang topology in neutrino detectors, which is however extended over length scales comparable with the dimensions of the atmosphere due to the Lorentz boost at the higher energies involved.

Chapter 4

Gamma-ray and neutrino astrophysical sources

We described in Chap. 1 the processes leading to cosmic-ray acceleration, as well as neutrino and gamma-ray production. It remains to be discussed what are the astrophysical environments in which these processes can happen. This is the subject of the present chapter. Following the literature, we divide the discussion in two qualitatively different environments for neutrino and gamma-ray production. In the first one, the so-called cosmic accelerators, pp and $p\gamma$ collisions happen directly in the same environment in which the cosmic-rays are initially accelerated. In the second one, named cosmic reservoirs, cosmic-rays are injected in a larger environment, typically with the dimensions of galaxies or galaxy clusters, and are confined within it by the collisions with interstellar material. For each class, we review the main astrophysical sources proposed and what we currently know about their multi-messenger production. Our discussion is mostly focused on those properties of the source which are relevant for pp and $p\gamma$ collisions, and on how neutrino and gamma-ray observation can provide information in this respect. Therefore, the discussion is not meant to be a comprehensive review of the astrophysics of these sources, which is a wide field of study.

4.1 Cosmic accelerators

The sources in which cosmic-rays are accelerated are natural candidates for the production of hadronic neutrinos and gamma-rays; these secondary particles could escape the source and reach the Earth, providing unique information on the presence of hadronic cosmic-rays within the source (the escape of gamma-rays is of course possible only if the source is gamma-ray transparent). By definition nearby these sources we have a population of high-energy cosmic-rays which may collide hadronically with targets of low-energy photons or nucleons. In this section we will describe some of the main candidates for cosmic-ray accelerators, focusing on the expectations for neutrino and gamma-ray production in these sources. These candidates include first of all supernova remnants, which are in a sense the paradigmatic model of cosmic-ray accelerators in our galaxy. We will later discuss other candidate sources for extragalactic cosmic-ray acceleration and subsequent neutrino and gamma-ray production, including Active Galactic Nuclei (AGN), gamma-ray bursts (GRBs), and tidal disruption events (TDEs). Before doing that, however, let us briefly discuss on what properties should a source have in order to be a good candidate for cosmic-ray acceleration.

Ultra-high energy cosmic-ray acceleration

In Eq. 1.10 we saw that for a given duration of the acceleration process only a maximal energy can be attained. This condition can be formulated by using the acceleration time introduced in Sec. 1.1.2. Substituting the Bohm diffusion coefficient, we find

$$t^{-1} = \frac{3\eta V Z e B}{10E}, \quad (4.1)$$

where $\eta = V/2$ is the efficiency of the shock acceleration, defined in such a way that at each collision with the shock the relative gain in energy is $\frac{\delta E}{E} = \eta$. For clarity, we will refer only to protons, but the conditions can be easily translated to heavier nuclei. With this notation the energy gain per unit time is $\frac{dE}{dt} = \frac{\eta E}{T_{\text{acc}}}$. The condition in Eq. 1.10 can then be expressed as the requirement that the total duration $t = \int dt = \int^{E_{\text{max}}} \frac{dE}{dE/dt} = \int^{E_{\text{max}}} dE \frac{T_{\text{acc}}}{\eta E}$.

Another condition can be formulated which is valid independently of the duration of the event. It is necessary that the time needed for the particle to be accelerated to an energy E_{max} is smaller than the time it takes to be advected with the downstream velocity $V/4$ (we remind that in diffusive shock acceleration particles escape downstream). The former time is $\int^{E_{\text{max}}} dE \frac{T_{\text{acc}}}{\eta E}$, while the latter is $4R/V$, where R is the size of the source: in conclusion, neglecting numerical factors, we find the condition

$$E_{\text{max}} \lesssim \eta Z e B R. \quad (4.2)$$

This relation has been derived for the diffusive shock acceleration model, but it has a somewhat more general validity. For example, in one-shot acceleration models in which particles are accelerated by the electric field induced by Lenz law (as would be the case in a unipolar inductor), the induced electric field is of order $\mathcal{E} \sim V B \sim \eta B$, and therefore the total work that can be done over a distance R is exactly $\eta Z e B R$. Of course this is not coincidental, since from the dimensional parameters characterizing any mechanism of acceleration which involves magnetic fields there is no other combination that can be constructed having the dimension of energy.

The most conservative condition that can be formulated on any candidate source of cosmic-rays is that the charged particles are confined within the source of dimension R by the magnetic field. This leads to the estimate $E_{\text{max}} \lesssim Z e B R$. This condition is weaker than Eq. 4.2, since it is independent of any specific acceleration mechanism, and is known as the Hillas criterion 115 (in fact in Ref. 115 also Eq. 4.2 was derived).

High-energy sources are often characterized by rapidly expanding jets, in which this condition holds only in the frame comoving with the jet. If Γ is the Doppler factor of the jet¹, and we identify as primed the quantities in the frame comoving with the jet, it follows that 115

$$E \lesssim \Gamma \eta Z e B' R'. \quad (4.3)$$

The Hillas condition leads to a classification of the candidate source for acceleration of the ultra-high energy cosmic-rays in the $R - B$ plane. An example Hillas plot is shown in Fig. 4.1

The Hillas condition suggests that larger magnetic fields allow for larger maximal proton energies. This situation cannot be verified for arbitrarily large magnetic fields, since magnetic fields induce

¹ Γ is defined in such a way that the energies in the laboratory and in the comoving frame are connected by $E = \Gamma E'$. This factor generally depends upon the viewing angle in the laboratory frame: Lorentz transformations easily give $\Gamma = \frac{1}{\gamma(1 - V \cos \theta)}$, where V is the velocity of the jet and $\gamma = \frac{1}{\sqrt{1 - V^2}}$. Since the opening angle θ , due to relativistic beaming, is typically of order $\theta \sim \gamma^{-1}$ for very large V , it follows that $\Gamma \simeq \gamma$.

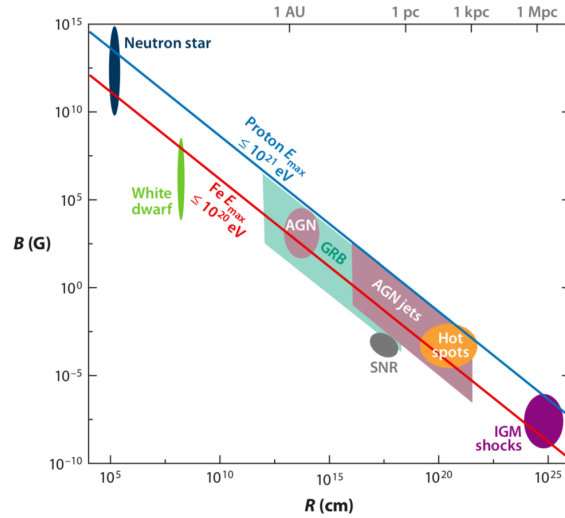


Figure 4.1: Updated version of Hillas plot. Above the blue line the maximal proton energy is larger than 10^{21} eV; above the red line the maximal energy for iron nuclei is larger than 10^{20} eV. The regions indicate the uncertainties connected with each source, including neutron stars, white dwarfs, AGN, GRBs, AGN jets, supernova remnants (SNR), hot spots, and intergalactic medium (IGM) shocks. Figure taken from Ref. [116].

synchrotron losses for charged particles. The timescale associated with synchrotron energy losses can be written as

$$T_{\text{synch}} = \frac{9m^4}{4e^4 B^2 E'} \quad (4.4)$$

If this timescale is much smaller than the acceleration timescale, protons lose energy more efficiently than they gain it. This imposes the condition

$$E \lesssim \Gamma \sqrt{\frac{9\eta m^4}{4Z^3 e^3 B'}} \quad (4.5)$$

The maximal proton energy will be determined by the stronger among Eq. 4.3 and 4.5

Neutrino fluxes from cosmic accelerators

Before discussing each class of cosmic accelerators separately, we provide a general discussion on the expected neutrino fluxes. The main process that is expected to produce neutrinos and gamma-rays in accelerators is $p\gamma$ interactions (although there are exceptions, including models of pp production in AGN [117, 118]). The target photons are often of non-thermal nature, because in most cases they are the result of leptonic emission from the electron component of cosmic-rays. Furthermore, they are often located in the environment of jets, such as in the case of AGN and GRBs. In $p\gamma$ interactions, the interaction rate of protons with energy E_p is proportional to the amount of target photons which can interact with them. In fact the optical depth for a proton with energy E_p is

$$\tau_{p\gamma} = \int d\varepsilon_\gamma \sigma_{p\gamma}(E_p, \varepsilon_\gamma) n_\gamma(\varepsilon_\gamma). \quad (4.6)$$

In the Δ -resonance approximation, as we have seen in Chap. [1](#), protons interact mostly with photons of energy ε_γ [keV] $\sim \frac{70 \text{ TeV}}{E_p}$, which leads to the expression

$$\tau_{p\gamma} \simeq \sigma_\Delta [\varepsilon_\gamma n_\gamma(\varepsilon_\gamma)]_{\varepsilon_\gamma [\text{keV}] = \frac{70 \text{ TeV}}{E_p}}, \quad (4.7)$$

where σ_Δ is a suitable energy average of the Δ -resonance cross section. Thus we see that the optical depth for photo-meson production in general depends on the proton energy. If the target photon spectrum is a power law $n(\varepsilon_\gamma) \propto \varepsilon_\gamma^{-\alpha}$, then the rate of interaction of protons with soft photons is proportional to $E_p^{\alpha-1}$. Since the spectrum of produced neutrinos and gamma-rays is proportional both to the original proton spectrum and to the interaction rate, if protons are accelerated with a power-law spectrum $E_p^{-\gamma}$, it follows that the spectrum of produced neutrinos and gamma-rays is proportional to $E_\nu^{-\gamma+\alpha-1}$. Since α is typically larger than 1, the neutrino and gamma-ray spectrum in $p\gamma$ sources is generally harder than their parent proton spectrum^{[2](#)}. This analytical argument will be described in more detail in Chap. [6](#) and in App. [D](#).

This discussion was only referred to the spectral shape of the neutrino and gamma-ray flux. Let us now discuss the question of the normalization of the expected diffuse extragalactic flux. There is a well-known upper bound in the literature on the maximum flux that can be observed at Earth from cosmic accelerators, known as the Waxman-Bahcall bound [\[119,120\]](#), which we will now derive.

Since neutrinos are expected to be produced by ultra-high energy cosmic-rays, let us first of all determine the production rate of these particles. Following Ref. [\[119\]](#), we assume that cosmic-rays are produced by a collection of extragalactic sources with a spectrum E_{CR}^{-2} , such that the production rate per unit volume in the local universe is

$$E_{\text{CR}}^2 \frac{dN_{\text{CR}}}{dt dV dE_{\text{CR}}}(z=0) \sim 10^{44} \text{ erg Mpc}^{-3} \text{ yr}^{-1}, \quad (4.8)$$

which is obtained from ultra-high energy cosmic-ray observations. Cosmic-rays lose a fraction ϵ of their energy in photo-meson production inside their sources: here we are assuming that the sources are optically thin to cosmic-rays, so that they can freely escape from them apart from this small energy loss. This means that the derivation does not apply to sources such as the cosmic reservoirs which we will discuss in the next section, in which cosmic-rays are trapped inside the source by hadronic collisions^{[3](#)}. The energy generation rate of charged pions is therefore

$$E_\pi^2 \frac{dN_\pi}{dt dV dE_\pi}(z) \simeq \frac{K_\pi \epsilon}{1 + K_\pi} E_{\text{CR}}^2 \frac{dN_{\text{CR}}}{dt dV dE_{\text{CR}}}(z), \quad (4.9)$$

where K_π is the ratio of charged to neutral pions defined in Chap. [1](#). Since pions carry on average a fixed fraction of the proton energy, their spectrum is still a power law with spectral index 2. The factor $\frac{K_\pi}{1+K_\pi}$ is therefore the fraction of energy carried by charged pions. The energy generated in pions is of course not directly observable, because pions decay in neutrinos and gamma-rays. We can use the relations derived in Sec. [1.3](#) to relate the neutrino energy generation rate to the pion

²This estimate only describe the neutrino spectrum in the approximation that the neutrino energy is a fixed fraction of the proton energy. In reality neutrinos are produced with an approximately flat distribution in energy from the pion decay. Therefore, if the effective neutrino spectral index $-\gamma + \alpha - 1 > 0$, our estimate predicts a spectrum which is too hard; in this case the spectrum becomes flat in energy, or, equivalently, $E_\nu^2 Q_\nu \propto E_\nu^2$, where Q_ν is the production rate of neutrinos.

³However, confinement by diffusion on magnetic perturbations is not sufficient to evade the Waxman-Bahcall bound, as observed by the authors in Ref. [\[120\]](#). The reason is that in $p\gamma$ collisions also neutrons are produced which can escape the source without feeling the effect of magnetic fields and decay into protons, contributing to the cosmic-ray flux. On the other hand, pp interactions can confine cosmic-rays without producing neutrons.

one. In particular, since 3 neutrinos are produced in each pion decay, each of which carries 1/4 of the parent pion energy on average, we have

$$E_\nu^2 \frac{dN_\nu}{dt dV dE_\nu}(z) \simeq \frac{3K_\pi \epsilon}{4(1+K_\pi)} E_{\text{CR}}^2 \frac{dN_{\text{CR}}}{dt dV dE_{\text{CR}}}(z), \quad (4.10)$$

where we are referring to the all-flavor neutrino energy generation rate. For $p\gamma$ interaction, we have seen in Sec. [L.3](#) that $K_\pi = 1$. Finally, the diffuse all-flavor neutrino flux can be written as

$$E_\nu^2 \frac{d\Phi}{dE_\nu d\Omega} = \int_0^{+\infty} \frac{dz}{4\pi H(z)} \frac{3\epsilon}{8(1+z)^2} E_{\text{CR}}^2 \frac{dN_{\text{CR}}}{dt dV dE_{\text{CR}}}(z). \quad (4.11)$$

The factor $(1+z)^2$ in the denominator comes from the redshifting of E_ν^2 . In terms of the Hubble timescale $t_H = \int \frac{dz}{(1+z)H(z)}$ and the energy generation rate of cosmic-rays at $z=0$, this flux can be expressed as

$$E_\nu^2 \frac{d\Phi}{dE_\nu d\Omega} = \frac{3\epsilon}{8} \frac{1}{4\pi} t_H \xi_z E_{\text{CR}}^2 \frac{dN_{\text{CR}}}{dt dV dE_{\text{CR}}}(0), \quad (4.12)$$

where

$$\xi_z = \frac{\int_0^{+\infty} \frac{dz}{(1+z)^2 H(z)} E_{\text{CR}}^2 \frac{dN_{\text{CR}}}{dt dV dE_{\text{CR}}}(z)}{t_H E_{\text{CR}}^2 \frac{dN_{\text{CR}}}{dt dV dE_{\text{CR}}}(0)}. \quad (4.13)$$

Finally we obtain for the all-flavor diffuse neutrino flux

$$E_\nu^2 \frac{d\Phi}{dE_\nu d\Omega} \simeq 2 \times 10^{-8} \xi_z \text{ GeV cm}^{-2} \text{ s}^{-1} \text{ sr}^{-1}. \quad (4.14)$$

The factor ξ_z is of order unity: to estimate it, we can follow different benchmark choices for the redshift evolution of the sources. If we assume no redshift evolution $\xi_z \simeq 0.6$; if we assume evolution with a distribution approximately following the star formation rate

$$f_{\text{SFR}}(z) = \begin{cases} (1+z)^3, & z < 1.9, \\ (1+1.9)^3, & 1.9 < z < 2.7, \\ (1+1.9)^3 e^{-\lambda(z-2.7)}, & z > 2.7, \end{cases} \quad (4.15)$$

we find that ξ_z varies from 3.1 to 2.7 as λ varies from 0 to 3.

The flux in Eq. [4.14](#) has indeed the order of magnitude of the diffuse neutrino flux measured by IceCube. This estimate also suggests that the neutrino flux should be comparable with the observed cosmic-ray flux.

The Waxman-Bahcall bound is an interesting application of the multi-messenger connection between high-energy neutrinos and cosmic-rays. One might wonder whether the connection between neutrinos and gamma-rays could also be used to estimate the expected neutrino fluxes from the observed gamma-rays. However, this turns out to be more difficult. While cosmic accelerators are by definition thin to cosmic-rays, they are not so for gamma-rays: on the contrary, the presence of a target of soft photons, necessary for the $p\gamma$ production of neutrinos, acts as an absorption target for gamma-rays. In other words, the more efficient the $p\gamma$ production is in the source, the more we expect gamma-rays to be suppressed due to $\gamma\gamma$ absorption inside the source. The optical depth for $\gamma\gamma$ absorption $\tau_{\gamma\gamma}$ can be related to the depth^{[4](#)} for $p\gamma$ collision $f_{p\gamma}$: they differ only in the cross

⁴If $f_{p\gamma}$ is defined as the distance determining the energy loss by photohadronic interaction, then for $f_{p\gamma}$ small it corresponds to the ϵ fraction defined in the proof of the Waxman-Bahcall bound. In the general case they are proportional.

section for the two processes. In Ref. [121] this relation is estimated as

$$\tau_{\gamma\gamma}(\varepsilon_c) \simeq 1000 f_{p\gamma}(E_p), \quad (4.16)$$

where $\varepsilon_c = \frac{2m_c^2 E_p}{m_p \varepsilon_\Delta}$ and $\varepsilon_\Delta = 0.3$ GeV. Thus there is a considerable uncertainty on whether $p\gamma$ sources such as cosmic accelerators could act as gamma-ray sources as well, and a definite connection between the neutrino and gamma-ray fluxes is necessarily model-dependent (we refer the reader to the literature, e.g. Ref. [121], for a more detailed discussion on this point).

4.1.1 Supernova remnants

One of the classical candidates for cosmic-ray acceleration is the supernova explosion. Core-collapse supernovae typically accompany the end of very massive stars, with masses larger than about 8 solar masses. For these stars, the production of heavy nuclei via nuclear fusion ends up in the formation of an iron core. At this point, the pressure support that maintained the dynamical equilibrium of the star rapidly drops for various reasons. First of all, at such high temperatures photons can break up the iron nuclei, effectively undoing the fusion process the star has undergone so far. The process is endothermic, and thus lowers the temperature and the pressure in the core of the star. Furthermore, the protons and electrons at these large temperatures can produce neutrons via inverse beta decay. This process produces neutrinos which escape the star cooling it, and furthermore it depletes the population of electrons, which do not support anymore the star with their degeneracy pressure. With the lack of pressure support the star collapses until the density reaches the order of magnitude of the nuclear saturation density. At this point the short-ranged nuclear forces rapidly stop the collapse, sending an outgoing shock wave. Numerical simulations show that at this point this shock wave stalls, because most of its energy is lost in dissociating the iron nuclei around the core. At the same time, the proto-neutron star that is formed at the center radiates about 10% of its mass in the form of neutrinos emitted in the conversion of protons into neutrons. By a mechanism which is not completely clear yet, the release of energy by neutrinos triggers an explosion of the original stellar mantle. This leads to the supernova explosion, which leaves a neutron star as a remnant. In the explosion, about 10^{53} erg are liberated in the form of the neutrinos, and about 10^{51} erg are liberated in the explosion of the stellar mantle.

Since supernovae are such high-energy processes, they have long been associated with cosmic-ray acceleration. The original argument for this, proposed by Ginzburg and Syrovatskii [122], was based on the energetics of the process. Indeed, assuming a supernova explosion every 30 years in the galaxy, a cumulative luminosity of 10^{42} erg/s is achieved. On the other hand, the mean energy density of observed cosmic-rays is of the order of 0.5 eV/cm³ [8]. Since these cosmic-rays have been confined in the galaxy for a time of 10^7 years, and the galaxy has a volume of the order of 45 kpc³, one can infer a luminosity in cosmic-rays of the order of 10^{40} erg/s. This suggested that if supernovae could transfer even only a few percent of their energy to cosmic-rays via some acceleration mechanisms, it would be enough to account for their observed energetics. The possibility of diffusive shock acceleration further supported this argument, since in supernova remnant a strong shock is formed which might accelerate the surrounding cosmic-rays. We now discuss the evolution of the shock wave in the supernova remnant, and the conditions under which it can accelerate cosmic-rays.

Immediately after the supernova, independently of the precise mechanism of formation, a shock wave is sent in the gas surrounding the star. The process can be idealized as an instantaneous release of energy E in a point-like way. The development of the shock wave proceeds in three distinct phases (see, e.g., Ref. [8]):

- initially the mass of gas ejected by the explosion is much larger than the mass of the gas swept up by the shock wave. In this case the expansion proceeds as if it were in the vacuum,

and therefore this phase is generally known as free expansion. The constancy of the energy requires a constant velocity of expansion $V = \sqrt{2E/M_{\text{ej}}}$, where M_{ej} is the mass of the ejected gas (we are assuming non-relativistic motion). For typical values one can assume $E \sim 10^{51}$ erg and M_{ej} of the order of a few solar masses, leading to typical velocities at this stage of the order of 10^4 km/s. The formation of a shock wave is confirmed by the observation that this velocity is much larger than the speed of sound in the rarefied interstellar medium, which is about 10 km/s. Free expansion ends when the mass of the surrounding medium that has been swept up by the shock becomes non-negligible, namely when $\rho \frac{4}{3}\pi V^3 t^3 \sim M_{\text{ej}}$. Here ρ is the density of the interstellar medium surrounding the shock: assuming that there is on average one hydrogen atom per cubic centimeter, the time at which this condition is verified is of the order of hundreds of years;

- after the free expansion ends, the shock wave propagates in a medium with non-negligible inertia. In this case the wave is slowed down because its initial energy E has to be shared with the ever-increasing mass of gas that it sweeps up. The self-similar solution to the equation of hydrodynamics has been obtained by Sedov and Taylor (see, e.g., Ref. [7]), and describes the motion of the fluid both inside and outside the shock. Nevertheless, the main qualitative features can be grasped by simple arguments. Since the mass of gas swept up by the gas is $M(t) \sim \rho \frac{4}{3}\pi R^3(t)$, the constancy of the energy requires $\frac{\rho \dot{R}^2}{2} \frac{4}{3}\pi R^3(t) \sim E$. From this equation we see that $R(t) \propto t^{2/5}$, and thus the velocity $V(t) = \dot{R}(t) \propto t^{-3/5}$. In this argument we are assuming a negligible heating or cooling of the gas behind the shock wave;
- during the Sedov-Taylor expansion the temperature of the gas behind the shock progressively lowers. When the temperature goes below 10^6 K, the initial energy, which up until now was completely contained in the shock, starts to be radiated away as photons, and the Sedov-Taylor solution, based on the conservation of energy, is not valid anymore. This happens typically for an age of the remnant of about 10000 years. In this case the driving force guiding the expansion is initially the gas pressure; afterwards, when radiative losses become too severe, the remnant enters the so called snowplow phase in which only the total momentum of the gas is conserved, leading to the conservation equation $\rho \frac{4}{3}\pi R^3(t) \dot{R}(t) = \text{const.}$. This equation admits the similarity solution $R(t) \propto t^{1/4}$.

The most interesting phase from the viewpoint of cosmic-ray acceleration is the Sedov-Taylor phase. From Chap. [1] we know that the maximum energy that can be reached at a given time in the shock evolution is $E_{\text{max}} = \frac{3}{20} ZeBV(t)R(t)$, where $R(t)$ is the shock radius. Since in the Sedov-Taylor phase $R(t) \propto t^{2/5}$, it follows that $E_{\text{max}} \propto t^{-1/5}$, and thus the particles with highest energies are produced at the beginning of the Sedov-Taylor phase, after hundreds to thousands of years after the supernova explosion. Using as order of magnitude $B \sim 1 \mu\text{G}$, $R \sim 1 \text{ pc}$, $t \sim 10^3 \text{ yr}$, we find $E_{\text{max}} \sim 10$ TeV as the highest energy to which cosmic-rays can be accelerated at the beginning of the Sedov-Taylor phase. Therefore, it is not clear whether supernova remnants can accelerate cosmic-rays up to the highest observed energies of 10 to 100 PeV (see, e.g., Ref. [123]). Larger values for the magnetic field may lead to higher values for the maximal proton energies [124–126]: these high magnetic fields may indeed be typical for starburst galaxies [127]. A considerable impact on the cosmic-ray spectrum comes also from the escape of protons and nuclei from the supernova remnant [128–131], which happens around 1000 years after the remnant formation. An experimental confirmation that supernova remnants in our galaxy can efficiently accelerate cosmic-rays up to energies of PeV is still lacking. Very recently, observation of galactic sources producing gamma-rays at 100 TeV have been reported [132]. If these gamma-rays are of hadronic origin, this observation is consistent with a cosmic-ray population accelerated up to energies of PeV.

Assuming that the observed gamma-rays from supernova remnants are indeed of hadronic origin, emission of high energy neutrinos by the same process can also be expected. Indeed, this production has been studied in Refs. [133, 137].

Supernova remnants discussed in this section are well-known candidates for the acceleration of galactic cosmic-rays. On the other hand, they are more difficult to relate to extragalactic emission. The reason is that by definition these remnants are embedded in a dense column of interstellar medium. This gas can act as a target for pp interaction and partially or totally confine the cosmic-rays in the environment surrounding the remnant. This is indeed the scenario proposed for cosmic reservoirs such as starburst galaxies, which we will discuss in more detail in Sec. 4.2 and in Chap. 5.

4.1.2 Active galactic nuclei

Active galactic nuclei (AGN) constitute a small fraction of the galaxies with a compact central region, smaller than 1 pc^3 , having a luminosity which can be even 10^4 times the luminosity of a normal galaxy. In fact, it can range between typical values of 10^{42} erg/s and 10^{48} erg/s . The origin of this energetic emission is believed to be a supermassive black hole at the center of the galaxy. Such supermassive black hole accretes matter from the surrounding in the form of an accretion disk. The precise mechanism by which the gravitational energy of the matter infalling on the black hole is converted into the observed luminosity is not completely clear: the most likely explanation is the mechanism proposed by Blandford and Znajek [138], who solved the general relativistic equations around a spinning black hole surrounded by a magnetized plasma. Indeed the solution leads to the formation of a jet along the direction of the black hole spin. Heuristically this can be understood by an analogy between the spinning black hole and a rotating conductor: if a conductor rotates in an external magnetic field, an effective potential difference is established by virtue of the Lorentz force. This potential difference can be seen as the origin of the jet production [139, 140]. This scenario is generally known as the membrane paradigm, and it offers a heuristic way of understanding the solution. It is not a rigorous description of the process, as it has been shown that in this way the electromotive force would be generated in a region that is causally disconnected from the outside [141, 142]; nevertheless, the Blandford-Znajek solution remains correct, and in Ref. [143] it has been shown that the origin of the electromotive force is rather to be found in the change in the electromagnetic field equations due to the gravitational field of the spinning black hole. We do not enter the details of this mechanism, and only assume that the accretion by supermassive black hole can be accompanied by the emission of an energetic jet. The size of this jet can reach in some cases up to hundreds of kpc.

Since the energy is mainly emitted in a jet, the observable properties of AGN are strongly determined by the angle under which we observe them. The classification of AGN makes use of various observable properties. A first criterion is whether a powerful radio jet is observed, which might be triggered by the mechanism described above. Therefore AGN are classified in radio-loud or radio-quiet according to their radio-loudness, namely $R = \log\left(\frac{f_{1 \text{ GHz}}}{f_{\text{B}}}\right)$, where $f_{1 \text{ GHz}}$ is the flux at 1 GHz and f_{B} is the flux in the optical B band. If $R > 1$ the AGN is classified as radio-loud. A complementary criterion of classification relies on the optical, rather than radio, band, depending on whether the AGN presents broad emission lines and bright continuum (type I) or narrow emission lines and weak continuum (type II). The distinction between the two is probably related to the viewing angle. In the current paradigm, in fact, the AGN consists of a central supermassive black hole emitting jets, surrounded by an accretion disk and a so-called broad-line region (BLR). In this region small clouds of gas emit Doppler-broadened emission lines. The entire structure is surrounded by a dusty toroidal structure. Therefore the distinction between type I and type II is probably due to the viewing angle: if the object is viewed in the transverse direction the broad emission lines and

the strong continuum are absorbed by the dusty torus, whereas at smaller viewing angles from the jet they are visible.

A further classification of AGN is based on their radio morphology. In particular, the so-called radio galaxies exhibit two radio-emitting lobes at the ends of the jet, whose distance from the core can vary from 10 kpc to 1 Mpc. Based on the distance between the lobes relative to the overall size of the object, these sources are classified into Fanaroff-Riley type I (FR-I), with jets extending not far from the host galaxy, and Fanaroff-Riley type II (FR-II), with high-luminosity narrow jets extending far beyond the host galaxy. The lobes of radio galaxies have been proposed as candidate environments for the production of high-energy gamma-rays and neutrinos. The case for radio galaxies as significant sources of IceCube neutrinos has recently drawn attention [144, 148], due to the fact that these sources are individually less luminous than other candidates such as GRBs and blazars (see below).

AGN are characterized by an electromagnetic production spanning the whole of the spectrum from radio waves to gamma-rays. The continuum spectrum has a characteristic two-hump shape. The low frequency hump, which can peak from below 10^{14} Hz to above 10^{15} Hz, is generally attributed to synchrotron radiation from accelerated electrons. The nature of the higher hump is still not completely understood: in leptonic models this is believed to be produced by Inverse Compton radiation from electrons off target photons, which can either be external to the source or be the synchrotron photons themselves. In hadronic models, the second hump can be explained either by synchrotron emission from the high-energy protons, or from hadronic collisions with either low energy target photons or with target nuclei.

A special class of AGN which are most relevant for neutrino and gamma-ray production are those AGN with jets pointing towards the Earth, which are known as blazars. For a given Lorentz factor of expansion γ , the jet emission is mostly concentrated at viewing angles of order $1/\gamma$. It is clear that, if the orientation of AGN jets is random, only a small fraction of all the AGN in the Universe point to the Earth within such a small angle. Nonetheless, blazars are so luminous that about 80% of the extragalactic background light detected by Fermi-LAT can be estimated to be produced in blazars (see, e.g., Refs. [149, 150]).

Since blazars point to the Earth with a very small angle to their jet axis, they are strongly influenced by relativistic effects. In fact, if γ is the bulk Lorentz factor of the jet, the energy of emitted particles will be blueshifted in the Earth rest frame by a Doppler factor $\Gamma = \frac{1}{\gamma(1 - \beta \cos \theta)}$, where θ is the viewing angle (at high redshift the energy also suffers a cosmological redshift by a factor $1 + z$). For blazars, due to relativistic beaming, $\theta \sim \frac{1}{\gamma}$ and, correspondingly, $\Gamma \sim \gamma$. Furthermore, if the luminosity of the source in the frame comoving with the jet is L' , the luminosity measured in the rest frame of the central black hole is $L_{\text{phys}} = \gamma^2 L'$. On the other hand the intensity measured in the Earth rest frame is further modified by relativistic beaming and redshift. The solid angle in which the emission is concentrated is reduced by a factor γ^2 , and therefore the luminosity estimated by flux measurement at the Earth is $L = L_{\text{phys}} \frac{\gamma^2}{1+z}$. The bulk Lorentz factor of AGN jets is typically of order 10. Blazars are further classified according to the presence of broad emission lines in Flat-Spectrum Radio Quasars (FSRQs) or absence of these in BL Lacs. Typically BL Lacs have lower luminosities, around $10^{44} - 10^{45}$ erg/s, compared to FSRQs, for which they are around $10^{46} - 10^{47}$ erg/s.

While gamma-ray production is well assessed in AGN, neutrino production is much more uncertain [151, 157]. As we have discussed at various places in this work, neutrino production is a definite signature of the presence of high-energy protons and nuclei. Therefore, neutrinos might be a definite factor distinguishing between the leptonic and hadronic models discussed above. The presence of cosmic-rays in the source can be quantified by the so-called baryonic loading, namely

the ratio between the cosmic-ray and electron luminosity

$$\xi_{\text{CR}} = \frac{L_{\text{CR}}}{L_e} \simeq \frac{L_{\text{CR}}}{L_\gamma}, \quad (4.17)$$

where L_{CR} , L_e , and L_γ are the cosmic-ray, electron, and gamma-ray luminosity respectively. The equality holds when equipartition between electrons and gamma-rays is attained. Therefore the baryonic loading gives a measurement of the role of hadronic production compared to leptonic one.

The lack of spatial correlations between the observed IceCube neutrinos and the the 2LAC catalog of blazars detected by Fermi-LAT has allowed to constrain the contribution of blazars to the diffuse neutrino flux to be less than 27% (50%) for a spectral index of -2.5 (-2) [158] (see also [159]). Multimessenger observations of neutrino in spatial and temporal coincides with AGN flares are rare, also because of the rapid variability of AGN.

An important advance in the discrimination between leptonic and hadronic production in blazars has been the 2017 observation of a neutrino with a reconstructed energy of 290 TeV and with an estimated direction consistent with that of blazar TXS 0506+056. The subsequent follow-up measurements by radio, optical, and gamma-ray telescopes showed that the blazar was undergoing a flare at that time. Furthermore, archival measurements of IceCube showed that in 2014-15 there had been an excess of 13 neutrino events from the same region of the sky over 6 months of measurements. However, this excess was not accompanied by any gamma-ray observable flare. Both the 2017 and the 2014-15 flare are challenging to explain: the observation of a neutrino in 2017 suggests a hadronic production within the source. However, the $p\gamma$ mechanism would also lead to the production of gamma-rays. Due to $\gamma\gamma$ opacity, these gamma-rays would be reprocessed into X-rays and would exceed the observed flux at these energies. Hybrid pictures, in which the emission is dominated by a leptonic component with a subdominant hadronic component responsible for neutrino production, seem to be the only ones consistent with the data for the 2017 flare [160,161]. The 2014-15 flare also presents a problem in that no gamma-ray excess was found, which implies that the source was gamma-ray opaque at that time. Even with this assumption, the gamma-rays produced by $p\gamma$ interactions would be reprocessed at lower energies, so one must ensure that the gamma-ray measurements by Fermi-LAT are not exceeded (see, e.g., [38]).

4.1.3 Gamma-ray bursts

Gamma-ray bursts (GRBs) are very energetic explosions which have long been proposed as candidates for the acceleration of ultra-high energy cosmic-rays. These explosions are connected with the formation of jets with bulk Lorentz factors which can be as high as $\Gamma \sim 10^2 - 10^3$ and observed luminosity of the order of 10^{51} erg/s. These events can last from ms to tens of minutes, and the distribution in the duration of the events shows two distinct classes of events, which are distinguished according to whether they last more (long GRBs) or less (short GRBs) than 2 s. The physical origin of these two classes of events is believed to be different: long GRBs are associated with the core collapse of a massive star, whereas short GRBs are associated with a merger of two neutron stars. This last association has been strengthened by the 2017 observation of the gravitational wave event GW170817 from a neutron star merger, shortly followed by the GRB 170817A. The luminosities of the two classes of events are comparable: because of the longer duration, this means that long GRBs have a larger emission of energy. Both long and short GRBs are associated with the launching of a relativistic jet of material with Lorentz factors of the order of 100 – 1000.

The photon emission by GRBs is characterized by a prompt emission of gamma-rays, whose duration is identified as the duration of the GRB, followed by an afterglow emission spanning the radio band to the X-ray band, which can last from days to months. Both the prompt and the

afterglow radiation are non-thermal, and they are generally associated with synchrotron and Inverse Compton radiation [162,163].

The extreme nature of GRB events led to the suggestion that they may be efficient accelerators of cosmic-rays [164,165]. This was motivated both by the large ejected energies, which can reach 10^{53} erg, and by the shocks expected in the jet formation, similar to what happens in AGN. Since relativistic magnetized shock acceleration may be inefficient, an alternative possibility for particle acceleration may be constituted by magnetic reconnection. Independently of the cause, the presence of accelerated non-thermal electrons in the source provides the classic explanation for the gamma-rays, which are believed to be emitted by synchrotron radiation and Inverse Compton off accelerated electrons. In the most common scenario, the prompt phase is associated with acceleration at internal shocks, whereas the afterglow phase is associated with acceleration at external shocks, formed by the slowing down of the ejected relativistic flow in the external material.

The simultaneous presence of high-energy cosmic-rays and photons in GRBs led to the suggestion that neutrinos could be produced as well [166,167]. Since the observed photon spectrum in GRBs is well-described by a broken power law in energy, the neutrino spectrum is expected to be described by a broken power law. At energies of about 10 PeV neutrino production starts being damped by the large synchrotron losses of primaries. Therefore, the neutrino spectrum in most models peaks at energies of about 0.1-1 PeV [167]. While these estimates derive from the simple approach to $p\gamma$ processes which includes only the Δ resonance contribution, the results have been verified also accounting for multipion and higher resonances contributions [168-170].

However, neutrino production in GRBs is challenged by the non-observation of any IceCube neutrino in spatial coincidence with the known GRBs [171]. Stacking analyses have constrained the GRB contribution to the diffuse neutrino flux to be less than $\sim 1\%$ [172,173]. This conclusion is based on internal shock models of neutrino production. It is still possible that different models of GRB emission may relieve this constraint, as mentioned in Ref. [174]. Furthermore, even accounting for these constraints it is still possible that GRBs account for acceleration of ultra-high energy cosmic-rays [175-177]. Finally, the constraints from stacking analyses may be relieved for low-luminosity GRBs which are missing in the catalogs used for stacking analyses [178-185].

4.1.4 Tidal disruption events

Tidal disruption events (TDEs) originate from the tidal disruption of a star approaching a black hole. In this event, a fraction of the mass of the star is ejected, whereas the remaining part forms an accretion disk around the black hole. This may cause the formation of a jet, as was the case for the observed event SwiftJ1644+57 [186], in which non-thermal X-rays were observed over a duration of 10^6 s, with a total emitted energy estimated around $10^{51} - 10^{52}$ erg. The formation of the jet from the accretion disk is probably connected with the same Blandford-Znajek mechanism that was referred to in relation to the jet formation in AGN.

The cosmic-ray and neutrino production in TDEs has been discussed in the literature [187-194]. In the case of jetted TDEs, due to the presence of shock waves in the jet, it is relatively easy to accommodate a mechanism for accelerating cosmic-rays within the shocks. The production of neutrinos therefore requires only the presence of target photons, which may be radiated from the accretion disk of the material around the black hole, such as in Ref. [195]. The acceleration of cosmic-rays in non-jetted TDEs is less straightforward, but it is still possible if shock waves are present in the material surrounding the TDE. Stacking searches have shown that the TDE contribution to the diffuse neutrino flux observed by IceCube is limited to be at most 1% (26%) for jetted (non-jetted) TDEs [190,191,196]. A breakthrough in these studies has been the observation in 2019 of a neutrino event IC191001A in spatial coincidence with TDE AT2019dsg at a level of 3σ . The neutrino detection

happened about 150 days after the luminosity peak of the TDE. Such a late observation is difficult to explain in a concordance model: possible explanations have been discussed in Refs. [195,197].

4.2 Cosmic reservoirs

Another possibility for neutrino production in astrophysical sites is the presence of cosmic accelerators embedded in environments which confine cosmic-rays for a sufficiently long time. During such a time, the hadronic component of cosmic-rays can collide with the interstellar (and possibly intergalactic) medium via pp interactions, leading to the production of neutrinos and hadronic gamma-rays. This scenario is generally dubbed a cosmic reservoir, due to the containment of the cosmic-rays responsible for neutrino production. Typical examples of cosmic reservoirs, which will be discussed in more detail below, are star-forming and starburst galaxies, and galaxy clusters. AGN have also been proposed as possible cosmic reservoirs.

Since in cosmic reservoirs cosmic-rays are confined within the galactic environment, the Waxman-Bahcall bound, based on the assumption that cosmic-rays escape the sources leaving only a small fraction of their energy in neutrino and gamma-ray production, cannot be applied here. The connection between cosmic-rays and neutrinos is therefore broken by the absence of cosmic-ray escape. On the other hand, while in cosmic accelerators a photon target was necessary to ensure $p\gamma$ interactions producing neutrinos, in cosmic reservoirs the photon target may be absent. If this happens, high-energy hadronic gamma-rays may escape the source without significant absorption: for this reason, cosmic reservoirs are much more likely to be gamma-ray transparent than cosmic accelerators. If pp sources are indeed gamma-ray transparent, then their contribution to the diffuse neutrino flux is constrained by the requirement that they should not exceed the EGB observed by Fermi-LAT. This condition translates into an upper bound on the spectral index γ of the neutrino and gamma-ray flux [124]: in fact, if the spectrum were too soft, the diffuse all-flavor neutrino flux at 300 TeV ($E_\nu^2\Phi_\nu)_{300 \text{ TeV}} = 10^{-8} \text{ GeV cm}^{-2} \text{ s}^{-1} \text{ sr}^{-1}$) would imply a gamma-ray flux at 100 GeV, using the multi-messenger connection in Eq. 1.27

$$(E_\gamma^2\Phi_\gamma)_{100 \text{ GeV}} = 2 \times 10^{-8} \left(\frac{100 \text{ GeV}}{600 \text{ TeV}} \right)^{2-\gamma} \text{ GeV cm}^{-2} \text{ s}^{-1} \text{ sr}^{-1} = 2 \times 10^{-8} 6000^{\gamma-2} \text{ GeV cm}^{-2} \text{ s}^{-1} \text{ sr}^{-1}. \quad (4.18)$$

Since the observed EGB flux attributed to unresolved sources is about $10^{-7} \text{ GeV cm}^{-2} \text{ s}^{-1} \text{ sr}^{-1}$, the spectral index should be $\gamma \lesssim 2.1 - 2.2$. This conclusion is based purely on the assumption that gamma-ray transparent cosmic reservoirs explain the IceCube diffuse neutrino flux via pp interactions. Furthermore, this argument is conservative, since most of the unresolved EGB is expected to be dominated by unresolved blazars rather than pp sources. Even tighter constraints are obtained assuming that cosmic reservoirs are responsible for the diffuse neutrino flux at 100 TeV, where the flux is larger. Ref. [121] shows that in this case the gamma-ray flux from intergalactic cascades would overshoot the unresolved EGB if $\gamma \gtrsim 2$. Therefore the possible contribution of cosmic reservoirs to the diffuse neutrino flux is strongly constrained by the multi-messenger connection with gamma-rays, which is a fundamental ingredient to account for. In Chap. 5 we will indeed report the results of a multi-messenger analysis of the neutrino and gamma-ray production in starburst galaxies.

4.2.1 Starburst galaxies

Starburst galaxies (SBGs) are galaxies with an unusually high rate of star formation, which can reach values of $100 M_\odot \text{ yr}^{-1}$ (for comparison the average value in the Milky Way is around $3 M_\odot \text{ yr}^{-1}$). Star-forming processes happen mostly in the nuclei of the galaxies, with typical dimensions

of hundreds of parsec. The presence of enhanced star forming processes is generally connected with a large amount of ISM, with average number densities of 100 cm^{-3} . Due to these properties, SBGs exhibit enhanced far infrared luminosities, with energy densities $U \sim 10^3 \text{ eV cm}^{-3}$, and higher supernova rates, of the order of $0.1 - 1 \text{ yr}^{-1}$, compared to normal galaxies. Simulations have also shown that SBGs can have very large interstellar wind velocities of hundreds to thousands of kilometers per second.

The properties just discussed make SBGs very promising sources of hadronic neutrino and gamma-ray production. The large amount of ISM is an ideal target for pp collision, and the enhanced supernova rate suggest the significant presence of acceleration sites within the galaxy. For this reason the neutrino production in SBGs has been studied in the literature by various authors [198]. The scenario is typical of cosmic reservoirs: it is assumed that supernovae embedded in the SBG accelerate cosmic-rays via diffusive shock acceleration. The cosmic-rays injected by supernovae can undergo pp collisions with the interstellar medium, leading to the production of neutrinos and gamma-rays. The escape of gamma-rays from the source is free from absorption only up to a maximal energy, because of the presence of infrared target photons naturally connected with the processes of star formation.

The amount of gamma-rays and neutrinos produced depends of course on the time spent by cosmic-rays within the SBG. The escape mechanism of cosmic-rays is dominated by advection by galactic winds, and at very high energies by diffusive escape. The escape time t_{esc} is determined by the faster of these two processes. The normalization of the gamma-ray and neutrino flux is determined by the number of collisions that a cosmic-ray undergoes during the time t_{esc} , and therefore would appear to be proportional to t_{esc} . This is not true for arbitrarily large t_{esc} : if t_{esc} becomes too large, the cosmic-rays may lose all of their energies in pp collisions. This is the so-called calorimetric regime [198, 199], in which cosmic-rays are completely confined within the galaxy and transfer all of their energy to neutrino and gamma-ray fluxes: clearly this is an upper bound on the secondary production that can be achieved in a given SBG.

In Refs. [124, 126, 200] it was pointed out that star-forming galaxies (SFGs) and SBGs cannot be the dominant source of the whole TeV-PeV diffuse neutrino flux without exceeding the non-blazar component of the extragalactic gamma-ray background (EGB) measured by Fermi-LAT [201], unless their spectral shape was sufficiently hard. Recent works [202-204] have reexamined the neutrino and gamma-ray emissions from SBGs showing that these sources can indeed account for the IceCube through-going muon neutrino flux at hundreds of TeVs in agreement with gamma-ray data. In particular, Refs. [203, 204] have proposed a prototype-based method to compute the cumulative diffuse neutrino and gamma-ray fluxes from the SBGs population. This approach is based on the choice of the galaxy M82 as a benchmark SBG. Its properties are used as a standard for setting the physical parameters such as supernova rate, spectral index, magnetic field, velocity of the wind, density of the ISM. This scenario provides a good description of the through-going muon neutrino flux, even though it cannot accommodate the HESE neutrino flux below 100 TeV, in agreement with the results of Refs. [121, 124] and the arguments presented at the beginning of this section. In Chap. 5 we will revisit the neutrino and gamma-ray production in SBG in view of the HESE neutrino data and the Fermi-LAT EGB in a multi-component framework in which neutrinos are produced not only in SBGs but also in blazars.

4.2.2 Galaxy clusters

Galaxy clusters are the largest systems of matter gravitationally bound that are known in the Universe. The importance of clusters as reservoirs of cosmic-rays has been emphasized in various works, including Refs. [205-208]. When cosmic-rays escape from the galaxy in the intracluster medium,

they remain trapped by diffusion on the magnetic perturbations. During the time in which they are confined, they suffer pp interactions on the gas target, which has a number density of the order of 10^{-3} cm^{-3} . Because of the rarefied nature of the intracluster gas, galaxy clusters are not generally considered as calorimetric sources such as SBGs. Nevertheless, they can produce a significant amount of secondary neutrinos and gamma-rays. Besides their reservoir nature, acceleration of cosmic-rays in galaxy clusters has also been proposed by means of the shocks which form by accretion of intergalactic gas onto the cluster. These shocks could accelerate both electrons, which leptonicly produce gamma-rays [207, 208], and protons [209, 210], which hadronically produce both neutrinos and gamma-rays [124, 211, 212]. Since galaxy clusters are pp sources expected to be transparent to gamma-rays, they are subject to the same constraints described at the beginning of this section, namely that they can contribute to the diffuse IceCube neutrino spectrum only up to a maximum limit determined by the spectral index: this aspect has been emphasized, e.g., in Refs. [124, 211].

4.2.3 Galactic production

The possibility that neutrinos and gamma-rays may be produced by cosmic-rays within our own galaxy has been widely discussed in the literature [213–217]. Here we shortly discuss only the diffuse galactic emission.

The existence of a diffuse galactic emission of neutrinos and gamma-rays is essentially guaranteed by the simultaneous presence of propagating cosmic-rays and of interstellar material, which can act as a target for pp collisions. This component is clearly anisotropic, due to the concentration of interstellar material near the galactic center and in the galactic disk. The intensity of this component depends on the interplay between the spatial distribution of cosmic-ray sources, the propagation model of cosmic-rays, and the density of target material. The spectral shape of the galactic diffuse flux is expected to follow that of the parent protons, namely a power law with soft spectral index close to 2.7 and a cutoff at PeV energies.

The main experimental input for the determination of diffuse galactic flux is the observation by Fermi-LAT of the diffuse gamma-ray emission below tens of GeV [218, 219]. This allows to infer information on the properties of cosmic-rays and target material necessary to reproduce the observed gamma-ray emission. Models for the diffuse galactic gamma-ray emission include Refs. [220–222], as well as the numerical code for cosmic-ray propagation GALPROP [223]. In order to correctly reproduce the observed flux above 10 GeV, Refs. [224–226] propose the KRA γ model, which introduces a different cosmic-ray propagation model and a cutoff at an energy between 5 PeV and 50 PeV.

The gamma-ray emission is of course accompanied by a corresponding diffuse neutrino emission, which has been estimated, e.g., in Refs. [220, 227–229]. Since no significant excess in neutrinos has been detected from the galactic plane, at present only upper bounds on the diffuse flux can be obtained by neutrino measurements. In Ref. [230], a joint search in the ANTARES and IceCube data on high-energy neutrino fluxes has been conducted. Even though a non-zero component has been found as most likely, the significance is too low: therefore, the search was used to constrain the diffuse neutrino emission. The constraints are however too weak to exclude definitely the KRA γ model.

A recent development on the diffuse emission is the measurement by the Tibet air shower gamma (AS γ) experiment of the diffuse gamma-ray emission between 0.1 PeV and 1 PeV [231]. In Ref. [232], these data have been used to estimate the corresponding diffuse galactic neutrino flux, with the result that this should contribute less than 5 – 10% to the observed flux at IceCube at energies of 100 TeV. This is a further confirmation of the extragalactic nature of the dominant sources of IceCube neutrinos.

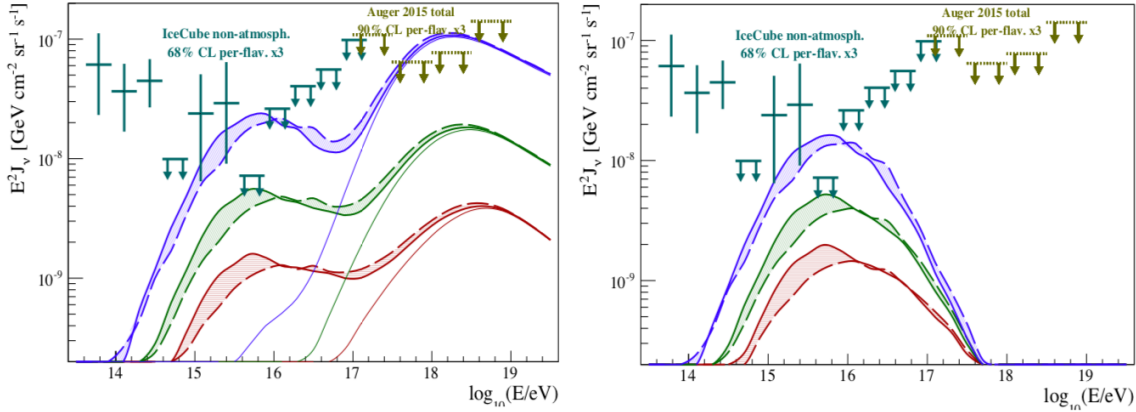


Figure 4.2: Cosmogenic neutrino flux for a pure proton model (left) and for a mixed composition ultra-high energy cosmic-ray model (right). The results are shown for three models of redshift evolution of the sources: no evolution (red), star-forming rate evolution (green), and evolution as AGN (blue). The uncertainty bands are related to EBL uncertainty. We also show the upper limits from IceCube [85, 233] and PAO [234]. Figure taken from Ref. [235].

4.3 Cosmogenic neutrinos

At ultra-high energies a guaranteed source of neutrinos is given by the photohadronic collisions of ultra-high energy cosmic-rays with the extragalactic background light, including the cosmic microwave background (CMB). These are the so-called cosmogenic neutrinos, first predicted in Ref. [236] and extensively studied, e.g. in Refs. [107, 237, 260]. For a target of CMB photons with typical energies $\varepsilon_\gamma \simeq 0.2$ meV, the $p\gamma$ interaction happens resonantly at a proton energy of about $E_p \simeq 10^{20}$ eV; since neutrinos typically carry a fraction 0.05 of the parent proton energy, cosmogenic neutrinos are mainly expected at energies of EeV. While the energy is quite well-known, the normalization of the flux is subject to considerable uncertainties related to the poorly known nature of the ultra-high energy cosmic-rays. In particular, the production of cosmogenic neutrinos is more efficient for collision of light nuclei and protons, whereas a heavier mass composition leads to inefficient production of neutrinos. A second source of uncertainty is related to the redshift evolution of the ultra-high energy cosmic-ray sources, which also impacts the normalization of the cosmogenic neutrinos.

In order to quantify the magnitude of the flux, as well as the entity of the uncertainties on it, we show in Fig. 4.2 the cosmogenic neutrino flux under the assumption of pure proton composition of cosmic-rays and a more realistic mixed composition with a minority of protons. We also show the impact of different models of source evolution. The results confirm the general tendency of heavier chemical composition, as well as of a stronger cosmic evolution of the sources, to dampen the cosmogenic neutrino flux. The upper limits set by IceCube and PAO are already able to disfavor some models of cosmological evolution: the measurements by the future neutrino radio telescopes have the main aim of complementing this information with either a measurement of cosmogenic neutrinos or stronger constraints on the magnitude of their flux.

Part II

Investigating the sources of neutrinos and gamma-rays

Chapter 5

Neutrino and gamma-ray production in starburst galaxies

As we discussed in Chap. 4, pp neutrino and gamma-ray production is often connected with the so-called cosmic reservoirs. One candidate class of sources that was described is the class of starburst galaxies (SBGs). In SBGs neutrinos can be produced via the collisions of protons from the cosmic-rays with the interstellar medium (ISM).

In Sec. 4.2 we examined the question of whether SBGs can be the main source of the neutrinos observed by IceCube. The main argument against this scenario is that a diffuse neutrino flux from SBGs with a spectral index around 2.2 (normalized to fit the HESE data at 100 TeV) would lead to a diffuse gamma-ray flux in tension with the Fermi-LAT observations [124]. We emphasize that this is not a tension between different data sets, but only between the IceCube and Fermi-LAT data and the hypothesis that they are produced by cosmic reservoirs. For brevity, throughout this section we will often refer to this as the IceCube-Fermi tension. This argument is based on the hypothesis that all SBGs contain a population of cosmic-rays with a power-law spectrum in energy with the same spectral index. Furthermore, if the highest energy neutrinos detected by IceCube above the PeV were produced in SBGs, then the parent cosmic-rays would have to be accelerated to energies of 100 PeV. While this may in fact be possible in the presence of magnetic field amplification near supernova remnants or of hypernovae [126, 204], it is at present unclear whether protons are really accelerated to such high energies.

In the work presented in this chapter, based on Ref. [150], we lift the single power-law assumption, considering a more realistic scenario where each starburst galaxy can have a different spectral index. This would seem to leave considerable freedom to the model, because we now have as a free parameter not just a single spectral index but a distribution of spectral indexes for all SBGs. For this reason, we do not consider this distribution as a free parameter, but rather we infer it from the information provided in Ref. [261], in which, from ten years of Fermi-LAT data, the spectral indexes are determined for a sample of 12 star-forming galaxies. We extract the distribution of spectral indexes from this sample and adopt it as a representative of the whole SBG population. With this data-driven approach, the neutrino flux at 100 TeV increases without enlarging the gamma-ray flux below 1 TeV: this mainly happens because of the presence of SBGs with a spectral index of about 2. This behavior could alleviate the tension that arises between neutrino and gamma-ray data when we try to explain them through hadronic-powered sources. In order to quantitatively estimate the agreement with the data, we perform a combined multi-messenger analysis of the extragalactic gamma-ray background (EBL) measured by Fermi-LAT and the neutrino flux observed by IceCube.

A good fit to the data is obtained by using a multi-component framework, similar to Ref. [262], where we include both the contribution of SBGs and blazars. The latter are modeled using the results of Ref. [157]. For both classes of sources we include the contribution of the gamma-ray emission from intergalactic electromagnetic cascades using the public code γ -Cascade [53]. We also introduce the diffuse gamma-ray emission from radio galaxies, which dominate the Fermi-LAT measurements below 1 GeV [69]. We leave as free parameters the three normalizations for SBGs, blazars and radio galaxies, as well as the maximal energy reached by the cosmic rays within SBGs.

Compared to previous analyses based on a single power-law model [204], we find that SBGs can explain a larger fraction of the IceCube flux without at the same time overshooting the EGB observed by Fermi-LAT. Furthermore, the maximal energies to which cosmic rays need to be accelerated are of the order of a few PeV, whereas larger values are required in the single power-law analyses.

5.1 Neutrino and gamma-ray fluxes from individual SBGs

In order to model the neutrino and gamma-ray fluxes from individual SBGs, we follow the approach suggested in Ref. [203], using a leaky box model to describe the transport of cosmic rays in the galaxy. The physical scenario is therefore the following: protons are accelerated near supernova remnants and injected uniformly in the SBG nucleus. They are subject to diffusion in the turbulent magnetic field of the galaxy and advection from the winds. Furthermore, they are subject to pp collisions with the ISM which are responsible for energy losses¹. If the density of the ISM is sufficiently large, the energy losses due to pp collisions will be the dominant process. Under these conditions cosmic protons are essentially confined within the galaxy, releasing most of their energy in gamma-rays and neutrinos. This regime is typically named calorimetric.

The condition for the calorimetric regime can be expressed as

$$T_{\text{loss}} \leq T_{\text{esc}}, \quad (5.1)$$

where T_{loss} is the typical CR timescale for interactions and T_{esc} is the timescale necessary for a CR to escape the source. Many authors focused on CR spectral features of SBGs [202, 203, 263–272] to deduce that CR electrons are well-confined inside starburst nuclei (SBN). On the other hand for high-energy protons the calorimetric regime will be attained only for sufficiently large ISM density and large escape times, in order to satisfy Eq. 5.1. In order to quantitatively obtain the timescales, we consider the SBN as a spherical region with advection time $T_{\text{adv}} = R/v_{\text{wind}}$ depending on the radius R of the region and on the wind velocity v_{wind} . For the diffusion timescale we need a description of the turbulent magnetic field. We assume a Kolmogorov-like scenario, with a density of the magnetic field $F(k) \propto k^{-d+1}$ with $d = 5/3$ and a regime of strong turbulence inside the SBN [203, 204]. These assumptions lead to a diffusion coefficient $D(p) \propto p^{1/3}$, which implies $T_{\text{diff}}(E) \propto E^{-1/3}$. For a magnetized fluid the Kolmogorov scenario should in principle be replaced by the Kraichnan model [273] for turbulence. It is however unclear if this is the case even in the most well-known case of our Galaxy, for which the Kolmogorov scenario seems to be favored. In any case, as shown by Refs. [203, 204], the diffusion timescale is larger than all the other timescales except at extremely high energies, so that the details of the turbulence model do not influence our conclusions. The escape time T_{esc} in Eq. (5.1) is given by

$$T_{\text{esc}} = \left(\frac{1}{T_{\text{adv}}} + \frac{1}{T_{\text{diff}}} \right)^{-1}. \quad (5.2)$$

¹We also take into account energy losses due to ionization and Coulomb interaction with the electrons.

For typical values ($R \sim 10^2$ pc and $v_{\text{winds}} \sim 10^2 - 10^3$ km/s, see Ref. [127]), we have that $T_{\text{adv}} \sim 10^5 - 10^6$ yr. As we already mentioned, the high level of turbulence and interstellar medium density makes $T_{\text{diff}} \gg T_{\text{adv}}$, so that $T_{\text{esc}} \simeq T_{\text{adv}}$. For the loss timescale of CRs, we take into account ionization, Coulomb interaction, and pp interaction. The timescale T_{loss} therefore depends on the proton energy and in particular, for energies much greater than the proton mass, it is mainly driven by the timescale of pp interactions. As shown in Ref. [203], T_{loss} usually becomes smaller than the advection timescale for energies higher than 10 TeV.

We now discuss how we obtain the particle spectra. For notational convenience, we write the particle spectra not as a function of the particle energy E , but as a function of their momentum p . This notation will be maintained throughout this section. In the ultra-relativistic limit we are interested in, the two variables are approximately equal: the main difference is that the phase-space element in momentum space is proportional to $d^3\mathbf{p} = 4\pi p^2 dp$ for isotropic distributions. Therefore, the relation between the number of particles per unit energy $n(E)$ and the number of particles per unit momentum $F(p)$ is written

$$n(E) = F(p)4\pi p^2 \frac{dp}{dE} \Big|_{p=\sqrt{E^2-m^2}}, \quad (5.3)$$

where m is the particle mass. This means that if particles are injected with an energy spectrum proportional to $E^{-\gamma}$, the corresponding momentum distribution in the ultra-relativistic limit is proportional to $p^{-\alpha}$ with $\alpha = \gamma + 2$.

Given the loss and escape timescales, the stationary number density of protons per unit energy $F_p(p)$ in the SBG is determined by the equilibrium between the number of protons injected by SNR per unit time and volume, $Q_p(p)$, and the number of protons lost either by escape from SBG or by energy loss. This condition leads to^{2]}

$$F_p = Q_p \left(\frac{1}{T_{\text{adv}}} + \frac{1}{T_{\text{loss}}} + \frac{1}{T_{\text{diff}}} \right)^{-1}. \quad (5.4)$$

An analogous equation can be set up for electrons. For the latter, we consider as energy losses ionization, synchrotron, Inverse Compton, and bremsstrahlung.

In terms of the particle momenta, the injection spectrum of protons, which is assumed to originate from SNRs, can be written

$$Q_p(p, \mathcal{R}_{\text{SN}}, \alpha, p^{\text{max}}) = \frac{\mathcal{N}_p \mathcal{R}_{\text{SN}}}{V_{\text{SBN}}} p^{-\alpha} e^{-p/p^{\text{max}}}, \quad (5.5)$$

where V_{SBN} is the volume of the starburst nucleus, and the cut-off energy p^{max} is considered a free parameter in the range 1-100 PeV. The normalization \mathcal{N}_p is fixed by the condition that each supernova releases into CRs a fraction $\xi = 0.1$ of its total explosion kinetic energy $E_{\text{SN}} = 10^{51}$ erg. In mathematical terms this means that

$$\int_0^\infty 4\pi p^2 T(p) \left(\frac{V_{\text{SBN}}}{\mathcal{R}_{\text{SN}}} Q_p(p) \right) dp = \xi E_{\text{SN}}, \quad (5.6)$$

with $T(p)$ being the single particle kinetic energy.

²Here we have in fact used an approximation. In fact the correct solution should be obtained from Eqs. [2.7] and [2.9] with the substitution $b(E) = \frac{E}{T_{\text{loss}}}$, $\tau_{\text{adv}} = T_{\text{adv}}$, and $\tau_{\text{loss}} = T_{\text{loss}}$. In the limit $T_{\text{loss}} \rightarrow \infty$, the solution is indeed given by Eq. [5.4]. In the opposite limit $T_{\text{adv}}, T_{\text{diff}} \rightarrow \infty$, the solution for a power-law spectrum $Q_p \propto E^{-\gamma}$ is $F_p = \frac{Q_p T_{\text{loss}}}{\gamma - 1}$, which indeed approximates Eq. [5.4] if γ is close to 2, which is our case. Therefore, we use Eq. [5.4] as a simple interpolation between these two regimes.

Similarly, for primary electrons we assume

$$Q_e(p, \mathcal{R}_{\text{SN}}, \alpha) = \frac{\mathcal{N}_e \mathcal{R}_{\text{SN}}}{V_{\text{SBN}}} p^{-\alpha} e^{-(p/p_e^{\text{max}})^2}, \quad (5.7)$$

with $p_e^{\text{max}} = 10$ TeV and $\mathcal{N}_e = \mathcal{N}_p/50$ according to Refs. [203, 204]. The lower cutoff for electrons is determined in Refs. [274, 275] taking into account the large synchrotron losses. The lower normalization of the electron spectrum compared to the proton one is fixed in analogy to our Galaxy.

In order to compute the spectra of neutrinos and gamma-rays, we need to determine the pion spectra. Pions are injected via pp interactions, for which we follow the treatment in Ref. [28] and assume that each pion carries a fraction ($K_\pi \simeq 0.17$) of the parent proton energy. Therefore, the pion injection spectrum is

$$Q_\pi(E_\pi) = \frac{c n_{\text{ISM}}}{K_\pi} \sigma_{pp}(E') n_p(E') \Big|_{E'=m_p+E_\pi/K_\pi}, \quad (5.8)$$

where σ_{pp} is the proton-proton cross-section, n_p denotes the energy distribution function of injected high-energy protons obtained by solving the leaky-box model equation, and m_p is the proton mass.

Finally, the neutrino production spectrum (averaged over flavour) is

$$Q_\nu(E_\nu) = 2 \int_0^1 \left(\frac{f_{\nu_e}(x) + f_{\nu_\mu^1}(x) + f_{\nu_\mu^2}(x)}{3} \right) Q_\pi \left(\frac{E_\nu}{x} \right) \frac{dx}{x}, \quad (5.9)$$

where the decay functions $f_\nu(x)$ have been defined in Sec. [1.3] with different notations. We account for neutrino oscillations during propagation by changing the flavour ratio (1:2:0) at the source to (1:1:1) at the Earth. By virtue of the low magnetic fields inside the SBN, we only consider a pion-beam flavor composition for the neutrino fluxes. Hence, the single-flavour neutrino flux at the Earth is given by

$$\phi_\nu(E, z) = \frac{V_{\text{SBN}}}{4\pi d_c^2(z)} Q_\nu(E(1+z)), \quad (5.10)$$

where $d_c(z)$ is the comoving distance between the source and the Earth as a function of the redshift z .

Pion decay also produces secondary electrons, whose injection spectrum we parameterize as

$$Q_e(E_e) = 2 \int_{E_e}^{+\infty} Q_\pi(E_\pi) f_e \left(\frac{E_e}{E_\pi} \right) \frac{dE_\pi}{E_\pi}, \quad (5.11)$$

where f_e is the decay function for electrons.

For the gamma-ray production rate we account not only for the production from π^0 decay, but also for the leptonic production (bremsstrahlung, synchrotron and Inverse Compton) emitted by primary and secondary electrons. The photon emissivity $\epsilon_\gamma(E)$ from π^0 , namely the number of photons injected per unit energy, time, and solid angle, is given by

$$\epsilon_\gamma(E) = \frac{2}{4\pi} \int_{E_{\text{min}}}^{+\infty} \frac{Q_\pi(E_\pi)}{\sqrt{E_\pi^2 - m_\pi^2}} dE_\pi. \quad (5.12)$$

The minimal pion energy E_{min} is estimated by observing that the maximal gamma-ray energy E for the pion energy E_{min} is given by $E = \frac{E_{\text{min}}}{2} + \frac{\sqrt{E_{\text{min}}^2 - m_\pi^2}}{2}$; inverting we find $E_{\text{min}} = E + \frac{m_\pi^2}{4E}$.

The photon emissivity from bremsstrahlung $\epsilon_{\text{brem}}(E)$ is obtained by integrating the cross section in Eq. [1.11](#) and is

$$\epsilon_{\text{brem}}(E) = \frac{n_{\text{ISM}}\sigma_{\text{brem}}}{4\pi E} \int_E^{+\infty} N_e(E_e) dE_e, \quad (5.13)$$

where $N_e(E_e)$ is the stationary distribution of primary and secondary electrons, $\sigma_{\text{brem}} \simeq 3.4 \times 10^{-26} \text{ cm}^2$ is the bremsstrahlung cross section. Here the usual shape $E^{-1}\theta(E_e - E)$ is assumed for the bremsstrahlung spectrum from each electron with energy E_e .

For the synchrotron and Inverse Compton emissivities we use the expressions from Ref. [203](#). In particular, we assume a benchmark magnetic field $B = 200 \mu\text{G}$. For the Inverse Compton emissivity, the physical target of photons is taken as the spectrum shown in the upper panel of Fig. 6 of Ref. [203](#). However, to simplify the calculation and to avoid the double integration over the electron and the photon energies, we replace the physical target of photons by an effective monochromatic spectrum centered around the peak energy of the photon target and normalized to the same total energy density U_{rad} . This is the same procedure followed in Ref. [203](#) and leads to a factor of 2 of uncertainty in the Inverse Compton flux. Nevertheless, the Inverse Compton is subdominant in the total gamma-ray flux, so we consider this to be acceptable.

While neutrinos freely escape the SBG after the production, gamma-rays are not completely free due to the possibility of $\gamma\gamma$ collisions on the low energy target photons (which again are taken as the upper panel of Fig. 6 of Ref. [203](#)). This gives rise to an internal absorption (we name it internal to differentiate it from the external absorption in the intergalactic space). Over a fixed line of sight of length s , the intensity $I(E, s)$ of photons (number of photons per unit surface, energy and time) exiting the galaxy is

$$I(E, s) = \epsilon(E) \frac{1 - e^{-\eta(E)s}}{\eta(E)}, \quad (5.14)$$

where $\epsilon(E)$ is the total emissivity, $\eta(E) = \int \sigma_{\gamma\gamma}(E, E') n_{\text{bkg}}(E') dE'$ is the absorption coefficient, $\sigma_{\gamma\gamma}(E, E')$ is the photon-photon cross section and $n_{\text{bkg}}(E')$ is the target photon density from the upper panel of Fig. 6 of Ref. [203](#). The length of the line of sight depends on the direction of the photon. After averaging over all possible directions, we obtain the internal absorption coefficient as a function of the photon energy E

$$\text{Abs}(E) = \frac{3}{2\eta(E)R} \left[\frac{1}{2} - \frac{1 - e^{-2R\eta(E)}(1 + 2R\eta(E))}{4R^2\eta(E)^2} \right], \quad (5.15)$$

where R is the radius of the SBG. The final expression for the *direct* gamma-ray flux at Earth is

$$\begin{aligned} \phi_\gamma(E, z) &= \frac{V_{\text{SBN}}}{4\pi d_c^2(z)} Q_\gamma(E(1+z)) \\ &\times \text{Abs}(E(1+z)) e^{-\tau_{\gamma\gamma}(E, z)}, \end{aligned} \quad (5.16)$$

where $\tau_{\gamma\gamma}$ is the optical depth from CMB and EBL [52,276](#) accounting for external absorption. We add to this a contribution from electromagnetic cascades in the intergalactic space, obtained using the public code γ -Cascade [53](#).

Finally, let us discuss the values of the cutoff energy p^{max} . This is the maximal energy to which protons can be accelerated in SNR, which has been discussed in Chaps. [1](#) and [4](#). In the simple

scenario of Bohm diffusion around the SNR the maximal proton energy is estimated as [124]–[126]

$$p^{\max} \approx 3.1 \text{ PeV} \left(\frac{n_{\text{ISM}}}{1 \text{ cm}^{-3}} \right)^{-1/3} \left(\frac{B}{10^{-3.5} \text{ G}} \right) \times \left(\frac{E_{\text{ej}}}{10^{51} \text{ erg}} \right)^{1/3} \left(\frac{v_{\text{ej}}}{10^9 \text{ cm/s}} \right)^{1/3}, \quad (5.17)$$

where B is the magnetic field, E_{ej} is the ejected energy, and v_{ej} is the ejected velocity. Therefore, the maximal energy seems to be limited to 1 PeV at most. Higher cutoff energies could be obtained if the magnetic field is larger, of the order of (1 – 30 mG), as could be expected in the case of non-linear amplification. Another possibility is that at high redshift hypernovae are more common than supernovae, so the typical ejected velocity is larger. In this work we do not need these scenarios, because we can explain the IceCube neutrinos with values of the maximal proton energy just of the order of PeV. Of course this means that SBGs in our model cannot be responsible for UHECRs, because they produce protons with too low maximal energies. A multi-messenger scenario which accounts simultaneously for gamma-rays, neutrinos and cosmic-rays is therefore outside the scope of our work, and we restrict to the first two components only, namely gamma-rays and neutrinos.

5.2 Diffuse neutrino and gamma-ray fluxes

In this section we compute the diffuse neutrino and gamma-ray fluxes produced by SBGs, which will be compared in the following sections with the Fermi-LAT and IceCube observations.

The diffuse neutrino and gamma-ray fluxes should be obtained by summing the individual fluxes from each SBG in Eq. 5.10 and Eq. 5.16 over all SBGs in the Universe. In doing this, we should *i*) make an assumption on how the individual properties change between different SBGs, and *ii*) make an assumption on how SBGs are distributed with redshift. Let us discuss each of these assumptions.

Given that SBGs are astrophysical reservoirs, we expect that their non-thermal emission is not driven by the structural details of the source. Thus we assume that most of the properties for different SBGs are identical to the benchmark case of M82, for which we take the parameters from Ref. [203]. The only exceptions are the supernova rate, which determines the normalization of the neutrino spectrum, and the spectral index, which determines its shape. We assume that the supernova rate is proportional to the Star Formation Rate (SFR) of the SBG, normalizing it to the supernova rate of M82 given in Ref. [203]. For the spectral index we take a distribution which is inferred by experimental data. More specifically, we consider 12 SFGs and SBGs observed in gamma-rays for which the photon spectral index has been obtained by a fitting procedure with a power-law function [261]–[277]. We show the histogram of these spectral indexes in Fig. 5.1 together with a Gaussian fit $\mathcal{N}(\alpha|\mu_\alpha, \sigma_\alpha^2)$ to the histogram with mean index $\mu_\alpha = 4.2$ and standard deviation $\sigma_\alpha^2 \simeq 0.04$. The small size of the sample, as well as the uncertainties on the spectral indices estimated for each member of the sample, lead to an uncertainty on this distribution³. Nevertheless, the result shows in a definite way that the typical assumption of a spectral index $\alpha \sim 4.2$ is good for the *average* spectral index, and it may not capture the global behavior of all SBGs.

Regarding the redshift distribution of the SBGs, we describe it by means of a modified Schechter function $\Phi_{\text{SFR}}(z, \psi)$ reported by Ref. [204], which has been obtained by fitting in the redshift interval $0 \leq z \leq 4.2$ the IR+UV data of a Herschel Source sample [278] after subtracting the AGN

³We have also tested approaches other than the maximum likelihood fit to the sample. For example, we have performed a kernel density estimation starting from the data and their uncertainties, finding results similar to the ones shown in Fig. 5.1

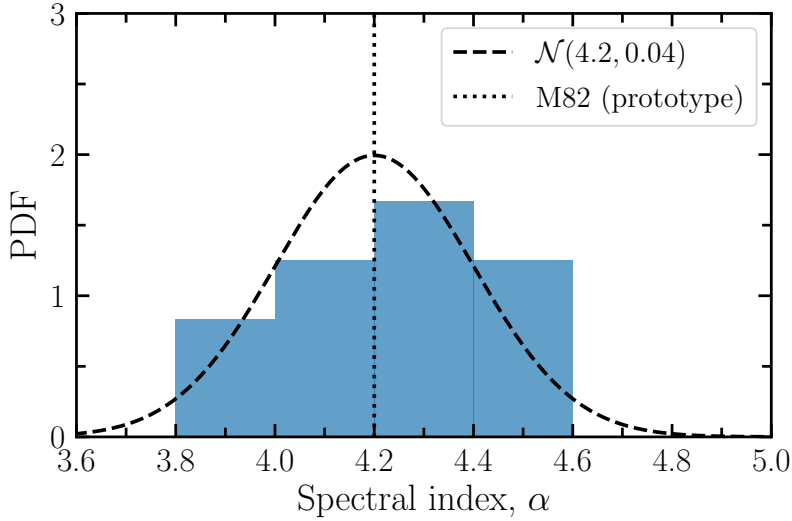


Figure 5.1: Number of observed SBGs with different spectral indexes α according to the analysis in Ref. [261]. The dashed line shows the underlined Gaussian probability distribution function with mean $\mu_\alpha = 4.2$ and variance $\sigma_\alpha^2 = 0.04$ used in the present analysis. The vertical dotted line displays the spectral index of M82 generally adopted as prototype [204].

contamination [279]. This is the number of SBGs per unit of comoving volume and logarithmic SFR ψ .

At this point the diffuse neutrino and gamma-ray spectra can be obtained by summing over the distribution $\Phi_{\text{SFR}}(z, \psi)$. However, before doing that, we introduce a lower SFR below which we cut the integration. The reason is that for low SFRs the SBG violates the condition [5.1] and exits the calorimetric regime. Low SFRs are in fact connected with low ISM densities by the Kennicutt relation [280, 281]. For low ISM densities, the protons collide rarely via pp collisions and escape from the SBG releasing only little of their energy to neutrinos and gamma-rays. The threshold value for the SFR is $\psi_* = 2.6 M_\odot \text{ yr}^{-1}$ [204].

Finally, the diffuse differential neutrino and gamma-ray flux are given by

$$\begin{aligned} \Phi_{\nu, \gamma}^{\text{SBG}}(E, p^{\text{max}}) &= \int_0^{4.2} dz \int_{\psi_*}^{\infty} d \log \psi \frac{c d_c(z)^2}{H(z)} \\ &\times \Phi_{\text{SFR}}(z, \psi) \left\langle \phi_{\nu, \gamma}(E, z, \psi, p^{\text{max}}) \right\rangle_\alpha, \end{aligned} \quad (5.18)$$

where by $\langle \rangle_\alpha$ we mean the average over the distribution $\mathcal{N}(\alpha | \mu_\alpha, \sigma_\alpha^2)$. We will refer to this average as *blending* of spectral indexes.

The difference between the single power law and the blended spectrum is shown for a benchmark parameter choice in Fig. [5.2]. We show in blue and yellow the neutrino and the gamma-ray fluxes respectively; the blended (single power-law) case is represented with a short-dashed (long-dashed) linestyle. The spectra are normalized so that the integrated SBG gamma-ray flux gives 30% of the integrated EGB flux, namely

$$J_{>50 \text{ GeV}}^{\text{SBG}} = N_{\text{SBG}} \int_{50 \text{ GeV}}^{820 \text{ GeV}} \Phi_\gamma^{\text{SBG}}(E_\gamma) dE_\gamma = 0.3 J_{>50 \text{ GeV}}^{\text{EGB}}, \quad (5.19)$$

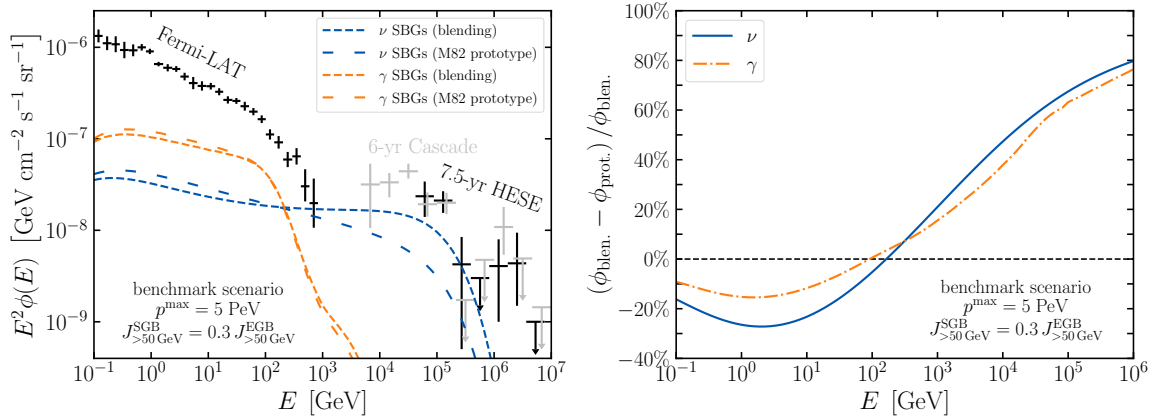


Figure 5.2: *Left*: comparison between the diffuse emission of starburst galaxies modeled with the blending of spectral indexes (short-dashed lines) and with the assumption of M82 as prototype [204] (long-dashed lines) for the benchmark case with $p^{\text{max}} = 5 \text{ PeV}$. The normalization of the SBG emission is fixed to account for 30% of the total EGB integrate flux above 50 GeV (see Eq. (5.19)). The blue (orange) color corresponds to the neutrino (gamma-ray) flux. *Right*: Relative difference of the two different SBG modelings with blending (blen.) and prototype (prot.) for the diffuse neutrino (blue solid line) and the gamma-ray (orange dot-dashed line) fluxes as a function of energy. Below (above) the horizontal dashed line, the blending of the spectral indexes leads to a lower (higher) flux.

giving $N_{\text{SBG}} \simeq 0.73$. With this condition we are consistent with the limits on the non-blazar component of the EGB above 50 GeV [149, 282].

The neutrino blended flux exhibits a characteristic convex structure, due to the softer spectral indexes dominating at low energy and the harder ones at high energy. On the other hand, the gamma-ray flux is not very different in the two approaches. This is due to the EBL absorption, which suppresses the spectrum at lower energies compared to the neutrino one, so that the effect of the component of SBGs with harder spectral indexes is not felt at all. This is confirmed by the right panel of Fig. 5.2, where we show the relative difference between the single power-law and the blended spectra: indeed both the neutrino and the gamma-ray flux show a significant difference in the high-energy range, but at these energies the gamma-ray flux is suppressed.

The net effect of the blending is therefore to introduce a hard component into the neutrino spectrum without affecting too much the gamma-ray spectrum. This change goes in the direction of relieving the IceCube-Fermi tension under the assumption that the IceCube data at 100 TeV are explained by SBGs, as discussed in Sec. 4.2. The crucial point discussed there was in fact that only hard spectral indices could explain the neutrinos at energies of 100 TeV without overshooting the EGB. This observation, which at present is only qualitative, will be quantified in the next section with a full multi-messenger analysis of the IceCube and Fermi-LAT data.

A final comment is in order here, regarding the variability of parameters in SBG. We have accounted for the variability of spectral indexes, but a natural question would be what influence do the other parameters have. The maximal proton energy p^{max} cannot be inferred by gamma-ray observations, because gamma-ray spectra are suppressed at much lower energy by EBL absorption, and for this reason we do not attempt an hypothesis on different p^{max} for different SBGs. The magnetic field, for which we use the benchmark choice $B = 200 \mu\text{G}$ as in Ref. [204], is estimated for

a sample of SBGs for example in Ref. [127]. However, in our approach the magnetic field only enters the diffusive timescale. As discussed in the previous section, the diffusive timescale is much longer than the other ones anyway (except at the very highest energies), so changing the magnetic field does not significantly change our results (notice however that, if we had modeled the SNR acceleration in a complete way, the magnetic field would change the maximal proton energy p^{\max} as in Eq. ??). In conclusion, the spectral index variability already captures the most important features of the SBG diffuse flux.

5.3 Multi-messenger analysis

In this section we describe the combined analysis of the IceCube and Fermi-LAT EGB data samples. The purpose of this analysis is to show that the blending of spectral indexes, with a consequent injection of a hard component in the neutrino flux, does indeed relieve the IceCube-Fermi tension. We focus on two IceCube data samples: the 7.5-year HESE data [283] and the 6-year high-energy cascade data [284]. The latter only includes shower-like events (mostly electron and tau neutrino flavours) and it extends down to few TeV thanks to the smaller background contamination. For the gamma-ray data, we use the EGB measured by Fermi-LAT [201]. Most of the EGB comes from resolved and unresolved blazars, leaving only small space for other sources [69, 149, 282]. Therefore, if we want to perform a combined analysis, we need to account for non-SBG components. We collect here all the source classes we take into account in this analysis:

- **Neutrinos**

- **Starburst galaxies:** this component has been discussed in the previous sections;
- **Blazars:** for this subclass of Active Galactic Nuclei, we follow Ref. [157] where the blazar neutrino flux has been computed by assuming the baryonic loading directly linked to the blazar sequence trend [285] and taking the same blazar distribution as used by [69]. (see also Ref. [153]). In Ref. [157], three different models for the blazar neutrino flux are provided according to different assumptions on the baryonic loading. We have checked that our results do not depend on the particular blazar model considered. Therefore, in the following we just use as a benchmark the “scenario 1” (see Figure 5 in Ref. [157]) where the baryonic loading is assumed to be constant (see also Ref. [286]). We always check that, in our best-fit scenarios, the blazar neutrino component is consistent with the IceCube stacking limit [287].

- **Gamma-rays**

- **Starburst galaxies:** this component has been discussed in the previous sections;
- **Blazars:** we include in this class the diffuse gamma-ray flux from BL Lacs and Flat Spectrum Radio Quasars. This contribution has been estimated in Ref. [69]. However, this estimate does not account for electromagnetic cascades in the intergalactic space. For this reason, we have integrated the use of the γ -Cascade code to obtain the diffuse blazar flux, using the best-fit values for the Luminosity-Dependent Density Evolution (LLDE) model provided in Ref. [69], together with the contribution of electromagnetic cascades. We find that the latter can enlarge the diffuse blazar spectrum by even 20%, causing significant changes in the multi-messenger analysis;
- **Radio galaxies:** we take this contribution from Ref. [69] (see also Refs. [288, 289]). Radio galaxies are expected to provide a large gamma-ray flux below 1 GeV. We do not

account for an electromagnetic cascade component from radio galaxies, because their spectrum is quite soft and therefore the cascade component should be subdominant. For simplicity we do not consider a relevant contribution from radio galaxies to the neutrino flux. However, recent works like Ref. [290] have proposed radio galaxies to be an important source of high-energy neutrinos. Hence, a negligible high-energy neutrino emission from these sources should be regarded as an assumption of our work, in agreement with analyses like Refs. [291].

We determine a chi-squared likelihood for both the neutrino and the gamma-ray component. For the neutrino component, we use as chi-squared function

$$\chi_\nu^2 = \sum_i \left(\frac{\Phi_{\nu,i}^{\text{IC}} - N_{\text{Blazars}} \Phi_{\nu,i}^{\text{Blazars}} - N_{\text{SBG}} \Phi_{\nu,i}^{\text{SBG}}(p^{\text{max}})}{\sigma_{\nu,i}^{\text{IC}}} \right)^2, \quad (5.20)$$

where $\Phi_{\nu,i}^{\text{IC}}$ is the diffuse single-flavour flux observed by IceCube in each energy interval i with uncertainties $\sigma_{\nu,i}^{\text{IC}}$, whereas $\Phi_{\nu,i}^{\text{Blazars}}$ and $\Phi_{\nu,i}^{\text{SBG}}$ are the neutrino flux of blazars and SBG sources, respectively. The free parameters in the neutrino chi-squared function are the maximal proton energy p^{max} , and the two normalizations N_{SBG} and N_{Blazars} for the diffuse SBG and blazar components.

For the gamma-ray component, we follow Refs. [39, 69, 292], considering two independent normalizations for the blazar component N_{Blazars} and for the radio galaxies component N_{RG} . For both these normalizations we insert a prior term in the chi-squared function, accounting for the theoretical uncertainties on the magnitude of the fluxes. This prior distribution is obtained by averaging the theoretical uncertainties on the flux predictions in Ref. [69] over the energy range of interest. In this way we obtain the following chi-squared for the gamma-rays

$$\begin{aligned} \chi_\gamma^2 = & \sum_i \frac{1}{\sigma_{\gamma,i}^{\text{EGB}^2}} \left(\Phi_{\gamma,i}^{\text{EGB}} - N_{\text{RG}} \Phi_{\gamma,i}^{\text{RG}} - N_{\text{Blazars}} \Phi_{\gamma,i}^{\text{Blazars}} - N_{\text{SBG}} \Phi_{\gamma,i}^{\text{SBG}}(p^{\text{max}}) \right)^2 + \\ & + \left(\frac{N_{\text{Blazars}} - 1}{\sigma_{\text{Blazars}}} \right)^2 + \left(\frac{N_{\text{RG}} - 1}{\sigma_{\text{RG}}} \right)^2 \end{aligned} \quad (5.21)$$

where the quantities $\Phi_{\gamma,i}^{\text{EGB}}$ are the EGB data with uncertainties $\sigma_{\gamma,i}^{\text{EGB}}$, while $\Phi_{\gamma,i}^{\text{RG}}$, $\Phi_{\gamma,i}^{\text{Blazars}}$ and $\Phi_{\gamma,i}^{\text{SBG}}$ are respectively the radio galaxies, blazar and SBG contributions to the EGB. The last two terms are the priors accounting for the uncertainty on the normalization of the two non-SBG components. The average uncertainties are estimated as $\sigma_{\text{Blazars}} = 0.26$ and $\sigma_{\text{RG}} = 0.65$ [69].

Differently from Ref. [292], we take into account a further prior distribution from the estimate of Ref. [149] that $0.68_{-0.08}^{+0.09}$ of the EGB above 50 GeV consists of resolved point sources. This implies that a sufficiently large fraction of the EGB consists of blazars, since most of the blazars are seen as resolved sources. In order to estimate how much of the EGB is made up of blazars, we compute the fraction of the diffuse blazar flux that comes from resolved sources, defined as sources with a total flux larger than 10^{-8} ph/cm²/s according to Ref. [69]. Averaging this fraction over the energy range above 50 GeV, we find that 81% of the blazar flux above 50 GeV comes from resolved blazars. If we assume that most of the point sources detected in the EGB are blazars, this means that the fraction of the EGB above 50 GeV made up of blazars is $0.84_{-0.10}^{+0.11}$. This corresponds to a normalization of the blazar flux of 0.80 ± 0.11 , so we add a corresponding prior term to the chi-squared

$$\chi_{\text{pos}}^2 = \left(\frac{N_{\text{Blazars}} - 0.80}{0.11} \right)^2. \quad (5.22)$$

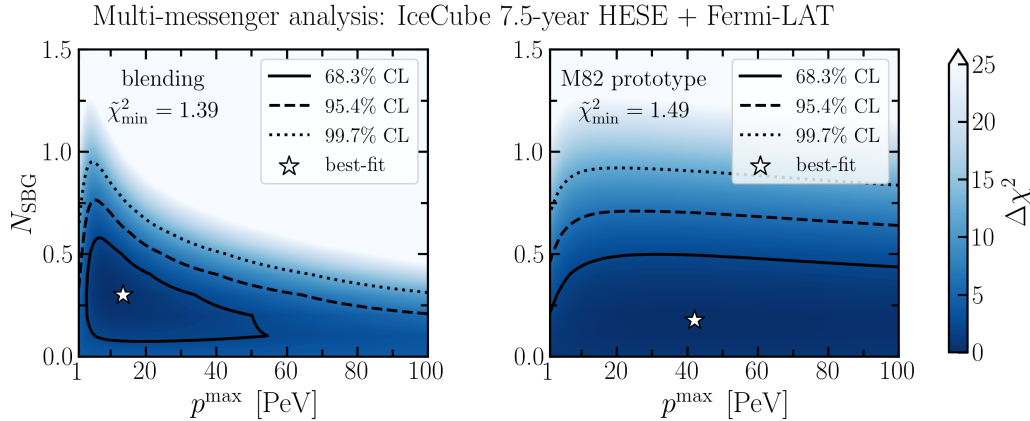


Figure 5.3: Profile likelihoods for the SBG parameters obtained in the multi-messenger analysis of IceCube 7.5-year HESE neutrino data and Fermi-LAT gamma-ray data with energy above 0.1 GeV. The left (right) panel corresponds to the blending (M82 prototype) model for the SBG emission. The solid, dashed and dotted lines represent the likelihood contours at 68.3% CL, 95.4% CL and 99.7% CL, respectively. The white stars display the best-fit points.

In the combined analysis we use a single chi-squared defined as the sum of the three:

$$\chi_{\nu+\gamma}^2(N_{\text{RG}}, N_{\text{Blazars}}, N_{\text{SBG}}, p^{\text{max}}) = \chi_{\nu}^2 + \chi_{\gamma}^2 + \chi_{\text{pos}}^2, \quad (5.23)$$

in which now four free parameters appear, namely N_{RG} , N_{Blazars} , N_{SBG} and $p_{\text{SBG}}^{\text{max}}$.

As a final comment, let us discuss the physical meaning of the normalization N_{SBG} . This is mainly determined by the efficiency of energy release in SNRs, as in Eq. (5.6). There is also a slight dependence on the threshold value ψ^* which defines which SBGs are in the calorimetric regimes. Using the Kennicutt relation, it can be proved that for low ψ^* the normalization of the diffuse flux varies as

$$N_{\text{SBG}} = \left(\frac{\xi}{0.1}\right) \left[1.47 - 0.32 \left(\frac{\psi^*}{1 \text{ M}_{\odot} \text{ yr}^{-1}}\right)^{0.4}\right]. \quad (5.24)$$

The dependence on ψ^* is very mild, so the normalization of SBGs gives us information mainly on the acceleration process in SNRs.

5.4 Results

As discussed in the previous section, our analysis focuses on two different neutrino data sets, namely the 7.5-year HESE and the 6-year cascade events. The counterpart in gamma-rays are the data corresponding to the Fermi EGB. Furthermore, for the two data set choices, we perform two different analysis, either with the spectral index blending or with a single power-law with the spectral index of M82 as a prototype. For each case we determine a test statistic defined as $\Delta\chi^2 = \chi_{\nu+\gamma}^2 - \min\chi_{\nu+\gamma}^2$. In all cases we find that the chi-squared exhibits a well-defined minimum, so that the Wilks' theorem applies. The latter ensures us that, for each parameter choice, the $\Delta\chi^2$ is approximately distributed as a chi-squared variable with a number of degrees of freedom equal to the number of free parameters. We use this information to determine the 68.3%, 95.4%, and 99.7% confidence level contours for the

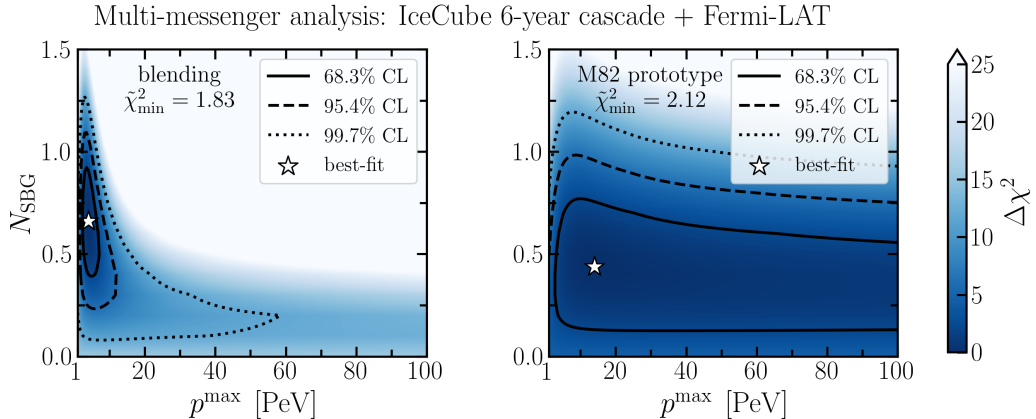


Figure 5.4: Profile likelihoods for the SBG parameters obtained in the multi-messenger analysis of IceCube 6-year cascade neutrino data and Fermi-LAT gamma-ray data with energy above 0.1 GeV. The left (right) panel corresponds to the blending (M82 prototype) model for the SBG emission. The solid, dashed and dotted lines represent the likelihood contours at 68.3% CL, 95.4% CL and 99.7% CL, respectively. The white stars display the best-fit points.

parameters in each of the four analyses (7.5-year HESE and 6-year cascade with M82 prototype or spectral index blending).

We show in Figs. 5.3 and 5.4 the contours of the test statistic in the p^{\max} - N_{SBG} plane. The remaining two parameters (N_{Blazars} and N_{RG}) are marginalized over by minimizing the test statistic over their values. The contours corresponding to 68.3%, 95.4%, and 99.7% confidence level have been highlighted. The comparison between the left (spectral index blending) and right (M82 prototype) panels shows that, both for the HESE and for the cascades, the spectral index blending prefers a larger SBG flux to explain the neutrino and gamma-ray data. For the HESE case the normalization of the SBG flux is different from zero at the 1-sigma level in the blending case, whereas it is consistent with zero in the M82 prototype case. For the cascades the difference is even more noticeable, and the normalization of SBGs is different from zero at the 3-sigma level in the case of blending. The best-fit parameters for all cases are collected in Table 5.1, together with the reduced chi-squared. Both for the HESE and the cascade data sets, the blending case leads to smaller reduced chi-squared and thus to a better agreement with the data. The best-fit solution exhibits a blazar flux slightly smaller ($N_{\text{blazar}} < 1$) than the literature [69]. There are two reasons for this: on the one hand, the inclusion of the electromagnetic cascades in the blazar component would produce too many photons in the low energy range, so that the normalization is required to be lower; on the other hand, a lower blazar flux in gamma-rays allows for a higher SBG flux, both in gamma-rays and neutrinos, relieving the IceCube-Fermi tension. The radio galaxies flux is on the other hand slightly larger ($N_{\text{RG}} > 1$) than the prediction in the literature [69], to account for the low energy photons which are not explained by blazars.

We reproduce the best-fit neutrino and gamma-ray fluxes for the case of spectral index blending in Fig. 5.5. As discussed above, the gamma-ray flux is dominated by the blazar component above 1 GeV, and by radio galaxies at lower energies. On the other hand, the neutrino production is dominated by SBGs for energies below the PeV, which is the reason why the maximal proton energy in Table 5.1 is of the order of 10 PeV. In this multi-component framework, the higher energy neutrinos can be explained by the blazar flux, which is peaked between 1 PeV and 10 PeV. The analysis on the

IceCube 7.5-year HESE + Fermi-LAT		
SBG model		
Parameters	Blending	M82 prototype
p^{\max}	13.6	42.0
N_{SBG}	0.30	0.18
N_{Blazars}	0.72	0.77
N_{RG}	2.24	2.19
$\tilde{\chi}^2 = \chi^2/32$	1.39	1.49
IceCube 6-year cascade + Fermi-LAT		
SBG model		
Parameters	Blending	M82 prototype
p^{\max}	4.0	14.0
N_{SBG}	0.66	0.44
N_{Blazars}	0.59	0.68
N_{RG}	2.24	2.15
$\tilde{\chi}^2 = \chi^2/38$	1.83	2.12

Table 5.1: Best-fit points obtained in the multi-messenger analyses of IceCube 7.5-year HESE (left) and 6-year high-energy cascade (right) neutrino data and the extragalactic gamma-ray background data measured by Fermi-LAT. The second (third) column in each table refers to the SBG model with the data-driven spectral index blending (a single power-law behaviour set by M82 prototype). The last row reports the reduced chi-squared.

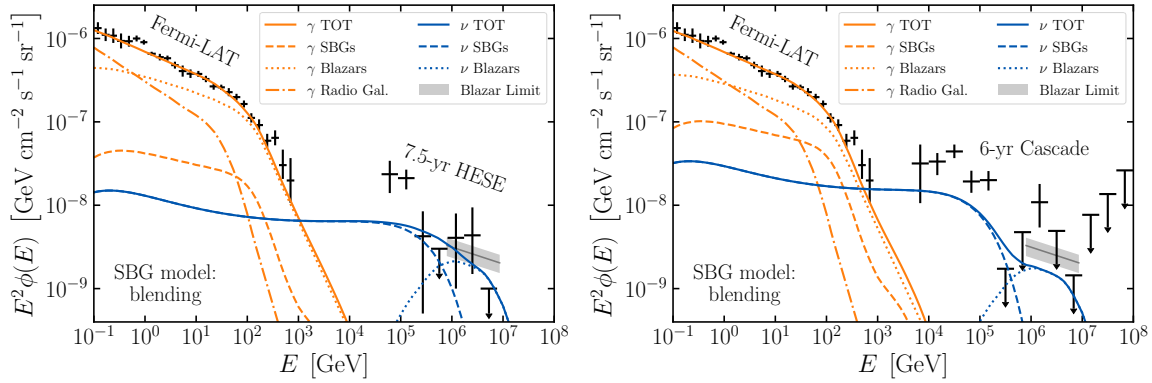


Figure 5.5: Best-fit gamma-ray (orange lines) and single-flavour neutrino (blue lines) fluxes for the SBG model with data-driven blending of spectral indexes. The left (right) plot corresponds to the multi-messenger analysis with IceCube 7.5-year HESE (6-year cascade) neutrino data. The dashed, dotted and dot-dashed lines correspond to the contributions of SBGs, blazars and radio galaxies, respectively. The grey area displays the IceCube stacking limit affecting the blazar component [287].

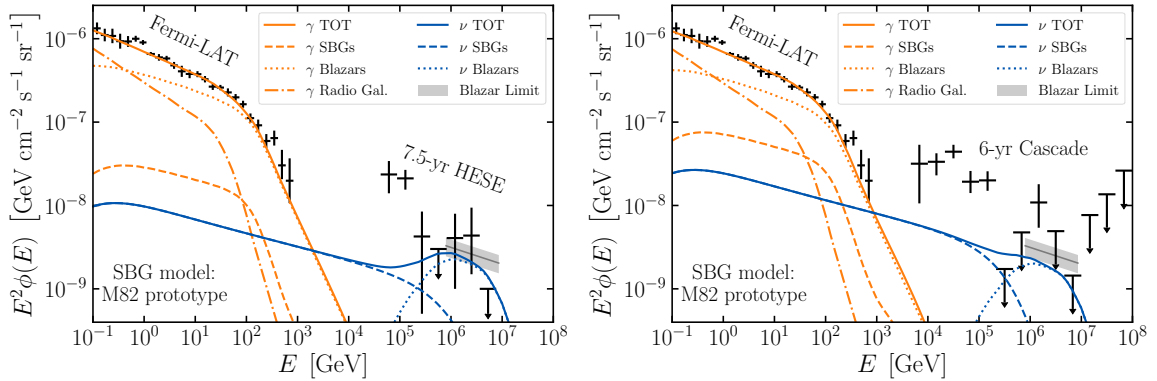


Figure 5.6: Best-fit gamma-ray (orange lines) and single-flavour neutrino (blue lines) fluxes for the SBG prototype-based model with a single power-law behaviour. The left (right) plot corresponds to the multi-messenger analysis with IceCube 7.5 year HESE (6-year cascade) neutrino data. The dashed, dotted and dot-dashed lines correspond to the contributions of SBGs, blazars and radio galaxies, respectively. The grey area displays the IceCube stacking limit affecting the blazar component [287].

6-year cascade data sample indicates a larger role of the SBG component. This is mainly because of the increased amount of data in the neutrino sector, which are explained by SBGs at 100 TeV.

These results are to be compared with the best-fit fluxes obtained in the single power-law case based on the M82 prototype, shown in Fig. 5.6. In this case the SBG contribution is much lower, leading to a noticeably increase in the tension with the neutrino data at 100 TeV. The reason is again connected with the relatively large value of the spectral index (to be compared with the threshold value determined in Sec. 4.2), whereas in the case of blending the presence of a hard component with spectral indices close to $\alpha = 4$ ($\gamma = 2$) allowed to relieve this tension.

The best-fit curves do not provide a complete overview of the allowed SBG neutrino and gamma-ray fluxes. For such an aim, we represent in Fig. 5.7 the 1-sigma and 2-sigma bands for the SBG fluxes only for the case of spectral index blending and for each of the two data samples. For both of them the SBG flux is non vanishing at 68.3% confidence level. For the 6-year cascade data sample this is true even at the 95.4% confidence level, due to the increased statistics in the neutrino sector. In neither of the two cases the neutrino flux from SBG can saturate the observed flux at 100 TeV, meaning that the IceCube-Fermi tension is relieved by the spectral blending, but not completely eliminated.

Finally, to strengthen this point, we show in Fig. 5.8 the percentage of the IceCube HESE events that are accounted for by SBGs, both in the cases of spectral index blending and in the case of M82 prototype. The number of neutrino events after 7.5-year of data taking is obtained by integrating the SBG neutrino flux above 30 TeV over the HESE effective area [293]. Confirming our previous discussion, in the case of spectral index blending SBGs can account for the 40% ($\sim 50\%$) of the total HESE events at 95.4% (99.7%) CL. On the other hand, in the M82 prototype scenario, they can only explain no more than 20% ($\sim 30\%$) of HESE events at 95.4% (99.7%) CL. Such a comparison further highlights the impact of the spectral index blending in quantifying the allowed SBGs contribution to the diffuse neutrino flux measured by IceCube. The contribution from local SBGs, located within a distance of 250 Mpc, is smaller than 1%, consistently with the constraints on nearby SFGs and SBGs [294–298].

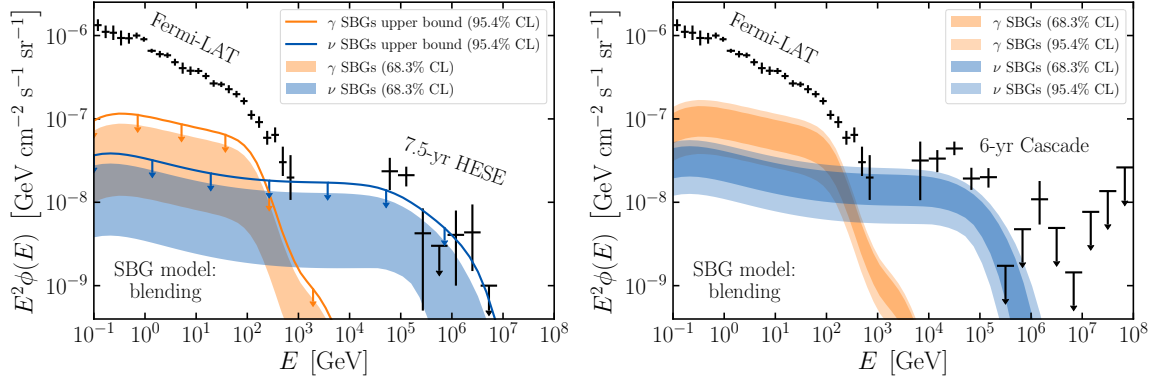


Figure 5.7: Gamma-ray (orange) and single-flavour neutrino (blue) uncertainty bands at 68.3% CL (dark colors) and 95.4% CL (light colors) for the SBG component deduced by the multi-messenger analysis in case of data-driven blending of spectral indexes. The left (right) plot corresponds to the multi-messenger analysis with IceCube 7.5-year HESE (6-year cascade) neutrino data. In the left plot, the solid lines correspond to upper bounds at 95.4% CL.

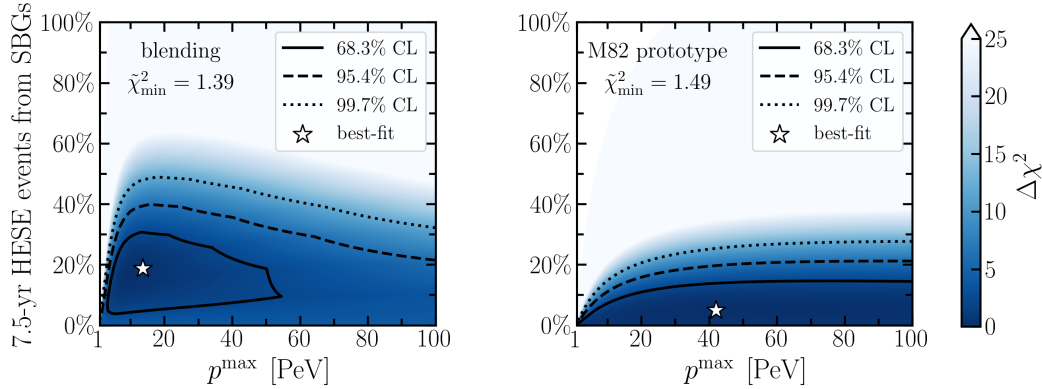


Figure 5.8: Percentage of IceCube 7.5-year HESE neutrino events above 30 TeV accounted for by starburst galaxies with blending (left plot) and M82 prototype (right plot) models. The solid, dashed and dotted lines represent the likelihood contours at 68.3% CL, 95.4% CL and 99.7% CL, respectively, according to the corresponding multi-messenger analysis (see Fig. 5.3). The white stars display the best-fit points.

5.5 Discussion

In the work presented in this chapter we have revisited the production of neutrinos and gamma-rays in SBGs. The main novelty we introduce, compared to previous models in the literature, is that we account for the different spectral shapes of cosmic-ray, neutrino, and gamma-ray fluxes from individual SBGs. We account for this difference using experimental data, in particular the gamma-ray observations of 12 SFGs and SBGs, as a guide to infer a distribution for the spectral indexes. The limited statistics is of course an obstacle to a robust determination of this distribution, and this will only be overcome when more precise observations, possibly by the future IACTs such as CTA, will be available. However, the present information is already able to show that some of the SBGs may have a harder spectrum compared to the benchmark case of M82. The presence of harder SBGs allows the diffuse flux to acquire a characteristic blended shape with a harder component at high energies, thereby relieving the IceCube-Fermi tension.

In order to perform a quantitative estimate, we perform a multi-messenger analysis on the Fermi-LAT EGB and the IceCube data, focusing on the 7.5-year HESE and the 6-year cascade data samples. We perform a multi-component analysis, accounting not only for SBGs but also for blazars and radio galaxies. The introduction of blazars allows to explain the neutrinos with energy above 1 PeV. Correspondingly, we find that the maximal proton energy required in SBG models is of the order of 1 PeV. This is a natural scale for SNR acceleration, which does not require specific models, such as magnetic field amplification, to be explained. The spectral index blending allows to explain a larger fraction, at most 40%, of the HESE data, compared with the single power-law approach which only explains up to 20%. The reason is again the presence of harder spectral indexes, which, as discussed in Sec. 4.2, predict a lower number of photons in the Fermi-LAT range and therefore do not exceed the EGB. Even accounting for spectral index blending, this model is still not able to completely explain the excess of neutrinos at 100 TeV. This may in principle be due to a different astrophysical component of Galactic origin, or even to a non-standard component, e.g. Dark Matter decay (see Chap. 7). Nevertheless, this work shows that accounting for the variability of different members of the SBG source class, and possibly also of other source classes, can have a significant impact on the comparison with experimental observations.

Chapter 6

Unified model of photohadronic neutrino production

Photohadronic production was discussed in general terms in Chap. 1, and we referred to specific examples of photohadronic sources in Chap. 4. Both discussions showed that $p\gamma$ sources are considerably more difficult to describe than pp sources. The main reason is that in $p\gamma$ sources the resulting neutrino¹ spectrum depends both on the cosmic-ray spectrum and on the target photon spectrum, whereas in pp sources the neutrino spectrum follows the energy dependence of the cosmic-ray spectrum. The spectral shape of the neutrino flux can significantly affect the detection prospects, since it determines the energy range in which the flux is peaked. Because of the dependence on the target photon spectrum, different classes of photohadronic sources are typically dealt with on a case-by-case basis, with separate modelings devoted to each class of astrophysical sources. While this approach allows to account in a precise way for the detailed properties of each source class, it is rather unsuited for analyses which require a systematic scan over many source classes at once: these include, for example, neutrino multiplet studies leading to constraints on the source density and stacking analyses. Furthermore, studying the effects of BSM physics on neutrino fluxes also requires a parameterization of the astrophysical neutrino production which is sufficiently flexible so as to capture different classes of sources at once.

Previous approaches in the literature to the general modeling of $p\gamma$ sources, such as Refs. 22, 299, 300, have assumed that target photons originate from synchrotron radiation from co-accelerated electrons. This assumption may not necessarily be true in most of the $p\gamma$ sources interesting for neutrino production. In Ref. 301 a broken power-law spectrum is assumed for the target photons, assessing the detectability of various transient photohadronic sources. However, a broken power-law is described by a rather large number of parameters, which is an obstacle to a practical analysis of the whole parameter space of the model.

In the work described in this chapter, based on Ref. 35, we propose a model which is able to describe in a unified way the spectral shape of the neutrino fluxes from the main classes of photohadronic sources. In this model, we adopt a thermal target photon spectrum parameterized by its temperature only. We show that, by suitably adjusting the temperature, the model can reproduce quite accurately the neutrino production also in sources in which the target photons are non-thermal, such as AGN and GRBs. The good reproduction is ensured by choosing the thermal

¹In the work presented in this chapter we focus only on neutrino production and do not discuss gamma-ray production, which is considerably more model-dependent because of the presence of internal attenuation and reprocessing due to $\gamma\gamma$ collisions.

spectrum to be peaked at the photon energy contributing to the production of the neutrinos near the peak of the energy flux. Therefore, this model allows to parameterize the whole variability of target photons in terms of the temperature of an effective blackbody spectrum. We propose two applications of this model: as a first application, we study the sensitivity of neutrino detectors with different energy ranges of sensitivity, focusing on how this sensitivity depends on the astrophysical properties of the source. As a second application, we determine how these astrophysical properties affect the flavor composition of the neutrino flux.

These applications illustrate the typical class of problems for which a unified framework, such as the thermal model proposed here, can provide a solution. Indeed, the model is an ideal tool for those studies requiring to encompass many different source classes at once, including, for example, multiplet and stacking searches. Furthermore, it could provide a useful tool for searches of Beyond Standard Model effects on astrophysical neutrinos (such as those discussed in Part [III](#) of this thesis), where one often needs to parameterize the standard neutrino production in astrophysical sources.

6.1 Thermal model

The key idea of the thermal model can be summarized as follows. The neutrino spectral shape is influenced by the target photon spectrum, which can take widely different shapes in different sources: there are many examples of sources in which the target photon spectrum is non-thermal, such as in AGN and GRBs. For other candidate sources, a thermal spectrum has been assumed in the literature: this is the case, e.g., for TDEs [\[195\]](#). Within the thermal model, we assume that there is a single target photon energy $\bar{\varepsilon}'_\gamma$ which contributes most to the photohadronic neutrino production, and we replace the photon spectrum by an effective blackbody spectrum, peaked at this energy $\bar{\varepsilon}'_\gamma$. In this section, we will detail on this idea: first of all we will present the rule associating to a given (non-thermal) target photon spectrum the energy $\bar{\varepsilon}'_\gamma$, and consequently the effective blackbody spectrum used in the reproduction. We will later introduce the parameterization used for the cosmic-ray spectrum and the choice of maximal proton energy. Finally, we will provide explicit examples of the performance of the thermal model on the two benchmark cases of AGN and GRBs.

6.1.1 Temperature mapping

In this subsection we discuss how we can associate to a generic target photon spectrum a single photon energy $\bar{\varepsilon}'_\gamma$ contributing most to the neutrino production. Equivalently, to this energy we can associate an effective temperature for the blackbody spectrum such that the effective blackbody number density is peaked at $\bar{\varepsilon}'_\gamma$. For this reason, we refer to this procedure as the mapping from a generic target photon spectrum to the temperature of the effective blackbody spectrum.

Before entering the discussion, let us fix some notation. We will refer by unprimed quantities to the quantities in the Earth reference frame. We will also assume that cosmic-rays are accelerated in a rapidly expanding jet, as is the case in AGN, GRBs and TDEs. The quantities in the frame comoving with the jet are denoted as primed. In particular, the energies in the two frames are related by a Doppler factor as $E = \mathcal{D}E'$, with $\mathcal{D} = \frac{1}{\Gamma(1-v\cos\theta)}$: here v is the expansion velocity, Γ is the corresponding Lorentz factor, and θ is the observer viewing angle. Due to relativistic beaming, the emission is most pronounced in directions close to the jet axis: choosing $\theta \sim 1/\Gamma$, we see that the Doppler factor is typically $\mathcal{D} \sim \Gamma$. In the following we will use directly Γ to denote the Doppler factor of expansion. If, in addition, the source is at a cosmological redshift z , the energy will be further redshifted by a factor $1+z$, so that $E = \frac{\Gamma E'}{1+z}$. In the following, we will neglect the factor

$1 + z$ which can be suitably absorbed in the definition of the Doppler factor.

We denote by $n(\varepsilon'_\gamma)$ the number of target photons per unit volume per unit energy. For a proton with energy E'_p , the interaction rate with the target photon field will be

$$\Gamma_{p \rightarrow \pi}(E') = \int d\varepsilon'_\gamma n(\varepsilon'_\gamma) \sigma(\varepsilon'_\gamma, E'). \quad (6.1)$$

Here $\sigma(\varepsilon'_\gamma, E')$ is the total cross-section for interaction. The specific form of $\sigma(\varepsilon'_\gamma, E')$, as was mentioned in Chap. [1](#) is typically obtained by simulations, and it involves the interplay of different processes, including the Δ -resonance interaction and the multi-pion processes. In App. [D](#) we will discuss in detail approximate parameterizations for the cross-section which allow to derive the results in this section more rigorously. Here, we limit to observe that the interaction rate increases with the photon number density $\varepsilon'_\gamma n(\varepsilon'_\gamma)$. Furthermore, the interaction rate vanishes when ε'_γ is below the kinematical threshold for pion photoproduction: specifically, for a proton with energy E' , only those photons can interact which satisfy the condition $\varepsilon'_\gamma \gtrsim y_\Delta m_p / E'$, where m_p is the proton mass and $y_\Delta \simeq 0.2$ GeV corresponds to the reasonable pitch-angle averaged ‘‘threshold’’ for the interaction (see Fig. 4 in Ref. [30](#)). If the proton distribution has a maximal proton energy $E'_{p,\max}$ (the value of which is discussed in the next subsection), then the photons which participate to photohadronic interactions have energies

$$\varepsilon'_\gamma > \frac{y_\Delta m_p}{E'_{p,\max}}. \quad (6.2)$$

In this range, we assume the simple criterion that the photohadronic production mainly comes from those photons with energy maximizing the photon number density $\varepsilon'_\gamma n(\varepsilon'_\gamma)$. Therefore, we identify the energy $\bar{\varepsilon}'_\gamma$ with the position of the maximum of $\varepsilon'_\gamma n(\varepsilon'_\gamma)$.

There is an important case for which this criterion is not sufficient to determine the dominant energy $\bar{\varepsilon}'_\gamma$, namely when the photon number density is flat in an energy interval from ε'_1 to ε'_2 . In other words, in this region $n(\varepsilon'_\gamma) \propto \varepsilon'^{-1}_\gamma$. As we will see, this is just the expected behavior for our benchmark model of GRB. In this case, there is no well-defined maximum in the photon number density. We will show in App. [D](#) that, due to multi-pion processes, the correct neutrino spectrum can nevertheless approximately be recovered with the choice $\bar{\varepsilon}'_\gamma = \varepsilon'_2$, namely the higher energy of the range in which the photon number density is flat. With this specification, we have a well-defined rule mapping a generic target photon spectrum to an energy $\bar{\varepsilon}'_\gamma$ dominating the photohadronic production.

Finally, we introduce an effective black-body target spectrum

$$n_\gamma^{\text{th}}(\varepsilon'_\gamma) d\varepsilon'_\gamma = \frac{\varepsilon'^2_\gamma}{\pi^2} \frac{1}{e^{\varepsilon'_\gamma/T'} - 1} d\varepsilon'_\gamma. \quad (6.3)$$

In order for the blackbody photon number density to be peaked at the same energy $\bar{\varepsilon}'_\gamma$, we choose

$$T' = \frac{\bar{\varepsilon}'_\gamma}{2.8}. \quad (6.4)$$

By explicitly maximizing $\varepsilon'_\gamma n_\gamma^{\text{th}}(\varepsilon'_\gamma)$, it can be proved that this choice indeed leads to the correct peak energy.

In Sec. [6.1.3](#) we will show some explicit examples of the performance of the thermal model in reproducing the neutrino production from sources with non-thermal target photons. It is however useful to discuss for which choices of the target photon spectrum the thermal model performs better.

The performance of the thermal model is of course best for photon number densities which are peaked at a definite energy. However, also power-law and broken power-law spectra can be approximately reproduced. The most difficult case is for nearly flat photon number densities, namely when $n(\varepsilon'_\gamma) \propto \varepsilon'^{-\alpha}_\gamma$ with α close to one. For $\alpha \lesssim 1$, we will explicitly show in App. D that the thermal model is quite accurate. For $\alpha \gtrsim 1$ the model reproduces correctly the peak in the neutrino spectrum. However, the spectral index below the peak is not well reproduced for α close to 1. The reproduction becomes increasingly better as α increases. The spectral index below the peak is recovered exactly for $\alpha \geq 3$.

6.1.2 Cosmic-ray spectrum

A fundamental ingredient in the determination of the neutrino spectrum is the parent cosmic-ray spectrum. For this work, we model the cosmic-ray number density per unit energy as $N_p(E') \propto E'^{-2} \exp[-E'/E'_{p,\max}]$, as expected from the standard first-order Fermi acceleration mechanism, with a maximal proton energy $E'_{p,\max}$ determined by the properties of the source. More specifically, the maximal proton energy is determined by the condition that the acceleration timescale for protons $\tau'_{\text{acc}} = E'/(\eta e B')$, where B' is the source magnetic field and η is the acceleration efficiency, is smaller than the energy loss timescale and the escape time. As energy losses we only consider the dominant process of synchrotron radiation. For the acceleration efficiency we take the benchmark value $\eta = 0.1$.

For weak magnetic fields, the maximal proton energy is well-described by the Hillas condition

$$E'_{p,\max} \simeq 3 \times 10^7 \text{ GeV} \frac{B'}{1 \text{ G}} \frac{R'}{10^{10} \text{ km}} \frac{\eta}{0.1}, \quad (6.5)$$

which also corresponds to the confinement condition for $\eta = 1$. On the other hand, for strong magnetic fields, the maximal proton energy is determined by the balance between the acceleration timescale and the timescale for synchrotron losses [22] and it can be approximated as

$$E'_{p,\max} \simeq 5.9 \times 10^{10} \text{ GeV} \left(\frac{B'}{1 \text{ G}} \right)^{-1/2} \left(\frac{\eta}{0.1} \right)^{1/2}. \quad (6.6)$$

We compactly show the maximal proton energy as a contour plot in the Hillas plane $R' - B'$ in Fig. 6.1. The shape of the contours indeed follows the typical behavior of the Hillas criterion (corresponding to a constant product $R'B'$) for low magnetic fields, while they become horizontal (corresponding to a constant B') for high magnetic fields, where synchrotron losses dominate.

Therefore, in the thermal model introduced here we can parameterize the neutrino spectral shape in terms of four parameters only: the source size R' and magnetic field B' , which determine the cosmic-ray spectrum; the target photon temperature T' ; the Doppler factor Γ . For each choice of the parameters we use the software NeuCosmA [22, 30, 302, 303] to obtain the produced neutrino spectrum. The software determines the secondary pion, kaon, and neutron spectrum produced in the $p\gamma$ collisions: the $p\gamma$ cross section is based on a parameterization of the simulations by SOPHIA [32]. Subsequently, it determines the injection of secondary muons by the pion decay, using the decay functions in Ref. [29]. For both secondary pions and muons, cooling due to synchrotron losses in the source magnetic field are accounted for by solving the stationary transport equation for the energy distribution. For the neutrinos produced in the neutron decay, we assume a monochromatic spectrum, which may lead to an inaccurate reproduction of the flavor composition in the low energy region. However, since the flavor composition in this energy region is difficult to reproduce correctly even independently of this effect, we do not investigate further the changes induced by a different choice.

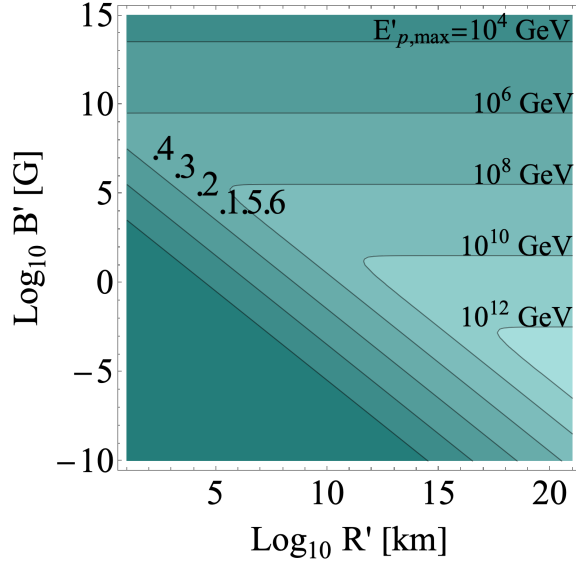


Figure 6.1: Maximal proton energy in the relativistically comoving frame as a function of B' and R' in our maximal proton energy model for $\eta = 0.1$. Test points are identified by the numbers 1 to 6.

6.1.3 Benchmark examples

In this section, we present two benchmark examples of sources with non-thermal target photons, illustrating the performance of the thermal model in approximating the neutrino production. We take as examples the cases of AGN and GRBs, in both of which the target photons are usually described by means of a broken power law

$$n_\gamma(\varepsilon'_\gamma) \propto \begin{cases} (\varepsilon'_\gamma/\varepsilon'_b)^{-\alpha}, & \varepsilon'_{\min} \leq \varepsilon'_\gamma \leq \varepsilon'_b \\ (\varepsilon'_\gamma/\varepsilon'_b)^{-\beta}, & \varepsilon'_b < \varepsilon'_\gamma \leq \varepsilon'_{\max} \end{cases} \quad (6.7)$$

Such a spectrum is parameterized by the two spectral indices α and β , the minimal energy ε'_{\min} , the break energy $\varepsilon'_{\text{break}}$, and the maximal energy ε'_{\max} . We collect in Table 6.1 our benchmark parameter choices for both AGN and GRB, as well as the effective temperatures determined by the mapping in Sec. 6.1.1

For both sources, we show in Fig. 6.2 the all-flavor neutrino spectra (left panel), as well as the flavor composition (right panel), computed using the broken power-law model (solid) and the thermal model (dashed). In Fig. 6.2 $\phi_{\nu\alpha} = \frac{dN_{\nu\alpha}}{dt dE dS}$ is the number of particles per unit time per unit energy per unit surface and $\alpha = e, \mu, \tau, \bar{e}, \bar{\mu}, \bar{\tau}$. Furthermore, $\phi_\nu = \sum_\alpha \phi_{\nu\alpha}$; since we are dealing with point sources, we do not consider the differential flux per unit solid angle.

The neutrino spectral shape is well-reproduced near the peak by the thermal model for both AGN and GRB. Interestingly, for GRB the accuracy in the reproduction depends critically on the multipion production: if we had accounted only for the Δ -resonance contribution, the thermal model would have produced a peaky neutrino spectrum, not in agreement with the solid line spectrum. The reason why multipion production allows a more accurate reproduction is discussed in more detail in App. D. The flavor composition is also well-reproduced by the thermal model except at the very lowest energies, where the thermal model predicts an overproduction of electron neutrinos.

Source	Γ	B' [G]	R' [km]	ε'_{\min} [eV]	ε'_b [keV]	ε'_{\max} [keV]	α	β	T' [eV]
AGN	10	1	10^{11}	-	3×10^{-5}	1	1	2.64	0.2
GRB	100	3×10^5	10^7	0.3	14.8	1000	1	2	5300
TDE	10	90	10^9	-	-	-	-	-	840

Table 6.1: Summary of numerical values for the parameters used for the benchmark spectra shown in this work. For AGN we extract the parameters of the target-photon spectrum by a broken power-law fit to the low energy spectrum in Ref. [304]; the astrophysical parameters Γ , B' and R' are fixed to typical values for AGN jets in Ref. [22]. For GRB the parameters of the target-photon spectrum and the magnetic field are taken from the reference values of Ref. [302], the Doppler factor is fixed to a typical value and the size of the accelerating region is taken to be the shell thickness $R' = \frac{\Gamma t_v}{1+z}$ with $t_v = 0.3$ s being the variability timescale and $z \ll 1$. For TDE the parameters of the target-photon spectrum and the magnetic field are taken from Ref. [195]; the Doppler factor is fixed to a typical value and the size of the accelerating region is taken to be the shell thickness $R' = \frac{\Gamma t_v}{1+z}$ with $t_v = 300$ s and $z \ll 1$.

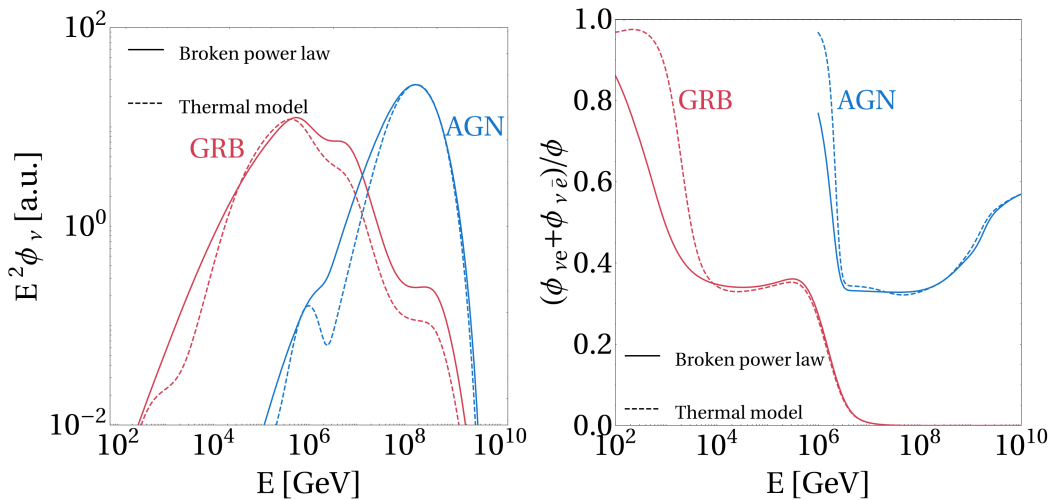


Figure 6.2: Comparison between the benchmark astrophysical neutrino fluxes, parameterized as broken power laws, and their reproduction using the thermal model. In the left panel we show the comparison for the neutrino fluxes produced in AGN and GRBs. We show the all-flavor neutrino flux $E^2\phi$ in $\text{GeV cm}^{-2} \text{s}^{-1}$ (normalization in arbitrary units) as a function of the energy in the observer rest frame. In the right panel we show the fraction of electron neutrinos and antineutrinos in the differential flux at the source as a function of the energy in the observer rest frame, in the energy region in which the flux is at least 1/1000 of its peak value. The solid curves are obtained from the astrophysical broken power-law source model, the dashed curves are obtained with the thermal model, the dotted curve is obtained from the Band function model for the GRB target photon spectrum. The parameters used in the generation of the astrophysical neutrino spectra are summarized in Table 6.1.

The reason is that at low energies the production is dominated by electron neutrinos from neutron decay, which produce a bump in the spectral distribution: the specific shape of this bump depends on the details of the target photon spectrum, and therefore are difficult to recover with the thermal

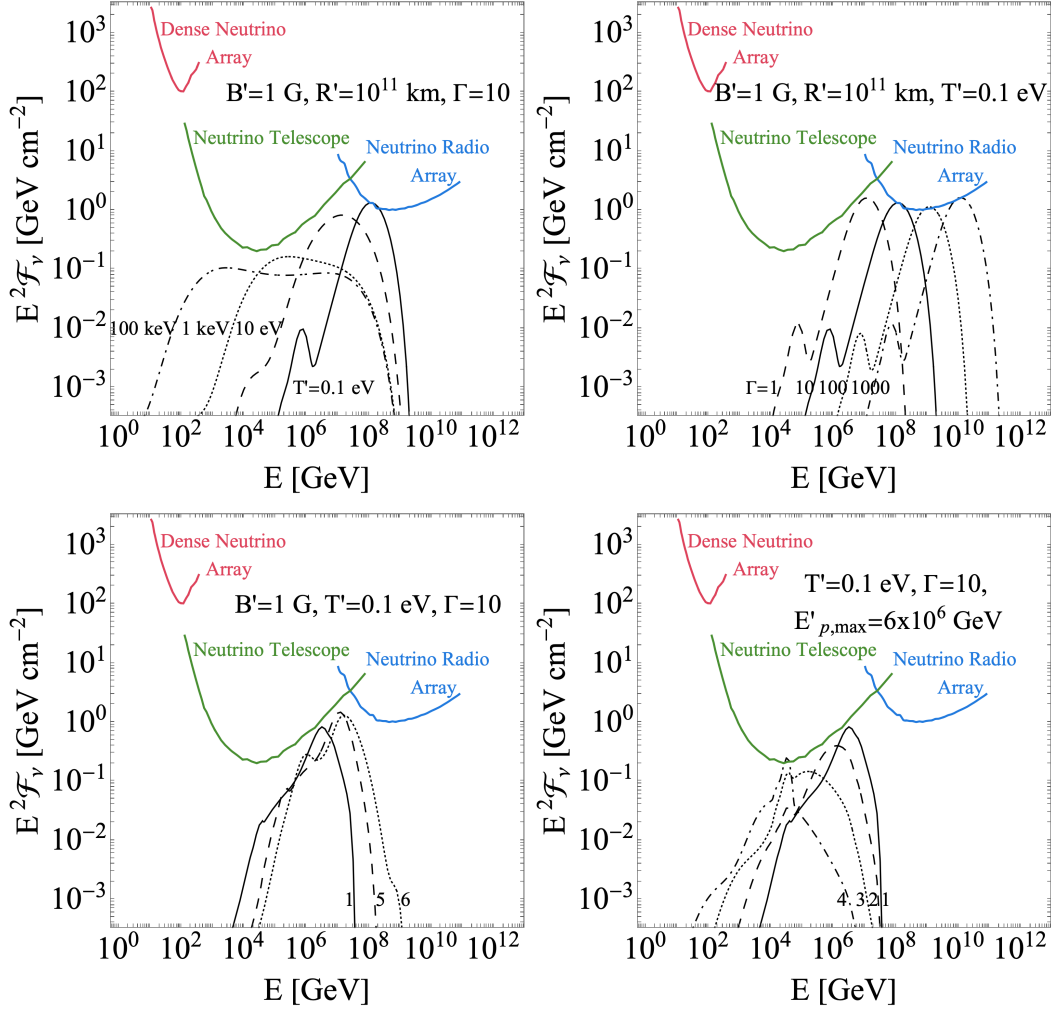


Figure 6.3: Experimental sensitivities for different model parameters. The figures show the differential limits (colored curves) and the sensitivities to certain benchmark fluences (black curves) as a function of (observed) neutrino energy, where the curves refer to all flavors. In the upper left panel we show different choices of the effective temperature T' , in the upper right panel we show different choices of Γ . In the lower left and right panels, we show curves for different proton energies and magnetic fields, respectively, referring to the test points identified in Fig. 6.1. The fluences are normalized so that the sum of the expected events at all three experiments together is 2.44.

model. However, this inaccuracy only affects the flavor composition in the low energy region, far from the peak of the spectrum. The qualitative behavior of the flavor composition as a function of the energy will be discussed in more detail in Sec. 6.3.

Let us comment on one final point. We have shown two examples of how the thermal model can simulate neutrino production from non-thermal sources. However, we emphasize that there could also be sources which naturally have a target of photons which is thermal in nature. One

such example may be TDEs: in Ref. [195] the target photons are indeed modeled as a blackbody spectrum. In Sec. 6.2 we will use TDE as a benchmark astrophysical source: in Table 6.1 we collect the parameters we use to model its neutrino production.

In conclusion, within the thermal model the neutrino spectral shape is specified by four parameters

$$T', B', R', \Gamma, \quad (6.8)$$

where T' is the effective temperature of the target photons, B' is the magnetic field, R' is the source dimension and Γ is the Doppler factor. Furthermore, the acceleration efficiency η , which we fix to 0.1 in the following, and the spectral index of the cosmic-rays, which we fix to 2, are in principle other free parameters of the model.

6.2 Sensitivity of neutrino detectors

In this section we discuss the potentialities of neutrino detectors sensitive in different energy ranges for the detection of the neutrino fluxes from a $p\gamma$ astrophysical source. We parameterize the properties of the source by the four parameters in Eq. 6.8, and we study how the results are influenced by these parameters. We divide the neutrino detectors of interest in three classes, based on their energy ranges of sensitivity:

- *Dense neutrino arrays*, between 1 GeV and 10^5 GeV (e.g. PINGU, ORCA, DeepCore);
- *Neutrino telescopes*, between 10^5 GeV and 10^7 GeV (e.g. IceCube, KM3NeT, Antares);
- *Neutrino radio arrays*, between 10^7 GeV and 10^{12} GeV (e.g. ARIANNA, IceCube-Gen2 Radio Array, GRAND).

We choose as representatives DeepCore [305] for dense neutrino arrays, KM3NeT [306] for neutrino telescopes and IceCube-Gen2 Radio Array [307] for neutrino radio arrays, respectively. In particular, we choose DeepCore since it has a better sensitivity above 100 GeV, and KM3NeT and IceCube-Gen2 Radio Array for their slightly larger effective areas compared to the others on the lists; see also Ref. [308] for effective volumes of future neutrino telescopes. However, experiments in the same class lead generally to similar performances.

The detection of neutrinos from a source in general depends on the exposure time of the experiment to the source. In this work, for simplicity, we will stick to a background-free approximation and consider the integrated fluence \mathcal{F}_ν , which is the flux times the observation time $\mathcal{F}_{\nu\alpha} = \phi_{\nu\alpha}t$ for a steady flux (in units of $\text{GeV}^{-1} \text{cm}^{-2}$). A constant fluence leads to a constant expected number of detected events, and therefore in the background-free approximation we can define a minimum fluence needed for detection at each given experiment. The validity of the background-free approximation is sufficiently justified for the neutrino radio telescopes and the neutrino telescopes. It is not in general reasonable for dense neutrino radio arrays, for which atmospheric neutrinos constitute a rather large background. In Ref. [35], we discuss the changes induced by accounting for the background.

In order to quantify the potentiality for detection of a source with a given choice of parameters, for each experiment we normalize the fluence so as to have 2.44 expected events, namely the background-free Feldman-Cousins 90% sensitivity limit [309]. With this criterion, we are determining the minimum normalization of the neutrino flux leading to a 90% detection. In order to relate this normalization to a physical requirement on the source, we introduce the quantity

$$\xi = \int E \mathcal{F}_\nu dE. \quad (6.9)$$

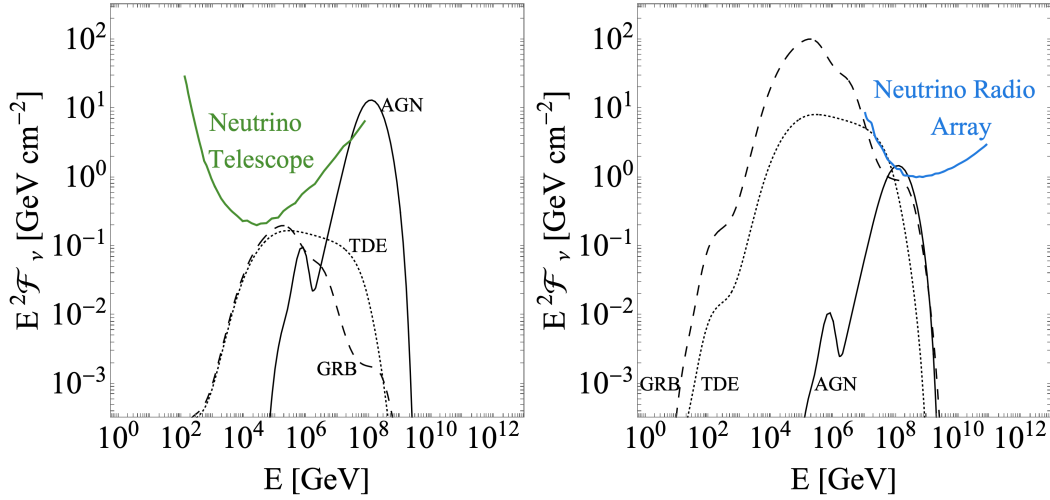


Figure 6.4: Experimental sensitivity to neutrino fluences from benchmark sources. In the left (right) panel we show the differential limit of our benchmark Neutrino Telescope (Neutrino Radio Array) in color, together with the sensitivities $E^2 \mathcal{F}_\nu$ in GeV cm^{-2} for sources with a thermal photon spectrum simulating GRBs, AGN and TDEs; all the spectra are normalized to the 90% Feldman-Cousins limit for signal detection at the corresponding experiment. The numerical values for the parameters are reported in Table [6.1](#).

This quantity is a measure of how much energy must be injected by the source in neutrinos in order to have a 90% detection. More specifically, if E_ν is the isotropically-equivalent energy injected in neutrino production by the source and $d_L(z) = (1+z) \int_0^z \frac{1}{H(t)} dt$ ($H(z)$ being the Hubble parameter), we have $E_\nu = 4\pi\xi d_L^2(z)/(1+z)$. Therefore, the larger ξ , the more energy needs to be injected in neutrino production in order to have a detection, and thus lower values of ξ are associated with a better sensitivity to neutrino detection.

We emphasize that the energy injected in neutrino production is not associated in a straightforward way with the energetic requirements on the source. In fact, the emitted neutrino energy E_ν (assuming an optically thin source) is directly proportional to the injected (non-thermal) energy of protons E_p and the fraction of the proton energy going into pion production, namely the “pion-production efficiency” f_π . Thus $E_\nu \propto f_\pi E_p$. E_p is generally taken as a free parameter, connected with the X-ray or gamma-ray luminosity through a quantity called “baryonic loading”. On the other hand, f_π strongly depends on the size, geometry, and Lorentz factor of the production region. Therefore, an interpretation in terms of the source parameters and of E_p goes beyond the scope of this study. In what follows, we will refer to the sensitivity only in terms of the energy injected in neutrinos E_ν .

In order to show how the astrophysical parameters influence the neutrino spectral shape, we show in Fig. [6.3](#) the neutrino fluences for selected parameter choices, together with the 90% differential limits of the three benchmark experiments studied here. In the four different panels we vary one parameter at a time, namely T' (upper left panel), Γ (upper right panel), maximal proton energy (lower left panel), and magnetic field (lower right panel). We now discuss the effects of each of these parameters separately.

Lower effective temperatures are associated to rather peaked spectra near their maximal ener-

Source	ξ at Neutrino Telescope [erg cm ⁻²]	ξ at Neutrino Radio Array [erg cm ⁻²]
AGN	4.5×10^{-2}	5.2×10^{-3}
GRB	1.2×10^{-3}	6.2×10^{-2}
TDE	1.7×10^{-3}	8.3×10^{-2}

Table 6.2: Summary of the minimal energy fluences ξ necessary for detection at different experiments for the benchmark spectra (reproduced in the thermal model) shown in this work.

gies, and therefore are generally easier to detect at neutrino radio arrays. Increasing the effective temperature leads to the formation of a flat region, originating from the multi-pion interaction. The Doppler factor simply induces a boost of the neutrino energies, and therefore a parallel translation of the spectral shape at higher energies (we are here considering only the spectral shape in arbitrary units: the luminosity of the source is actually also affected by the Doppler factor).

In the bottom panel, we vary the maximal proton energy and the magnetic field. Since the two parameters we have at our disposal are B' and R' , we cannot vary each of them separately. Rather, we choose a series of test points highlighted in Fig. 6.1. The test points 1, 5, and 6 are chosen at a fixed magnetic field, varying only the maximal proton energy, whereas the test points 1, 2, 3, and 4 are chosen along lines of constant maximal proton energy $E'_{p,\max}$, varying only the magnetic field. The other criteria we adopt for the choice of the test points is to look for a region in which most of the physically realistic sources appear (see, e.g., Ref. 22), and in which the magnetic field is sufficiently large to produce observable effects.

Increasing the maximal proton energy, as in the bottom left panel of Fig. 6.3, leads to an increase in the upper cutoff of the spectrum. On the other hand, increasing the magnetic field, as in the bottom right panel, leads to a steepening of the spectrum at the highest energies, which is caused by synchrotron losses.

A more directly interesting result is the neutrino spectrum for the three benchmark astrophysical sources discussed in Sec. 6.1.3, namely AGN, GRB, and TDE. We show in Fig. 6.4 the neutrino fluences (obtained using the thermal model parameters in Table 6.1) for all three sources, compared with the differential limits of neutrino telescopes (left) and neutrino radio arrays (right). For each panel the neutrino fluence is normalized to 2.44 expected events at the corresponding experiment. We also provide the values of ξ for detection of each source at the two experiments in Table 6.2. Both from the figure and from the table we see that AGN require a smaller normalization (and therefore a smaller injected energy in neutrinos) for detection at neutrino radio arrays rather than neutrino telescopes. This is due to the peaked structure of the flux at the highest energies. For TDE and GRB, on the other hand, the flux is distributed over a wider range of energies and is more easily detected at neutrino telescopes. We do not show the result for dense neutrino arrays, which are sensitive at too low energies for detecting neutrinos from these sources.

Finally, we perform a systematic scan of the parameter space to determine what is the best experiment class for neutrino detection. As a criterion, for each parameter choice we choose as most suitable experiment the one requiring the least value of ξ for a detection. We show the result in Fig. 6.5, where we classify the Hillas plane with different colors according to the most suitable experiment. We present three different choices of the parameters Γ and T' , and we identify the parameter choices corresponding to the three benchmark sources outlined above. We find that most of the parameter space can be probed by neutrino telescopes and neutrino radio arrays, requiring an energy fluence of the order of 10^{-3} erg cm⁻². Dense neutrino arrays require larger energy fluences, of the order of about 1 erg cm⁻²; they become competitive only in the range of very large magnetic fields and large temperatures. Finally, we find that neutrino radio arrays are mostly sensitive in the

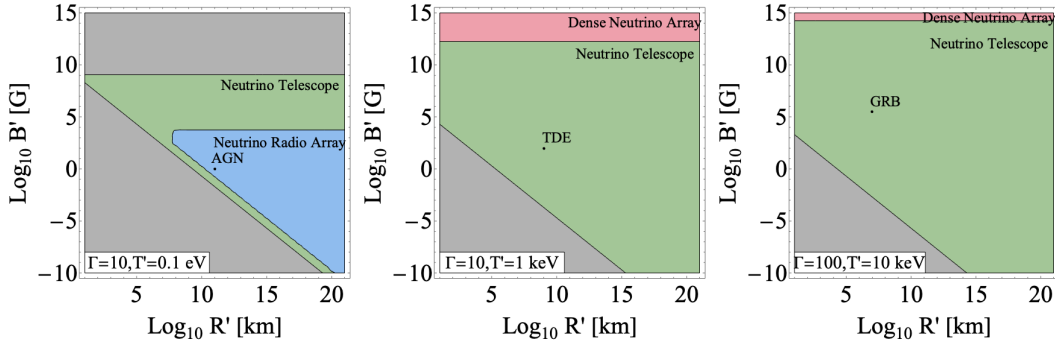


Figure 6.5: Determination of the most suitable experiment for the detection of astrophysical sources with parameters Γ , T' , B' and R' . We show the Hillas plane divided according to which experiment is most suitable for detection: the red, green and blue regions correspond, respectively, to our benchmark Dense Neutrino Array, Neutrino Telescope and Neutrino Radio Array as most sensitive experiments. The three panels correspond to different values for the effective temperature and Doppler factor. Typical values of B' , R' , T' and Γ for AGN, TDE and GRB sources are identified (the sources are identified by the order of magnitude of the effective temperature rather than by the precise value). In the gray regions, pion production, and therefore neutrino production, is inefficient, because the maximal proton energy is below the threshold for pion photoproduction for all target photons.

region of low temperatures, corresponding to peaked spectra at high energies which could not be probed by neutrino telescopes.

6.3 Flavor composition

In this section we discuss how the flavor composition is influenced by the properties of the astrophysical source in the framework of the thermal model. Since the flavor composition changes with the energy, its relation with the astrophysical parameters is difficult to convey in a compact form. As a first step, we will exhibit the flavor composition as a function of the energy for some benchmark choices of parameters. As we will see, this already allows to understand qualitatively what is the impact of the different astrophysical parameters on the flavor composition.

We show in Fig. 6.6 the neutrino fluxes (top panels) and the flavor composition (bottom panels) as a function of the energy for three benchmark choices of source size and magnetic field, identified by the test points A, B, and C in Fig. 6.7. The effective temperature is varied in each panel from 0.1 eV to 10 keV. We quantify the flavor composition by the ratio between the muon neutrino flux and the electron and tau neutrino flux $\phi_{\nu\mu}/(\phi_{\nu e} + \phi_{\nu\tau})$. We only consider fluxes summed over neutrinos and antineutrinos.

The flavor composition in all cases transitions between different regimes. At low energies, the flux is dominated by the bump of neutrinos coming from neutron decay, and is in the neutron-beam regime. At intermediate energies, the full decay chain of pions and muons is active, leading to the pion-beam regime. Finally, at the highest energies, synchrotron losses dampen the muon energy, so that only pion decay is a source of neutrinos: the flux enters therefore the muon-damped regime. The influence of the different astrophysical parameters can also be inferred from Fig. 6.6. For decreasing magnetic fields (from left to right panel), the transition to the muon-damped regime is pushed to

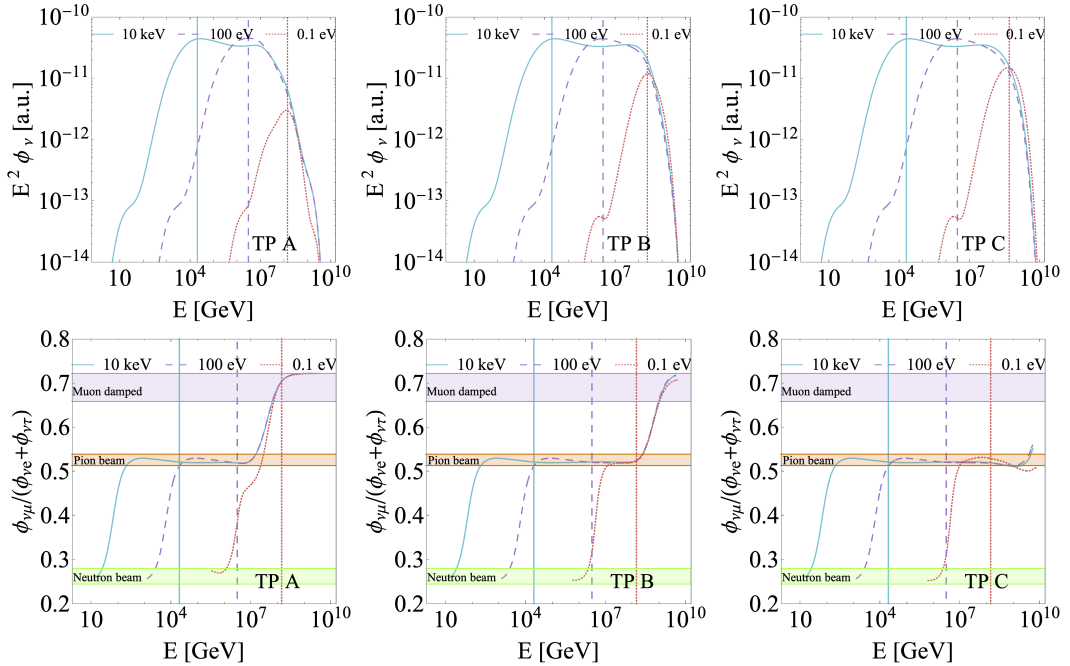


Figure 6.6: Neutrino fluxes and flavor ratios at Earth as a function of energy. In the top panels we show the all-flavor neutrino fluxes as a function of the energy for the three TPs in Fig. 6.7, which are chosen to simulate lower magnetic fields from left to right. The three curves in each panel correspond to $T' = 0.1$ eV, $T' = 100$ eV and $T' = 10$ keV; in all cases $\Gamma = 10$. In the bottom panels we show the ratio between the muon and the sum of electron and tau neutrino and antineutrino differential flux as a function of the energy. The curves are represented only in the region in which the flux is at least 1/1000 of its peak value. The horizontal bands identify the different flavor regime according to the quantitative criterion defined in the caption of Fig. 6.7. For the neutrino mixing parameters the best-fit parameters of Ref. 61 are chosen. Both in the top and the bottom panels we identify the peak energies of the neutrino fluxes with vertical lines: each color corresponds to the effective temperature according to the legend.

higher energies. This should be expected, since decreasing the magnetic field reduces the impact of synchrotron losses. On the other hand, lowering the effective temperature has the main effect of pushing the spectrum to higher energies, as seen in the top panels. For this reason, the neutron-beam region moves to higher energies as well, and the peak of the spectrum is pushed closer to the muon-damped region (because of this effect, for TPA at a temperature of 0.1 eV the peak of the spectrum is completely in the muon-damped regime).

In order to systematize these conclusions, we now focus on the flavor composition at the peak of the spectrum only (in Fig. 6.6 the peak of the spectrum for each case was identified by vertical lines), namely the maximum of $E^2\phi_\nu$. We classify the parameter space according to whether the flavor composition at the peak is pion beam, neutron beam, muon damped. The result of this classification is shown in Fig. 6.7, where we identify with different colors the regions corresponding to different flavor compositions. The three panels correspond to three different effective temperatures.

The region of low magnetic fields always lead to the pion-beam regime at the peak of the spectrum. Increasing the magnetic field leads into a region of muon damping. At the very highest magnetic

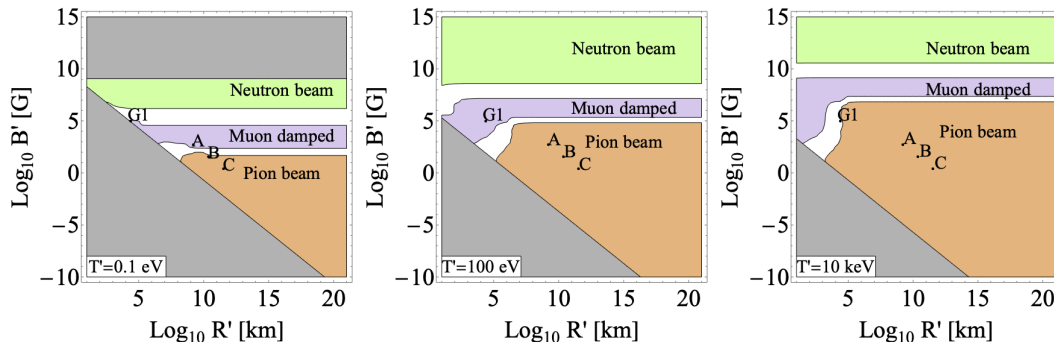


Figure 6.7: Flavor structure at the peak of the spectrum as a function of R' and B' (Hillas plot). We divide the Hillas plane according to the flavor composition at the peak of the spectrum: the neutron-beam region has a flavor ratio (at the source) between $(0.9 : 0.1 : 0)$ and $(1 : 0 : 0)$; the muon-damped region has a flavor ratio between $(0.1 : 0.9 : 0)$ and $(0 : 1 : 0)$; the pion-beam region has a flavor ratio between $(0.31 : 0.69 : 0)$ and $(0.36 : 0.64 : 0)$. In the white regions the flavor composition does not belong to any of the previous regimes. The three panels correspond to $T' = 0.1 \text{ eV}$, $T' = 100 \text{ eV}$ and $T' = 10 \text{ keV}$. The gray regions correspond to inefficient pion production. Test points are indicated by A, B and C and by G1.

fields, both pions and muons are damped by synchrotron losses and the spectrum is dominated by neutrinos from neutron decay. The effect of lowering the temperature is that of moving the transition to muon-damped and neutron-beam regimes to lower magnetic fields. We refer to Ref. [35] for a complementary discussion of the observable effects of the energy-dependent flavor composition on the track-to-shower ratio at neutrino telescopes.

6.4 Conclusions

As the amount of data from neutrino telescopes progressively increases, the extraction of information from it requires a flexible modeling of the astrophysical production of neutrinos. The thermal model described here represents one possible answer to this necessity. By using an effective blackbody representation for the target photons within the source, the model is able to approximately reproduce the neutrino production even for sources which are highly non-thermal.

In the discussion proposed here, we apply the model to determine how astrophysical parameters influence the sensitivity of different neutrino experiments and the flavor composition of the produced neutrinos. However, these are just two examples of the possible applications of this model, which is ideally suited for systematic studies encompassing many different source classes at once. Examples of such systematic studies may include multiplet and stacking searches. A particularly promising application for the model is the search of Beyond Standard Model effects in astrophysical neutrino production (such as the works discussed in Part III of this dissertation).

Part III

Beyond Standard Model physics

Chapter 7

Decaying Dark Matter at neutrino and gamma-ray telescopes

The very high energies of cosmic neutrinos and gamma-rays allow to test particle physics at an unprecedented energy scale, as was discussed in the Preface. The next three chapters are devoted to examples of what we can infer from neutrinos and gamma-rays on BSM physics. In particular, in this chapter we shall be concerned with indirect detection of dark matter.

Dark Matter (DM) is literally matter composed of particles which do not interact electromagnetically, and for this reason are dubbed dark. The only granted interaction of DM is the gravitational one, since it is the one which hinted at DM existence in the first place. The first indications of DM were connected with the measurements of velocities of galaxies in galaxy clusters [310] and of rotation curves of galaxies [311] (see Ref. [312] for a more detailed history of DM). These measurements showed that the velocities of visible matter (of galaxies in galaxy clusters, and of stars and gas in galaxies) were larger than what one could have expected from the virial theorem and from gravitational dynamics given the mass of the objects. The natural conclusion was that the objects were more massive in their central region due to the presence of a dark component. This component should interact gravitationally with conventional matter to explain the large observed velocities of course. These local indications of a dark component were later complemented by cosmological hints, including the realization that DM is a fundamental component for structure formation.

Even though the DM paradigm is the generally accepted explanation for the above mentioned problems, there is as yet no direct observation of it via non-gravitational interactions. A promising method in this direction is to search for indirect signatures of DM, for example the products of DM decay or annihilation. There is no guarantee that DM decays or annihilates, but if it does it might produce Standard Model particles which could be detected by Earth experiments. For this reason, the dawning of multi-messenger astronomy has significantly improved the indirect search for DM, because the experiments described in Chap. 3 can in principle detect cosmic-rays, gamma-rays, and neutrinos produced in the decay or annihilation of DM particles. A very important role has been played both by gamma-ray experiments, such as Fermi-LAT, KASKADE [313], CASH [314], CASA-BLANCA [315], and by cosmic-ray experiments, such as PAMELA [316], AMS-02 [317, 318], TA [319], KASKADE-Grande [320], and the Pierre Auger Observatory (PAO) [321]. The neutrino counterpart of these experiments is constituted by neutrino telescopes and neutrino radio arrays. Among neutrino telescopes, IceCube has already observed neutrinos of astrophysical origin, as mentioned repeatedly in this work, and in fact this observation has already allowed to draw information on indirect searches of DM particles with masses larger than 100 TeV [322, 340].

On the other hand, neutrino radio telescopes probing the EeV energy range have not yet taken data: their observations will allow to test even larger masses for the DM particles.

In this chapter we will present two related works in which we have discussed indirect detection of DM decay. In the first work [335] we have focused on the energy range of the IceCube neutrinos. As was discussed in Sec. 3.2.1 the HESE data sample from IceCube indicates a softer spectrum than the throughgoing muons one. This softer spectrum could be explained by an excess of neutrinos around 100 TeV, which for some reasons is only seen within the HESE data sample. DM might be a possible explanation for this excess: since, as we will see, most of the neutrinos from DM decay come from the Galactic center, they should be visible within the HESE data sample. In this first work we have investigated whether neutrinos from DM decay can explain the HESE data without requiring too soft an astrophysical spectrum. Since DM decay might produce simultaneously neutrinos and gamma-rays, we have performed a multi-messenger analysis to check whether the gamma-rays from DM decay overshoot the present bounds from gamma-ray telescopes.

In the second work [341] we have focused on the ultra-high neutrino energy range, which will be the domain of neutrino radio telescopes. The measurements of these experiments will provide new information on whether decaying DM produces neutrinos, and in particular they will be able to constrain the parameter space of decaying DM. A quantitative estimate of the strength of these constraints was however lacking in the literature. In this second work we have performed such an estimate, using GRAND, IceCube-Gen2 Radio Array and the Radio Neutrino Observatory (RNO) as benchmark examples of future neutrino radio telescopes.

A third work on this subject [342], which we do not discuss here, deals with the constraints on heavy decaying DM obtained by gamma-ray observations. Compared to the previous literature, we systematically obtain the constraints on model of DM decaying into leptons, quarks, gauge bosons, and neutrinos. Beside its relevance as a way to constrain the model, these results provide a useful comparison with the projected constraints obtainable by neutrino radio-telescopes studied in Ref. [341], allowing to understand how much these future experiments will improve upon the current knowledge.

7.1 Neutrinos and gamma-rays from dark matter decay

Indirect DM searches look for the products of possible DM decay or annihilation. It is clear that any such search depends on some specific underlying model for DM, since in principle DM candidates could be stable against both decay and annihilation and therefore be invisible to indirect detection. Nevertheless, these searches have proved to be a powerful method of constraining DM models. In this section, we describe how neutrinos and gamma-rays, which are the focus of this thesis, could be produced in DM decay and annihilation. In particular, we will show by an order-of-magnitude argument that high-energy astrophysical particles are most effective in constraining the decay of very heavy DM candidates. Therefore, all the subsequent numerical work will be devoted to this specific choice of DM candidate.

A fundamental property of DM is that it should be stable against decay on cosmological timescales. In other words, its lifetime should be larger than the lifetime of the Universe. However, DM could still decay with larger lifetimes, and therefore a sizable fraction of the cosmological DM would be decaying at present times. If DM admits some coupling with the Standard Model particles, then such particles could be produced in the final state of this decay. Since the only stable particles that we know of in the Standard Model are protons, electrons, photons, and neutrinos (we neglect here gravitons), DM decay may give rise to a signal of cosmic-rays, gamma-rays, and neutrinos. In a similar way, if DM can annihilate, as is the case in many models in which DM is thermally

produced, then the products of its annihilation could be stable Standard Model particles amenable to detection.

In both cases we can distinguish two conceptually different sources of particles from DM decay and annihilation, namely a galactic and an extragalactic one. The galactic component, originating from the galactic distribution of DM, is generally expected to be dominant over the extragalactic one, which is instead originated from the cosmological DM distribution. Let us estimate the order of magnitude of the galactic contribution to the neutrino flux in the case of DM decay and annihilation (see also Ref. [324]). In the first case, we assume a single DM candidate decaying with a lifetime $\tau \gg H_0^{-1}$, where H_0 is the Hubble constant, and with mass m_{DM} . Therefore, if ρ_{DM} is the density of DM and $L \simeq 10$ kpc is a characteristic propagation length in the galaxy, the resulting neutrino flux must be of order

$$\phi_{\nu,\text{dec}} \sim \frac{n_\nu \rho_{\text{DM}} L}{\tau m_{\text{DM}}} \sim 10^{-16} \text{ cm}^{-2} \text{ s}^{-1} n_\nu \left(\frac{\rho_{\text{DM}}}{0.4 \text{ GeV}^{-1} \text{ cm}^{-3}} \right) \left(\frac{10^9 \text{ GeV}}{m_{\text{DM}}} \right) \left(\frac{10^{29} \text{ s}}{\tau} \right), \quad (7.1)$$

where n_ν is the average number of neutrinos emitted per DM decay. For comparison, the average flux measured by IceCube at 100 TeV is about $\phi_{\text{IC}} \sim 10^{-13} \text{ cm}^{-2} \text{ s}^{-1} \text{ sr}^{-1}$. Assuming conservatively that the portion of solid angle subtended by the Galactic Center is between 0.1 sr and 1 sr, we see that the two fluxes are comparable if

$$n_\nu \left(\frac{10^7 \text{ GeV}}{m_{\text{DM}}} \right) \left(\frac{10^{28} \text{ s}}{\tau} \right) \gtrsim 1. \quad (7.2)$$

On the other hand, at very high energies, in the range of the neutrino radio telescopes, the sensitivities of future experiments such as GRAND and IceCube-Gen2 Radio Array are expected to be of the order of $\phi_{\text{RA}} \sim 10^{-18} \text{ cm}^{-2} \text{ s}^{-1} \text{ sr}^{-1}$. Assuming again a fraction of solid angle between 0.1 sr and 1 sr, we see that the flux is detectable if

$$n_\nu \left(\frac{10^{10} \text{ GeV}}{m_{\text{DM}}} \right) \left(\frac{10^{30} \text{ s}}{\tau} \right) \gtrsim 1. \quad (7.3)$$

Thus we see that IceCube is apt to testing decaying DM in the hundreds of TeV to PeV region, whereas the future neutrino radio-telescopes will probe the region with masses larger than 10^{10} GeV [1].

Let us now adapt the same reasoning to the case of annihilating DM. The process is here parameterized not by the lifetime τ , but by the cross-section for collision σ_{DM} . In terms of this quantity, the neutrino flux from DM annihilation is

$$\phi_{\nu,\text{ann}} \sim \frac{n_\nu \rho_{\text{DM}}^2 \sigma_{\text{DM}} v_{\text{DM}} L}{m_{\text{DM}}^2}, \quad (7.4)$$

where $v_{\text{DM}} \simeq 10^{-3}$ in natural units is the average velocity of DM in the Galactic Center. The cross-section cannot take arbitrarily large value, and is bounded by the unitarity limit [343] $\sigma < 4\pi/m_{\text{DM}}^2 v_{\text{DM}}^2$, as can be obtained by partial wave expansion. Substituting this value we find

$$\phi_{\nu,\text{ann}} \lesssim 10^{-27} \text{ cm}^{-2} \text{ s}^{-1} \left(\frac{\rho_{\text{DM}}}{0.4 \text{ GeV}/\text{cm}^3} \right)^2 \left(\frac{10^9 \text{ GeV}}{m_{\text{DM}}} \right)^4 \left(\frac{10^{-3}}{v_{\text{DM}}} \right). \quad (7.5)$$

¹There is of course also a reason of energy shape for this difference. Neutrino radio-telescopes are more sensitive to higher energy neutrinos produced in the decay of heavier DM.

By comparison we see that for masses around 10 PeV this flux is barely detectable above the IceCube flux, whereas at masses larger than 10^9 GeV it is orders of magnitude below the sensitivity of the neutrino radio telescopes. For this reason, in the following we will be mainly concerned with the case of decaying DM: for studies of annihilating DM in the energy range of IceCube we refer to the literature [322, 334, 336, 338, 339, 344].

In the remaining part of this section, we discuss how we can determine the fluxes of particles from DM decay. It is clear that this can be done only in the context of specific models of decay, otherwise the factor n_ν in the equations above, determining how many neutrinos are produced in the decay, cannot be fixed. To remain as general as possible, in these works we examine a class of models in which DM decays into pairs of Standard Model particles. Therefore, if χ is the DM particle, we examine the decay $\chi \rightarrow p\bar{p}$, where p is any particle of the Standard Model. Thus a DM model is completely specified by three choices: the decay channel, namely the particle-antiparticle pair in which DM decays primarily; the DM mass m_{DM} ; the DM lifetime τ . The computation of the fluxes of particles from DM decay then reduces to two separate steps: the determination of the spectrum in the decay of a single DM particle, and the determination of the diffuse flux from the galactic and extragalactic distribution of DM. In the last step one has to account for the propagation effects of cosmic-rays, photons and neutrinos. We divide the discussion according to these two subjects.

7.1.1 Particle spectrum from dark matter decay

Even though the coupling between DM and the Standard Model is very simple, the final state of the decay may be very complicated. The reason is that the particles $p\bar{p}$ coupling to DM may behave as intermediate states for the production of other particles through their Standard Model couplings. In particular, if the particles $p\bar{p}$ are charged, they can produce low-energy photons; if they are quarks or hadronic particles, they will give rise to hadronization, with the consequent quark-gluon cascade ending in the production of hadrons. Furthermore, at the large masses ($m_{\text{DM}} \geq 1$ TeV) in which we are interested, the particles $p\bar{p}$ are also sufficiently energetic to emit W and Z bosons. For this reason, even decay channels such as $\chi \rightarrow \nu\bar{\nu}$ are affected by this showering process, leading to a multi-particle final state.

The difficulty in the description of this showering is the coexistence of processes of very different nature. The hadronization is a process that is best described by explicit simulation of the decay. This task is suited for simulation codes such as PYTHIA [24]. On the other hand, the electroweak showering is only partially dealt with PYTHIA (see below), and presents considerable difficulties, which we will now briefly describe qualitatively with no pretense of completeness (see, e.g., Refs. [345, 346]).

If the energy scale of the particles in DM decay is slightly above the mass M_W of the W boson, these particles can emit low-energy W bosons. This process is analogous to the emission of soft photons in QED and soft partons in QCD, with some differences. A first important difference is that the mass of the W boson introduces a physical infrared cutoff below which soft emission is inhibited, whereas soft gluons and photons are massless, and a fictitious mass is only introduced as an infrared cutoff. Explicit computations show that the probability of emission of a particle via electroweak interactions contains both logarithmic terms $\alpha \log(q^2/M_W^2)$ and double-logarithmic terms $\alpha \log^2(q^2/M_W^2)$, where α is the coupling constant and q is the energy scale. The presence of the double-logarithmic terms stands in contrast to the analogous parton showering in QCD or soft photon radiation in QED. In both theories, the double logarithms precisely cancel between the real and virtual corrections in all inclusive observables which are symmetric under the gauge group. For example, in QCD the double logarithms disappear once we average the final state over the color. However, in electroweak theory this averaging procedure cannot be done, because the

isospin of the final state is observable. Due to the double logarithms, at sufficiently large energies the corrections due to electroweak emission will become non-perturbative. In a similar fashion to the parton showering in QCD, the validity of perturbation theory can be restored by using the DGLAP evolution equations, which are able to resum the dominant logarithmic and double-logarithmic terms. The electroweak splitting processes are partially implemented in PYTHIA, which however does not include the triple boson coupling WWZ and $WW\gamma$, which can be rather important at high energies. Another approach available in the literature is the collection of spectra from DM decay obtained from the code PPPC [55], where leading order electroweak corrections are accounted for. This code adopts the approach of Ref. [345], which does not resum the leading logarithms and only solves the DGLAP equations to first order in $\alpha \log^2(q^2/M_W^2)$. Therefore, one expects it to be valid for $\alpha \log^2(q^2/M_W^2)/2\pi \ll 1$. Assuming that $q \sim m_{\text{DM}}$, this approach should give reliable results for $m_{\text{DM}} \ll 100$ TeV. For our first work [335], we used the code PPPC to generate the particle spectra from DM decay. Since we were interested in masses larger than 100 TeV, we extrapolated the results of the code by assuming scaling invariance: in other words, if $\frac{dN_i}{dE}(E, m_{\text{DM}})$ is the number of i -th particles per unit energy from the decay of a single DM particle of mass m_{DM} , we assumed that above 100 TeV

$$\frac{dN_i}{dE}(E, m_{\text{DM}}) = f\left(\frac{E}{m_{\text{DM}}}\right), \quad (7.6)$$

where $f(x)$ is a function determined by matching the results below 100 TeV. The validity of a scaling assumption at these energies is not rigorously true. Indeed, dimensional analysis arguments are broken by the presence of a physical fixed scale, namely M_W . Nevertheless, we showed that the results from PPPC extrapolated in this way were consistent, even for $m_{\text{DM}} \sim 10$ PeV (the highest masses we were interested in for this work), with the corresponding results obtained with PYTHIA.

More recently, a new solution to the problem of electroweak showering has been proposed in Ref. [346]. Here, the full DGLAP equations are solved down to the electroweak energy scale, and the results are then matched with the results of PYTHIA for lower energy scales, where electroweak showering is unimportant. The results for the particle spectra from DM decay are collected in the code `HDMSpectra`. In the second work discussed here [341], we used this code to determine the spectra of particles from DM decay.

In both approaches, using PPPC and `HDMSpectra`, the output from the numerical codes are the functions $\frac{dN_i}{dE}(E, m_{\text{DM}})$ defined above. In the next subsections we will describe how these functions can be used as input for the determination of the diffuse galactic and extragalactic fluxes of neutrinos and gamma-rays.

7.1.2 Neutrino fluxes

Two components need separately be taken into account in DM decay, the extragalactic and galactic one. The decay of DM on extragalactic scale leads to a diffuse flux per unit energy and solid angle

$$\frac{d\Phi_{\nu\alpha, \text{EG}}}{dE d\Omega} = \sum_{\beta} P_{\alpha \rightarrow \beta} \frac{\Omega_{\text{DM}} \rho_{\text{cr}}}{4\pi m_{\text{DM}} \tau} \int_0^{+\infty} \frac{dz}{H(z)} \frac{dN_{\nu\beta}[E(1+z)]}{dE}. \quad (7.7)$$

Here $H(z) = H_0 \sqrt{\Omega_{\Lambda} + \Omega_m(1+z)^3}$, Ω_{DM} , Ω_{Λ} and Ω_m are the fractions of the critical density of the Universe composed respectively of DM, dark energy and matter, ρ_{cr} is the critical density of the Universe. Furthermore, α runs over the neutrino flavor (we sum the fluxes for neutrinos and antineutrinos), and $P_{\alpha \rightarrow \beta}$ are the averaged oscillation probabilities defined in Eq. [2.17]

Differently from the extragalactic component, the galactic component of decaying DM has an anisotropic distribution. The reason is of course that the galactic distribution of DM is mainly

concentrated around the galactic center. For this reason, the galactic flux should be expressed in terms of the angular direction, parametrized by the galactic coordinates b and l . In terms of these the galactic flux can be written as

$$\frac{d\Phi_{\nu_{\alpha},G}}{dEd\Omega} = \sum_{\beta} P_{\alpha\rightarrow\beta} \frac{1}{4\pi m_{\text{DM}}\tau} \frac{dN_{\nu_{\beta}}(E)}{dE} \int_0^{+\infty} \rho_{\text{DM}}[r(s,l,b)], \quad (7.8)$$

where $r(s,l,b) = \sqrt{s^2 + R_{\odot}^2 - 2sR_{\odot} \cos \ell \cos b}$ and $R_{\odot} = 8.5$ kpc. $\rho_{\text{DM}}(r)$ is the DM density in the galaxy, which we assume to be given by the Navarro-Frank-White (NFW) profile [347]

$$\rho_{\text{DM}}(r) = \frac{\rho_s}{r/r_s(1+r/r_s)^2}, \quad (7.9)$$

with $r_s = 24$ kpc and $\rho_s = 0.18$ GeV cm⁻³ for the Milky Way [55].

7.1.3 Gamma-ray fluxes

The production of gamma-rays from decaying DM is more complicated than neutrinos. This subject has already been studied in various works (see, e.g., [328, 330] and, at lower energies, [348]). The main difficulty for gamma-rays, compared to neutrinos, is that there is a secondary production of gamma-rays via leptonic processes from the electrons produced in the DM decay. Accordingly, we separate the discussion for primary or prompt gamma-rays, directly produced in the DM decay, and secondary gamma-rays, produced by leptonic processes.

Prompt gamma-rays

The prompt production is very similar to the neutrino one, separating again in an extragalactic and a galactic component. The extragalactic flux is

$$\frac{d\Phi_{\gamma,EG}}{dEd\Omega} = \frac{\Omega_{\text{DM}}\rho_{\text{cr}}}{4\pi m_{\text{DM}}\tau} \int_0^{+\infty} \frac{dz}{H(z)} \frac{dN_{\gamma}[E(1+z)]}{dE} e^{-\tau(E,z)}, \quad (7.10)$$

where $\tau(E,z)$ is the optical depth for attenuation from EBL. For the work presented in Ref. [335] we used the attenuation coefficient presented in Ref. [55]. The galactic flux is

$$\frac{d\Phi_{\gamma,G}}{dEd\Omega} = \frac{1}{4\pi m_{\text{DM}}\tau} \frac{dN_{\gamma}(E)}{dE} \int_0^{+\infty} \rho_{\text{DM}}[r(s,l,b)]. \quad (7.11)$$

We do not account for a possible attenuation of the galactic gamma-ray flux from collisions with CMB or starlight and infrared light in the galaxy. This effect is studied in detail in Ref. [328], where it is shown that at galactic distances the effects of CMB attenuation are significant at energies above 1 PeV. In this region, the attenuation factor can be as much as 50% from the galactic center, where most of the gamma-rays come from.

Secondary gamma-rays

Secondary gamma-rays are produced by the radiation of electrons from DM decay. As we have seen in Chap. 2, the most important radiative processes are: bremsstrahlung, which in this case would originate from scattering off nuclei of the interstellar and intergalactic medium; synchrotron radiation, in the intergalactic and galactic magnetic fields; IC from collision with the CMB and

the EBL in the extragalactic space, and with CMB, starlight and infrared radiation in the galactic space. For our purposes the last process is the most important one. In fact, the typical energies of synchrotron photons are much lower than the energies of the prompt photons, and the energy emitted in bremsstrahlung is typically subdominant compared to the IC production (see, e.g., [348]). For this reason, here we focus on the Inverse Compton production only. We begin our discussion with the extragalactic component.

In order to determine the IC flux from electrons injected by DM decay, we need the distribution of such electrons. Since we are interested in the steady diffuse flux, we can treat the problem as the stationary injection of electrons from a uniform and isotropic DM distribution. Under these conditions, we know from our discussion in Chap. 2 that the electron number per unit energy and volume $n_e(\mathbf{x}, E)$, depending also on the spatial position \mathbf{x} , obeys the transport equation²

$$\nabla \cdot (D(\mathbf{x}, E) \nabla n_e(\mathbf{x}, E)) - \frac{\partial}{\partial E} (b(E) n_e(\mathbf{x}, E)) = q_e(E), \quad (7.12)$$

where $D(\mathbf{x}, E)$ is the diffusion coefficient in the intergalactic space, $b(E) = \langle dE/dt \rangle$ is the average energy loss per unit time, and $q_e(E)$ is the injection spectrum of electron from DM decay per unit time. The first term describes the spatial diffusion of electrons, while the second one describes the diffusion in energy space. At very large energies, the first term can be neglected. The reason is that energy losses increase with energy as E^2 , as we will see below, while the diffusion coefficient $D(E)$ increases with the energy as E^δ , with δ between 0.3 and 0.6. Therefore, at the high energies we are interested in, the characteristic length for energy losses are much smaller than the ones for spatial diffusion. In other words, before an electron can diffuse in space in a significant way, it loses all of its energy by radiative losses described by the term $b(E)$. For this reason, we will neglect the first term in the following discussion. The same conclusion is also reached in Ref. [328], where it is also supported by a numerical solution of the full equation with spatial diffusion.

In the intergalactic space the main cause of energy loss is IC emission itself. The energy losses can be written as

$$b_{\text{IC}}(E) = 3\sigma_T \int_0^{+\infty} \epsilon d\epsilon \int_{\frac{1}{4\gamma^2}}^1 dq n_\gamma(\mathbf{x}, \epsilon) \frac{(4\gamma^2 - \Gamma_\epsilon)q - 1}{(q + \Gamma_\epsilon q)^3} \left[2q \ln q + q + 1 - 2q^2 + \frac{(\Gamma_\epsilon q)^2(1 - q)}{2(1 + \Gamma_\epsilon q)} \right]. \quad (7.13)$$

Here σ_T is the Thomson cross section, n_γ is the number of target photons per unit energy and volume, γ is the Lorentz factor of the electron, and $\Gamma_\epsilon = 4\gamma\epsilon/m_e$. As we mentioned above, the target photons in the extragalactic space are composed of the CMB and the EBL. For the work presented here we take into account only the CMB component. Since CMB photons have lower energies than the EBL ones, they are the most relevant ones for the high energy production. This choice considerably simplifies the problem, because n_γ does not depend on the position. Therefore, Eq. [7.12] admits the solution

$$n_e(E) = \int_E^{+\infty} dE' \frac{q_e(E')}{b(E)}. \quad (7.14)$$

²We assume that the characteristic distances for energy losses and spatial diffusion are much smaller than the Hubble length: if this were not true, we would have to write a redshift-dependent equation and the assumption of stationarity would be violated. This also allows us to neglect the energy loss term due to energy redshifting. In other words, we are assuming that the electrons injected by DM decay reach an equilibrium distribution locally compared to the Hubble length.

Having determined the equilibrium distribution of electrons injected from DM decay, we can determine the IC photons emitted by this distribution using the IC emissivity

$$P_{\text{IC}}(E_\gamma, E_e) = \frac{3\sigma_T E_\gamma}{4\gamma^2} \int_{1/4\gamma^2}^1 dq \left[1 - \frac{1}{4q\gamma^2(1-\epsilon)} \right] \frac{n_\gamma(E_\gamma^0)}{q} \left[2q \ln q + q + 1 - 2q^2 + \frac{\epsilon^2(1-q)}{2(1-\epsilon)} \right], \quad (7.15)$$

where $\epsilon = E_\gamma/E_e$, $E_\gamma^0 = m_e^2 E_\gamma [4qE_e(E_e - E_\gamma)]^{-1}$. Using Eq. [7.14](#) in terms of the emissivity the extragalactic gamma-ray spectrum is

$$\frac{d\Phi_{\text{IC,EG}}}{dE d\Omega} = \frac{\rho_{cr} \Omega_\chi}{2\pi E m_{\text{DM}} \tau} \int_0^{+\infty} \frac{dz}{H(z)(1+z)} e^{-\tau(E,z)} \int_{E(1+z)}^{m_{\text{DM}}/2} dE_e \frac{P_{\text{IC}}(E(1+z), E_e, z)}{b(E_e)} \int_{E_e}^{m_{\text{DM}}/2} \frac{dN_e}{dE'} dE'. \quad (7.16)$$

For the galactic component we adopt a similar formalism, since also in this case we have an injection of electrons from DM decay which reaches a stationary distribution after losing their energy³. The sources of energy loss are IC scattering off the CMB, which has the same expression as the extragalactic case, and synchrotron radiation, for which the energy loss takes the form

$$b_{\text{SYN}}(E) = \frac{4\sigma_T E^2 \mathbf{B}^2(\mathbf{x})}{3m_e^2} \frac{1}{2}. \quad (7.17)$$

For the galactic magnetic field we adopt the parameterization [55](#)

$$B(r, z) = B_0 \exp \left\{ -\frac{|r - R_\odot|}{r_B} - \frac{|z|}{z_B} \right\}, \quad (7.18)$$

with $B_0 = 4.78 \mu\text{G}$, $r_B = 10 \text{ kpc}$, $z_B = 2 \text{ kpc}$, and r and z being the radial and vertical distances from the Galactic center, respectively. We neglect the turbulent halo magnetic field; this assumption mainly influences the very energetic electrons, for which IC losses are smaller than the synchrotron ones. As shown in Ref. [328](#), these effects become relevant at photon energies of order 100 TeV.

The galactic IC flux is produced by scattering off CMB, starlight, and infrared light. However, we have numerically verified that the former gives the largest contribution, both because of the larger spatial density of CMB photons, and because of their lower energy compared with the starlight and infrared ones. Because of their lower energy, they are the most relevant at high energies.

7.2 Neutrinos from dark matter decay at IceCube

In this section we compare the neutrino flux from DM decay with the IceCube data. Our key question is whether the introduction of a DM component is able to relieve the tension between the spectral indexes of the HESE and the throughgoing muons data sample. We first of all describe the statistical methodology, and then show our results. Finally, for the best-fit models fitting the IceCube data, we determine the gamma-ray flux and compare it with the data from Fermi-LAT, KASCADE and CASA-MIA.

³In the case of galactic DM we are assuming that the energy losses occur on lengths much shorter than the galactic dimensions, otherwise we should account for the effects of escape from the Galaxy.

7.2.1 Methods

We assume a double-component origin of the IceCube neutrinos

$$\phi = \phi_{\text{Astro}} + \phi_{\chi}, \quad (7.19)$$

where ϕ_{χ} is the DM flux, while the astrophysical spectrum is parameterized as a power-law spectrum isotropic and equipartitioned in flavor

$$\frac{d\phi_{\text{Astro}}}{dE d\Omega} = \phi_0 \left(\frac{E}{100 \text{ TeV}} \right)^{-\gamma} \quad (7.20)$$

where γ is the spectral index and ϕ_0 is the normalization of the power law.

This flux produces a distribution of expected events in the detector. To obtain it rigorously, we would have to account for the stochastic relation between the true neutrino energy and the energy it deposits in the detector, as described in detail in Ref. [349]. A simpler procedure adopted here is to consider only the average energy deposited in the detector for a given neutrino energy (in other words, we approximate the distribution of the deposited energy given the true energy as a delta function centered around the average value). The average relation between the two energies is obtained from Ref. [350] for the three different cases of charged-current shower events, track events and neutral-current shower events.

Our procedure is the following. We divide the energy range according to the binning with which the IceCube HESE data have been presented in Ref. [283]. In each energy bin we determine the expected number of track, shower, and neutral current events respectively as

$$\begin{aligned} N_{T,i} &= \int d\Omega \int_{E_i}^{E_{i+1}} dE \frac{d\phi_{\mu}}{dE d\Omega} p_T^{\mu} A_{\text{eff}}(E, \Omega), \\ N_{S,i} &= \int d\Omega \int dE_{E_i}^{E_{i+1}} \sum_{\alpha=e,\tau} \frac{d\phi_{\alpha}}{dE d\Omega} p_S^{\alpha} A_{\text{eff}}(E, \Omega), \\ N_{NC,i} &= \int d\Omega \int dE_{E_i}^{E_{i+1}} \sum_{\alpha=e,\mu,\tau} \frac{d\phi_{\alpha}}{dE d\Omega} p_{NC}^{\alpha} A_{\text{eff}}(E, \Omega). \end{aligned} \quad (7.21)$$

Here $A_{\text{eff}}(E, \Omega)$ is the angular and energy dependent effective area provided by the IceCube Collaboration [293]. The weights assigned to each topology p_T^{α} , p_S^{α} , and p_{NC}^{α} are obtained by the procedure in Ref. [351], and are given by

$$\begin{aligned} p_S^{e,\tau} &= \frac{\sigma_{CC}^{e,\tau} M_{CC}^{e,\tau}}{\sigma_{NC}^{e,\tau} M_{NC} + \sigma_{CC}^{e,\tau} M_{CC}^{e,\tau}}, & p_T^{\mu} &= \frac{\sigma_{CC}^{\mu} M_{CC}^{\mu}}{\sigma_{NC}^{\mu} M_{NC} + \sigma_{CC}^{\mu} M_{CC}^{\mu}}, \\ p_{NC}^{e,\tau} &= 1 - p_S^{e,\tau}, & p_{NC}^{\mu} &= 1 - p_T^{\mu}, \end{aligned} \quad (7.22)$$

where σ_{CC} and σ_{NC} are the charged and neutral current cross section [352] and M_{NC} , $M_{CC}^{e,\mu,\tau}$ are the effective detector masses [293].

To compare our prediction with the data, we assume a Poisson likelihood for each bin at energies above 60 TeV. We denote the total number of events from astrophysical sources and DM by μ_i and the expected number of background atmospheric events by b_i : the latter is estimated by the IceCube Collaboration. Therefore the likelihood function is

$$\mathcal{L}(n_i | \mu_i, b_i) = \prod_i (\mu_i + b_i)^{n_i} \frac{e^{-(\mu_i + b_i)}}{n_i!}, \quad (7.23)$$

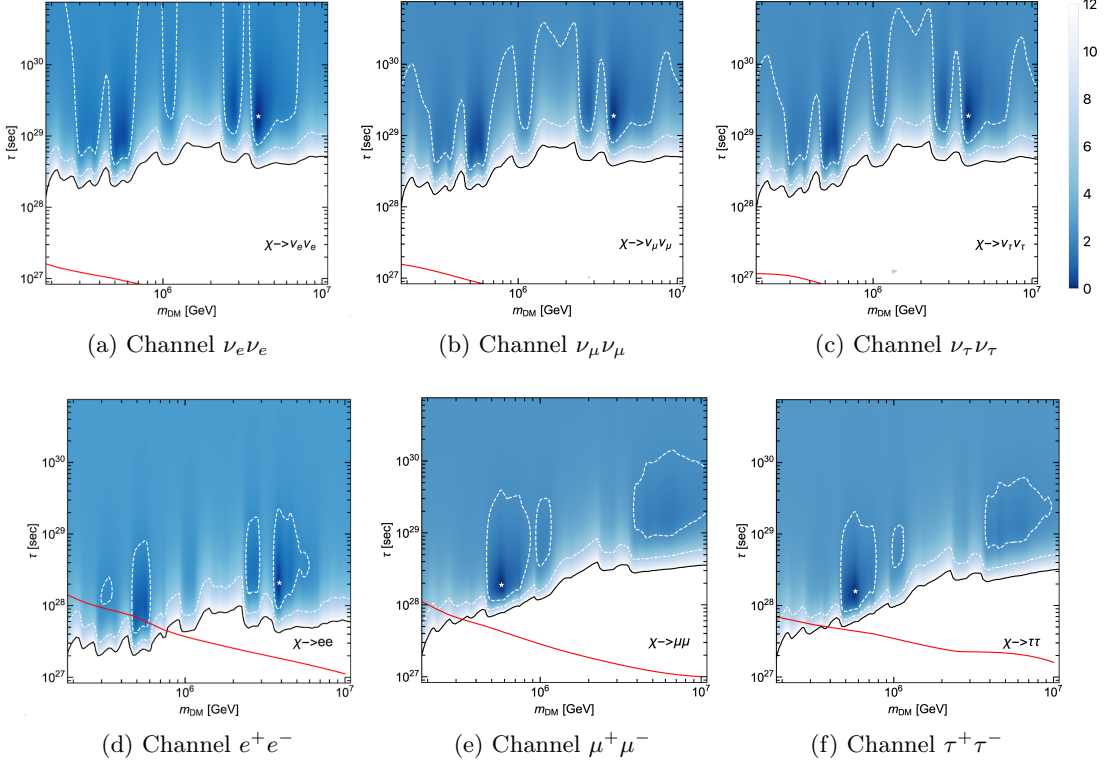


Figure 7.1: Likelihood contours for the leptonic channels in the $m_{\text{DM}}\text{-}\tau$ plane. The red line represents the exclusion region coming from the Fermi-LAT data (the excluded region is below the line). The dashed lines are the 68% confidence levels, the dot-dashed lines are the 95% confidence levels and the continuous lines are the 99.7% confidence levels. The best-fit solutions are identified by white stars.

which depends on the DM mass m_{DM} , the DM lifetime τ , the normalization ϕ_0 , and the spectral index γ of the astrophysical power-law flux. Here n_i are the observed number of events presented in Ref. [283].

To check the reliability of our method, we set the DM lifetime $\tau \rightarrow \infty$, corresponding the case of no neutrinos from DM decay, and obtain the best-fit values for the astrophysical parameters as $\phi_0 = (1.9 \pm 0.3) \times 10^{-15} \text{ TeV}^{-1} \text{ cm}^{-2} \text{ s}^{-1} \text{ sr}^{-1}$ and $\gamma = 3.02 \pm 0.13$. The uncertainties provided here are the 68% confidence levels. These values are indeed consistent with the best-fit values obtained in Ref. [283].

In our analysis, we apply the likelihood in Eq. [7.23] to define a test statistic

$$\Lambda = 2 \ln \frac{\mathcal{L}(\hat{\theta})}{\mathcal{L}(\theta_0)}, \quad (7.24)$$

where $\mathcal{L}(\hat{\theta})$ is the likelihood evaluated at the best-fit values of the parameters and $\mathcal{L}(\theta_0)$ is the likelihood evaluated at the best-fit values of the parameters restricted to the region with only astrophysical sources (namely when $\tau \rightarrow \infty$). According to the Wilks theorem [353], in the pure

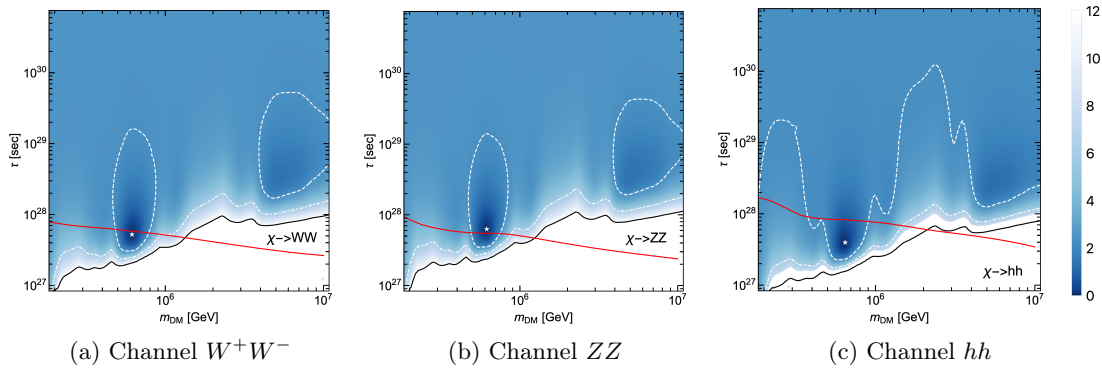


Figure 7.2: Likelihood contours for the bosons channels in the $m_{\text{DM}}\text{-}\tau$ plane. The description is the same as in figure [7.1](#).

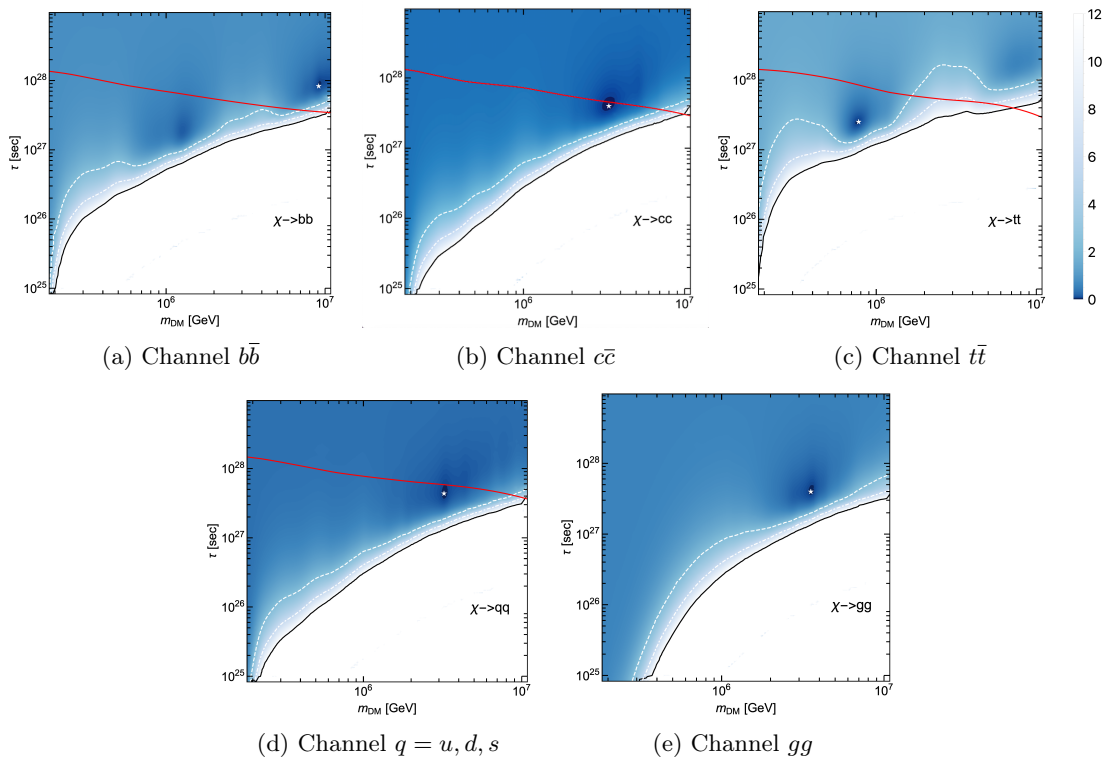


Figure 7.3: Likelihood contours for the quark and gluonic channels in the $m_{\text{DM}}\text{-}\tau$ plane. The description is the same as in figure [7.1](#).

astrophysical source case this test statistic would be distributed as a chi-squared variable with two degrees of freedom.

7.2.2 Results

In this section we report the results of our statistical analysis. In Figs. 7.1, 7.2 and 7.3, we show the contour plots of the test statistic for all the decay channels analyzed in this work, grouped by leptonic, gauge bosons and hadronic decay channels. We highlight the 68%, 95%, and 99.7% confidence levels for all plots. The contours are shown in the $m_{\text{DM}} - \tau$ plane only, and the parameters of the astrophysical flux are treated as nuisance parameters. The likelihood at each point of the plane has therefore been maximized with respect to them, where, in particular, γ is chosen in the range between 1.5 and 5. We also show with red lines the exclusion contours obtained using the Fermi-LAT data in Ref. 330.

The structure of the likelihood is non-trivial, and for most of the cases it exhibits more than one maximum. The choice of the dominant maximum, which we identify as the best-fit solution for each channel, might depend on the details of the analysis, such as the relation between the true and the deposited neutrino energy. We collect in Table 7.1 the parameters for the best-fit solutions for all channels.

Channel	$\phi_0^{\text{best}} (\times 10^{-15} \text{f.u.})$	γ^{best}	$\tau^{\text{best}} (\times 10^{28} \text{s})$	$m_{\text{DM}}^{\text{best}} (\text{TeV})$
$\nu_e \nu_e$	2.24	3.33	19.10	4017.35
$\nu_\mu \nu_\mu$	2.24	3.33	19.10	4017.35
$\nu_\tau \nu_\tau$	2.24	3.33	19.10	4017.35
$e^+ e^-$	2.14	3.86	2.09	3846.63
$\mu^+ \mu^-$	0.66	2.64	1.91	569.17
$\tau^+ \tau^-$	0.74	2.69	1.59	570.00
$W^+ W^-$	0.68	2.67	0.53	620.81
ZZ	0.72	2.69	0.63	621.00
hh	0.67	2.66	0.39	645.65
$b\bar{b}$	1.15	3.19	0.83	9168.11
$c\bar{c}$	0.78	2.78	0.40	3376.76
$t\bar{t}$	0.73	2.69	0.25	776.47
$q\bar{q}$	0.88	2.81	0.44	3233.26
gg	0.77	2.74	0.40	3526.63

Table 7.1: Summary of the neutrino analysis: the best fit parameters are given for each analyzed channel. The ϕ_0 is expressed in flux units of $\text{f.u.} \equiv \text{TeV}^{-1} \text{cm}^{-2} \text{s}^{-1} \text{sr}^{-1}$.

The reason for the presence of two likelihood maxima can be qualitatively understood as follows. In the absence of DM, the data are approximately fit by a single power law with spectral index around 3. When DM is added, its contribution can improve the fit in two different ways: either the DM neutrinos are produced at energies of the PeV, so that the astrophysical power law is soft in order to reproduce only the data at 100 TeV, or the DM neutrinos are produced at energies of 100 TeV, so that the astrophysical power law is hard and with a lower normalization in order to capture the data in the PeV region. This explains the presence of two nearly degenerate maxima for the likelihood. The first solution is hard to reconcile with the gamma-ray data and the throughgoing muons. Indeed, as we have discussed in Chap. 4, a soft power-law flux of neutrinos normalized to the 100 TeV IceCube data would be connected with a gamma-ray flux exceeding the Fermi-LAT EGB, unless its sources are opaque to gamma-rays. Furthermore, the throughgoing muons suggest a diffuse astrophysical neutrino flux with a hard neutrino spectrum. The second solution has the potentiality to relieve the tension between the HESE and the throughgoing muons: the astrophysical

power law would be harder, in agreement with the throughgoing muon data.

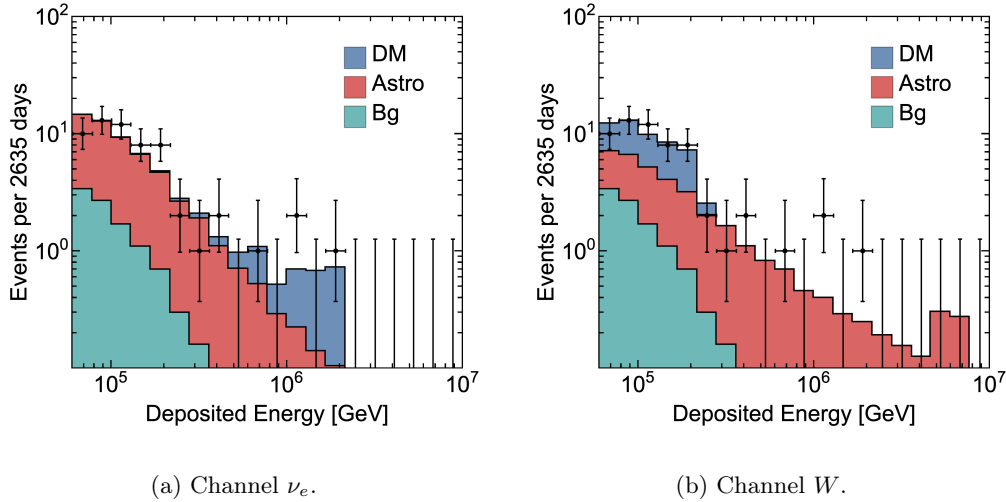


Figure 7.4: Numbers of neutrino events represented as a function of the neutrino energy for the two-component spectrum in the two decay channels of $\chi \rightarrow \nu_e \nu_e$ and $\chi \rightarrow \mu\mu$. The astrophysical and Dark Matter parameters are evaluated at their best-fit values reported in Table 7.1. The contribution to the number of events are shown in blue (neutrinos from DM decay), red (neutrinos from astrophysical sources), and green (atmospheric neutrinos).

The presence of these two solutions is most easily seen by representing the distribution of events from DM decay and from the astrophysical power law in each of the two scenarios. We do this in Fig. 7.4 for two representative channels: the decay into $\nu_e \nu_e$, for which the DM mass is at 4 PeV at its best-fit, and WW , for which the DM mass is at hundreds of TeV at its best-fit. In the first case the astrophysical power law dominates in the low-energy range, below 500 TeV, while DM neutrinos explain the spectrum at higher energies. In this case the astrophysical power law is rather soft, with a spectral index of 3.33. In the second case DM neutrinos clearly create an excess around 100 TeV, while the hard astrophysical power law, with a spectral index of 2.67, explains the high-energy data.

Furthermore, at least for the neutrinophilic and some of the leptophilic channels in Fig. 7.1, the best-fit solutions are indeed not excluded by the Fermi-LAT data. The reason is that for these decay channels the neutrino production can be larger than the gamma-ray one, explaining the excess at 100 TeV without overshooting the Fermi-LAT observations. Finally, we observe that for all cases the 2σ contours are open, meaning that the pure astrophysical spectrum cannot be rejected at more than the 2σ levels.

7.2.3 Gamma-ray fluxes: comparison with the experiments

The best-fit solutions we have found in this section can only be accepted if they do not overshoot the upper bounds on the diffuse gamma-ray flux imposed by the gamma-ray experiments. A rigorous discussion in this sense would require a full multi-messenger combined analysis of neutrino and gamma-ray data, which goes beyond the aim of this work. Here we limit ourselves to verifying for which channels the best-fit cases found above do not exceed the gamma-ray upper limits. We

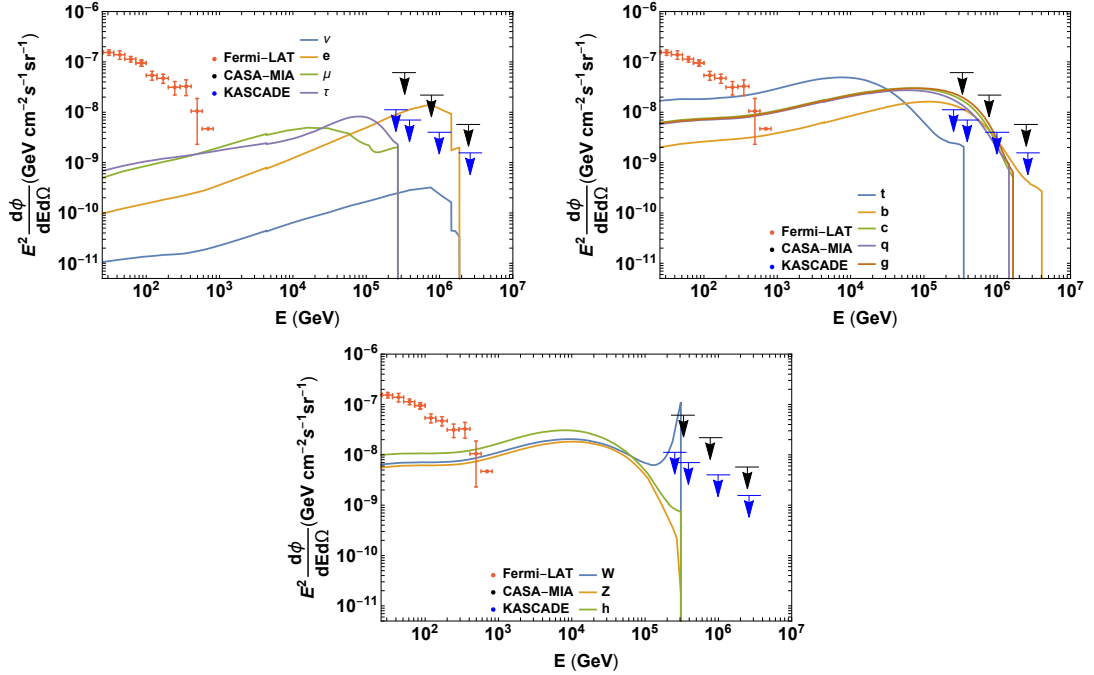


Figure 7.5: Expected diffuse photon spectra over the 4π solid angle for all best-fit channels. Data from Fermi-LAT, CASA-MIA and KASCADE are shown in red, black and blue points, respectively.

show in Fig. 7.5 the diffuse gamma-ray fluxes for each decay channel computed according to the procedure in Sec. 7.1 the DM parameters are fit to their best-fit values in Table 7.1. In the same figure we also show the data and upper limits on the diffuse gamma-ray flux collected by Fermi-LAT EGB, KASCADE [354], and CASA-MIA [355]. These figures show that in the leptophilic and neutrinophilic case the gamma-ray flux do not exceed the observation and are therefore allowed; for the same reason, in Fig. 7.1 the best-fit points are well above the constraints from Fermi-LAT. On the other hand, for hadronic channels and gauge boson channels, the gamma-ray flux exceed the Fermi-LAT data, and therefore are already excluded. This again is confirmed by Figs. 7.2 and 7.3, where the best-fit points are below or very close to the Fermi-LAT exclusion contours. Therefore, we reach the conclusion that a good fit to the IceCube data, which explains the neutrino excess at 100 TeV, is only allowed for the gamma-rays for leptophilic and neutrinophilic decay channels.

7.3 Neutrinos from dark matter decay at radio telescopes

The results discussed so far relate to DM with masses up to 10 PeV, since larger masses would produce neutrinos with energies too large to be observed by IceCube. The natural prosecution of indirect detection with neutrino observations at higher masses is the observation of neutrinos at the EeV energies with the future radio telescopes. In this section we present the analysis of Ref. [341], in which we determine the projected sensitivity of the radio telescopes to decaying DM. We focus on four benchmark neutrino radio telescopes, namely RNO-G, GRAND 10k, GRAND 200k, and IceCube-Gen2 radio array.

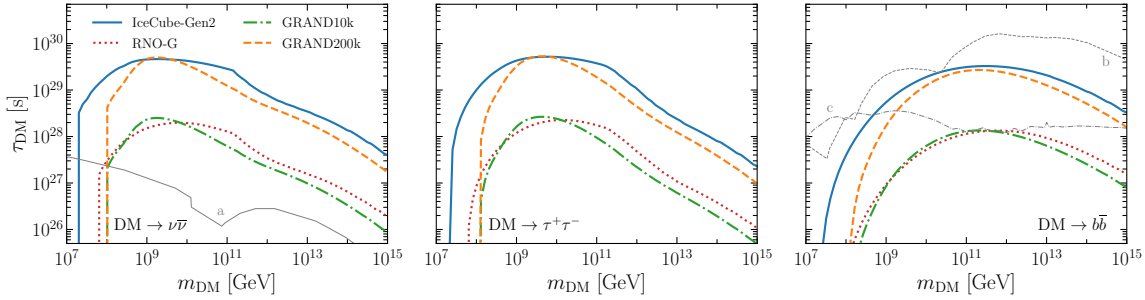


Figure 7.6: Potentiality for detection of a dark matter signal at the upcoming neutrino telescopes in 3 years of observation. The lines show the 95% CL region for dark matter detection under the assumption of negligible contamination from background and astrophysical sources. Each panel corresponds to a different decay channel of DM particles. The thin gray lines are the existing constraints in the literature: a) for the $\nu\bar{\nu}$ channel with neutrino data from IceCube, PAO and ANITA [323]; b) for the $b\bar{b}$ channel with galactic multimessenger data [337]; c) for the $b\bar{b}$ channel with extragalactic multimessenger data [337].

The first ingredient to estimate the sensitivity of radio telescopes is the determination of the neutrino flux from DM decay. We address this problem with the same methods described in Sec. 7.1. It is worth noticing that the angular profile of the neutrinos from galactic DM decay depends upon the assumed DM profile, which we choose to be a Navarro-Frank-White one. However, since here we use only the information on the total number of events, and not their angular distribution, as we will discuss below, a change in the DM angular distribution does not affect significantly the results.

With the neutrino fluxes available, we need only discuss how they are used to determine the sensitivity of the experiments. We describe first of all our method for obtaining the sensitivity for detection of neutrinos from DM decay. Subsequently, assuming that the experiments will detect no signature of DM decay, we discuss the projected constraints on the DM lifetime.

7.3.1 Dark matter detectability

Following the approach in the previous section, we discuss the sensitivity to neutrinos from DM decay into different possible decay channels $\chi \rightarrow p\bar{p}$. For this work we focus on three different decay channels, namely into b quarks, τ leptons, and directly into neutrinos. These different scenarios are representatives of hadronic, leptophilic and neutrinophilic DM decay, respectively. For the ν channel, we take equipartition among neutrino flavours at production.

The expected number of neutrino events at a given telescope, for an observation time T_{obs} , is

$$n_{\text{DM}}(m_{\text{DM}}, \tau) = T_{\text{obs}} \int dE_{\nu} \sum_{\alpha} \left(\frac{d\Phi_{\nu\alpha, \text{G}}}{dE_{\nu}} + \frac{d\Phi_{\nu\alpha, \text{EG}}}{dE_{\nu}} \right) A_{\text{eff}}(E_{\nu}). \quad (7.25)$$

Here $\frac{d\Phi_{\nu\alpha, \text{EG}}}{dE_{\nu}}$ and $\frac{d\Phi_{\nu\alpha, \text{G}}}{dE_{\nu}}$ are the extragalactic and galactic flux, as given by Eqs. 7.7 and 7.8, integrated over the solid angle; $A_{\text{eff}}(E_{\nu})$ is the effective area of the relevant experiment. From Eq. 7.25 we see that for this analysis only the total number of events over the entire solid angle is used to probe detection of DM. This is a very conservative method of analysis, since we do not account for the unique spectral and angular features of the DM distribution. On the other hand, it also gives robustness to the obtained results, which do not depend on the choice of the spatial profile

of galactic DM. We also observe that all flavors are summed in Eq. 7.25. The reason is that all the radio telescopes under construction studied in this work do not provide an effective area separated per flavor, but only an average one. Our procedure for obtaining the number of events is therefore rigorously correct for equipartitioned flavor compositions, for which the effective areas have been determined by the collaborations. The effective areas are reported in the relative papers from the collaborations: if these were not explicitly reported, we have obtained an estimate for the area from the flux sensitivity [94, 95, 97].

The sensitivity for detection of neutrinos from DM decay can now be determined using the Feldman-Cousins approach [309], according to which a detection at 95% confidence level requires at least 3.09 expected neutrino events, if DM is the only source of neutrinos (i.e., neglecting the contribution of neutrinos from astrophysical sources; this will be discussed in more detail below). By equating the number of expected events to 3.09 we are therefore able to obtain the threshold lifetime below which DM can be probed.

We show the resulting sensitivity reach in the $m_{\text{DM}} - \tau$ plane in Fig. 7.6. The observation time is fixed to $T_{\text{obs}} = 3$ yr; we show the results for the radio telescopes RNO-G (dotted red lines), IceCube-Gen2 (solid blue lines), GRAND10k (dot-dashed green lines), and GRAND200k (dashed orange lines). The regions below the lines correspond to the parameter space that can be probed at 95% confidence level under the assumption of negligible contribution from other sources. The three panels correspond to the different decay channels considered. If present, the gray lines display the existing constraints deduced by present neutrino telescopes as well as by gamma-ray and cosmic-ray observations. In particular, for the neutrino channel ($\chi \rightarrow \nu\bar{\nu}$), limits on the DM lifetime have been obtained from the data taken by IceCube, PAO, and ANITA experiments [323] (solid gray line in the leftmost plot). A more recent study based on updated neutrino and gamma-ray data is provided by ref. [332]. However, we note that their γ , e^\pm and ν spectra from DM decay do not agree with the ones used in the present analysis, since they are much harder at lower energies with respect to the ones computed with the `HDMSpectra` package [346], and consequently lead to stronger limits on DM lifetime. Therefore, we cannot consistently compare their results with ours, and for this reason we avoid showing their constraints in the plots. For the decay channel into bottom quarks (rightmost plot), the dashed (b) and dot-dashed (c) lines correspond to the constraints placed by a recent analysis of existing galactic and extragalactic multimessenger data, respectively [337]. For the tau channel we have not found similar multimessenger constraints in the literature. Indeed, this was the main motivation for our subsequent work [342], in which we have obtained the constraints from gamma-ray experiments for hadronic, leptonic, and neutrinophilic decay channels.

Therefore, our conclusion is that upcoming neutrino radio telescopes will probe a parameter space which is still unexplored for decaying DM for leptophilic and neutrinophilic scenarios. Hadronic channels are already strongly constrained by gamma-ray observations. Nevertheless, we emphasize that many of these constraints, originating from galactic searches, suffer from large systematic uncertainties related to the dark matter halo in the inner regions of the Milky Way [356, 357]. Therefore, even for these hadronic channels, neutrino radio telescopes will constitute an independent and robust source of information which does not suffer from such uncertainties (since we have not used the information on the angular distribution of DM neutrinos).

7.3.2 Dark matter constraints

In this section we shift our viewpoint on DM and, rather than predicting the sensitivity for detection, we examine the complementary potentiality of constraining the models with decaying DM. Whereas in the previous section we assumed detection of DM neutrinos only, in this section we take the more realistic case that neutrinos also come from astrophysical sources. We consider two different

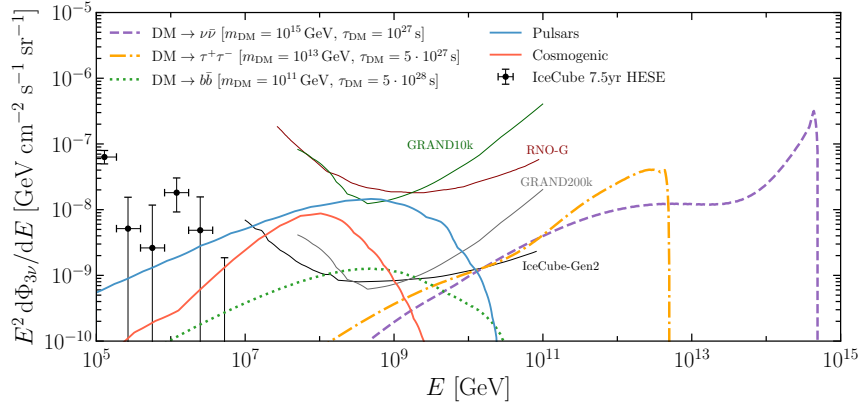


Figure 7.7: All-flavour neutrino fluxes predicted in two astrophysical scenarios (red line for cosmogenic neutrinos and blue line for newborn pulsar neutrinos) and in three different benchmark cases of decaying dark matter. The thin lines show the 3-year sensitivity reach of upcoming neutrino radio telescopes, while the data points correspond to the 7.5 year IceCube HESE sample [358].

scenarios:

- **Cosmogenic neutrinos.** These are a guaranteed contribution to the UHE neutrino flux, as discussed in Chap. 4. However, the normalization and shape of the flux are very uncertain, because of the uncertainties on the composition of the UHECRs. For this work we conservatively use the largest estimate shown in Ref. [97] for the cosmogenic flux. As will be more clear later, a larger flux from astrophysical sources would result in weaker constraints on dark matter.
- **Newborn pulsar neutrinos.** UHE neutrinos can of course also be produced in high-energy astrophysical sources: these include active galactic nuclei [153, 359], gamma-ray bursts [33], flat-spectrum radio quasars [360], black-hole jets embedded in large-scale structures [361] and newborn pulsars [362]. Here we consider the neutrino fluxes produced in newborn pulsars reported in Ref. [97], which produce the largest predicted flux and, therefore, leads to the most conservative projected bounds on DM.

Fig. 7.7 shows the all-flavour neutrino fluxes in both these scenarios, together with three benchmark fluxes from DM decay that could potentially be detected according to the results of the previous section. As a matter of comparison, we also show the sensitivity of the four neutrino radio telescopes under study.

In order to determine the projected constraints on DM in each of these two scenarios, the scheme is as follows. We assume that neutrinos only come from either cosmogenic neutrinos or newborn pulsars, depending on the chosen scenario, and we produce a mock data sample in a given observation time at each of the studied radio telescopes under this assumption. For each mock data sample we determine the constraints on DM decay, under the only conservative requirement that the neutrinos predicted from DM decay do not exceed the observed events. Let us detail the procedure. In each scenario of astrophysical sources, the probability to observe N_{obs} events, assuming that N_{astro} events are expected, is

$$p(N_{\text{obs}}|N_{\text{astro}}) = \frac{(N_{\text{astro}})^{N_{\text{obs}}} e^{-N_{\text{astro}}}}{N_{\text{obs}}!}. \quad (7.26)$$

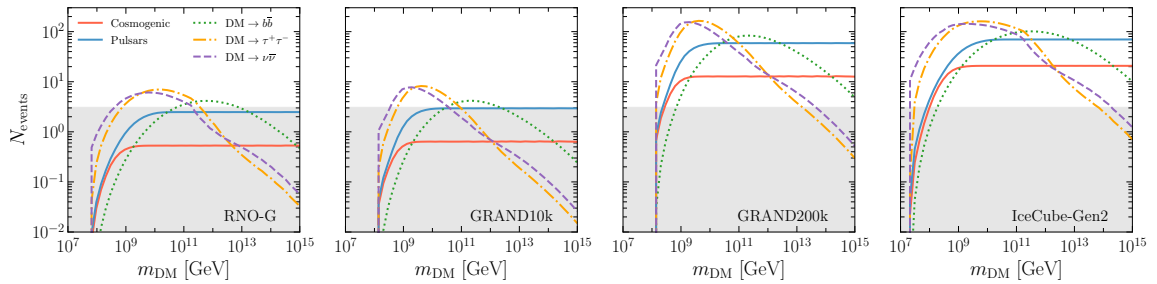


Figure 7.8: Expected number of neutrino events with an energy smaller than $E_{\max} = m_{\text{DM}}/2$ in each neutrino telescope after 3 years of data-taking. The solid lines correspond to the astrophysical signal events while the dashed, dotted and dot-dashed are the ones corresponding to the expected signals coming from the different decay channels with a lifetime $\tau_{\text{DM}} = 10^{28}$ s. The number of astrophysical events is obtained by using Eq. (7.27) and fixing $E_{\max} = m_{\text{DM}}/2$. The gray shaded area highlights the threshold of 3.09 events required for a detection at 95% CL.

In terms of the all-flavor astrophysical neutrino flux $\frac{d\Phi_{\nu}^{\text{astro}}}{dE_{\nu}}$, the expected number of events N_{astro} is

$$N_{\text{astro}}(E_{\max}) = T_{\text{obs}} \int_0^{E_{\max}} dE_{\nu} \frac{d\Phi_{\nu}^{\text{astro}}}{dE_{\nu}} A_{\text{eff}}(E_{\nu}). \quad (7.27)$$

The maximum energy fixes the energy range in which we perform the analysis. A simple choice to strengthen the constraints is $E_{\max} = m_{\text{DM}}/2$. Indeed, at energies larger than this value no neutrino from DM decay is expected. Therefore, restricting the analysis to this interval allows us to test all the DM signal and at the same time minimize the neutrinos from astrophysical sources. We show in Fig. 7.8 the number of expected neutrino events from cosmogenic neutrinos (solid red lines) and newborn pulsars (solid blue lines) below $E_{\max} = m_{\text{DM}}/2$ as a function of m_{DM} . The observation time is fixed to $T_{\text{obs}} = 3$ yr. The expected number of events from astrophysical sources increases with the DM mass, because of the larger energy range, until it saturates to a constant value. In agreement with our comments above, newborn pulsars give rise to an expected number of events larger than cosmogenic neutrinos. We also show the expected number of events from DM decay for all three channels. The lifetime is fixed to $\tau = 10^{28}$ s. The gray shaded area denotes the threshold of 3.09 events required for 95% confidence level detection. Thus, signals above the gray area can be detected by the telescopes.

For an observed number of events N_{obs} , we can determine the lower bound on admissible lifetimes for DM which does not exceed the observed signal at 95% confidence level. We follow the procedure in Ref. [363], accounting only for upper fluctuations. Therefore, we define the test statistic

$$\text{TS}(m_{\text{DM}}, \tau) = \begin{cases} 0 & \text{for } n_{\text{DM}} < N_{\text{obs}} \\ -2 \ln \left(\frac{\mathcal{L}(N_{\text{obs}} | n_{\text{DM}})}{\mathcal{L}(N_{\text{obs}} | N_{\text{obs}})} \right) & \text{for } n_{\text{DM}} \geq N_{\text{obs}} \end{cases} \quad (7.28)$$

where the likelihood \mathcal{L} is assumed to be a Poisson distribution. With this definition we are assuming perfect agreement between data and theory if $n_{\text{DM}} < N_{\text{obs}}$, and we are only testing the hypothesis that n_{DM} exceeds N_{obs} . The distribution of this test statistic under the assumption that the events had been generated by DM neutrinos only can be easily obtained. In fact, under this assumption, the observed number of events would be larger than n_{DM} with probability 0.5, in which case the test statistic would be identically 0, and it would be smaller than n_{DM} with probability 0.5, in

which case the test statistic would be a chi-squared variable. Therefore, the distribution of TS is a half-chi-squared distribution under the assumption of events generated by DM only⁴

Therefore, we can exclude the DM hypothesis at 95% confidence level when $\text{TS}(m_{\text{DM}}, \tau) = 2.71$. For a fixed value of the DM mass and for a fixed N_{obs} , we can determine the lower limit for the allowed DM lifetime $\bar{\tau}(m_{\text{DM}}|N_{\text{obs}})$ with this method. Our procedure for obtaining the allowed constraints is as follows. We randomly generate N_{obs} according to the Poisson probability $p(N_{\text{obs}}|N_{\text{astro}})$ for the two astrophysical scenarios considered. For each Monte Carlo generation we determine the lower bound $\bar{\tau}(m_{\text{DM}}|N_{\text{obs}})$. From the whole mock data sample we obtain the confidence intervals in which the lower limit is expected. Similarly to what we did to estimate the detection sensitivity, we do not include an energy and angular binning, which would be an additional source of information, allowing a better rejection of the neutrinos from astrophysical sources.

The results of this analysis are collected in Fig. 7.9 where we show the 2σ bands of the lower limit for the DM lifetime at 95% CL, for all the combinations of DM decay channel, experiment, and astrophysical scenario adopted to simulate data. The dashed and dot-dashed colored lines represent the expected lower limit according to the Poisson distribution in Eq. (7.26) under the assumption of observing cosmogenic and newborn pulsar neutrinos, respectively. We also show, with dark-blue solid lines, the constraints that could be potentially placed in the case of zero detected events ($N_{\text{astro}} = 0$). These are the most optimistic constraints that could be placed, and they do not represent an unrealistic situation. Even the cosmogenic neutrino fluxes, which are a guaranteed contribution to the UHE neutrino flux, have an uncertainty band so large that they could be well below the sensitivity of the future neutrino radio telescopes. As in Fig. 7.6, we show with thin gray lines the existing constraints for the channels for which they are available.

Due to the lower number of events, the cosmogenic signal case (red) leads to stronger constraints than the newborn pulsar case (blue). The difference can be rather marked for large neutrino telescopes such as GRAND200k and IceCube-Gen2, for which astrophysical sources could lead to a large number of events. The sharp cut-off at low DM masses, which is especially evident for the $\nu\bar{\nu}$ and $\tau^+\tau^-$ channels, is due to the low sensitivity of radio telescopes for $E_\nu \lesssim 10^8$ GeV. For this reason, at low DM masses, where the energy range (with energies smaller than $E_{\text{max}} = m_{\text{DM}}/2$) is smaller and the number of expected events from astrophysical sources is consistent with 0, statistical fluctuations are practically absent, so that the 2σ contours close into a single line corresponding to the case of zero observed events.

In all the analysis described above, we have made no mention of a possible background component. Indeed, neutrinos from astrophysical sources act as a kind of background (or, rather, as a neutrino floor in the sense of Ref. 364) to the neutrinos from decaying DM. A real background contamination is generally expected to be very low: for example, for GRAND200K the estimated background is 0.1 events per year 97. Including this background would increase the number of expected neutrino events and therefore weaken the lower limits in Fig. 7.9. With the estimates furnished by the collaborations for the background, the constraints on DM lifetime might weaken by $\sim 30\%$ for the cosmogenic case and $\sim 10\%$ for the newborn pulsars case. This weakening is well within the 2σ bands reported in Fig. 7.9, and furthermore it could be reduced by accounting for the expected background event rate in the method of analysis. Therefore, we expect our results to be robust against a small background component.

⁴This is actually not the hypothesis we want to reject: rather, we want to reject the hypothesis that the events were generated by DM and by astrophysical sources. However, testing the assumption that the events came from DM decay only leads to more conservative (i.e., weaker) constraints. Testing the hypothesis of DM plus astrophysical sources cannot be done without having a solid prediction for the neutrinos from astrophysical sources: as we have seen, this is not feasible at present.

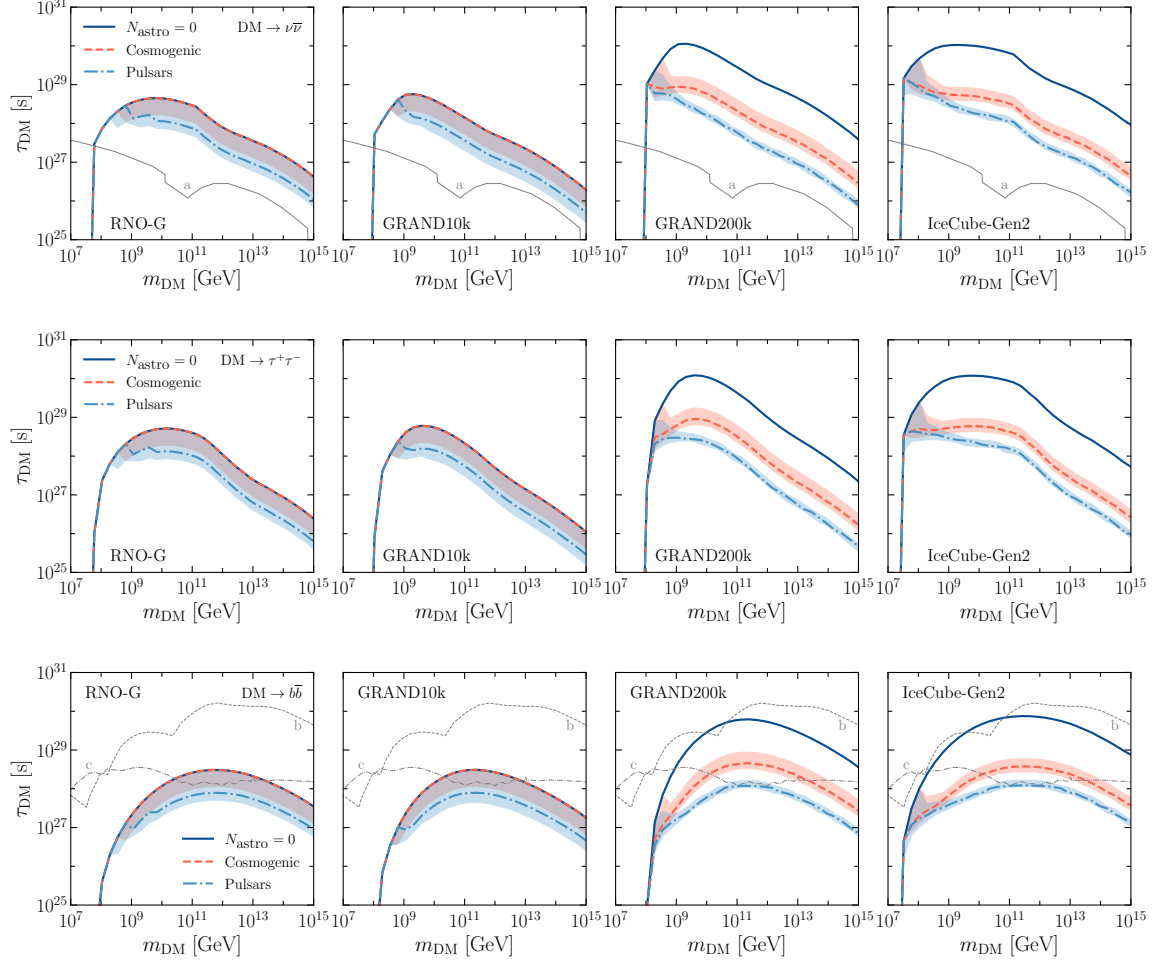


Figure 7.9: Projected 3-year constraints at 95% CL in the plane $m_{\text{DM}}-\tau$. Each row corresponds to a different DM decay channel, while each column to a different upcoming neutrino radio telescope. The bands represent the 2σ intervals according to the Poisson distribution in Eq. (7.26) of observing a given number of events in the cosmogenic (red color) and the newborn pulsars (blue color) scenario. The red dashed and blue dot-dashed lines show the most probable constraints on τ_{DM} assuming the observation of astrophysical neutrinos. The dark-blue solid lines display the limits obtained in the case of zero detected events ($N_{\text{astro}} = 0$). The thin gray lines are the existing constraints in the literature: a) for the $\nu\bar{\nu}$ channel with neutrino data from IceCube, PAO and ANITA [323]; b) for the $b\bar{b}$ channel with galactic multimessenger data [337]; c) for the $b\bar{b}$ channel with extragalactic multimessenger data [337].

7.4 Discussion

The aim of this chapter was to show that neutrino experiments, ranging from 100 TeV to more than 1 EeV, can bring considerable information on indirect searches of heavy decaying DM searches.

The energy range from 100 TeV to the PeV is already being scrutinized by IceCube. In the first work discussed here, we have shown that the HESE data set is sufficient to test the hypothesis that part of the neutrinos were produced from decay of DM with masses between 100 TeV and 10 PeV. Indeed, a DM component decaying into leptons or neutrinos could help relieve the tension between the 100 TeV neutrinos, the throughgoing muons, and the Fermi-LAT data. Hadronic channels fail in this respect because they overproduce gamma-rays which would exceed the Fermi-LAT observed gamma-rays. The improvements in the constraints from future gamma-ray experiments, such as LHAASO, may soon exclude also other decay channels for DM as a possible source of the 100 TeV IceCube neutrinos.

The energy range above 10 PeV will be probed by the future neutrino radio telescopes, including RNO-G, GRAND, and IceCube-Gen2 radio array. In the second work described in this chapter we have obtained the projected sensitivity for detection and constraint of decaying DM at each of these future experiments. Our results show that they will be able to probe decaying DM with masses from 10 PeV to 10^6 EeV. The potentiality of constraint will definitely improve the present constraints from gamma-ray and cosmic-ray data for neutrinophilic and leptophilic channels. For hadronic channels the sensitivity is comparable with the present bounds: however, the method we have used is very robust against the uncertainties on the DM galactic profile and the models of neutrinos from astrophysical sources. Therefore for all channels we expect the future radio telescopes to produce reliable upper bounds on the decay rate of heavy DM which are either comparable or stronger than the present gamma-ray and cosmic-ray experiments.

Chapter 8

Active-sterile secret interactions at neutrino telescopes

A natural sector of BSM physics that can be probed by astrophysical neutrino observations is the sector of non-standard neutrino physics. Since neutrinos are such elusive particles, there are many extensions of the Standard Model connected with neutrino physics. One common feature of these extensions is the presence of non-standard neutrinos which do not participate in the weak interaction, and which for this reason are named sterile neutrinos, as opposed to the standard ones which are generally named active neutrinos. The mass of the sterile neutrinos is not fixed *a priori*, and in fact different assumptions could be used to address different issues of the Standard Model. As an example, sterile neutrinos with masses around the grand unification scale $M_{\text{GUT}} \sim 10^{15}$ GeV could naturally explain the small masses of the active ones via the seesaw mechanism [56–58]. This mechanism could also be extended to account for the generation of the baryon asymmetry of the Universe within the so called leptogenesis [365]. On the other hand, sterile neutrinos with masses around the eV might explain the anomalies in the appearance probability of electron neutrinos measured by LSND [366] and MiniBoone [367]. These two extreme examples already show the huge range of values that the sterile neutrino masses can take within different models.

Another extension of the Standard Model involving the neutrino sector is the presence of non-standard interactions involving neutrinos. Among these, interactions involving neutrinos alone are particularly hard to test, given the rarity of environments with large neutrino densities: for this reason they are often named secret interactions [368–384]. Typically these interactions involve a massive particle mediating the interaction and allowing resonant scattering between neutrinos (even though effective models with a four-point interaction are also studied). Secret interactions could lead to observational signatures in extreme environments of dense neutrinos, such as the cosmological plasma and the core of supernovae. A more direct test of secret interactions is however hard to obtain using Earth-bound instruments, due to the lack of neutrino beams.

The observation of astrophysical neutrinos made by IceCube offers new possibilities for testing these extensions of the Standard Model. The presence of sterile neutrinos mixing with active ones may lead to a change in the flavor composition of astrophysical neutrinos, due to the non-standard oscillations with the new species [385–392]. Secret interactions among active neutrinos have also been shown to induce signatures on the energy shape and flavor composition of the astrophysical neutrino flux [255, 393–400].

The sector of secret interactions between active and sterile neutrinos is on the other hand much less studied. Since this involves a coupling between standard neutrinos and a non-standard species,

it is even harder to constrain. A model with this active-sterile interaction was originally studied in Ref. [401] as a way to relax the constraints from Big Bang Nucleosynthesis on light sterile neutrinos. The effect of active-sterile interactions on the astrophysical neutrino fluxes was first pointed out in Ref. [402]. A systematic study of this model, in view of the constraints that can be drawn from cosmology and particle physics, is however lacking. For example, in Ref. [402] the constraints from laboratory experiments could not be taken into account because they had never been studied.

In our works [403,404] we systematically study a model with active-sterile secret interactions. Our analysis involves a classification of the constraints coming from laboratory experiments, cosmology and astrophysical environments, in particular supernovae. Furthermore, we show the existence of signatures both on the energy shape and the flavor composition of astrophysical neutrino fluxes. The origin of these signatures is the collision, via secret interaction, of the astrophysical neutrinos with the low-energy neutrinos from the Cosmic Neutrino Background (CNB). The latter is the cosmological background of relic neutrinos left over from the primordial plasma, and is analogous to the Cosmic Microwave Background. The collision with the CNB causes a dip in the energy fluxes, and the energy at which the dip appears depends on the mass of the interaction mediator. We show that this effect can be relevant both in the energy range of IceCube and at higher energies, within the reach of future neutrino radio telescopes such as GRAND, ARA, ARIANNA and IceCube-Gen 2 Radio Array. Indeed, to our knowledge Ref. [403] suggests for the first time that neutrino radio telescopes can shed considerable light on the subject of secret interaction. Furthermore, depending on the relative coupling of different flavors, the interaction can induce additional energy-dependent changes in the flavor composition.

In this chapter we will review the results that we have obtained. In particular, in Sec. [8.1] we define the phenomenological model we use in this work. In Sec. [8.2] we obtain the constraints on this model from laboratory experiment, cosmology and astrophysics. In Sec. [8.3] we discuss the astrophysical production both with and without the presence of secret interactions, describing the methods we adopt to treat the non-standard propagation of neutrinos. Finally, in Sec. [8.4] we present our results and discuss them.

8.1 The model

We study a model which contains a sterile neutrino ν_s and a mediator φ in addition to the standard particles. For definiteness, we assume that both the sterile neutrino and the active neutrinos of the Standard Model are Majorana particles. The secret interaction comes from a term in the Lagrangian

$$\mathcal{L}_{\text{SI}} = i \sum_{\ell} \lambda_{\ell} \varphi \bar{\nu}_{\ell} \gamma_5 \nu_s, \quad (8.1)$$

where $\ell = e, \mu, \tau$ is a flavor index, ν_{ℓ} is the active neutrino field and λ_{ℓ} are the three coupling constants. The pseudoscalar contraction of Majorana spinors $\bar{\nu} \gamma_5 \nu$ is purely imaginary, so the couplings are real. The opposite situation would be true for a scalar coupling $\bar{\nu} \nu$, which is identically real: at the high energies of interest to IceCube the two choices would lead to the same results, and we limit ourselves to the pseudoscalar choice only for definiteness. Furthermore, in order to conserve parity, we assume φ to be a pseudoscalar particle.

The Lagrangian in Eq. [8.1] violates the $\text{SU}_L(2)$ group of the Standard Model, as do all the models with neutrino secret interactions only. This violation could come from a spontaneous breaking of the symmetry group, for example with an additional scalar field acquiring an expectation value: the study of such general models is beyond the scope of this work, in which we focus only on the phenomenological consequences of the interaction. We should however mention that the addition of

a sterile neutrino necessarily requires a change in the mass term for the neutrinos. In particular, it will lead to a 4×4 mass matrix parameterized by three mixing angle among active neutrinos, as in the Standard Model, and three new mixing angle among active and sterile neutrinos. In this work we will assume the latter three angles to be so small as to neglect their effects, in order to disentangle the mixing from the consequences of the interaction.

The interaction is characterized by 5 parameters: these are the mass of the pseudoscalar mediator M_φ , the mass of the sterile neutrino m_s and the three couplings λ_e , λ_μ , and λ_τ . A natural choice for the coupling would be $\lambda_e = \lambda_\mu = \lambda_\tau$; however, we will see that also the choice $\lambda_e = \lambda_\mu = 0$ is of particular interest since it is the most difficult to constrain using laboratory experiments (the same conclusion is reached for a model with active-active secret interaction in the more recent Ref. [400]). On the other hand, for the two masses M_φ and m_s , which set the energy scale of the model, we will see that the constraints favor a region of interest between 10 MeV and 1 GeV.

8.2 Constraints

In this section we explore the constraints that can be drawn on the model from laboratory experiment, cosmology, and astrophysics. Laboratory experiments are able to constrain the model mainly because of the new channels which open up for meson decay with the new interaction. This allows to put bounds on how strong the interaction can be without changing the branching ratios for these decays; this has already been done for active-active secret interactions, for example in Ref. [405]. Cosmology can be a source of powerful constraints on these models, both because additional species influence the rate of expansion of the Universe, and because secret interactions can change the properties of the dense primordial plasma. For this reason, both primordial nucleosynthesis and the formation of the CMB are taken into account in this work. Finally, astrophysical compact objects, in particular supernovae, are environments with large concentrations of neutrinos which could in principle be sensitive to secret interactions: as we will discuss, however, we find no competitive constraints from supernovae.

8.2.1 Laboratory constraints

As mentioned above, secret interactions open new decay channels for mesons. In the standard scenario mesons can decay leptonically as $M \rightarrow \nu_\ell \ell$, where M represents a meson (π^+ , K^+ , D^+) and $\ell = e, \mu, \tau$. The new channels opened by the secret interaction are $M \rightarrow \nu_s \ell \varphi$ and $M \rightarrow \nu_s \ell \bar{\nu}_\ell \nu_s$. The corresponding Feynman diagrams are shown in Fig. [8.1]. We remark again that the active-sterile mixing angle is assumed small, since otherwise it would cause new decay channels such as $M \rightarrow \nu_{\ell'} \ell \varphi$.

The conditions for the process $M \rightarrow \nu_s \ell \varphi$ are that the corresponding $\lambda_\ell \neq 0$ and the kinematical requirement

$$m_s + M_\varphi \lesssim m_M - m_\ell, \quad (8.2)$$

where m_M is the mass of the decaying meson and m_ℓ the mass of charged lepton ℓ . We provide in Table [8.1] the maximal allowed values for $m_s + M_\varphi$, namely $m_M - m_\ell$. Some of the processes ($\pi^+, K^+, D^+ \rightarrow e \varphi \nu_s$ and $K^+, D^+ \rightarrow \mu \varphi \nu_s$) have a large phase space available, whereas others ($\pi^+ \rightarrow \mu \varphi \nu_s$ and $D^+ \rightarrow \tau \varphi \nu_s$) are only marginally allowed and are not expected to be very constraining. Finally, the processes $\pi^+, K^+ \rightarrow \tau \varphi \nu_s$ are not kinematically allowed.

Among all these processes, we focus on the decay $K^+ \rightarrow \mu \varphi \nu_s$. There are various reasons for this choice: first of all, as also discussed in Ref. [405], this process leads to stronger limits than the corresponding decay in electron $K^+ \rightarrow e \varphi \nu_s$. This is mainly due to the higher precision with which

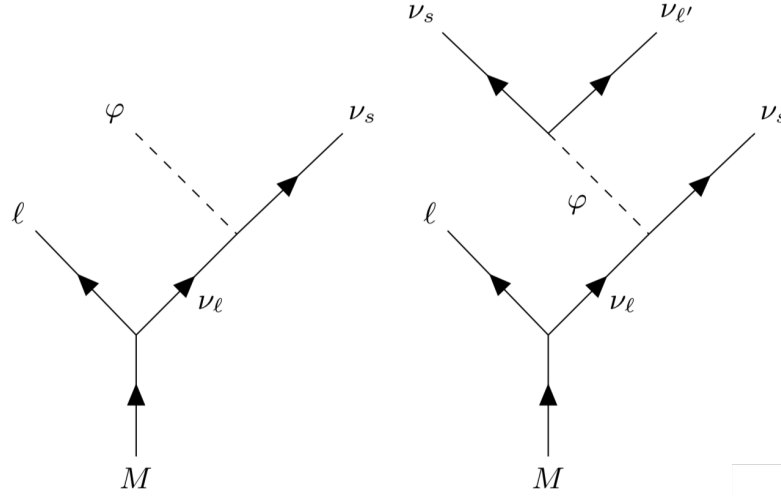


Figure 8.1: Feynman diagrams for the new meson decay channels introduced by the interaction: time runs along the vertical axis.

Meson	$(m_s + M_\varphi)_{\max}(\text{MeV})$
$\pi^+ \rightarrow e\varphi\nu_s$	140
$\rightarrow \mu\varphi\nu_s$	35
$\rightarrow \tau\varphi\nu_s$	–
$K^+ \rightarrow e\varphi\nu_s$	493
$\rightarrow \mu\varphi\nu_s$	388
$\rightarrow \tau\varphi\nu_s$	–
$D^+ \rightarrow e\varphi\nu_s$	1870
$\rightarrow \mu\varphi\nu_s$	1765
$\rightarrow \tau\varphi\nu_s$	93

Table 8.1: New decay channels for light mesons induced by the interaction and relative maximal allowed values for $m_s + M_\varphi$. When the numerical value is missing it means that the corresponding process is kinematically forbidden.

the branching ratios are known for the first process compared with the second one. Furthermore, due to the larger phase space available, constraints from kaon decay are stronger than the ones from π^+ and D^+ decay. The only exception is the case of only $\lambda_\tau \neq 0$, since this implies that only the process $D^+ \rightarrow \tau\varphi\nu_s$ is kinematically allowed. We have explicitly analyzed the rate of this process finding that, for masses M_φ and m_s consistent with the cosmological constraints, the constraints from D^+ decay are so weak that $\lambda_\tau = 1$ is always allowed.

The four-body decay $M \rightarrow \nu_s \ell \bar{\nu}_{\ell'} \nu_s$ can also constrain the model. The decay is kinematically allowed if

$$2m_s \lesssim m_M - m_\ell. \quad (8.3)$$

Since the four-body decay contains an additional vertex of interaction (see Fig. [8.1](#)), it is suppressed by a factor λ^2 compared to the three-body decay; therefore we expect it to be important only for

$\lambda \sim 1$.

Our purpose is to compare the decay rates for the three-body and four-body processes with the experimental constraints. First of all we discuss the explicit form of the decay rates of mesons. We limit the discussion to the kaon decay into muon for the reasons discussed above, even though it is straightforward to obtain the decay rate for a different meson decay M into the leptonic channel ℓ by simply replacing in all the subsequent formulas m_K by m_M and μ by ℓ .

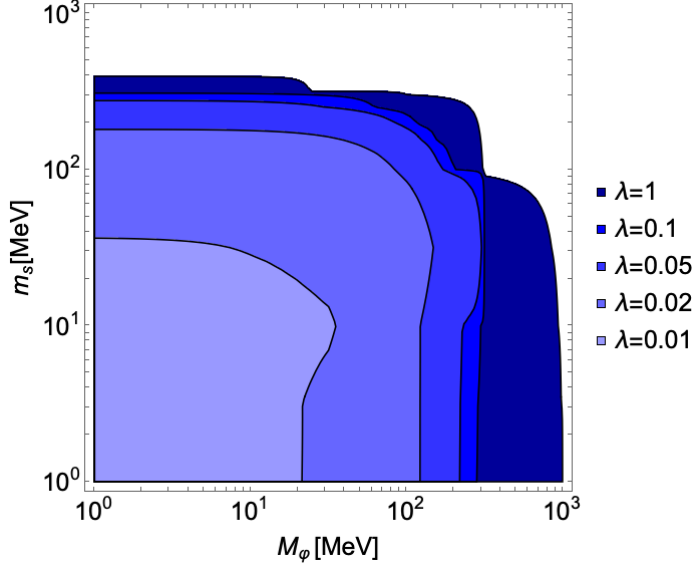


Figure 8.2: Exclusion contours in the $M_\varphi - m_s$ plane for different values of the coupling $\lambda = \lambda_e = \lambda_\mu = \lambda_\tau$, for the choice of equal flavor coupling: the region below the contours is excluded.

For the three-body decay $K^+ \rightarrow \mu\nu_s\varphi$, the decay rate in the limit of vanishing active neutrino masses is

$$\begin{aligned} d\Gamma_{K \rightarrow \mu\nu_s\varphi} &= \\ &= \frac{f_K^2 G_F^2 |\lambda_\mu|^2}{16m_K (2\pi)^3} \int dE_p dE_k \frac{Q}{(m_K^2 + m_\mu^2 - 2m_K E_p)^2}, \end{aligned} \quad (8.4)$$

where

$$\begin{aligned} Q &= 8M_\varphi^2 [2(m_K E_k - E_p E_k + \mathbf{p} \cdot \mathbf{k}) \times \\ &\quad (2E_p(m_K - E_p) - m_K E_p + m_\mu^2) - \\ &\quad (m_K^2 + m_\mu^2 - 2m_K E_p)(E_p E_k + \mathbf{p} \cdot \mathbf{k})]. \end{aligned} \quad (8.5)$$

We have defined with p, q, k , and P respectively the μ, φ, ν_s and K four-momenta, and in bold face their spatial three-momenta. f_K is the Kaon decay form factor. Notice that for fixed values of E_p and E_k , the product $\mathbf{p} \cdot \mathbf{k}$ is unambiguously determined by kinematics, which is why no angular integration appears in Eq. [8.4](#).

With the same notation, for the four-body decay $K^+ \rightarrow \mu\nu_s\nu_s\bar{\nu}'_\ell$, the decay rate is

$$d\Gamma_{K \rightarrow \mu\nu_s\nu_s\nu_s} = \frac{G_F^2 f_K^2 |\lambda_\mu|^2 (\sum_\ell |\lambda_\ell|^2)}{(2\pi)^6 M} \int \frac{|\mathbf{p}|^2 d|\mathbf{p}| |\mathbf{q}|^2 d|\mathbf{q}| |\mathbf{k}| d|\mathbf{k}| d\cos\theta d\phi}{E_p E_q E_k |\mathbf{p} + \mathbf{q}|} \frac{q \cdot l Q'}{s^4 [(q+l)^2 - M_\varphi^2]^2}, \quad (8.6)$$

where p, q, l, k and P are the four-momenta respectively of $\mu, \nu_s, \nu'_\ell, \nu_s$ and K . For convenience, we introduced the notation $s = P - p$ and we defined

$$Q' = 4k \cdot sp \cdot Ps \cdot P - 2k \cdot sp \cdot sm_K^2 - 2k \cdot Pp \cdot Ps^2 + k \cdot pm_K^2 s^2. \quad (8.7)$$

In this case, there are 5 independent variables to parameterize the decay, which we chose to be $|\mathbf{p}|, |\mathbf{q}|, |\mathbf{k}|$, the angle θ between \mathbf{p} and \mathbf{q} , and the azimuthal angle ϕ between \mathbf{k} and the plane determined by \mathbf{p} and \mathbf{q} . In case \mathbf{p} and \mathbf{q} were collinear, this should be interpreted as the azimuthal angle around the direction of \mathbf{p} .

The three-body and four-body decay processes would both be observed as $K \rightarrow \mu$ +missing energy. The Particle Data Group review [61] lists a process $K \rightarrow \mu\nu\bar{\nu}$ with the same observational signature and with an upper limit on the branching ratio of 2.4×10^{-6} at 90% confidence level. For this reason we impose that the branching ratio for the three-body and four-body decay processes together is smaller than this limit.

As we mentioned above there are three independent couplings for the three flavors. As a benchmark choice we assume here $\lambda_e = \lambda_\mu = \lambda_\tau = \lambda$, and we show in Fig. 8.2 the region excluded by kaon decay in the $M_\varphi - m_s$ plane for various values of the coupling λ . The contours exhibit a bump in the right part of the exclusion contours; this comes from the four-body decay, which does not contain φ in the final state and thus mainly constrains m_s . As we discussed above, this bump is most pronounced for $\lambda = 1$, where the four-body decay is not suppressed by the factor λ^2 compared to the three-body one.

The benchmark choice of equal flavor couplings captures the most important qualitative aspects. There is however a choice for which the results are completely different, namely $\lambda_e = \lambda_\mu = 0$ and $\lambda_\tau \neq 0$. This choice is in fact essentially unconstrained from meson physics.

8.2.2 Cosmological bounds

Cosmology can constrain secret interactions in two ways. On the one hand, Big Band Nucleosynthesis (BBN) is very sensitive to the number of relativistic degrees of freedom, and requires that there are no relativistic species beyond the Standard Model at the time of the BBN. In the model studied here, this constraints is naturally verified if the new species φ and ν_s are non-relativistic and in thermal equilibrium before and during BBN. In this way, their distributions are suppressed by the Boltzmann factor $e^{-m/T_{\text{BBN}}}$, with $T_{\text{BBN}} \simeq 1$ MeV. A second constraint comes from the requirement that the active neutrinos are free-streaming (and thus non-interacting) at the time at which the CMB forms.

The full solution of the BBN and CMB equations in the presence of active-sterile secret interactions is beyond the scope of this work. In our papers we limit ourselves to finding a region of the parameter space which is safe from these constraints, leaving for future works to determine whether more refined approaches change significantly the results. For this reason, we also refer to an effective coupling λ for the interaction instead of the three couplings λ_ℓ . This effective coupling is chosen as the largest coupling between the three.

Big Bang Nucleosynthesis

As discussed above, we require the new species to be *i*) non-relativistic at the time of the BBN and *ii*) in kinetic and chemical equilibrium throughout the passage from relativistic to non-relativistic. We emphasize again that this is a sufficient, but not necessary, condition. The first requirement is naturally met if both M_φ and m_s are larger than about 10 MeV: in this way, the Boltzmann factor $e^{-m/T_{\text{BBN}}}$ is smaller than 10^{-4} , so the species are non-relativistic. To verify the second requirement, we now compare the rates of the processes responsible for the equilibrium with the rate of the expansion of the Universe, in order to determine the decoupling temperature for each process.

- $\nu_\ell \nu_s \rightarrow \nu_\ell \nu_s$ and $\nu_s \nu_s \rightarrow \nu_\ell \nu_\ell$: the cross section for these processes, mediated by φ , can be estimated by dimensional arguments as $\frac{\lambda^4 T^2}{M_\varphi^4}$. For a non-relativistic distribution of sterile neutrinos the number density grows as $n \sim (T m_s)^{3/2} e^{-m_s/T}$. The decoupling temperature is set by the condition $n\sigma \sim H$, where H is the Hubble parameter, which translates into the condition $n\sigma \sim \frac{T^2}{M_{\text{Pl}}}$, where M_{Pl} is the Planck mass. This leads to the relation

$$\left(\frac{T}{m_s}\right)^{3/2} e^{-m_s/T} \sim \frac{M_\varphi^4}{M_{\text{Pl}} m_s^3 \lambda^4}.$$

An approximate solution for this equation, in the regime in which $M_{\text{Pl}} m_s^3 \lambda^4 \gg M_\varphi^4$, is then

$$T_s \sim \frac{m_s}{\log \left[\frac{M_{\text{Pl}} m_s^3 \lambda^4}{M_\varphi^4} \right]}.$$

The factor in the denominator depends only logarithmically on the parameters, and for typical values of the masses between 10 MeV and 1 GeV and λ between 0.01 and 1 is of the order of 10 to 100. Therefore the decoupling temperature is of the order of $\frac{m_s}{10}$, which means that these processes are able to maintain both kinetic and chemical equilibrium for sterile neutrinos even after the latter have become non-relativistic.

- $\varphi\varphi \rightarrow \nu_s \nu_s$ or $\varphi\varphi \rightarrow \nu_\ell \nu_\ell$: the most efficient is the first process which is mediated by active neutrinos. The cross section is estimated as $\frac{\lambda^4}{m_\ell^2}$, where m_ℓ is the active neutrino mass. Assuming a non-relativistic distribution for φ , we find the condition

$$\left(\frac{T}{M_\varphi}\right)^{-1/2} e^{-M_\varphi/T} \sim \frac{m_\ell^2}{M_{\text{Pl}} M_\varphi \lambda^4}.$$

The decoupling temperature, in the regime $m_\ell^2 \ll M_\varphi M_{\text{Pl}} \lambda^4$, is approximately

$$T_\varphi \sim \frac{M_\varphi}{\log \left[\frac{M_\varphi M_{\text{Pl}} \lambda^4}{m_\ell^2} \right]}.$$

The factor in the denominator is typically of order 10 to 100, so we find again that the φ particles remain in equilibrium throughout their passage from relativistic to non-relativistic, and therefore become Boltzmann suppressed.

In summary, if the new species are sufficiently massive, namely

$$m_s \gtrsim 10 \text{ MeV and } M_\varphi \gtrsim 10 \text{ MeV,} \quad (8.8)$$

the BBN bounds are satisfied.

Cosmic Microwave Background

When the CMB forms, ν_s and φ are no longer present. Secret interactions can still be relevant among active neutrinos alone via two separate processes: on the one hand, if there is a small mixing angle between active and sterile neutrinos, the process $\nu_\ell \nu_s \rightarrow \nu_\ell \nu_s$ can be converted via mixing to an active-only process $\nu_\ell \nu_{\ell'} \rightarrow \nu_\ell \nu_{\ell'}$; on the other hand the active neutrinos might interact via a box diagram, converting into sterile neutrinos with a first exchange of mediator and then back into active neutrinos with a second exchange. This gives rise again to the effective process $\nu_\ell \nu_{\ell'} \rightarrow \nu_{\ell'} \nu_{\ell'}$. Since we have always assumed negligible mixing angles between active and sterile neutrinos, we focus only on the last process.

The presence of active-active induced interactions can in principle disrupt the free-streaming state of active neutrinos at the time of the CMB and leave an imprint on it. For this reason, we now estimate the decoupling temperature of the active-active process and verify that it is larger than the CMB formation temperature. The cross section can be estimated in order of magnitude as $\frac{\lambda^8 T^{10}}{M_\varphi^8 m_s^4}$. Since active neutrinos are relativistic at the CMB formation, the decoupling temperature is

$$\begin{aligned} T_{\nu_\ell \nu_{\ell'}}^{\text{dec}} &= \left(\frac{M_\varphi^8 m_s^4}{\lambda^8 M_{\text{Pl}}} \right)^{1/11} \simeq \\ &\simeq 10^5 \text{eV} \left(\frac{M_\varphi}{10 \text{MeV}} \right)^{8/11} \left(\frac{m_s}{10 \text{MeV}} \right)^{4/11} \lambda^{-8/11}. \end{aligned}$$

We require T^{dec} to be larger than the temperature of CMB formation, which is around 1 eV; one can verify by direct substitution that this is the case for all the parameter space of interest.

8.2.3 Astrophysical bounds

Supernovae are another environment with dense concentrations of neutrinos, in which secret interactions can leave observational signatures. The non-observation of these signatures can be used to put constraints, as has been recently done for active-active secret interactions [406, 407]. The typical energies of neutrinos in the supernovae core are of the order of tens of hundreds of MeV, sufficient to produce non-relativistic sterile neutrinos. Provided that the mean free path of these sterile neutrinos is sufficiently large, they could escape the supernova core and lead to an appreciable energy loss. For the supernova SN 1987A an upper bound on the luminosity that can be emitted in sterile neutrinos is estimated as $L_s^{\text{SN}} \simeq 2 \times 10^{52}$ erg/s.

Our model could be in tension with this bound if two conditions are met: *i*) the mean free path of sterile neutrinos inside the core, namely $(\sigma_{is \rightarrow js} n_a)^{-1}$, with $\sigma_{is \rightarrow js}$ the cross section for scattering of a sterile neutrino on an active neutrino in the i -th mass eigenstate, and n_a the number density of active neutrinos in the core, is larger than the radius of the supernova core, which is around 10 km; *ii*) the total luminosity injected in sterile neutrinos L_s is larger than L_s^{SN} . We estimate L_s as

$$L_s = \int \sum_{i,j} \frac{d\sigma_{ij \rightarrow ss}}{dE} E dE f_i(E', r) f_j(E'', r) dE' dE'' 4\pi r^2 dr,$$

where $f_i(E, r)$ is the distribution, assumed thermal, of active neutrinos in the i -th mass eigenstate inside the supernova core. The temperature profile $T(r)$ is taken from Ref. [406].

The cross sections needed for this calculation will be discussed in detail in App. E, using these results, we have numerically verified that the two conditions just mentioned never occur simultaneously throughout all the parameter space we considered, with m_s and M larger than 10 MeV.

The reason is that for large couplings λ the energy injected in the sterile sector is large, but the active-sterile interaction is so strong that the sterile neutrinos do not escape the supernova; rather, they thermalize, leading to no appreciable energy loss. On the other hand, for small couplings λ sterile neutrinos are free to escape, but they are produced in smaller quantity and therefore do not exceed the SN 1987A bounds. In conclusion, we find no relevant constraints from supernovae.

8.3 Neutrino fluxes

The main purpose of the work discussed here is to study the signatures of active-sterile secret interactions on astrophysical neutrinos. In this section we describe the methodology we adopt. First of all, we have to specify a standard astrophysical source of high-energy neutrinos, in order to determine how these neutrinos change in the presence of the secret interaction. In the first part of the section we describe the standard astrophysical sources of neutrinos we have studied. In the second part we discuss how secret interactions change the standard scenario, and the method we have used to quantitatively compute this effect.

8.3.1 Standard astrophysical sources

In our work we focus on two benchmark choices for the standard astrophysical sources of neutrinos: *i*) a diffuse class of neutrinos with a power-law energy spectrum with parameters obtained by the fit to the IceCube data given in Ref. [408], which might simulate, for example, the high-energy neutrinos produced in SBGs and in general in cosmic reservoirs (see Sec. 4.2.1 and Chap. 5); *ii*) a simple parameterization for the cosmogenic neutrino fluxes (see Sec. 4.3).

We have no pretense of completeness by these two choices alone. In the energy range of IceCube, as we have discussed repeatedly, neutrinos need not come from cosmic reservoirs, and their spectral shape could be different. In the ultra-high energy range cosmogenic neutrinos are a guaranteed contribution, but the magnitude of this flux is not known and recent studies have shown that a competing source of neutrinos could still be of astrophysical nature, provided for example by blazars [153] and Flat Spectrum Radio Quasars (FSRQ) [360]. However, we are not interested in giving a complete overview of all the possible spectral shapes that could be expected at IceCube: rather, the two benchmark choices used here allow us to test the effects of secret interactions over a large energy scale from the TeV-PeV to the EeV, which is our main aim. We now discuss separately these two choices.

TeV-PeV range: power-law model

We consider a collection of astrophysical neutrino sources, each one producing a power law spectrum per unit solid angle¹ in energy

$$\frac{dN_\nu}{dE dt d\Omega} = f_{\text{PL}}(E) = \mathcal{N} E^{-\gamma}, \quad (8.9)$$

where $f_{\text{PL}} \equiv \phi_{\nu_e} + \phi_{\nu_\mu} + \phi_{\nu_\tau} + \phi_{\bar{\nu}_e} + \phi_{\bar{\nu}_\mu} + \phi_{\bar{\nu}_\tau}$ and γ is the spectral index. The IceCube analysis gives as best fit value for the throughgoing-muons $\gamma = 2.28$ [283]. We assume that the sources are distributed according to the Star Forming rate $\rho(z)$ [409, 410], where $\rho(z)$ is defined as the comoving number density. The normalization \mathcal{N} is chosen to reproduce the best-fit for the diffuse neutrino

¹If the source is anisotropic, the spectrum is evaluated in the direction of the Earth.

flux measured by the IceCube Collaboration for the throughgoing-muons. The flux arriving at Earth from the point-like source, expressed in terms of $f_{\text{PL}}(E)$, is

$$\frac{d\phi}{dE} = \frac{f_{\text{PL}}[E(1+z)]}{r^2(z)}, \quad (8.10)$$

where $r(z) = \int_0^z \frac{dz'}{H(z')}$.

Therefore, the diffuse astrophysical spectrum is

$$\frac{d\phi_\nu}{dEd\Omega} = \int \frac{dz'}{H(z')} \rho(z') f_{\text{PL}}[E(1+z')]. \quad (8.11)$$

We assume for definiteness a flavor structure at the source (1 : 2 : 0), corresponding to pion beam sources.

Throughout our analysis we use the best fit values from the NuFit 3.2 global fit data for the active oscillation parameters [411], assuming normal neutrino mass ordering.

EeV range: cosmogenic

A complete computation of the cosmogenic neutrino flux requires to solve the coupled differential equations for the heavy nuclei in cosmic-rays colliding with the CMB. For this work we have more simply used the results of Ref. [410]. In particular we have parameterized the cosmogenic spectrum as

$$\frac{d\phi_\nu}{dEd\Omega} = \int \frac{dz'}{H(z')} \rho(z') f_{\text{cosmo}}[E(1+z')], \quad (8.12)$$

where $\rho(z)$ is the Star Forming rate [409]. The function $f_{\text{cosmo}}(E)$ was determined in such a way as to reproduce the cosmogenic flux of Ref. [410]. There are in principle infinite possible choices to obtain the function $f_{\text{cosmo}}(E)$: we observed that the integrand function contains $\frac{\rho(z')}{H(z')}$, which is rather peaked at $z' = 1$. Therefore we can approximately evaluate $f_{\text{cosmo}}[E(1+z')]$ at $z' = 1$ and take it out of the integral. This gives a unique solution

$$f_{\text{cosmo}}(2E) \simeq \frac{d\phi_\nu^{\text{th}}}{dEd\Omega} \frac{1}{\int \frac{dz'}{H(z')} \rho(z')}, \quad (8.13)$$

where $\frac{d\phi_\nu^{\text{th}}}{dEd\Omega}$ is the cosmogenic flux in Ref. [410]. We have verified that inserting back $f_{\text{cosmo}}(E)$ from Eq. [8.13] into Eq. [8.12] reproduces very precisely the correct cosmogenic spectrum. For cosmogenic neutrinos we assume again a flavor structure at the source (1 : 2 : 0).

8.3.2 Secret interaction

As also mentioned in the introduction to this chapter, secret interactions change the propagation of neutrinos from their sources to the Earth. More specifically, the active neutrinos produced at the source can collide with low energy neutrinos from the CNB producing a flux of secondary sterile neutrinos. Part of these sterile neutrinos can collide themselves with neutrinos from the CNB to produce new active neutrinos, in a process we will name regeneration throughout this work. This cascading process has the most important effect of depleting the active flux by transferring part of its energy to the sterile sector. This results in an effective absorption which is the effect we want to highlight. The cascade process is in principle described by a set of coupled transport equations for the active and sterile neutrino fluxes.

We define by $\Phi_i(z, E)$ the flux of active neutrinos in the i -th ($i = 1, 2, 3$) mass eigenstate per unit energy interval per unit solid angle at a redshift z , while $\Phi_s(z, E)$ denotes the flux of sterile neutrinos. The flux at Earth is $\frac{d\phi_\nu}{dE d\Omega} = \Phi(0, E)$. We assume that the propagation is diagonal in the mass eigenstates: in fact the mean free path between collisions is much larger than the oscillation lengths, so the fast oscillations average out the neutrino density matrix to its diagonal form in the mass basis. In other words, in between two collisions a neutrino decoheres to mass eigenstates.

The transport equations take the form:

$$H(z)(1+z) \left(\frac{\partial \Phi_i(z, E)}{\partial z} + \frac{\partial \Phi_i(z, E)}{\partial E} \frac{E}{1+z} \right) = \sum_j n_j(z) \sigma_{ij \rightarrow ss} \Phi_i(z, E) \quad (8.14)$$

$$- \int dE' \Phi_s(z, E') \sum_j \frac{d\sigma_{js \rightarrow is}}{dE} (E' \rightarrow E) n_j(z) - \rho(z)(1+z) f(E) \xi_i,$$

where $f(E)$ is the neutrino spectrum produced at the source (this is f_{PL} for the power-law flux and f_{cosmo} for cosmogenic neutrinos) and ξ_i is the fraction of neutrinos produced at the source in the i -th mass eigenstate. Similarly, for the sterile flux we write:

$$H(z)(1+z) \left(\frac{\partial \Phi_s(z, E)}{\partial z} + \frac{\partial \Phi_s(z, E)}{\partial E} \frac{E}{1+z} \right) = \sum_{i,j} n_j(z) \sigma_{js \rightarrow is} \Phi_s(z, E) \quad (8.15)$$

$$- 2 \sum_{i,j} \int dE' \Phi_i(z, E') \frac{d\sigma_{ij \rightarrow ss}}{dE} (E' \rightarrow E) n_j(z) - \sum_{i,j} \int dE' \Phi_s(z, E') \frac{d\sigma_{js \rightarrow si}}{dE} (E' \rightarrow E) n_j(z).$$

Here n_j is the number density of CNB neutrinos in the j -th mass eigenstate: we assume equipartition among mass eigenstates (justified by the small mass difference between them compared with the mass chosen at 0.1 eV). For $m_s > M_\varphi$, we also account for the decay of sterile neutrinos: this is discussed in App. [F](#).

The regeneration process corresponding to the last term in Eq. [8.15](#) makes the equations hard to solve since they are coupled to one another. However, we found that for the benchmark fluxes we have chosen regeneration plays only a negligible role. The reason is that the regenerated flux from sources at high redshifts is subdominant compared with the direct flux from sources at low redshifts. We verified this both by solving the coupled transport equations numerically for some benchmark cases and by treating the regeneration term perturbatively to first order: the last approach showed that the first order correction is indeed smaller than the flux without regeneration. An important exception to this rule is the case $m_s > M_\varphi$, where the decay of sterile neutrinos leads to another process which can regenerate active neutrinos. In this case we find that regeneration can significantly change the flux: we refer again the reader to App. [F](#) where we describe how we deal with this case.

Neglecting regeneration, we only need to solve Eq. [8.15](#) without the last term. This admits the analytical solution for the flux at Earth

$$\Phi_i(E) = \int_0^{+\infty} \frac{dz}{H(z)} \rho(z) f[E(1+z)] \times$$

$$\exp \left[- \int_0^z \frac{dz'}{H(z')(1+z')} \sum_j n_j(z') \sigma_{ij \rightarrow ss} [E(1+z')] \right] \xi_i. \quad (8.16)$$

8.4 Results

In this section we show the effect of secret interactions on the benchmark sources of astrophysical neutrinos discussed above. We divide our discussion according to the two sources.

8.4.1 TeV-PeV range: power-law model

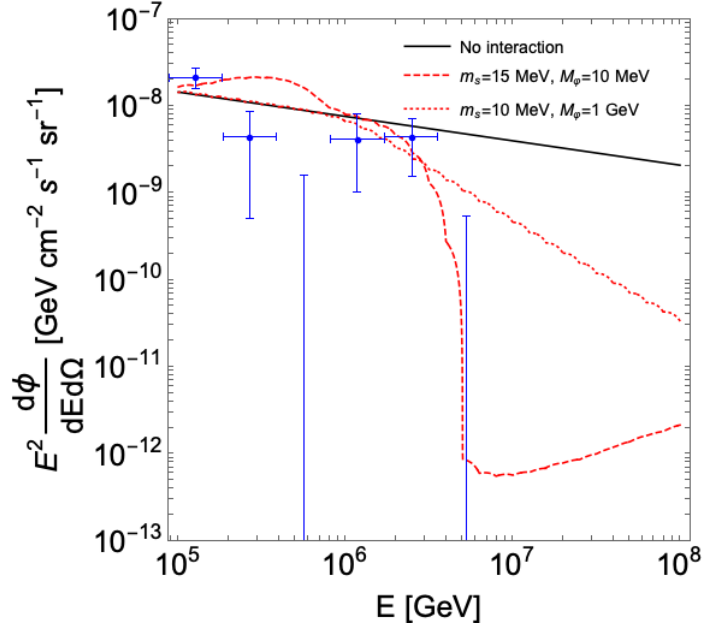


Figure 8.3: Astrophysical all-flavor neutrino power-law spectrum: the thick curve is the flux with no interaction, while the dotted curve corresponds to the case of $\lambda_{af} = 1$ and the dashed one corresponds to the case $\lambda_\tau = 1$, as described in the text. The experimental points are the neutrino fluxes inferred from the IceCube HESE data [204].

In the region below 100 PeV the active-sterile interaction is kinematically forbidden unless the sterile mass is sufficiently low. The condition is that the center-of-mass energy of the active astrophysical neutrino and the CNB neutrino at rest is larger than twice the sterile mass². For ultra-relativistic astrophysical neutrinos of energy E this condition gives $\sqrt{2mE} > 2m_s$; for a typical sterile neutrino mass of $m_s = 10$ MeV and an active neutrino mass of $m = 0.1$ eV we find $E > 1$ PeV.

We distinguish between the two benchmark possibilities for the flavor structure of the interaction: either $\lambda_e = \lambda_\mu = \lambda_\tau = \lambda_{af}$ (where af denotes all flavors), or $\lambda_e = \lambda_\mu = 0$ and $\lambda_\tau \neq 0$.

In the first case, the kaon decay strongly constrains the possible values of the coupling (see Fig. 8.2). In order to have noticeable effects, small sterile masses, large mediator masses, and large couplings $\lambda_{af} \simeq 1$ are required. We take as benchmark values $m_s = 10$ MeV and $M_\varphi = 1$ GeV. In this case the interaction takes place with a large coupling, but it is not resonant (the resonance condition with a mediator mass $M_\varphi = 1$ GeV would require energies of 10 EeV).

²The factor of 2 comes from the two neutrinos produced in the interaction.

In the second case, with $\lambda_e = \lambda_\mu = 0$, there are no constraints from meson decays. Thus $\lambda_\tau = 1$ is presently unconstrained even for small masses of the mediator and the sterile neutrino. We choose the benchmark values of $m_s = 15$ MeV, $M_\varphi = 10$ MeV, and $\lambda_\tau = 1$, which maximize the effect. For this choice the interaction is not only kinematically allowed, but also in resonance at the energies of interest³.

We show the spectra for both parameter choices in Fig. 8.3 together with the power-law flux in the absence of secret interaction. The first choice (dotted curve) leads to a weaker absorption effect which is mainly evident at higher energies, due to the out-of-resonance character of the interaction. On the other hand, the second choice (dashed curve), which is resonant, leads to a pronounced absorption dip starting at the threshold for sterile neutrino production. This second case is also special in that it has $m_s > M_\varphi$, so the sterile neutrino can decay as discussed in App. F. This is the origin of the small pile-up of neutrinos in the low energy part of the spectrum.

The flavor structure also changes in view of the secret interaction, because different mass eigenstates are absorbed with different strengths during the propagation. To illustrate this point, we show in Fig. 8.4 the flavor ratios as a function of the energy for both the parameter choice discussed above.

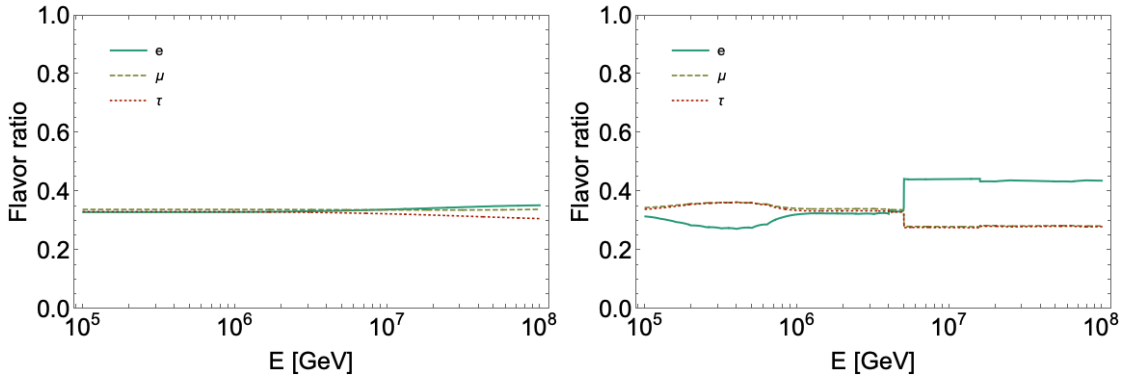


Figure 8.4: Flavor ratio at Earth as a function of the energy for the first benchmark case ($m_s = 10$ MeV, $M_\varphi = 300$ MeV, $\lambda_e = \lambda_\mu = \lambda_\tau = 1$) (top panel) and second benchmark case ($m_s = 15$ MeV, $M_\varphi = 10$ MeV, $\lambda_\tau = 1$) (bottom panel). We show in different colors and linestyles the fraction of electron (green solid), muon (yellow dashed) and tau (red dotted) neutrinos.

For the first case the flavor composition is only slightly different from the standard one (namely (1:1:1)) at very high energies. On the other hand, the second case shows a characteristic behavior with a small change of the flavor ratio at low energies, due to the pile-up effect, and a cutoff at high energies above which the flavor composition changes even more significantly. The presence of the cutoff coincides however with the sharp drop in flux due to the absorption of neutrinos on their path to Earth. The energy dependence of the flavor composition from secret interactions is a unique signature which could be very important in the future in disentangling possible effects on the energy flux from the uncertainties on the astrophysical standard neutrino fluxes.

The flavor composition can also be represented in the flavor triangle, where it can be directly compared with the sensitivities of the future experiments. We do so for the second benchmark case ($\lambda_\tau = 1$) in Fig. 8.5, where the red and the orange points correspond to an energy of 10^5

³Actually, since the sterile mass is slightly heavier than the mediator, the interaction becomes kinematically allowed slightly after the resonance energy; however, the resonance enhancement is still quite visible in Fig. 8.3

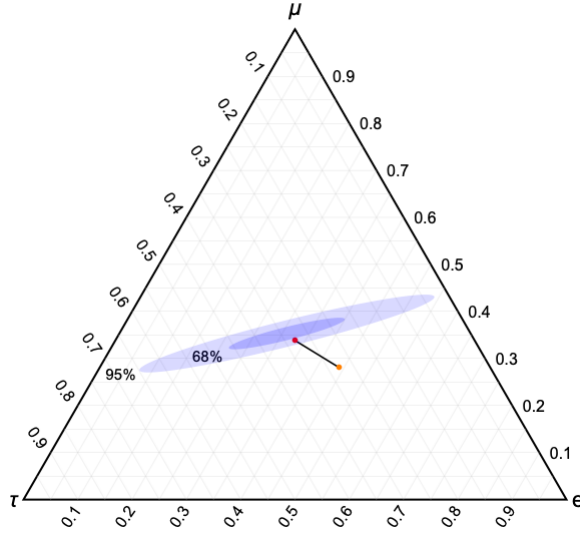


Figure 8.5: Flavor ratio, reproduced in the flavor triangle, for varying energy for the second case in the text ($m_s = 15$ MeV, $M_\phi = 10$ MeV, $\lambda_\tau = 1$). The red and orange points correspond to an energy of 10^5 GeV and 10^8 GeV, respectively. The projected sensitivity of IceCube-Gen2 [412] is shown as well.

GeV and 10^8 GeV, respectively. The comparison with the sensitivity of IceCube-Gen2 is at present mainly indicative, because that sensitivity was estimated for a flavor composition constant in energy, whereas in our case the flavor ratio depends on the energy. However, this comparison already shows that future experiments might be able to distinguish the presence of secret interactions and possibly to constrain them.

8.4.2 EeV range: cosmogenic

For the case of cosmogenic neutrinos the interaction happens resonantly for masses of the mediator so large (of the order of GeV) that the constraints from kaon decay are essentially irrelevant. For this reason, we do not consider different flavor structures for the interaction, which is unconstrained anyway. Rather, we refer to a simplified one-flavor scenario treated in our first paper [403].

At present there is no detection of neutrinos in the ultra-high energy range above 100 PeV. The radio-experiments discussed in previous chapters will play an important role in unveiling the sources of neutrinos in this energy region. For our present discussion, we report the sensitivities of the GRAND experiment, the 90% exclusion limit found by the Pierre Auger Observatory (PAO), and the sensitivity of the ARIANNA experiment

Our results are shown in Fig. [8.6] both in the absence and in the presence of secret interactions, for some benchmark values of the sterile and mediator masses. These spectra have been obtained under the assumption of a purely protonic UHECRs flux (left panel) and purely helium cosmic rays (right panel). For all fluxes the coupling has been fixed to $\lambda = 1$. We find that larger mediator masses correspond to weaker absorption at higher energy scales, as expected.

If the UHECRs composition is mainly protonic, then the cosmogenic normalization is sufficiently large that GRAND and ARIANNA might detect the flux already after 3 years of data taking. Therefore, they might possibly infer the presence of spectral distortions coming from secret interactions.

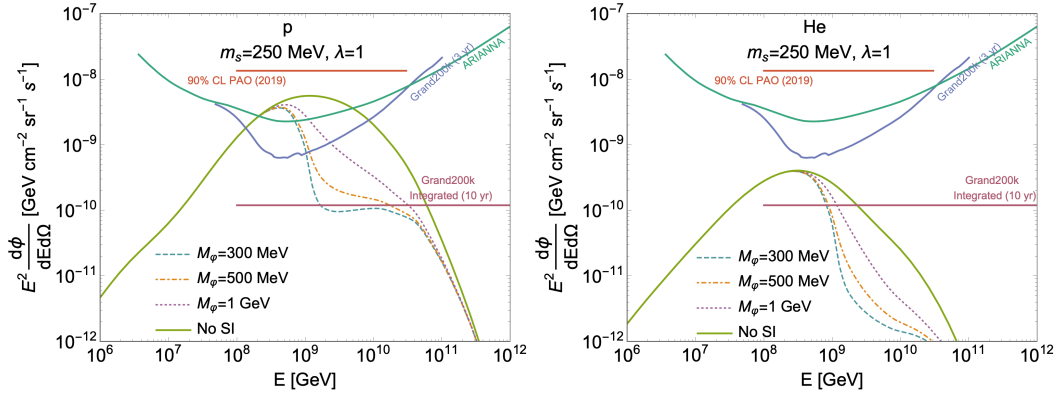


Figure 8.6: Effects on the cosmogenic spectrum expected in the case of proton (left panel) and helium (right panel) cosmic-rays. The solid green curve is the cosmogenic spectrum expected in the absence of secret interactions, the dashed, dot-dashed and dotted curves are the spectrum for secret interactions with $m_s = 250$ MeV and $M_\varphi = 300, 500, 1000$ MeV respectively. The sensitivity of the GRAND experiment, the 90% confidence level exclusion of PAO [413], the integrated sensitivity of GRAND after 10 years of data [97] and the sensitivity of the ARIANNA experiment [414] are also shown.

The non-observation of these spectral distortions might be used to constrain values of the coupling close to 1, which would be otherwise unconstrained for such large values of the sterile and mediator masses.

If the UHECRs composition is made of heavier nuclei, such as the case of helium, the normalization of cosmogenic fluxes lowers significantly. It is still above the integrated sensitivity for GRAND200k, but of course the detection of a distortion of the spectral shape would be harder to perform with these radio experiments. In this case, the neutrino production in the EeV range might be dominated by astrophysical sources, such as blazars [153], which might be used again to detect spectral distortions induced from secret interactions.

8.5 Discussion

In the work presented in this chapter we have considered a specific model of active-sterile secret interactions, and studied its connection with the neutrino observations at IceCube. Whereas active-active secret interactions have been the target of many studies along these lines, in our work for the first time we point out that an interaction connecting the standard neutrino sector with a sterile one can also lead to significant effects. Since this model has been rarely taken into account in the literature, we have first of all obtained the constraints coming from present knowledge of particle physics, astrophysics, and cosmology. The latter in particular are difficult to obtain in a rigorous way, since they require a precise solution of the Big Bang Nucleosynthesis and the Cosmic Microwave Background transport equations. For the purpose of our work we only used order of magnitude estimates, leaving for future work a refined treatment. In this way, we have determined a region of the parameter space of the model which is allowed by present constraints, and which leads to significant distortions of the spectral shape and flavor composition of the astrophysical neutrino fluxes. The mechanism is based on the collisions between astrophysical neutrinos and the low energy

neutrinos from the CNB. The collisions convert the neutrinos into sterile, invisible neutrinos, causing an absorption-like behavior. We have shown the presence of this effect in two different energy ranges: the PeV energy range, which is of interest for IceCube observations and neutrino telescopes, and the EeV energy range, which will be probed by the future generation neutrino radio telescopes. In both cases we find that the secret interaction leads to absorption dips in the spectrum, which could be large enough to be detected either by IceCube or by the future neutrino radio telescopes such as GRAND. The interaction also makes the flavor composition energy-dependent, since different mass eigenstates are absorbed with different rates. The energy-dependent flavor composition, combined with the dip signature in the shape of the energy spectrum, could be a way to uniquely identify the secret interaction. In conclusion, we remark that the choice of the active-sterile sector is a special one which has been rarely studied in the literature. However, the features that we have identified are present also for the more general case of a non-standard interaction involving neutrinos, making the high-energy neutrino observations an ideal source of information for constraining and investigating these models.

Chapter 9

Testing Violation of Equivalence Principle with neutrinos

The equivalence principle is one of the cornerstones of general relativity. The whole connection between gravitation and the geometrical structure of space-time is in fact based on the observation that all bodies (neglecting their extension) move in the same way in a given gravitational field. This observation goes back to the equality between inertial and gravitational mass, proposed as an empirical statement in Newtonian mechanics and then promoted to a founding principle in the general theory of relativity. However, this theory, as well known, is probably incomplete at very high energies, as hinted at by its non-renormalizable behavior after quantization, and by the apparently unavoidable presence of singular solutions in the collapse of material bodies. For this reason, testing the principles at the basis of the theory is a fundamental research area, and there are many different kinds of experiments aimed at identifying a possible Violation of Equivalence Principle (VEP). These include torsion-balance experiments [415], motion of bodies in the solar system [416], spectroscopy of atomic levels [417] and pulsars [418-420].

High-energy neutrinos represent a complementary way of probing VEP. In the standard scenario, the neutrino eigenstates of free propagation do not coincide with the flavor eigenstates, and the relative dephasing between them cause the observed oscillations between different flavors. VEP induces a new source of dephasing, because different combinations of flavor eigenstates can couple with different strengths to an external gravitational potential. This mechanism was in fact proposed to explain the solar neutrino problem [421-431], before the conventional oscillation framework was established. Since the standard scenario is now confirmed, a change of perspective is suggested, using neutrino data to test and constrain VEP. Observations of neutrinos from many sources have led to competitive constraints in this direction [432-450].

In this work, we study the constraints on VEP that can be deduced from the IceCube data, discussing two alternative strategies. First of all, we analyze the large amount of IceCube data on atmospheric neutrinos: since these data mainly represent the muon neutrinos in the atmospheric flux, they are sensitive to a non-standard mechanism of oscillation which changes the fraction of muon neutrinos. Therefore, we constrain the VEP model by using the non-observation of signatures in the IceCube data samples. As a second strategy, we propose to use the flavor composition of astrophysical neutrinos as a VEP-sensitive observable. Depending on the model, VEP can in fact change the flavor composition by virtue of its non-standard oscillations. We show that already with the IceCube data on astrophysical neutrinos a 2-sigma tension is present for some regions of the parameter space. As a future perspective, we compare the predictions of VEP with the future

flavor sensitivity of IceCube-Gen2, showing that it will be able to constrain most of the parameter choices of the model. Our focus is on the complementarity between the two approaches, namely the atmospheric and the astrophysical one: the first is based on lower energy data, and therefore less sensitive to non-standard physics; the second uses higher energy data, whose mechanism of production is however not completely understood yet. A combination of the two allows to constrain most of the parameter space of the model.

9.1 Neutrino propagation in a gravitational field

A neutrino moving in a gravitational field exhibits a modified dispersion relation, which will be derived below. Since the dispersion relation influences the phase acquired by each mass eigenstate in a different way, gravitational fields will in general change the oscillation properties of neutrinos, even if the equivalence principle is verified. However, this change is completely negligible for weak gravitational fields, because the gravitational field acts in the same way on all mass eigenstates, so there is no observable effect. If the equivalence principle is violated, on the other hand, a relative dephasing arises even independently of the mass splitting, because different combinations of mass eigenstates couple with different strengths to the gravitational field. In this section we introduce the mathematical formalism for describing these effects.

Let us assume that the neutrino is described by a wave packet¹ with energy centered around E propagating over a (coordinate) time interval T and (coordinate) length l . For simplicity, we neglect the spin degree of freedom, to keep the discussion as similar as possible to the usual treatment of neutrino oscillations. Let m be the neutrino mass; for the moment we treat the case of a single mass eigenstate. We adopt the weak-field approximation for the line element in space-time

$$ds^2 = (1 + 2\phi)dt^2 - (1 - 2\phi)dl^2, \quad (9.1)$$

where ϕ is the gravitational potential in natural units. If ϕ is independent of time, the motion of the neutrino admits an integral of motion corresponding to the energy

$$E = m(1 + 2\phi)\frac{dt}{ds}. \quad (9.2)$$

The phase acquired by a neutrino in its propagation can be written as

$$\bar{\Phi} = \int p_\mu dx^\mu = \int mg_{\mu\nu} \frac{dx^\mu}{ds} dx^\nu, \quad (9.3)$$

where $g_{\mu\nu}$ is the space-time metric. The term corresponding to $\mu = \nu = 0$ in the sum can be written as $\int E dt$, and since E is an integral of motion it can be integrated to give ET . When we deal with different mass eigenstates, this term is common and equal for all of them, and therefore does not induce any relative dephasing among them: for this reason, we introduce a modified phase $\Phi = \bar{\Phi} - ET$ which does not include this term. This second term is written

$$\Phi = - \int m(1 - 2\phi) \frac{dl}{ds}. \quad (9.4)$$

¹At first sight the assumption of a particle with definite energy propagating over a definite length and time interval might seem in contradiction with the basic principles of quantum mechanics. However, such a description is in fact admissible for a wave packet, provided that the propagation time and length are sufficiently large: the uncertainty on the time is, by the uncertainty principle, larger than $\Delta T \gtrsim \Delta E^{-1}$. This can easily respect the condition $\Delta T \ll T$ provided that $T\Delta E \gg 1$. A different choice, for example a state with definite space-time position (and uncertain energy and momentum), leads to a wrong factor of 2 in the dephasing of the mass eigenstates (see, *e.g.*, Ref. [451](#)).

We can express $\frac{dl}{ds}$ in terms of the energy using the on-shell condition

$$m^2 = \frac{E^2}{1 + 2\phi} - (1 - 2\phi)m^2 \left(\frac{dl}{ds} \right)^2. \quad (9.5)$$

Obtaining $\frac{dl}{ds}$ from Eq. 9.5 and substituting in Eq. 9.4 we finally arrive to the result

$$\Phi = - \int E \sqrt{\frac{(1 - 2\phi)(1 - (m/E)^2 + 2(m/E)^2\phi)}{1 + 2\phi}} dl. \quad (9.6)$$

For ultra-relativistic neutrinos, this can be expanded in terms of the small variables $(m/E)^2$ and ϕ to give

$$\Phi = - \int \left[E - 2\phi E - \frac{m^2}{2E} \right] dl \quad (9.7)$$

Let us now assume the presence of three mass eigenstates, identified by the Latin index i . If the equivalence principle is maintained, the first two terms are a common phase to all three mass eigenstates and can be neglected: the third term, on the other hand, is proportional to m_i^2 for each of the three eigenstates, and induces a relative dephasing, leading to conventional oscillations. The gravitational potential therefore does not produce any effect.

A more interesting case arises if the equivalence principle is violated. In this case, the first term in Eq. 9.7 remains a common phase, but the central term could be different for different combinations of mass eigenstates. We emphasize that these different combinations should not necessarily coincide with the mass eigenstates. However, for simplicity in our initial treatment, let us assume that each mass eigenstate couple with different intensity to the gravitational potential: in other words, the i -th mass eigenstate feels an effective potential $\gamma_i\phi$, where γ_i is a dimensionless factor. If $\gamma_i = 1$, there is no violation of equivalence principle; if γ_i are different among each other, each mass eigenstate acquires a different phase. Introducing the array of the amplitudes of being in each of the mass eigenstates c , with components c_i , we can write a propagation equation in the compact form

$$i \frac{dc}{dl} = 2\phi E \Gamma c + \frac{M^2}{2E} c, \quad (9.8)$$

where $\Gamma = \text{diag}(\gamma_1, \gamma_2, \gamma_3)$ and $M^2 = \text{diag}(m_1^2, m_2^2, m_3^2)$. Since only relative phases are important, these matrices are usually redefined as $\Gamma = \text{diag}(0, \gamma_{21}, \gamma_{31})$ and $M^2 = \text{diag}(0, \Delta m_{21}^2, \Delta m_{31}^2)$. While Eq. 9.8 was derived in the basis of the mass eigenstates, it is of course true in any basis, including the basis of flavor eigenstates, provided that the Γ and M^2 matrices are correspondingly rotated.

All the above derivation refers to the propagation of neutrinos in vacuum. If neutrino propagate in matter, there is a further contribution to the dephasing to take into account. This comes from the elastic forward collisions between neutrinos and the electrons in matter. This is a process analogous to coherent refraction of electromagnetic waves in a continuous medium: for collisions at a generic angle, the incident wave (neutrino in our case, light in the case of electromagnetic waves) produces a scattered wave which is generally out of phase. The dephasing between the two waves depend on the precise position of the center of scattering, and so the total field diffused by a collection of scatterers averages to zero if the wavelength is much smaller than the distance between them. Only in the case of forward scattering, the scattered wave is in phase with the original wave independently of the position of the scattering center: in this case there is a non-vanishing total scattered field from all of the scattering centers [19]. For neutrinos in matter this process is described by the Fermi

interaction Hamiltonian [\[452\]](#)²

$$\mathcal{H}_{\text{int}} = \frac{G_F}{\sqrt{2}} \bar{e} \gamma_\mu (1 - \gamma_5) \nu_e \bar{\nu}_e \gamma^\mu (1 - \gamma_5) e, \quad (9.9)$$

where G_F is the Fermi constant. This term can be rearranged by a Fierz transformation to

$$\mathcal{H}_{\text{int}} = \frac{G_F}{\sqrt{2}} \bar{e} \gamma_\mu (1 - \gamma_5) e \bar{\nu}_e \gamma^\mu (1 - \gamma_5) \nu_e. \quad (9.10)$$

When the neutrino propagates in matter, this term can be averaged over the state of the electrons in matter, which are assumed to be at rest and to be in each of their spin states with equal probabilities. In this case, an explicit computation shows that only the term with $\mu = 0$ in the sum survives, and that the average value $\langle \bar{e} \gamma_0 (1 - \gamma_5) e \rangle = N_e$, the electron number density. After decomposing the spinor ν_e into the left and right-handed components ν_{eL} and ν_{eR} , the interaction Hamiltonian becomes

$$\mathcal{H}_{\text{int}} = -\sqrt{2} G_F N_e \bar{\nu}_{eL} \nu_{eR}, \quad (9.11)$$

which behaves as an effective mass term for the electron neutrino [\[3\]](#). Inserting this term into Eq. [\[9.8\]](#), we express the final propagation equation in the flavor basis using the PMNS matrix: the final result is

$$i \frac{dc_\alpha}{dl} = \sum_{j,\beta} U_{\beta j} U_{\alpha j}^* \frac{M_{jj}^2}{2E} c_\beta + V(\mathbf{r}) \delta_{\alpha e} c_e + 2E\phi \sum_{i,\beta} U_{\beta i} U_{\alpha i}^* \Gamma_{ii} c_\beta, \quad (9.12)$$

where $V(\mathbf{r}) = \sqrt{2} G_F N_e(\mathbf{r})$ will be hereby denoted matter term, and we have used Greek indices to indicate the flavor eigenstates.

As a final comment, until now we have stuck to the assumption that different mass eigenstates couple to gravity diagonally with different strengths. This is only a benchmark assumption, however, and in general the states coupling diagonally to gravity need not be the mass eigenstates: we will refer to them throughout this work as gravitational eigenstates. If the gravitational eigenstates are not equal to the mass eigenstates, they can always be expressed as a combination of flavor eigenstates through a unitary matrix \tilde{U} , which does not anymore coincide with the PMNS matrix: in this case in the last term of Eq. [\[9.12\]](#) the matrix U should be replaced by \tilde{U} , leading to the equation

$$i \frac{dc_\alpha}{dl} = \sum_{j,\beta} U_{\beta j} U_{\alpha j}^* \frac{M_{jj}^2}{2E} c_\beta + V(\mathbf{r}) \delta_{\alpha e} c_e + 2E\phi \sum_{i,\beta} \tilde{U}_{\beta i} \tilde{U}_{\alpha i}^* \Gamma_{ii} c_\beta. \quad (9.13)$$

9.2 VEP effects on atmospheric neutrinos

Having ascertained in which way a VEP can change the oscillation properties of neutrinos, we now turn to the observable consequences of this effect. Since the last term in Eq. [\[9.12\]](#) increases with energy, high energy neutrinos are the ideal candidates to exhibit VEP effects. In this section, we discuss how VEP influences atmospheric neutrinos.

Atmospheric neutrinos propagate from the top of the atmosphere to the Earth surface; in particular, upgoing atmospheric neutrinos pass through the Earth before reaching the detector, for

²There is also a corresponding term coming from neutral current interaction, which however acts in the same way on all flavors and therefore does not cause any relative dephasing: for this reason we neglect it.

³While this derivation is easy from the computational standpoint, it may outshadow the connection with forward scattering. In fact the same result could be obtained by summing the forward scattered amplitude over a collection of electrons, in the same way as done for the electromagnetic field in Ref. [\[453\]](#).

example IceCube, and therefore have to travel a much longer path. This property makes them more sensitive to VEP effects, because the oscillations can accumulate over the traveled distance. For this reason (and also because of the smaller contamination from atmospheric muons), we focus on upgoing atmospheric neutrinos. We will first of all describe qualitatively the effect of VEP oscillations on atmospheric neutrinos; later we will discuss the data sets used for our analysis and the statistical methods used, showing our results for the constraints on the strength of the VEP.

9.2.1 Propagation of atmospheric neutrinos under VEP

During their propagation through the Earth, atmospheric neutrinos are subject to conventional oscillations, the matter potential discussed at the end of the previous section, and possibly VEP oscillations: the latter is the effect we would like to test. Even though the dominant gravitational field is the terrestrial one, the gravitational potential turns out to be dominated by a constant background originating from the Great Attractor, a gravitational anomaly which generates a potential of the order of $\phi \sim 3 \times 10^{-5}$ in natural units [454] (this value should be compared, for example, with the gravitational potential generated by the Earth, which is of the order of 10^{-9} in natural units, thus being completely negligible). Since this value is not known with precision, it is customary to provide constraints not on the γ_{21} and γ_{31} parameters, but rather on the combinations $\gamma_{21}\phi$ and $\gamma_{31}\phi$, assuming that the gravitational potential has a constant value of the order of 10^{-5} . We can therefore identify different qualitative behaviors for the neutrino propagation:

- at low energies ($E \lesssim 1$ GeV) the first term in Eq. 9.12, due to conventional oscillations, dominates, and neutrinos oscillate as in vacuum;
- at intermediate energies ($1 \text{ GeV} \lesssim E \lesssim 100$ GeV) the matter term dominates, pinning the electron flavor and stopping it to participate to the oscillations; in this case there will only be conventional oscillations restricted to the μ and τ flavor;
- at higher energies ($100 \text{ GeV} \lesssim E$) the wavelength for conventional oscillations becomes larger than the diameter of the Earth, so they become irrelevant for upgoing atmospheric neutrinos; in the standard scenario there are therefore no oscillations;
- depending on the value of γ (meaning the largest among γ_{21} and γ_{31}), the wavelength for VEP oscillations can become smaller than the Earth diameter $2R_{\oplus}$ at an energy of the order $E \sim \frac{1}{4R_{\oplus}\gamma\phi} \sim 8.3 \text{ TeV} \left(\frac{\gamma\phi}{10^{-27}}\right)^{-1}$. At these energies the matter effect is still dominant, meaning that the VEP oscillations will only be active between the μ and τ flavors.

In principle for energies even higher the VEP effect will start to dominate even over the matter effect: however, we will see that these values of γ can already be excluded. For this reason, in this section we focus on the last condition in this list. In this case we can simply neglect the electron flavor, since electron neutrinos do not participate to the oscillations. Furthermore, since the gravitational potential from the Great Anomaly is essentially constant even over the length scale of the Solar System, both the terms of conventional and VEP oscillations in Eq. 9.12 are constant. The problem therefore reduces to a simple two-flavor oscillation in vacuum with the additional presence of VEP oscillations. For the results shown in this work we use this approximation, after having explicitly verified it for some benchmark cases against the numerical solution of the full system in Eq. 9.12

9.2.2 Statistical analysis

We now describe the IceCube data samples analyzed in order to draw bounds on VEP. This strategy was first followed, to our knowledge, in Ref. [449]. The data samples analyzed in this work had been collected by IceCube in its first stages, namely IC40 and IC79, with only 40 and 79 strings operating respectively. Furthermore, for IC79 the effective areas had not been released by the collaboration, so that they were obtained using a scaling from the ones of IC40.

In this work we provide an updated analysis using the recently released IceCube data relative to more than 6 years of operation in the full IC86 mode with 86 operating strings. We focus on the IC79 data sample after one year of observation and on the IC86 data sample in 2011, hereby denoted as IC86-11: both these data samples have been released in Ref. [455]. IceCube has also released in Ref. [456] six years of data-taking in the full IC86 configuration: we will refer to this data set as IC86-12/18. All three data samples correspond to track events identified by IceCube, allowing for a rather precise angular reconstruction; the energy reconstruction is less accurate, but there is no drawback to our study since we will only need the total number of events over the entire energy range of the experiment. An improvement over this method of analysis focusing on the angular information only has been proposed in Ref. ??, where an energy and angular binned analysis has been conducted on a more restricted IceCube data sample.

Since the data released refer only to tracks, and therefore to muon neutrinos⁴, VEP mainly causes the conversion of some of the atmospheric muon neutrinos into tau neutrinos, and therefore it reduces the number of observed events. The reduction depends on the zenith angle with which the neutrino reaches the detector, because of the different path length traversed, and on the energy, because the VEP effects are more important at high energies. We emphasize again however that we integrate over all observed neutrino energies. The signature we look for is therefore an angular-dependent decrease in the observed number of events compared to the theoretical expectations. The non-observation of this signature allows us to constrain the strength of the VEP interaction.

The three data samples of IC79, IC86-11 and IC86-12/18 are composed respectively of 48362, 61313, and 760923 upgoing neutrino events with a zenith angle between 90° and 180° . Since we are interested in the angular distribution, for each data sample we group the data in ten bins in $\cos\theta$, where θ is the zenith angle, from 0 to -1 (upgoing neutrinos come from below the detector). The expected number of events in each bin and in an observation time T , as a function of γ_{21} and γ_{31} , is

$$N_i^{\text{th}}(\gamma_{21}, \gamma_{31}) = \int dE \int_{\cos\theta_i}^{\cos\theta_{i+1}} d\cos\theta 2\pi \Phi_\mu(\cos\theta, E) P_{\mu\mu}(\cos\theta, E, \gamma_{21}, \gamma_{31}) A_{\text{eff}}(\cos\theta, E) T, \quad (9.14)$$

where A_{eff} is the effective area for the experiment of interest, provided for IC79, IC86-11, and IC86-12/18 by IceCube together with the corresponding data set, Φ_α is the atmospheric flux of muon neutrinos and antineutrinos (see Ref. [457]). T is respectively of 316, 333, and 2198.2 days for IC79, IC86-11, and IC86-12/18. Finally, $P_{\mu\mu}(\cos\theta, E, \gamma_{21}, \gamma_{31})$ is the survival probability of muon neutrinos in the two-flavor scenario described in the previous subsection. We integrate over the entire energy range from 100 GeV to 100 TeV. At the very highest energies in this range a contamination from astrophysical neutrinos is expected: however, these are much less than the atmospheric neutrinos over the entire energy range (IceCube has detected around 100 astrophysical events, whereas the data sample analyzed here contains over 10000 events). For the same reason, the introduction of a component from the prompt decay of charm also does not change our results: we have verified this explicitly modeling this component as in Ref. [458].

⁴We neglect a possible small contamination of track events from tau neutrinos.

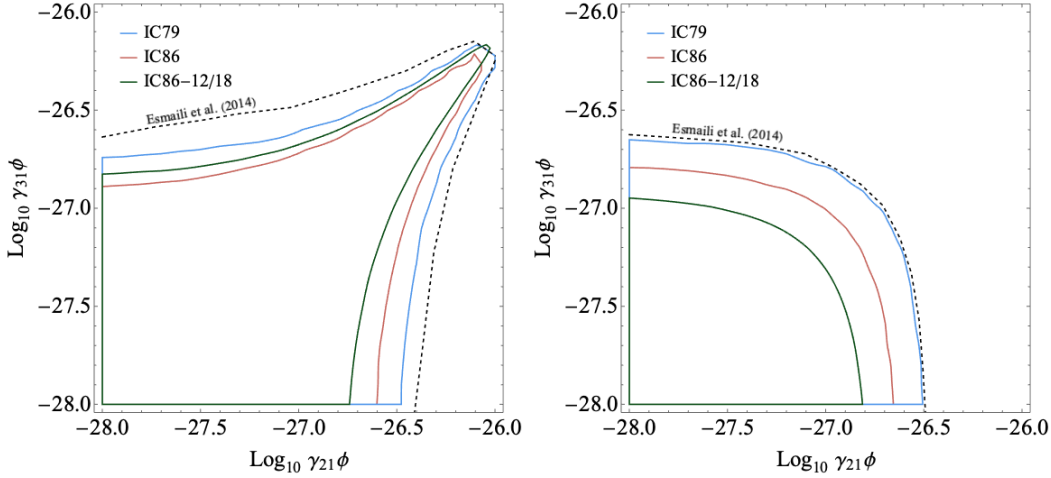


Figure 9.1: Allowed regions at 90% confidence level in the $\gamma_{21} - \gamma_{31}$ plane for the IC79, IC86-11 and IC86-12/18 dataset shown in blue, orange and green respectively for the VEP direct (left) and inverse (right) ordering scenario. The allowed region is within the contours. The black dashed curve is the 90% confidence level exclusion contour obtained in Ref. [449].

Having determined the theoretically expected number of events, we compare this with the experimental data using a maximum likelihood analysis for each data sample: the chi-squared function, following Ref. [449], is written as

$$\chi^2(\gamma_{21}\phi, \gamma_{31}\phi, \alpha, \beta) = \sum_i \frac{[N_i^{\text{data}} - \alpha(1 + \beta(0.5 + \cos\theta))N_i^{\text{data}}]^2}{\sigma_{i,\text{stat}}^2 + \sigma_{i,\text{sys}}^2} + \frac{(1 - \alpha)^2}{\sigma_\alpha^2} + \frac{\beta^2}{\sigma_\beta^2}, \quad (9.15)$$

where α and β account for the systematic uncertainties on the normalization and the angular distribution respectively of the atmospheric flux and N_i^{data} are the number of events per bin; the average values of α and β are respectively 1 and 0 and the uncertainties on these values $\sigma_\alpha = 0.24$ and $\sigma_\beta = 0.04$ [457]. We consider a statistical uncertainty given by the Poisson estimate $\sigma_{i,\text{stat}} = \sqrt{N_i^{\text{data}}}$ and a systematic uncertainty $\sigma_{i,\text{sys}} = fN_i^{\text{th}}$. The systematic uncertainty is a crucial point of this analysis: since IceCube provides no independent estimate for it, we use a value for f which guarantees agreement between the data and the atmospheric fluxes without VEP within 90% confidence level, similarly to the approach of Ref. [449]. We treat α and β as nuisance parameters and we marginalize over them, obtaining an effectively two-dimensional likelihood.

The sign of γ_{21} and γ_{31} is of course a free parameter of the model. However, since the conventional oscillations and the VEP oscillations dominate in separate energy ranges (for the small values of γ of interest to us), they do not interfere. Therefore, the oscillation probability is only sensitive to the relative sign between γ_{21} and γ_{31} ⁵. For this reason, we distinguish between a case of VEP direct ordering (γ_{21} and γ_{31} with the same sign) and VEP inverse ordering (γ_{21} and γ_{31} with opposite signs).

We show in Fig. [9.1] the exclusion contours at 90% confidence level in the plane $\gamma_{21}\phi - \gamma_{31}\phi$ for both the orderings of the VEP parameters. We also show the contours obtained in Ref. [449] with

⁵We do not take into account the possibility of an interference between the matter term and the VEP term: we take for granted that VEP is always subdominant to the matter term, whose effect is to block the electron neutrinos from participating to the oscillation, as discussed in the previous subsection.

the IC79 data and the effective areas available at the time.

The result depends on the value chosen for the systematic uncertainty, and a more conservative choice with a larger value of f may lead to weaker constraints: for this reason a robust result could only be obtained if an independent estimate of f were known. Nevertheless, our results show that for all data sets the constraints on VEP can be improved by even a factor of 2 compared to the previous results. A somewhat counterintuitive feature is that the constraints for IC86-12/18, with 6 years of data-taking, are comparable with the ones from IC86, corresponding to just one year of data. The reason is that the systematic uncertainty is completely dominating over the Poisson fluctuations: increasing the size of the sample leads to a proportional increase of the systematic uncertainty on it, and therefore to no significant gain of information; this behavior should be contrasted with the case of no systematic uncertainty, when the Poisson uncertainty increases only as the square root of the size sample. Based on these observations, we expect that a mere increase in the number of events by IceCube will not improve these results unless the systematic uncertainty is correspondingly reduced. These conclusions are confirmed in our subsequent work [459], which we do not discuss at length here. In this work, we show that the projected constraints obtainable with 10 years of data taking of KM3-NeT, which has a larger effective volume, do not substantially improve on the current results from IceCube. An interesting alternative to the reduction of the systematic error is proposed in Ref. [460], already mentioned before, in which the combined analysis of the zenith and energy distribution of the atmospheric events leads to a substantial improvement in the bounds obtained.

9.3 VEP effects on astrophysical neutrinos

In the previous section we have shown how atmospheric neutrinos, with energies below 100 TeV, can probe VEP. Since the VEP effects increase with energy, one might expect that astrophysical neutrinos, which have the highest measured energies, could improve these constraints. In this section we show that this is only partially true.

Before doing that, however, we must return on the question of the gravitational basis, namely the basis in which the VEP interaction is diagonal. Until now we have assumed as a benchmark case that the gravitational basis coincides with the mass basis. However, there is no a priori reason for this choice. The mass basis is in fact selected by the Yukawa couplings of neutrinos with the Higgs field, and is not preferred in determining the coupling with the gravitational field. If the gravitational basis differs from the mass basis, it will be expressed in terms of a new unitary matrix \tilde{U} , and the propagation equations become Eq. 9.13. The results given in the previous section can correspondingly change. As an extreme example, if the gravitational basis coincides with the flavor basis, the matrix \tilde{U} becomes the identity matrix. In this case propagation is diagonal in flavor space and neutrinos do not oscillate at all, so that atmospheric neutrinos above 100 GeV (when conventional oscillations are negligible) exhibit no observable effects. Mild constraints could be determined even for this choice of the gravitational basis by an analysis of the lower energy data, as in Ref. [450], since in this range the interplay between VEP and conventional oscillations, which are diagonal in the mass basis, could produce observable effects. However, these experiments can test values of $\gamma_{ij}\phi$ of the order of 10^{-24} [450], since at lower energies the effects of VEP are weaker.

Astrophysical neutrinos are an alternative for investigating these different choices of gravitational basis. Neutrinos produced in astrophysical sources propagate over long distances before reaching the Earth, and therefore could exhibit effects from VEP oscillations. To our knowledge, this possibility was first proposed in Ref. [446]. The main difficulty in using astrophysical neutrinos as a source of information is the need for a precise estimate of the intergalactic gravitational field. However, there is at least a region of the parameter space in which this need is not so stringent, and that is

the case in which VEP dominates over conventional oscillations. In this case, in fact, neutrinos are approximately subject only to VEP oscillations with a wavelength much smaller than the propagation distance⁶. As described in Sec. 2.3, when this happens the flavor composition oscillates very rapidly and only the average flavor composition is observable. The requirement that VEP dominates over conventional oscillations does not seem to be an extreme one. As discussed in Ref. 446, in fact, the gravitational potential in the Intergalactic space, mostly caused by the Great Attractor, has typical values of $\phi \sim 5 \times 10^{-6}$, comparable to those at the Earth. Since the energies are of the order of 100 TeV, or even larger, the VEP effects will dominate for $\gamma_{21}\phi, \gamma_{31}\phi \gtrsim 10^{-31}$. Under this assumption, if the fraction of neutrinos in the α -th flavor at the source is p_α^{source} , the corresponding average fraction of neutrinos after VEP oscillations is

$$p_\alpha^{\text{Earth}} = \sum_{i,\beta} |\tilde{U}_{\alpha i}|^2 |\tilde{U}_{\beta i}|^2 p_\beta^{\text{source}}. \quad (9.16)$$

If the gravitational basis coincides with the mass basis, as we have assumed in the previous section, then $\tilde{U} = U$ and the predictions of the VEP model are identical to the prediction of the Standard Model; in this case astrophysical neutrinos cannot probe VEP at all. On the other hand, for different choices of \tilde{U} the prediction of the model can differ significantly from the standard ones. We show this explicitly in the flavor triangle in Fig. 9.2, where the orange region corresponds to the flavor compositions obtained under all possible assumptions for \tilde{U} (constrained only by unitarity), assuming a pion beam at the source. This region, in the context of general unitarity bounds on flavor composition, has also been obtained in Refs. 462, 463. We highlight two regions corresponding to the cases of gravitational basis equal to the mass basis (black) or the flavor basis (green). In the first case, VEP is indistinguishable from the standard case, as discussed above, and indeed the black region is at the center of the triangle (the pion-beam flavor composition at the Earth is (1:1:1)). In the second case, VEP completely inhibits oscillations, so the flavor composition remains identical to the one at the source: the prediction is very different from the standard one in this case. We also show the exclusion contours from the most recent IceCube analysis, which shows that for some choices of \tilde{U} there is already a tension with the observed data, most notably for the green region. This tension should be interpreted as a tension between the data and a VEP with strength $\gamma_{21}\phi, \gamma_{31}\phi \gtrsim 10^{-31}$ for that choice of \tilde{U} . The comparison with the IceCube-Gen2 sensitivity shows that the constraining power of future neutrino telescopes will drastically improve, and will allow to exclude most possible choices of the gravitational basis.

This result has been deduced under the assumption of a pion-beam source. Of course the uncertainty on the flavor composition at the source introduces some difficulty in the comparison with the experimental data. However, most of the conclusions described here remain valid for all standard mechanisms of production of neutrinos. First of all, the pion-beam flavor composition is expected at least for sources with low magnetic fields, when the muons are not damped (the neutron beam is only expected at low energies). The ideal muon-damped scenario from Δ -resonance only is further disfavored by the recent observation of a Glashow resonance event 89, which requires the presence of electron antineutrinos (importantly, this argument is not changed by the presence of VEP, because it is based on the presence of antineutrinos, which would be absent in an ideal muon-damped scenario even if VEP did exist). The pion-beam assumption therefore seems to be the most reasonable one. Furthermore, the observation at 95% confidence level of a tau neutrino in IceCube 461 implies the presence of oscillations in the neutrino propagation independently of the flavor composition at the source, because the common neutrino production mechanisms produce no tau neutrinos at the

⁶Already the conventional oscillations have wavelengths much smaller than the propagation distance: if VEP oscillations are dominant, they necessarily must have the same property.

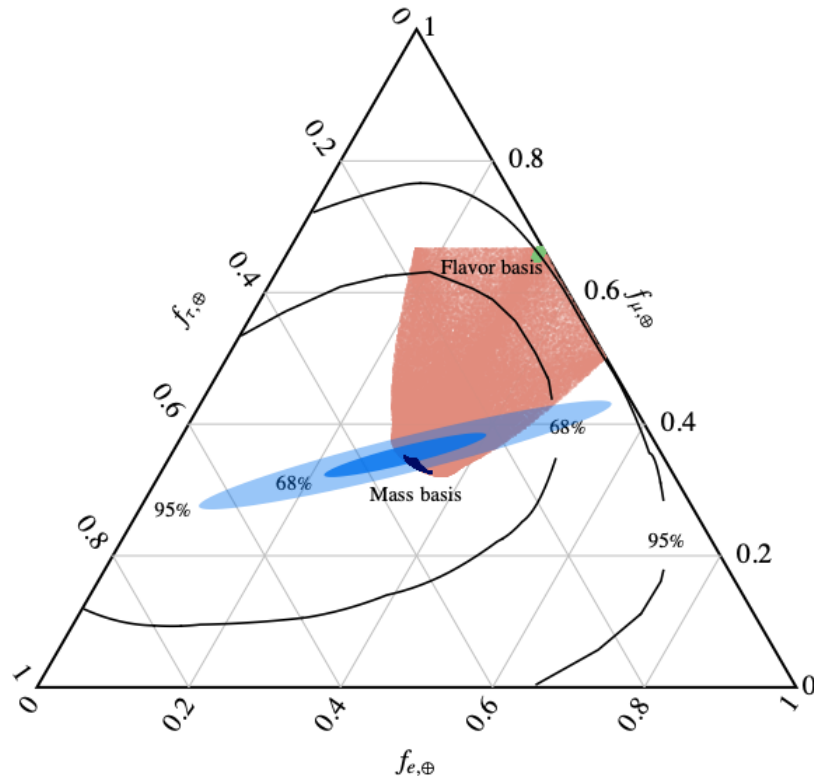


Figure 9.2: Flavor ratio at the Earth from a pion beam source after averaged VEP oscillations with $\gamma_{21}\phi, \gamma_{31}\phi > 10^{-31}$: the orange region spans the whole possibilities for the gravitational basis; the green region corresponds to the case of gravitational basis coinciding with flavor eigenstates, while the black region corresponds to the case of gravitational basis coinciding with mass eigenstates. In the latter case we vary the oscillation parameters in the 3σ intervals. The 68% and 95% confidence level obtained by IceCube [461] are shown (black contours), as well as the projected flavor sensitivity of IceCube-Gen2 [412] at 68% and 95% confidence level (blue ellipses).

source. Therefore, the conclusion that VEP diagonal in flavor basis is in tension with the IceCube data at 95% confidence level remains true independently of whether the source was pion-beam, muon-damped, muon-beam, or neutron-beam.

9.4 Discussion

The aim of this chapter was to show that high-energy neutrinos can probe BSM physics even in the gravitational sector, focusing on the case of VEP. This investigation can be achieved in two complementary ways, by looking at either atmospheric neutrinos or astrophysical neutrinos.

Atmospheric neutrinos are sensitive to VEP because of the depletion in muon neutrinos caused by VEP oscillations. Whereas their energies are lower than astrophysical neutrinos, and therefore less sensitive to VEP, the conditions in which they are produced are much better known. We showed that the data provided by IceCube are able to constrain VEP to the level of $\gamma_{21}\phi, \gamma_{31}\phi \sim 10^{-27}$. The analysis depends on the uncertainty of the data, which is dominated by a statistical component. We estimate this by requiring agreement between the data and the theoretically computed flux with no VEP. While an independent estimate of the systematic uncertainty would give robustness to the results, this methodology seems to be a reasonably conservative one to determine the constraints on the model. We find that the uncertainty is dominated by the systematic component. Therefore, a substantial improvement of this result with more data seems unlikely unless the systematic uncertainty is correspondingly reduced. Finally, we limited our analysis to a VEP model in which the gravitational basis is equal to the mass basis. The results are quite dependent on this choice, and in fact if the gravitational basis were equal to the flavor basis atmospheric neutrinos would not be able to constrain the model.

Astrophysical neutrinos are also sensitive to VEP, which can change their flavor composition. In principle this effect depends on the details of the intergalactic gravitational potential. However, at least if the VEP effect is sufficiently strong ($\gamma_{21}\phi, \gamma_{31}\phi \gtrsim 10^{-31}$), the VEP oscillations average out producing a result which depends only on the choice of the gravitational basis. We show that, depending on the latter, the flavor composition expected at Earth can be significantly different from the standard prediction. If the gravitational basis coincides with the flavor basis, VEP inhibits oscillations, so that the flavor composition at Earth is the same as at the source. This is already in a 2-sigma tension with the IceCube observations, in particular due to the detection of a tau neutrino. On the other hand, if the gravitational basis coincides with the mass basis, the flavor composition is the same as in the standard scenario. For this reason, we point out the complementarity among the two strategies using atmospheric and astrophysical neutrinos. These two methodologies work in different energy ranges and are able to probe complementary choices for the gravitational basis. The two methods together allow to constrain the parameter space for all possible choices of the gravitational basis.

Conclusions

Many of the unanswered questions of fundamental physics are connected with our ignorance of the processes at very high energies. The construction of accelerators has allowed us to reach the frontier of TeV energies, establishing the validity of the Standard Model at these energy scales. Understanding physics at higher energies may require different methods of investigation. The strategy we study in this thesis is multi-messenger astronomy, and specifically the investigation of high-energy neutrinos and gamma-rays from astrophysical sources. Thanks to the recent results obtained by neutrino and gamma-ray telescopes, this study is finally delivering the promise of clarifying our understanding of high-energy physics. In particular, we focus on multi-messenger astronomy as a tool to answer two questions: what are the dominant sources of cosmic-rays, and what physical processes beyond the Standard Model exist at high energy scales.

On the first subject, a common thread in the works presented here is the importance of a compact and detailed modeling of neutrino and gamma-ray production in astrophysical sources. In Chap. 5 we adopt the information on the gamma-ray spectra from individual starburst galaxies as a guide to infer their diffuse flux, and thus we account for the variability among different members of the source class. This is a novel strategy compared to the previous literature. We test it by comparing the IceCube and Fermi-LAT data with the starburst galaxy neutrino and gamma-ray flux, together with the contribution from other sources, namely blazars and radio-galaxies. Admittedly, this multi-component scenario cannot explain the whole of the diffuse neutrino flux, yet it clearly exemplifies the need for detailed modeling in the properties of the source. On a similar line, in Chap. 6 we emphasize the need for a compact description of the neutrino production in photohadronic sources. Our use of an effective blackbody target photon spectrum allows to describe the neutrino energy spectrum from most $p\gamma$ sources within a unified framework. The results of this paper are mainly of methodological nature, which may be helpful in systematically comparing many different classes of sources at once with the data, for example in order to extract information on BSM physics.

The study of BSM physics by means of multi-messenger astronomy is indeed the second main subject of this thesis. We have shown concrete examples of how BSM physics can induce signatures on the energy spectrum of gamma-rays and neutrinos and on the flavor composition of the latter. These include heavy decaying dark matter (Chap. 7), neutrino secret interactions (Chap. 8), and violations of the equivalence principle (Chap. 9). We show that already with current information multi-messenger astronomy can rule out part of the parameter space of all these extensions of the Standard Model. At present, we find no significant indication from neutrino and gamma-ray astronomy of BSM physics, except for the possible explanation of the 100 TeV excess of neutrinos by heavy dark matter decay. The better strategy to disprove this possibility remains in our opinion the study of gamma-ray data on the diffuse flux.

Finally, we emphasize that the two questions which until now have been presented as unrelated, namely the sources of astrophysical particles and the physics beyond the Standard Model, are in reality strongly intertwined. Indeed, in all the studies collected in this thesis, the main difficulty

in constraining and possibly identifying BSM effects was to distinguish them from the standard neutrino and gamma-ray production, which is by itself uncertain. As an example, distinguishing BSM effects on the flavor composition of astrophysical neutrinos at Earth is difficult, given that we do not know the flavor composition with which they were produced. This degeneracy between the systematic uncertainty on the astrophysical production and the presence of BSM physics may only be broken by an increased knowledge of the astrophysical sources. In this respect, the future neutrino telescopes, including KM3-NeT and IceCube-Gen2, and gamma-ray telescopes, including CTA and LHAASO, will provide within the next 5 to 10 years more information on the sources of astrophysical particles which can at the same time be used to identify more easily possible BSM effects. Furthermore, as we have emphasized at various places in this thesis (e.g. in Chaps. 7 and 8), the future neutrino radio-telescopes, including GRAND, IceCube-Gen2 RA, and RNO-G, will allow us to reach the frontier of the EeV energies. Besides allowing for the first time the possible identification cosmogenic neutrinos, this will dramatically push up the scale of energies at which we can test fundamental physics already within the next 10 years.

Appendix A

Second-order Fermi mechanism

In this appendix we discuss in more detail the second-order Fermi acceleration, and connect the derivation of this process with the first-order Fermi mechanism described in the text. As mentioned in Chap. 11 in the original mechanism proposed by Fermi, particles are accelerated by collisions with moving magnetic inhomogeneities, which can be schematized as macroscopic magnetic clouds. When the particle enters one of these clouds, its direction is isotropized inside it by the collisions. Let E_i be the energy of the (relativistic) particle before entering the cloud in the laboratory frame, and let U be the velocity of the cloud. After entering the cloud, the particle isotropizes in the cloud rest frame: in this frame, the energy of the particle is

$$E' = \gamma E_i (1 + U \cos \theta), \quad (\text{A.1})$$

where $\gamma = (1 - U^2)^{-1/2}$ and θ is the angle between the cloud and the particle direction. The geometry of the process is summarized in Fig. A.1.

When the particle manages to escape from the cloud, its energy in the cloud rest frame is unchanged, since the magnetic inhomogeneities are static in this frame. Its direction on the other hand will be different: let θ' be the angle between the exiting direction of the particle and the velocity of the cloud, as shown in Fig. A.1. When the particle exits the cloud, its energy in the laboratory frame can be simply obtained by a Lorentz transformation as

$$E_f = \gamma^2 E_i (1 + U \cos \theta)(1 + U \cos \theta'). \quad (\text{A.2})$$

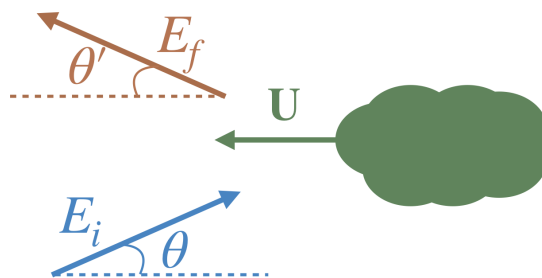


Figure A.1: Scheme of the collision between the particle and the cloud: quantities before (after) the impact are shown in blue (red); quantities referring to the cloud are shown in green.

Here it is important to observe that θ is the angle between the initial velocity and the cloud velocity in the laboratory frame, whereas θ' is the angle between the final velocity and the cloud velocity in the cloud rest frame. The result depends of course on the angles θ and θ' . Two assumptions are typically made at this point in the literature: in the first one, it is assumed that the particle is simply reflected by the cloud like a solid wall in the cloud rest frame. Due to relativistic aberration, this does not mean trivially that $\theta' = \theta$: rather, we should use the velocity aberration formula to obtain

$$\cos \theta' = \frac{\cos \theta + U}{1 + U \cos \theta}. \quad (\text{A.3})$$

Substituting this expression in Eq. [A.2](#), we find

$$E_f = \gamma^2 E_i (1 + 2U \cos \theta + U^2). \quad (\text{A.4})$$

The initial angle θ can itself take any value: to determine its probability distribution, we observe that the direction of each particle is isotropically distributed in the laboratory frame, and the rate of collisions is proportional to the quantity $\sqrt{|\mathbf{v}_p - \mathbf{U}|^2 - |\mathbf{v}_p \times \mathbf{U}|^2}$ [\[19\]](#), where \mathbf{v}_p is the particle velocity. By substitution we find that the rate of collisions is proportional to $(1 + U \cos \theta)$, and thus the distribution probability of θ should be taken as

$$P(\cos \theta) d \cos \theta = (1 + U \cos \theta) \frac{d \cos \theta}{2}, \quad (\text{A.5})$$

where the factor of 2 guarantees the correct normalization. By averaging the energy and its square in Eq. [A.4](#) we obtain the mean value of $\delta E = E_f - E_i$ and δE^2 : for simplicity, we report the result to second order in the small velocity U

$$\langle \delta E \rangle = \frac{8U^2 E_i}{3}, \quad \langle \delta E^2 \rangle = \frac{4U^2 E_i^2}{3}. \quad (\text{A.6})$$

Therefore we reach the conclusion that particles feel an average energy increase which is of second order in the cloud velocity, as already predicted by simpler arguments in Chap. [1](#). Furthermore, there is a mean square increase in the energy which is analogous to a random walk in the energy space: the meaning of this term is the same as the reacceleration term discussed in Chap. [2](#).

A different assumption for θ' can be found in the literature, according to which the particle is not reflected in the solid-wall approximation: rather, its direction is isotropized in the cloud rest frame, so that $\cos \theta'$ is a stochastic variable independent of θ and uniformly distributed. The distribution for θ is the same as in the previous case. The calculations proceed in the same way, leading to the final result

$$\langle \delta E \rangle = \frac{4U^2 E_i}{3}, \quad \langle \delta E^2 \rangle = \frac{2U^2 E_i^2}{3}. \quad (\text{A.7})$$

In both scenarios we reach the conclusion that the energy of the particle increases on average at each collision. To determine the final spectrum of the accelerated particles, we assume that the particles collide with the clouds with a rate τ_{coll}^{-1} . Furthermore, we assume that the particles have a probability τ_{esc}^{-1} per unit time of escaping from the galaxy in which they are contained.

Let us call ξ the average energy gain at each collision, namely $\xi = \langle \delta E \rangle / E_i$: in the second scenario, which we assume for definiteness, $\xi = \frac{4U^2}{3}$. After n collisions the particle reaches on average an energy $E_i(1 + \xi)^n$. In order for a particle to be accelerated to an energy larger than E , it must have undergone a number of collisions larger than

$$n > \bar{n}(E) = \frac{\log(E/E_i)}{\log(1 + \xi)}. \quad (\text{A.8})$$

The probability of being in the galaxy after $\bar{n}(E)$ collisions, which take on average a time $\bar{n}(E)\tau_{\text{coll}}$, is $e^{-\bar{n}(E)\tau_{\text{coll}}/\tau_{\text{esc}}}$. Therefore the number of particles with energy larger than E , after substituting Eq. [A.8](#), is

$$P(> E) \propto \left(\frac{E}{E_i}\right)^{-\frac{\tau_{\text{coll}}}{\tau_{\text{esc}} \log(1+\xi)}} \simeq \left(\frac{E}{E_i}\right)^{-\frac{\tau_{\text{coll}}}{\tau_{\text{esc}} \xi}}. \quad (\text{A.9})$$

Finally, the number of particles with energy between E and $E+dE$ is proportional to the differential of this probability, so that the spectral distribution of accelerated cosmic-rays is

$$\frac{dN}{dE} \propto \left(\frac{E}{E_i}\right)^{-\frac{\tau_{\text{coll}}}{\tau_{\text{esc}} \xi} - 1}. \quad (\text{A.10})$$

Thus we find that the mechanism naturally generates a power-law spectrum (which is natural given the lack of an energy scale in the problem) with a spectral index

$$\gamma = 1 + \frac{3\tau_{\text{coll}}}{4U^2\tau_{\text{esc}}}. \quad (\text{A.11})$$

The spectral index depends both on the confining time of the cosmic-rays in the galaxy and on the rate of collision with the clouds. It is true that if $\tau_{\text{coll}} \sim 10^7$ s (as one expects for collisions with a mean free path of order 0.1 pc), $\tau_{\text{esc}} \sim 10^7$ y and $U \sim 10^{-4}$ the second term is indeed of order 1, but the dependence on the precise values is too strong to give a definite prediction for the spectral index. If this were the real explanation for cosmic-ray acceleration, one would expect a rather large variability for the spectral index of cosmic-rays accelerated by different sources. Therefore the main failure of the second-order process is that it is not able to explain the ubiquitous presence of spectral indices close to 2 from many different astrophysical sources.

On the other hand, if the cloud above is replaced with a shock, we obtain again the results discussed in Chap. [1](#) for diffusive shock acceleration. In this case the probability distribution both for θ and for θ' is the same, and is

$$P(\cos \theta) = 2\Theta[\cos \theta] \cos \theta d \cos \theta, \quad (\text{A.12})$$

since the component of the particle velocity directed toward the plane shock is simply $\cos \theta$. The Heaviside theta accounts for the fact that only particles directed towards the shock can collide with it; the factor of 2 normalizes the distribution. Therefore $\langle \cos \theta \rangle = \langle \cos \theta' \rangle = 2/3$, and substituting in Eq. [A.2](#) we find

$$\delta E = \frac{4}{3} U E_i. \quad (\text{A.13})$$

This is indeed the same result we obtained in Chap. [1](#). Furthermore, as we have shown there, the probability that a particle escape downstream during one cycle of acceleration is $P_{\text{escape}} = 4u_2$ (see Eq. [1.8](#)). Therefore $\tau_{\text{esc}}^{-1} = 4u_2\tau_{\text{coll}}$. Substituting $u_2 = U/4$ we indeed find a spectral index $\gamma = 2$, in agreement with the results obtained in Chap. [1](#) by different means. The universality of this value depends upon the precise cancellation between the velocity dependence in the efficiency of acceleration and in the escape probability: this is achieved only for very strong shocks for which the relation $u_2 = U/4$ is verified.

Appendix B

Analytical solutions for cosmic-ray acceleration

In this appendix we describe both the stationary and a non-stationary solution to the transport equation for cosmic-rays near a shock wave (Eq. [1.5](#)). Let us start with the stationary solution.

Since $\nabla \cdot \mathbf{u}$ is non-vanishing only on the shock front, let us solve separately the equation on the two sides of the shock. In the upstream region the solution can be taken as

$$f_1(z, p) = f_u(p) + (\delta f(p) - f_u(p))e^{-\frac{u_1 z}{D}}, \quad (\text{B.1})$$

whereas in the downstream region the finiteness of the solution and the continuity at the shock require

$$f_2(z, p) = \delta f(p). \quad (\text{B.2})$$

In writing these two solutions, we have automatically taken into account the condition of continuity of $f(p)$ at the interface $z = 0$. The derivative $\partial f / \partial z$, on the other hand, is not necessarily continuous: to determine the corresponding boundary condition, we integrate the transport equation Eq. [1.5](#) over an infinitesimal interval around $z = 0$. In this way we obtain the condition

$$\frac{1}{3}(u_1 - u_2)p \frac{d\delta f}{dp} = u_1 [\delta f(p) - f_u(p)]. \quad (\text{B.3})$$

This is a linear ordinary differential equation. To fix the boundary condition, we note that $f_u(p)$ represents the particles infinitely far away from the shock in the upstream region, namely those particles that have not been accelerated yet. Correspondingly, $\delta f(p)$ represents the particles that have already crossed the shock, and indeed it is the only part that survives in the downstream region. Therefore, we impose as a boundary condition that $\delta f(0) = 0$, since particles can only be accelerated by the shock and therefore no particles can have zero momentum after crossing it. With this condition Eq. [B.3](#) admits a unique solution

$$\delta f(p) = \frac{3u_1}{u_1 - u_2} \int_0^p \frac{dp'}{p'} f_u(p') \left(\frac{p'}{p}\right)^{\frac{3u_1}{u_1 - u_2}}. \quad (\text{B.4})$$

This is the distribution function of the particles that have already been accelerated. The result we have obtained coincides with the results used in Chap. [1](#).

While this stationary solution has the advantage of simplicity, it suffers from a series of shortcomings that have been highlighted in Chap. [1](#) in particular, it predicts the presence of an infinite number of particles, some of which are accelerated to infinitely large energies. For this reason, we now discuss a time-dependent solution to the full equation

$$\frac{\partial f}{\partial t} + u(z)\frac{\partial f}{\partial z} + \frac{1}{3}(u_1 - u_2)\delta(z)p\frac{\partial f}{\partial p} = \frac{\partial}{\partial z} \left(D \frac{\partial f}{\partial z} \right). \quad (\text{B.5})$$

In doing this, for simplicity we assume that D is a constant independent of p . This assumption is not realistic, and we will later discuss how the results change if D depends on the energy: for the moment, we only notice that the stationary solution we have found above does not depend on this assumption^{[1](#)}.

As an initial condition for Eq. [B.5](#), we adopt the following expression [464](#)

$$f(t = 0, z, p) = \delta(z)\delta(p - p_0). \quad (\text{B.6})$$

In other words, we follow the evolution of a particle initially placed at the shock with an energy p_0 .

As a first step we perform a one-sided Fourier transform with respect to time

$$F(\omega, z, p) = \int_0^{+\infty} f(t, z, p)e^{-i\omega t} dt. \quad (\text{B.7})$$

Furthermore, we introduce the Mellin transform with respect to the variable p

$$\tilde{F}(\omega, z, s) = \int_0^{+\infty} p^{s-1} F(\omega, z, p) dp. \quad (\text{B.8})$$

In terms of \tilde{F} the transport equation becomes

$$i\omega\tilde{F} + u(z)\frac{\partial \tilde{F}}{\partial z} - \frac{s}{3}(u_1 - u_2)\delta(z)\tilde{F} = D\frac{\partial^2 \tilde{F}}{\partial z^2} + \delta(z)p_0^{s-1}. \quad (\text{B.9})$$

We follow the same approach as above and solve this equation separately on the two sides of the shock, obtaining a preliminary solution which is finite everywhere (on which we still have to impose the boundary condition at the shock)

$$\tilde{F}(\omega, z, s) = \alpha(s) \begin{cases} e^{k_{1+}z}, & z < 0 \\ e^{k_{2-}z}, & z > 0 \end{cases} \quad (\text{B.10})$$

where

$$k_{a\pm} = \frac{u_a \pm \sqrt{u_a^2 + 4i\omega D}}{2D}. \quad (\text{B.11})$$

We obtain the boundary condition by integrating Eq. [B.9](#) over a small interval in z surrounding the shock: in this way we find the function $\alpha(s)$ as

$$\alpha(s) = \frac{p_0^{s-1}}{D(k_{1+} - k_{2-}) - \frac{s}{3}(u_1 - u_2)}. \quad (\text{B.12})$$

¹In fact, the stationary solution does not depend on the diffusion coefficient at all: this is one of the reasons that prompt us to the study of a time-dependent solution.

The inverse Mellin transform can now be performed to recover the distribution in terms of the particle momentum

$$F(\omega, z, p) = \int_{-i\infty}^{+i\infty} \frac{ds}{2\pi i} \tilde{F}(\omega, z, s) p^{-s}. \quad (\text{B.13})$$

The integral in s can be easily performed by contour integration, and the only singularity lies in $s = \frac{3D(k_{1+} - k_{2-})}{u_1 - u_2}$, on the right of the integration path². The final result is

$$F(\omega, z, p) = \frac{3}{(u_1 - u_2)p_0} \left(\frac{p}{p_0}\right)^{-\frac{3D}{u_1 - u_2}(k_{1+} - k_{2-})} \begin{cases} e^{k_{1+}z}, & z < 0 \\ e^{k_{2-}z}, & z > 0 \end{cases} \quad (\text{B.14})$$

The inverse Fourier transform to obtain the original function $f(t, z, p)$, unfortunately, cannot be performed analytically, due to the presence of the square roots in the definition of $k_{a\pm}$. However, important information can be derived from this expression. Let us regard $f(t, z, p)$ as a (non-normalized) probability distribution for the time variable: in other words, $f(t, z, p)$ is the probability that a particle reaches a position z and a momentum p in the time interval between t and $t + dt$. Then by definition $F(\omega, z, p)$ is the characteristic function of this distribution, and its derivatives are the moments of the distribution. In particular, if we call $\langle t \rangle(z, p)$ the mean time after which a particle is expected to be at position z with impulse p , we have

$$\langle t \rangle(z, p) = \frac{i}{F(0, z, p)} \left[\frac{\partial F(\omega, z, p)}{\partial \omega} \right]_{\omega=0}. \quad (\text{B.15})$$

For simplicity, let us restrict to the case $z = 0$ and perform the derivative: we obtain that the mean time after which a particle is expected to reach momentum p is

$$\langle t \rangle(p) = \frac{3D}{u_1 - u_2} \log\left(\frac{p}{p_0}\right) \left(\frac{1}{u_1} + \frac{1}{u_2}\right). \quad (\text{B.16})$$

This is our final result, from which we see that in a finite time particles cannot reach an arbitrarily large energies. In particular, in our model with an energy-independent diffusion coefficient, the time required for acceleration grows logarithmically with the energy. In a very small interval of time we can obtain the infinitesimal increase in energy by differentiating Eq. [B.16](#) (we suppress the $\langle t \rangle$ notation for simplicity)

$$\frac{dp}{dt} = \frac{u_1 - u_2}{3D \left(\frac{1}{u_1} + \frac{1}{u_2}\right)} p. \quad (\text{B.17})$$

Whereas the result in Eq. [B.16](#) is only true for D independent of the energy, this Eq. [B.17](#) approximately holds for a generic dependence of D on the energy, since over small energy intervals the diffusion coefficient can be considered approximately constant. From this equation we easily recover the estimate for the maximum energy of cosmic-rays after a finite time that was obtained in Chap. [I](#).

²For this reason the integral gets a minus sign.

Appendix C

Formal treatment of cosmic-ray propagation

In this section we estimate the diffusion coefficient of cosmic-rays in turbulent magnetic fields in a more rigorous way: we adopt the so-called quasi-linear approximation [46], in which the turbulent field is assumed weaker than the regular component. Let us denote by $f(\mathbf{r}, \mathbf{v}, t)$ the phase-space distribution of the cosmic-rays, and let us assume that they move in a static magnetic field. This can be realized by passing to a frame comoving with the magnetohydrodynamic waves, but more simply, as we have observed in Sec. 1.1, the velocity of the Alfvén waves are non-relativistic, so they are approximately at rest compared with cosmic-rays. The propagation of the particles is described by the Vlasov equation, in which for simplicity we neglect the time dependence

$$\mathbf{v} \cdot \nabla f + \frac{q}{E} [\mathbf{v} \times (\mathbf{B} + \delta\mathbf{B}(\mathbf{r}))] \cdot \frac{\partial f}{\partial \mathbf{v}} = 0, \quad (\text{C.1})$$

where \mathbf{B} is the regular field directed along z . In the spirit of the quasi-linear theory, we separate the distribution function into a regular part and a fluctuating part, arising from the fluctuations of the turbulent field: $f = \langle f \rangle + \delta f$. We substitute this expression in Eq. C.1 and perform an ensemble average over the fluctuating field to obtain

$$\mathbf{v} \cdot \nabla \langle f \rangle + \frac{q}{E} [\mathbf{v} \times \mathbf{B}] \cdot \frac{\partial \langle f \rangle}{\partial \mathbf{v}} = - \left\langle \frac{q}{E} [\mathbf{v} \times \delta\mathbf{B}] \cdot \frac{\partial \delta f}{\partial \mathbf{v}} \right\rangle. \quad (\text{C.2})$$

On the other hand, by taking only the fluctuating terms in Eq. C.1 and neglecting higher order terms, we find an equation for δf

$$\mathbf{v} \cdot \nabla \delta f + \frac{q}{E} [\mathbf{v} \times \mathbf{B}] \cdot \frac{\partial \delta f}{\partial \mathbf{v}} = - \frac{q}{E} [\mathbf{v} \times \delta\mathbf{B}] \cdot \frac{\partial \langle f \rangle}{\partial \mathbf{v}}. \quad (\text{C.3})$$

Our strategy is therefore to obtain the fluctuating part in terms of the regular one from Eq. C.3 and replace it back in Eq. C.2 to obtain an equation in terms of the regular part alone. Let us decompose the turbulent field in its spatial Fourier components $\delta\mathbf{B} = \sum_{\mathbf{k}} \mathbf{B}_{\mathbf{k}} e^{i\mathbf{k} \cdot \mathbf{r}}$. The cylindrical symmetry suggests a parameterization in terms of the pitch-angle between the velocity and the axis z , and we denote by μ its cosine. Furthermore, we let ϕ be the azimuthal angle of the velocity around the axis z , so that $v_z = v\mu$, $v_x = v\sqrt{1-\mu^2} \cos \phi$, $v_y = v\sqrt{1-\mu^2} \sin \phi$, where v is the modulus of the velocity. We adopt a similar parameterization for the wave vector \mathbf{k} , writing $k_x = k_{\perp} \cos \psi$,

$k_y = k_\perp \sin \psi$. Decomposing Eq. [C.3](#) into its Fourier components¹ we obtain

$$ik_z v \mu \delta f_{\mathbf{k}} + ik_\perp v \sqrt{1 - \mu^2} \cos(\phi - \psi) \delta f_{\mathbf{k}} - \frac{qB}{E} \frac{\partial \delta f_{\mathbf{k}}}{\partial \phi} = \frac{q \delta B_{z\mathbf{k}}}{E} \frac{\partial \langle f \rangle}{\partial \phi} \quad (\text{C.4})$$

$$- \frac{q(\delta B_{x\mathbf{k}} \cos \phi + \delta B_{y\mathbf{k}} \sin \phi)}{E} \frac{\partial \langle f \rangle}{\partial \phi} \mu - \frac{q(\delta B_{y\mathbf{k}} \cos \phi - \delta B_{x\mathbf{k}} \sin \phi)}{E} \frac{\partial \langle f \rangle}{\partial \mu} \sqrt{1 - \mu^2}.$$

Since the regular magnetic field is assumed to be large, the Larmor frequency is correspondingly large and thus the variable ϕ changes very rapidly in time over the trajectory of a particle: for this reason, we are only interested in the average of $\langle f \rangle$ over ϕ . This allows us to neglect the terms containing $\frac{\partial \langle f \rangle}{\partial \phi}$. Eq. [C.4](#) can now be used to obtain $\delta f_{\mathbf{k}}$: we outline the steps of the calculation,

omitting the intermediate passages. After redefining $\delta f_{\mathbf{k}} = \chi_{\mathbf{k}} e^{i \frac{Ek_\perp v \sqrt{1 - \mu^2} \sin(\phi - \psi)}{qB}}$, we expand the function $\chi_{\mathbf{k}}$ as a Fourier series in ϕ and determine the Fourier coefficients from Eq. [C.4](#). The final result, expressed in terms of $\chi_{\mathbf{k}}$, is

$$\chi_{\mathbf{k}} = - \sum_l e^{-il\phi} \frac{\sqrt{1 - \mu^2} \frac{\partial \langle f \rangle}{\partial \mu}}{2B \left(l + \frac{Ek_z v \mu}{qB} - i\varepsilon \right)} \quad (\text{C.5})$$

$$\left[\delta B_{-\mathbf{k}} e^{i(l+1)\psi} J_{l+1} \left(\frac{Ek_\perp v \sqrt{1 - \mu^2}}{qB} \right) - \delta B_{+\mathbf{k}} e^{i(l-1)\psi} J_{l-1} \left(\frac{Ek_\perp v \sqrt{1 - \mu^2}}{qB} \right) \right],$$

with the notation $\delta B_{\pm\mathbf{k}} = \delta B_{x\mathbf{k}} \pm iB_{y\mathbf{k}}$. The ε factor is introduced in the denominator with the criterion that the turbulent magnetic field is inserted very slowly with time (see Ref. [45](#)). Finally, this result can be used in Eq. [C.2](#) and averaged over the variable ϕ , consistently with our observation that the function changes in ϕ with the Larmor frequency, which is very large. The result is

$$\mathbf{v} \cdot \nabla \langle f \rangle + \frac{q}{E} [\mathbf{v} \times \mathbf{B}] \cdot \frac{\partial \langle f \rangle}{\partial \mathbf{v}} = \frac{\partial}{\partial \mu} \left[D_{\mu\mu} \frac{\partial \langle f \rangle}{\partial \mu} \right], \quad (\text{C.6})$$

where

$$D_{\mu\mu} = \frac{qB(1 - \mu^2)\pi}{4E} \sum_l \delta \left(l + \frac{k_z v \mu E}{qB} \right) \left[\frac{\langle \delta B_+ \delta B_- \rangle}{B^2} (J_{l+1}^2 \left(\frac{Ek_\perp v \sqrt{1 - \mu^2}}{qB} \right) + J_{l-1}^2 \left(\frac{Ek_\perp v \sqrt{1 - \mu^2}}{qB} \right)) \right. \quad (\text{C.7})$$

$$\left. - \left(\frac{\langle \delta B_-^2 \rangle}{B^2} e^{2i\psi} + \frac{\langle \delta B_+^2 \rangle}{B^2} e^{-2i\psi} \right) J_{l+1} \left(\frac{Ek_\perp v \sqrt{1 - \mu^2}}{qB} \right) J_{l-1} \left(\frac{Ek_\perp v \sqrt{1 - \mu^2}}{qB} \right) \right].$$

The presence of the delta function shows that indeed the scattering happens resonantly, and that there are infinite resonances when the frequency felt by the particle $k_z v \mu$ is any integral multiple of the cyclotron frequency. This result is generally simplified by using the magnetostatic slab model, in which the turbulence is assumed to vary only in the direction of the regular magnetic field. The ensemble average over the magnetic field is performed assuming that $\langle \delta B_{x\mathbf{k}} \delta B_{y\mathbf{k}'} \rangle = 0$, $\langle \delta B_{x\mathbf{k}} \delta B_{x\mathbf{k}'} \rangle = \langle \delta B_{y\mathbf{k}} \delta B_{y\mathbf{k}'} \rangle = u_{\mathbf{k}} \delta_{\mathbf{k}, \mathbf{k}'} B^2 / 2$; according to the latter equation, $u_{\mathbf{k}}$ measures the ratio between the energy in the turbulent and in the regular magnetic field. The final result is

$$D_{\mu\mu} = \frac{\pi qB(1 - \mu^2)}{4E} \sum_{\mathbf{k}} \frac{qB}{Ev\mu} u_{\mathbf{k}} \left(\delta \left(k_z + \frac{qB}{Ev\mu} \right) + \delta \left(k_z - \frac{qB}{Ev\mu} \right) \right). \quad (\text{C.8})$$

¹We also use the fact that $\langle f \rangle$ varies over length scales much longer than $\delta \mathbf{B}$, so that we can assume it approximately constant.

This coefficient describes the diffusion in pitch-angle: to this diffusion there is associated a corresponding diffusion in physical space. To obtain this, we study the flux of particles arising in response to a small spatial gradient, assuming that the phase-space distribution (we neglect the $\langle \rangle$ from now on: we will always refer to the distribution ensemble averaged and averaged over the angle ϕ) can be decomposed as a spatially dependent isotropic part f_0 and a small anisotropic part arising in response to the gradient δf . Then Eq. [C.6](#) becomes

$$v\mu \frac{\partial f_0}{\partial z} = \frac{\partial}{\partial \mu} \left(D_{\mu\mu} \frac{\partial \delta f}{\partial \mu} \right). \quad (\text{C.9})$$

This equation can be integrated over μ to obtain

$$D_{\mu\mu} \frac{\partial \delta f}{\partial \mu} = -\frac{v}{2}(1-\mu^2) \frac{\partial f_0}{\partial z}. \quad (\text{C.10})$$

This anisotropic perturbation produces a current of particles which, when averaged over the angle, is $j = \int \frac{d\mu}{2} v\mu \delta f$. Integrating by parts, and using Eq. [C.10](#), this current can be expressed in the usual diffusion form as

$$j = -D \frac{\partial f_0}{\partial z}, \quad (\text{C.11})$$

where

$$D = \frac{v^2}{8} \int_{-1}^{+1} d\mu \frac{(1-\mu^2)^2}{D_{\mu\mu}}. \quad (\text{C.12})$$

This is our final result for the spatial diffusion coefficient of cosmic-rays in the turbulent magnetic fields. It is easy to see by explicit substitution that the order of magnitude is indeed the one predicted in Sec. [2.1](#).

Appendix D

Derivation of the thermal model

in Chap. 6 we showed that the neutrino spectrum produced in $p\gamma$ sources with a generic target photon spectrum can be reproduced quite accurately by replacing the target photons with a blackbody target. The mapping between the original photon spectrum and the temperature of the effective blackbody spectrum was provided, together with a sketch of the derivation. In this appendix, we provide more details on the derivation.

As a first step, let us recall some properties of $p\gamma$ interactions. In $p\gamma$ collisions the interaction can be regarded as a superposition of various contributions, which have been listed in Chap. 1. The contributions which mainly determine the shape and flavor composition of the neutrino spectrum are the Δ resonance and the multi-pion interaction. Indeed, these give the largest contribution to the interaction rate [30]. Let us denote by IT the different interaction types, which in our case are Δ resonance and multi-pion interaction. For both interaction types we can assume that each $p\gamma$ collision produces on average M_π^{IT} pions (the multiplicity), with an average energy $E'_\pi = \chi_\pi^{\text{IT}} E'_p$. As in Chap. 6, we use primes to refer to quantities in the comoving frame. The interaction rate for a proton, namely the number of collisions of a proton per unit time with a given interaction time, is given by

$$\Gamma^{\text{IT}}(E'_p) = \int d\varepsilon'_\gamma \int d\cos\theta \frac{1 - \cos\theta}{2} n(\varepsilon'_\gamma, \cos\theta) \sigma^{\text{IT}}(E'_{\text{CM}}). \quad (\text{D.1})$$

Here ε'_γ is the photon energy, θ is the angle between the proton and the photon direction, $n(\varepsilon'_\gamma, \cos\theta)$ is the photon number density, $E'_{\text{CM}} = \sqrt{\varepsilon'_\gamma E'_p (1 - \cos\theta)}$ is the center-of-mass energy, and $\sigma^{\text{IT}}(E'_{\text{CM}})$ is the cross section for the given interaction type. For an isotropic photon distribution, the angle integration can be performed once the cross-section for the interaction type is given. This allows to rewrite the interaction rate as

$$\Gamma^{\text{IT}}(E'_p) = \int d\varepsilon'_\gamma n(\varepsilon'_\gamma) f_{\text{IT}}\left(\frac{\varepsilon'_\gamma E'_p}{m_p}\right) = \int \frac{dy}{y} [\varepsilon'_\gamma n(\varepsilon'_\gamma)]_{\varepsilon'_\gamma = \frac{ym_p}{E'_p}} f_{\text{IT}}(y), \quad (\text{D.2})$$

where the variable y is defined as $y = E'_p \varepsilon'_\gamma / m_p$, and the functions $f_{\text{IT}}(y)$ have been determined in Ref. [30] by comparison with the results of SOPHIA.

Once we know how many collisions happen per second with a given interaction type (interaction rate $\Gamma^{\text{IT}}(E'_p)$), how many pions are produced at each collision (multiplicity M_π^{IT}), and how much energy each pion carries on average (a fraction χ_π^{IT}), we can determine the pion spectrum emissivity

(number of pions emitted per unit time per unit energy) from each interaction type as

$$Q_{\pi}^{\text{IT}}(E'_p) = \frac{N_p(E'_p/\chi_{\pi}^{\text{IT}})M_{\pi}^{\text{IT}}}{\chi_{\pi}^{\text{IT}}} \Gamma^{\text{IT}} \left(\frac{E'_p}{\chi_{\pi}^{\text{IT}}} \right). \quad (\text{D.3})$$

Here $N_p(E'_p)$ is the proton number density. For the rest of this appendix we assume

$$N_p(E'_p) \propto E'_p{}^{-2} e^{-E'_p/E'_{p,\text{max}}}. \quad (\text{D.4})$$

Let us now discuss separately the behavior of the functions $f_{\text{IT}}(y)$ for the two interaction types considered here.

For the Δ resonance interaction, due to the resonant character of the scattering, the function $f_{\text{IT}}(y)$ is strongly peaked at a value of $y \simeq y_{\Delta} = 0.2$ GeV. Therefore, in Eq. [D.2](#) the target photon spectrum can be evaluated with good approximation at $y = y_{\Delta}$ and carried outside the integral. The approximation breaks down of course when the photon energy $\varepsilon'_{\gamma} = y_{\Delta} m_p / E'_p$ falls in a region in which $n(\varepsilon'_{\gamma})$ is varying very rapidly. With this approximation, the pion emissivity (times the squared energy) via Δ resonance interaction depends on the energy as

$$E_{\pi}^{\prime 2} Q_{\pi}^{\Delta}(E'_{\pi}) \propto [\varepsilon'_{\gamma} n(\varepsilon'_{\gamma})]_{\varepsilon'_{\gamma} = \frac{y_{\Delta} m_p \chi_{\pi}^{\Delta}}{E'_{\pi}}} e^{-E'_{\pi}/E'_{p,\text{max}} \chi_{\pi}^{\Delta}}, \quad (\text{D.5})$$

where $\chi_{\pi}^{\Delta} = 0.22$.

For the multi-pion interaction, the scattering is not resonant and consequently $f_{\text{MP}}(y)$ does not exhibit any pronounced peak. In order to grasp the qualitative feature of the process, we can approximate this function as a constant \bar{f}_{MP} for $y \gtrsim y_{\text{MP}} = 0.5$ GeV. Therefore the interaction rate is

$$\Gamma^{\text{MP}} \left(\frac{E'_{\pi}}{\chi_{\pi}^{\text{MP}}} \right) = \bar{f}_{\text{MP}} \int_{y_{\text{MP}}}^{+\infty} \frac{dy}{y} [\varepsilon'_{\gamma} n(\varepsilon'_{\gamma})]_{\varepsilon'_{\gamma} = \frac{y m_p \chi_{\pi}^{\text{MP}}}{E'_{\pi}}} = \bar{f}_{\text{MP}} \int_{\frac{y_{\text{MP}} m_p \chi_{\pi}^{\text{MP}}}{E'_{\pi}}}^{+\infty} d\varepsilon'_{\gamma} n(\varepsilon'_{\gamma}), \quad (\text{D.6})$$

where we have already expressed it in terms of the pion energy using the fraction $\chi_{\pi}^{\text{MP}} = 0.2$. The interaction rate depends on the pion energy E'_{π} in a way that is not easy to discuss in general. However, we can understand the main features by considering the specific case where $\varepsilon'_{\gamma} n(\varepsilon'_{\gamma})$ has a single maximum at an energy $\bar{\varepsilon}'_{\gamma}$.

For low pion energies, such that $E'_{\pi} < \frac{y_{\text{MP}} m_p \chi_{\pi}^{\text{MP}}}{\bar{\varepsilon}'_{\gamma}}$, the energy $\bar{\varepsilon}'_{\gamma}$ is not contained in the integration range in Eq. [D.6](#). Therefore, the function is monotonically decreasing in the integration range and its value is determined mostly by the lower limit of integration. Assuming that $n(\varepsilon'_{\gamma})$ decreases as a power law in energy (as it typically happens), the integral can be estimated in order of magnitude as

$$\Gamma^{\text{MP}} \left(\frac{E'_{\pi}}{\chi_{\pi}^{\text{MP}}} \right) \simeq \bar{f}_{\text{MP}} [\varepsilon'_{\gamma} n(\varepsilon'_{\gamma})]_{\varepsilon'_{\gamma} = \frac{y_{\text{MP}} m_p \chi_{\pi}^{\text{MP}}}{E'_{\pi}}}, \quad (\text{D.7})$$

where we have neglected numerical factors coming from the integration. Therefore, for low pion energies, the interaction rate is proportional to the photon number density, just as the Δ resonance contribution.

For high pion energies, such that $E'_{\pi} > \frac{y_{\text{MP}} m_p \chi_{\pi}^{\text{MP}}}{\bar{\varepsilon}'_{\gamma}}$, the energy $\bar{\varepsilon}'_{\gamma}$ is contained in the integration range. The integral is dominated by the region near $\bar{\varepsilon}'_{\gamma}$, and therefore we can replace the lower limit in Eq. [D.6](#) with 0, obtaining

$$\Gamma^{\text{MP}} \left(\frac{E'_{\pi}}{\chi_{\pi}^{\text{MP}}} \right) \simeq \bar{f}_{\text{MP}} \int_0^{+\infty} d\varepsilon'_{\gamma} n(\varepsilon'_{\gamma}). \quad (\text{D.8})$$

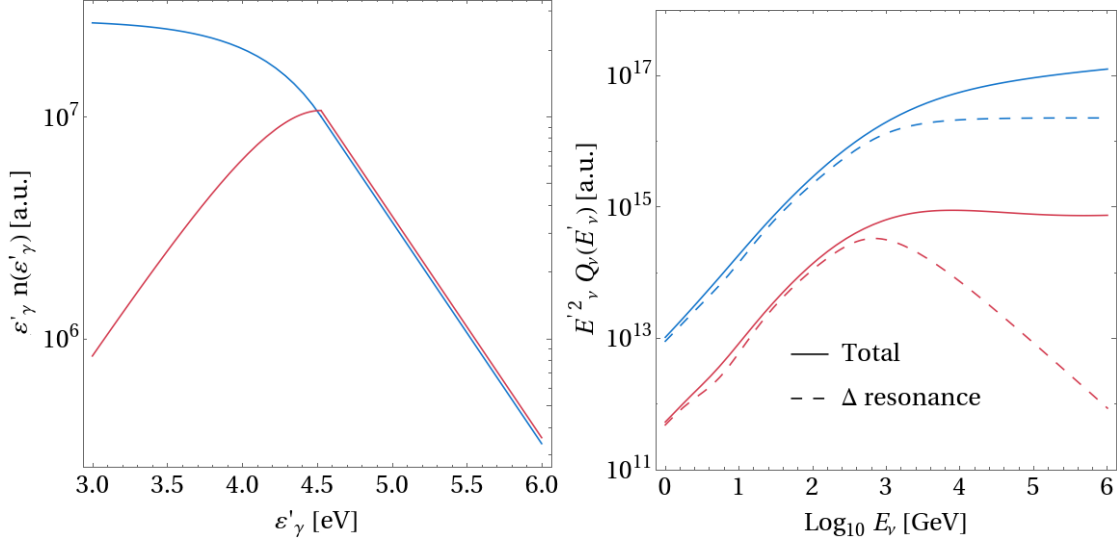


Figure D.1: Comparison between the Δ resonance and the multi-pion contribution to the neutrino production for two benchmark targets of photons with broken power-law spectra. In the left panel we show the two benchmark target photon spectra: for the red curve we choose the spectral indices so that $\varepsilon'_\gamma n(\varepsilon'_\gamma)$ is peaked. For the blue curve we choose the spectral indices so that $\varepsilon'_\gamma n(\varepsilon'_\gamma)$ is flat in energy below the break. In the right panel we show the corresponding neutrino spectra obtained using NeuCosmA (solid lines), as well as the contribution of the Δ resonance only (dashed lines).

The interaction rate does not depend in this case on E'_π .

Therefore we have the following situation: for $E'_\pi < \frac{y_{\text{MP}} m_p \chi_\pi^{\text{MP}}}{\varepsilon'_\gamma}$ both the Δ resonance and the multi-pion interaction rate grow with energy. Since $y_\Delta \simeq y_{\text{MP}}$ and $\chi_\pi^\Delta \simeq \chi_\pi^{\text{MP}}$, we can approximate the pion spectrum in this region as

$$E'^2_\pi Q_\pi(E'_\pi) \propto [\varepsilon'_\gamma n(\varepsilon'_\gamma)]_{\varepsilon'_\gamma = \frac{y_{\text{MP}} m_p \chi_\pi^{\text{MP}}}{E'_\pi}} e^{-E'_\pi / E'_{p,\text{max}} \chi_\pi^{\text{MP}}}. \quad (\text{D.9})$$

For $E'_\pi > \frac{y_{\text{MP}} m_p \chi_\pi^{\text{MP}}}{\varepsilon'_\gamma}$ the Δ resonance interaction rate follows the photon number density and decreases with energy, whereas according to Eq. [D.8](#) the multi-pion interaction rate is constant in energy. Therefore in this range multi-pion processes dominate, and the pion spectrum can be approximated as

$$E'^2_\pi Q_\pi(E'_\pi) \propto e^{-E'_\pi / E'_{p,\text{max}} \chi_\pi^{\text{MP}}}. \quad (\text{D.10})$$

As a graphical representation of these two behaviors, we show in Fig. [D.1](#) a peaked target photon spectrum (left panel, red curve) and the corresponding neutrino spectrum (right panel, red curve). We separately represent the Δ resonance contribution (dashed) and the total spectrum which also includes the multi-pion contribution (solid). The Δ resonance contribution falls off above the critical energy $\frac{y_{\text{MP}} m_p \chi_\pi^{\text{MP}} \chi_\nu}{\varepsilon'_\gamma}$, where $\chi_\nu \simeq 0.25$ is the fraction of the pion energy carried by the neutrino. On the other hand, the total neutrino production is dominated by multi-pion processes and the interaction rate remains constant.

The crucial point is that the pion spectrum for large pion energies becomes independent of the shape of the target photon spectrum because of the multi-pion contribution. This means that

any target photon spectrum peaked at an energy $\bar{\varepsilon}'_\gamma$ will give rise to the same pion spectrum (and therefore the same neutrino spectrum) for $E'_\pi > \frac{y_{\text{MP}} m_p \chi_\pi^{\text{MP}}}{\bar{\varepsilon}'_\gamma}$. Due to this observation, we can replace any target photon spectrum $\varepsilon'_\gamma n(\varepsilon'_\gamma)$ peaked at an energy $\bar{\varepsilon}'_\gamma$ by an equivalent blackbody spectrum peaked at the same energy, as we do by the mapping in Chap. 6.

A final comment is in order for the case in which the target photon spectrum $\varepsilon'_\gamma n(\varepsilon'_\gamma)$ does not have a single well-defined maximum. This case often appears in GRBs, where the target photon spectrum in the low energy range has often a behavior $n(\varepsilon'_\gamma) \propto \varepsilon'_\gamma$, leading to a flat behavior in energy for $\varepsilon'_\gamma n(\varepsilon'_\gamma)$.

For definiteness, we assume that $n(\varepsilon'_\gamma)\varepsilon'_\gamma$ becomes flat for energies lower than $\bar{\varepsilon}'_\gamma$. In this case, our estimate for the multi-pion interaction rate at pion energies $E'_\pi > \frac{y_{\text{MP}} m_p \chi_\pi^{\text{MP}}}{\bar{\varepsilon}'_\gamma}$ is not valid, since in obtaining it we assumed that most of the contribution to the integral came from the region near $\bar{\varepsilon}'_\gamma$. In the case at hand, instead, we can only assume that most of the contribution comes in the range from $\frac{y_{\text{MP}} m_p \chi_\pi^{\text{MP}}}{E'_\pi}$ to $\bar{\varepsilon}'_\gamma$. Therefore in this range the pion spectrum can be approximated as

$$E'^2_\pi Q_\pi(E'_\pi) \propto \log \left[\frac{\bar{\varepsilon}'_\gamma E'_\pi}{y_{\text{MP}} m_p \chi_\pi^{\text{MP}}} \right] e^{-E'_\pi / E'_{p,\text{max}} \chi_\pi^{\text{MP}}}. \quad (\text{D.11})$$

This behavior is again illustrated in Fig. D.1 by the blue curves. In this case, the Δ contribution to the pion and the neutrino spectrum becomes flat above the critical energy $\frac{y_{\text{MP}} m_p \chi_\pi^{\text{MP}}}{\bar{\varepsilon}'_\gamma}$, as expected from Eq. D.5. The total neutrino spectrum instead exhibits a slow growth due to the logarithmic factor in the multi-pion contribution of Eq. D.11.

This circumstance is harder to reproduce with an effective blackbody photon target. Indeed any peaked photon spectrum, such as a blackbody one, gives rise to a multi-pion contribution behaving as $Q_\pi(E'_\pi) \propto E'^{-2}_\pi e^{-E'_\pi / E'_{p,\text{max}} \chi_\pi^{\text{MP}}}$, and cannot capture the logarithmic factor in Eq. D.11. Nonetheless, the growth induced by the logarithmic factor in the pion and the neutrino spectrum is comparably slow in energy, so that if this region does not occupy an energy interval too wide the reproduction of the thermal model is still sufficiently accurate (see example below).

We provide in Fig. D.2 an example of the performances of the thermal model for power-law target photon spectra $n(\varepsilon'_\gamma) \propto \varepsilon'^{-\alpha}_\gamma$ with varying spectral indices α close to 1.

For $\alpha \gtrsim 1$, the target photon spectrum is monotonically decreasing in energy. Therefore, the energy contributing most to photohadronic production is the lower energy which can kinematically participate to the interaction, namely $\bar{\varepsilon}'_\gamma = \frac{y_{\Delta} m_p}{E'_{p,\text{max}}}$ from Eq. 6.2. Indeed, the peak of the neutrino spectrum is correctly reproduced by this choice within the thermal model (teal curves in the right panel). On the other hand, the behavior of the spectrum below the peak is not perfectly reproduced. This is due to the fact that, for $\varepsilon'_\gamma > \bar{\varepsilon}'_\gamma$, the power-law target photon spectrum decreases much more slowly than the thermal model. We now discuss the reason for this.

From Eq. D.5 we see that for the power-law case the pion emissivity increase in this region as $E'^2_\pi Q_\pi(E'_\pi) \propto E'^{\alpha-1}_\pi$. The neutrino emissivity for $\alpha < 3$ follows the same behavior. For $\alpha > 3$, while the pion spectrum still increases as $E'^2_\pi Q_\pi(E'_\pi) \propto E'^{\alpha-1}_\pi$, the produced neutrino spectrum reaches a universal form $E'^2_\nu Q_\nu(E'_\nu) \propto E'^2_\nu$. This is in fact the spectrum of neutrinos produced in the weak decay of pions.

On the other hand, for the thermal model, since the target photon spectrum decreases exponentially for $\varepsilon'_\gamma > \bar{\varepsilon}'_\gamma$, the neutrino spectrum always has the universal form $E'^2_\nu Q_\nu(E'_\nu) \propto E'^2_\nu$ induced by the energy dependence of the weak pion decay.

Therefore, for $\alpha > 3$ the power-law model and the thermal model give exactly the same shape for the neutrino spectrum. For $1 < \alpha < 3$ the agreement between the two is better as α is larger.

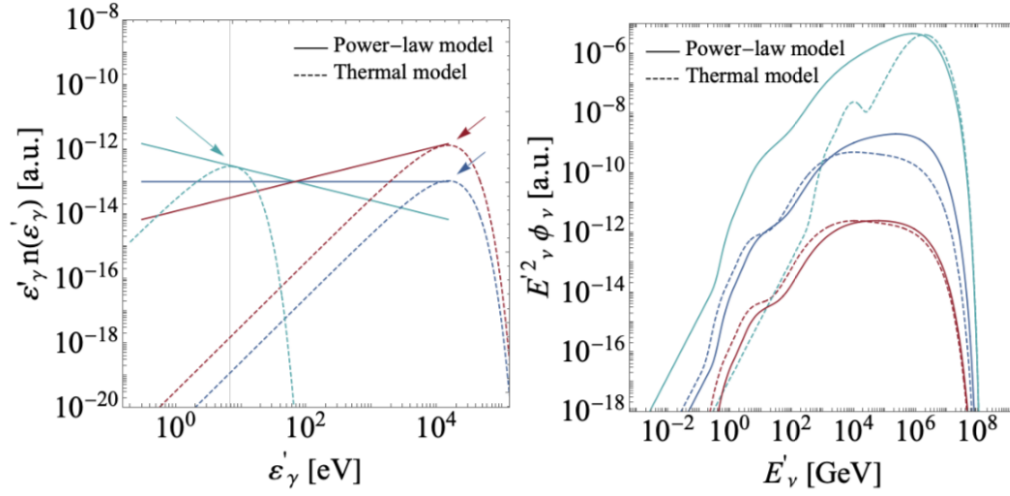


Figure D.2: Comparison between the neutrino spectra produced by power-law target photons and their reproduction within the thermal model. In the left panel we show the target photon spectra (in teal for $\alpha \gtrsim 1$, in blue for $\alpha = 1$, in red for $\alpha \lesssim 1$; solid lines), as well as the blackbody spectra used to simulate them in the thermal model (dashed lines). The arrows indicate the energies $\bar{\epsilon}'_\gamma$ for each case. In the right panel we show the neutrino spectra obtained using NeuCosmA: the color scheme and the line styles are chosen in the same way as for the left panel.

Indeed, in Fig. 6.2 the benchmark example for AGN, with $\alpha = 2$ for $\epsilon'_\gamma > \bar{\epsilon}'_\gamma$, shows a very good agreement between the broken power law and the thermal model.

For $\alpha \lesssim 1$, we see from Fig. D.2 (red curves in the right panel) that the reproduction of the thermal model is very accurate. This is because the high-energy behavior is completely determined by the multi-pion processes, which lead to a spectral shape independent of the properties of the target photon spectrum.

For $\alpha = 1$ (blue curves in the right panel), the power-law model for the neutrino spectrum exhibits a growth in energy that the thermal model does not capture. This is indeed caused by the logarithmic factor in Eq. D.11 that we discussed above. As can be seen, over four decades in energy this induces a discrepancy of about an order of magnitude between the power-law and the thermal model.

Appendix E

Cross sections for active-sterile interactions

As mentioned in the introduction to Chap. 8, the aim of the papers [403, 404] is to study the propagation of astrophysical neutrinos on their way to Earth. This requires the knowledge of the cross sections for interaction of two active neutrinos, and an active and sterile neutrinos, as we will discuss below. In this appendix, we collect the expressions for the relevant cross sections.

At tree level the new processes introduced by our new interaction are the four particle collisions $\nu\nu \rightarrow \nu_s\nu_s$, $\nu\nu_s \rightarrow \nu\nu_s$ and $\nu_s\nu_s \rightarrow \nu\nu$ (neglecting flavor indices). The first two ones, which are the most relevant for us, are shown in Fig. E.1

The process $\nu\nu \rightarrow \nu_s\nu_s$ is important to us because active astrophysical neutrinos can collide with active neutrinos from the CNB: we assume the latter to be at rest in the laboratory rest frame, which means that the CNB temperature is smaller than the neutrino mass. Let the active neutrinos be in their mass eigenstates, denoted by Latin indices, before the collision, so the interaction is $\nu_i\nu_j \rightarrow \nu_s\nu_s$. The squared amplitude for the process, written in terms of the Mandelstam invariants $s = (p+l)^2$, $t = (p-k)^2$ and $u = (p-q)^2$ (see Fig. E.1, left panel) is

$$\begin{aligned}
 |\mathcal{M}_{ij \rightarrow ss}|^2 = & \left| \sum_{\ell, \ell'} U_{\ell'i}^* U_{\ell'j}^* U_{\ell s} U_{\ell' s} \right|^2 \left[\frac{[t - (m - m_s)^2]^2}{(t - M_\varphi^2)^2 + \Gamma^2 M_\varphi^2} + \frac{[u - (m - m_s)^2]^2}{(u - M_\varphi^2)^2 + \Gamma^2 M_\varphi^2} \right. \\
 & - \frac{2[(t - M_\varphi^2)(u - M_\varphi^2) + \Gamma^2 M_\varphi^2]}{[(t - M_\varphi^2)^2 + \Gamma^2 M_\varphi^2][(u - M_\varphi^2)^2 + \Gamma^2 M_\varphi^2]} \left(\frac{(t - m^2 - m_s^2)^2}{4} + \frac{(u - m^2 - m_s^2)^2}{4} \right. \\
 & \left. \left. - \frac{s^2}{4} + s(m^2 + m_s^2 - m m_s) - 2m^2 m_s^2 \right) \right] \quad (\text{E.1})
 \end{aligned}$$

(for simplicity, we assume equal masses for the active neutrinos ν_ℓ and $\nu_{\ell'}$; this is justified because we will use the benchmark value $m = 0.1$ eV, which is larger than the mass splittings inferred by oscillations). Here m is the mass of the active neutrino ν , Γ is the decay rate of the scalar mediator given below, and M_φ is its mass. We remind that the squared amplitude depends on two Mandelstam invariants only, since the third is connected to the others by the relation $s + t + u = 2(m^2 + m_s^2)$.

The total cross section for the $\nu_i\nu_j \rightarrow \nu_s\nu_s$ reaction, in the laboratory rest frame, is then given by

$$\sigma_{ij \rightarrow ss} = \frac{1}{64\pi T^2} \int_{t_1}^{t_2} |\mathcal{M}_{ij \rightarrow ss}|^2(s, t) dt \quad (\text{E.2})$$

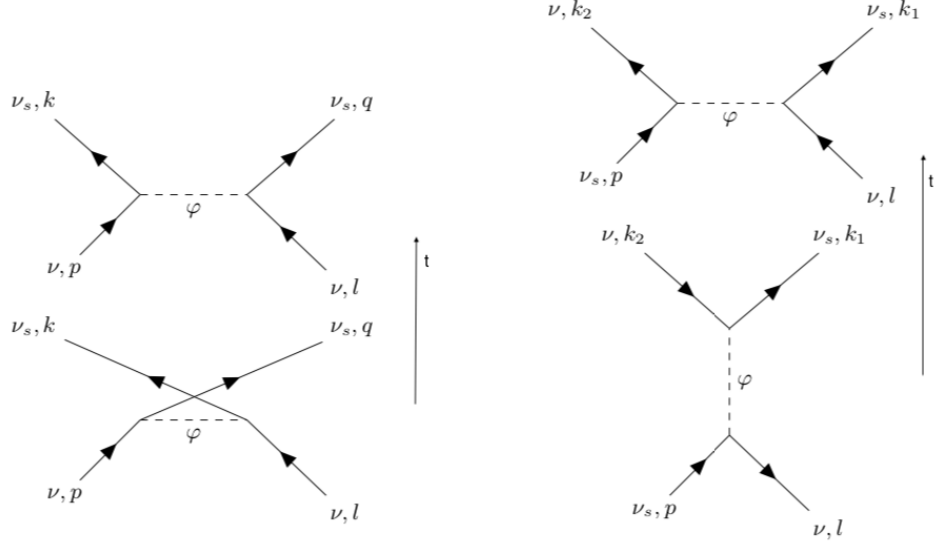


Figure E.1: Feynman diagrams for the scattering of two active neutrinos (left), and an active and a sterile neutrino (right) through the secret interaction. Flavor indices for the active neutrinos are neglected.

where

$$t_{1,2} = m^2 + m_s^2 - \frac{s}{2} \pm \sqrt{s} \sqrt{\frac{s}{4} - m_s^2}, \quad (\text{E.3})$$

and

$$I = \sqrt{\frac{2m^4 + s^2 - 4sm^2}{2}}. \quad (\text{E.4})$$

The differential cross section for the production of a sterile neutrino with energy E_s in the process $\nu_i \nu_j \rightarrow \nu_s \nu_s$ is

$$\frac{d\sigma_{ij \rightarrow ss}}{dE_s} = \frac{|\mathcal{M}_{ij \rightarrow ss}|^2 [2pm, m^2 + m_s^2 - 2m(E - E_s)] \theta\left(E - \frac{2mE_s^2}{2mE_s - m_s^2}\right) \theta\left(E_s - \frac{m_s^2}{2m}\right)}{32\pi EI}. \quad (\text{E.5})$$

Here E is the energy of the incident cosmogenic active neutrino.

The sterile neutrinos produced via the process just discussed can again collide, during their propagation, with the CNB neutrinos. For this reason the second process of interest to us is $\nu_i \nu_s \rightarrow \nu_j \nu_s$, where i and j again denote mass eigenstates of active neutrinos. We assume again that the initial momentum of the CNB neutrino is l , the momentum of the incident sterile neutrino is p , the momentum of the final sterile and active neutrinos are respectively k_1 and k_2 as shown in Fig. [E.1](#) (right panel). In this case the two final particles are distinguishable, so the choice of how to define the Mandelstam parameters is not equivalent: we choose the convention that $t = (p - k_2)^2 = (l - k_1)^2$. With this choice, the squared amplitude $|\mathcal{M}_{is \rightarrow js}|^2$ is identical to Eq. [E.1](#) with the s and the u

parameters exchanged in the corresponding equation. The total cross section is

$$\sigma_{is \rightarrow js} = \frac{1}{64\pi J^2} \int_{t_1}^{t_2} |\mathcal{M}_{is \rightarrow js}|^2 (m_s^2 + 2mE, t) dt \quad (\text{E.6})$$

with

$$t_{1,2} = m^2 + m_s^2 - \frac{(m_s^2 + 2mE)^2 - m_s^4}{2(m_s^2 + 2mE)} \pm \frac{2m^2 E^2}{2mE + m_s^2} \quad (\text{E.7})$$

and again the energy of the incident sterile neutrino is E and J is defined as

$$J = \sqrt{\frac{m^4 + m_s^4 + s^2 - 2sm^2 - 2sm_s^2}{2}}. \quad (\text{E.8})$$

The differential cross section for the production of an active neutrino of energy E_2 is then

$$\begin{aligned} \frac{d\sigma_{is \rightarrow js}}{dE_2} &= \frac{1}{32\pi EJ} \theta \left(\frac{2mE^2}{2mE + m_s^2} - E_2 \right) \times \\ &\times |\mathcal{M}_{is \rightarrow js}|^2 [m^2 + m_s^2 + 2mE, m^2 + m_s^2 - 2m(E - E_2)]. \end{aligned} \quad (\text{E.9})$$

The differential cross section for the production of a sterile neutrino of energy E_1 is (we invert the order of the subscripts i and s to emphasize the difference with the previous case)

$$\begin{aligned} \frac{d\sigma_{is \rightarrow sj}}{dE_1} &= \frac{1}{32\pi EJ} \theta \left((E - E_1)(2mEE_1 - m_s^2(E - E_1)) \right) \times \\ &\times |\mathcal{M}_{is \rightarrow js}|^2 [m^2 + m_s^2 + 2mE, m^2 + m_s^2 - 2mE_1]. \end{aligned} \quad (\text{E.10})$$

The total decay rate Γ of the scalar mediator, through the processes $\varphi \rightarrow \nu_\ell \nu_s$, is given by

$$\Gamma = \frac{\sum_\ell |\lambda_\ell|^2 \xi (mm_s + \sqrt{\xi^2 + m^2} \sqrt{\xi^2 + m_s^2} + \xi^2)}{2\pi M_\varphi (\sqrt{\xi^2 + m^2} + \sqrt{k^2 + m_s^2})} \theta(M_\varphi - m - m_s) \quad (\text{E.11})$$

where

$$\xi = \frac{\sqrt{m^4 - 2m^2 M_\varphi^2 + M_\varphi^4 - 2m^2 m_s^2 - 2M_\varphi^2 m_s^2 + m_s^4}}{2M_\varphi}. \quad (\text{E.12})$$

For $m_s \geq M_\varphi$, the decay rate of the scalar mediator vanishes, since the process $\varphi \rightarrow \nu_s \nu_\ell$ is kinematically forbidden. The divergences in the denominators of the matrix elements in Eq. [E.1](#) become therefore unregulated. The s -resonance can never be reached in the physical space of parameters, so it is not affected by any divergence anyway. On the other hand, for the process $\nu \nu_s \rightarrow \nu \nu_s$ only, the t -resonance can be reached for physical values of the energies¹; in fact, the resonance condition $t = M_\varphi^2$ gives for the energy of the final sterile and active neutrino respectively

$$E_s = \frac{m^2 + m_s^2 - M_\varphi^2}{2m}, E_a = \sqrt{p^2 + m_s^2} + \frac{m^2 - m_s^2 + M_\varphi^2}{2m}, \quad (\text{E.13})$$

where p is the impulse of the sterile neutrino in the laboratory frame. A similar divergence also appears in the cross section for Rutherford scattering of charged particles, where it is connected

¹This does not happen for the process $\nu \nu \rightarrow \nu_s \nu_s$, as can be seen by exchanging m and m_s in Eq. [E.13](#), which makes the energies negative.

with the long range nature of the classical electrostatic interaction. In this case there is no classical analogue of the interaction (since the secret interaction flips the neutrino from active to sterile), but the divergence can still be ascribed to a divergence in the interaction range. In reality, the cross section cannot of course exceed the transverse structure of the incident beam, so a regularization mechanism could be devised. However, a simpler possibility for regularizing the divergence is to give the mediator a small but non-vanishing decay rate. Indeed, it is uncommon for a particle to be completely stable, if this stability does not descend from some specific property or conservation law. Therefore, it is unlikely that our mediator is completely stable and it may have other decay channels, giving rise to a finite total decay rate Γ , which eliminates the divergence.

Appendix F

Secret interactions with sterile neutrino decay

In Chap. 8 we mentioned that, if $m_s > M_\varphi$, sterile neutrinos are not stable and can decay to an active neutrino and a scalar mediator. The cascading process, which originates from the collision of an active astrophysical neutrino and a CNB neutrino, can change drastically due to this decay channel. In this appendix, we discuss how we deal with this case.

First of all we need to determine the properties of the sterile neutrino decay. The lifetime for the decay of a sterile neutrino with energy E into an i -th active neutrino is

$$\tau_i = \frac{8\pi m_s^2 E}{|\sum_\alpha U_{\alpha i} \lambda_\alpha|^2 (m_s^2 - M_\varphi^2)^2}, \quad (\text{F.1})$$

where $U_{\alpha i}$ are the elements of the PMNS matrix.

Because of relativistic boosting the active neutrinos are produced nearly in the same direction as the original sterile neutrino. Their energy distribution is

$$\frac{dN}{dE_a}(E \rightarrow E_a) = \frac{m_s}{m_s^2 - M_\varphi^2} \frac{1}{\sqrt{\frac{E^2}{m_s^2} - 1}}, \quad (\text{F.2})$$

where E_a is the energy of the active neutrino, which can take values between the extrema

$$E_{1,2} = \frac{E(m_s^2 - M_\varphi^2)}{2m_s^2} \left[1 \pm \sqrt{1 - \frac{m_s^2}{E^2}} \right]. \quad (\text{F.3})$$

The probability of decaying into the i -th mass eigenstate is

$$P_i = \frac{|\sum_\alpha U_{\alpha i} \lambda_\alpha|^2}{\sum_i |\sum_\alpha U_{\alpha i} \lambda_\alpha|^2}. \quad (\text{F.4})$$

For masses of the sterile neutrinos even slightly larger than the mediator mass, the lifetime is so short that decay becomes the dominant process, and sterile neutrinos decay immediately after having been produced. The transport equations in this regime can be therefore approximated by assuming that the flux of sterile neutrinos injected per unit path length by the collisions of active neutrinos with

the CNB, namely

$$\begin{aligned}
 & -H(z)(1+z)\frac{\partial\Phi_s(z,E)}{\partial z} = \\
 & \sum_{i,j} \int dE' \Phi_i(z,E') \frac{d\sigma_{ij\rightarrow ss}(E' \rightarrow E)}{dE} n_j(z),
 \end{aligned} \tag{F.5}$$

is completely converted into an active neutrino flux with the energy distribution in Eq. (F.2). We then have only three equations for the active fluxes which are written as

$$\begin{aligned}
 & H(z)(1+z) \left(\frac{\partial\Phi_i(z,E)}{\partial z} + \frac{\partial\Phi_i(z,E)}{\partial E} \frac{E}{1+z} \right) = \\
 & \sum_j n_j(z) \sigma_{ij\rightarrow ss} \Phi_i(z,E) \\
 & - \int dE' \int dE'' \frac{dN}{dE}(E' \rightarrow E) P_i \times \\
 & \sum_{jk} \Phi_j(z,E'') \frac{d\sigma_{jk\rightarrow ss}(E'' \rightarrow E')}{dE'} n_k(z) \\
 & - \rho(z)(1+z) f(E) \xi_i.
 \end{aligned} \tag{F.6}$$

These are still three coupled transport equation which are hard to solve. We applied a perturbative approach, treating the regeneration term as a small perturbation, and we verified *a posteriori* whether this term was truly small. We found that the first order perturbative correction from the regeneration term can significantly change the spectrum, and indeed this is the origin of the bump in the flux (dashed line) of Fig. 8.3. Nevertheless, the second order correction was found to be negligible compared to the zero and first order term, which justifies our use of the latter two alone.

Acknowledgments

There are many people I would like to thank, who have in various ways allowed me to arrive at this point and write this thesis. First of all, I would like to thank my advisors, Gennaro Miele and Stefano Morisi, who originally introduced me to the subject of neutrino astrophysics. They have been constantly helping me in these years, both in physics and especially in growing as a researcher. I also thank Marco and Ninetta for their kindness and helpfulness: I always could count on their help during my PhD. I thank the whole astroparticle physics group of Napoli, and all the people I have collaborated with in these years: Antonio A., Roberta, Antonio M., Fabio, Gianpiero Mangano, Rasmi, and Walter Winter. A special thanks goes to Ofelia Pisanti and Pietro Santorelli, who have guided me a lot through their help and suggestions every time I needed them.

None of this work would have been possible without the help of my parents, who have been constantly supporting (and standing) me since I began studying. Besides the ever-present support, they have been an inspiration to me, partly motivating me in starting this journey. Thanks to my brother Federico, who probably had to endure even more than my parents did, and nonetheless is always ready to help me.

I thank my closest friends during these years, the "Semplic9 Lady Varia", with which I shared practically everything along these years. They have been always there in so many ways. A special thanks to Mattia, who has been close to me throughout this PhD, motivating and helping me in so many ways that I couldn't list them. Even the hardest times in these years have been much lighter next to him. Big thanks are also due to Angela, who was with me since day one and keeps being there for me all along. I'm glad that we have the chance to keep growing together. I thank Mara: without her, I never laugh the same way, and I am very grateful that we can still have so many moments together even if she's far away. I thank Milla, even though she graduated nearly without telling me: I am so thankful to still have her close to me even from another nation. (At one time she would have cried reading the acknowledgments, but right now I think we all cry more than her.) Last but not the least, thanks to Alfredo, who arrived later but progressively tried to steal the role of Milla.

I thank all my friends who have been with me outside of physics, Pierluca, Rosanna, Alessia, Cly, Martina, Simone, Renee: it is always beautiful to spend my time with all of you. I also want to thank all my friends from the department: Valeria, Ludovica, and Sara, the power of three; Gege, Bob, and Roberto, the other power of three; Francesco, who is the only one that can keep me company at the University at 7 a.m.; Ilaria, who I can always turn to for a non-sense moment. Finally, I would like to thank my historical friends, Valentina and Carla, who have managed to remain with me for more than 10 and 20 years respectively, which is a hard mission.

Bibliography

- [1] W. I. Axford, E. Leer, and G. Skadron. The Acceleration of Cosmic Rays by Shock Waves. In *International Cosmic Ray Conference*, volume 11 of *International Cosmic Ray Conference*, page 132, January 1977.
- [2] Germogen Filippovich Krymsky. Regular mechanism of charged particle acceleration on the shock wave front. In *Doklady Akademii Nauk*, volume 234, pages 1306–1308. Russian Academy of Sciences, 1977.
- [3] A. R. Bell. The acceleration of cosmic rays in shock fronts. II. *Mon. Not. Roy. Astron. Soc.*, 182:443–455, 1978.
- [4] R. D. Blandford and J. P. Ostriker. Particle Acceleration by Astrophysical Shocks. *Astrophys. J. Lett.*, 221:L29–L32, 1978.
- [5] Enrico Fermi. On the Origin of the Cosmic Radiation. *Phys. Rev.*, 75:1169–1174, 1949.
- [6] Lev Davidovich Landau, JS Bell, MJ Kearsley, LP Pitaevskii, EM Lifshitz, and JB Sykes. *Electrodynamics of continuous media*, volume 8. elsevier, 2013.
- [7] LD Landau and EM Lifshitz. Fluid mechanics. *New York*, 61, 1959.
- [8] Thomas K Gaisser, Ralph Engel, and Elisa Resconi. *Cosmic rays and particle physics*. Cambridge University Press, 2016.
- [9] DONALD C ELLISOÑ and D Eichler. Monte carlo shock-like solutions to the boltzmann equation with collective scattering. *The Astrophysical Journal*, 286:691–701, 1984.
- [10] AR Bell. The non-linear self-regulation of cosmic ray acceleration at shocks. *Monthly Notices of the Royal Astronomical Society*, 225(3):615–626, 1987.
- [11] SAEG Falle and JR Giddings. Time-dependent cosmic ray modified shocks. *Monthly Notices of the Royal Astronomical Society*, 225(2):399–423, 1987.
- [12] P Blasi, Stefano Gabici, and Giulia Vannoni. On the role of injection in kinetic approaches to non-linear particle acceleration at non-relativistic shock waves. *Monthly Notices of the Royal Astronomical Society*, 361(3):907–918, 2005.
- [13] JA Peacock. Fermi acceleration by relativistic shock waves. *Monthly Notices of the Royal Astronomical Society*, 196(2):135–152, 1981.
- [14] John G Kirk and Peter Schneider. On the acceleration of charged particles at relativistic shock fronts. *The Astrophysical Journal*, 315:425–433, 1987.

- [15] TN Kato and F Takahara. Application of random walk theory to the first-order fermi acceleration in shock waves. *Monthly Notices of the Royal Astronomical Society*, 321(4):642–660, 2001.
- [16] Uri Keshet and Eli Waxman. Energy spectrum of particles accelerated in relativistic collisionless shocks. *Physical Review Letters*, 94(11):111102, 2005.
- [17] Junichi Aoi, Kohta Murase, and Shigehiro Nagataki. The effect of energy amplification variance on shock acceleration. *Monthly Notices of the Royal Astronomical Society*, 383(4):1431–1438, 2008.
- [18] Eli Waxman. Gamma-ray-burst afterglow: supporting the cosmological fireball model, constraining parameters, and making predictions. *The Astrophysical Journal Letters*, 485(1):L5, 1997.
- [19] L. D. Landau and E. M. Lifschits. *The Classical Theory of Fields*, volume Volume 2 of *Course of Theoretical Physics*. Pergamon Press, Oxford, 1975.
- [20] Vladimir Borisovich Berestetskii, Evgenii Mikhailovich Lifshitz, and Lev Petrovich Pitaevskii. *Quantum Electrodynamics: Volume 4*, volume 4. Butterworth-Heinemann, 1982.
- [21] FW Stecker. Nasa special publication-cosmic gamma rays, 249,(baltimore: Mono book corp.) stecker, fw, 1973. *Astrophys. J*, 185:499, 1971.
- [22] S. Hummer, M. Maltoni, W. Winter, and C. Yaguna. Energy dependent neutrino flavor ratios from cosmic accelerators on the Hillas plot. *Astropart. Phys.*, 34:205–224, 2010.
- [23] Thanu Padmanabhan. *Theoretical Astrophysics: Volume 1, Astrophysical Processes*. Cambridge University Press, 2000.
- [24] Torbjörn Sjöstrand, Stefan Ask, Jesper R. Christiansen, Richard Corke, Nishita Desai, Philip Ilten, Stephen Mrenna, Stefan Prestel, Christine O. Rasmussen, and Peter Z. Skands. An introduction to PYTHIA 8.2. *Comput. Phys. Commun.*, 191:159–177, 2015.
- [25] Sergey Ostapchenko. Monte Carlo treatment of hadronic interactions in enhanced Pomeron scheme: I. QGSJET-II model. *Phys. Rev. D*, 83:014018, 2011.
- [26] Felix Riehn, Ralph Engel, Anatoli Fedynitch, Thomas K. Gaisser, and Todor Stanev. Hadronic interaction model Sibyll 2.3d and extensive air showers. *Phys. Rev. D*, 102(6):063002, 2020.
- [27] Alexandru Catalin Ene, Alexandru Jipa, and Lavinia-Elena Giubega. Study of Monte Carlo event generators for proton-proton collisions at LHC energies in the forward region. *Chin. Phys. C*, 43(8):083001, 2019.
- [28] S. R. Kelner, Felex A. Aharonian, and V. V. Bugayov. Energy spectra of gamma-rays, electrons and neutrinos produced at proton-proton interactions in the very high energy regime. *Phys. Rev. D*, 74:034018, 2006. [Erratum: *Phys.Rev.D* 79, 039901 (2009)].
- [29] Paolo Lipari, Maurizio Lusignoli, and Davide Meloni. Flavor Composition and Energy Spectrum of Astrophysical Neutrinos. *Phys. Rev. D*, 75:123005, 2007.
- [30] S. Hummer, M. Ruger, F. Spanier, and W. Winter. Simplified models for photohadronic interactions in cosmic accelerators. *Astrophys. J.*, 721:630–652, 2010.

- [31] A. Mucke, J. P. Rachen, Ralph Engel, R. J. Protheroe, and Todor Stanev. On photohadronic processes in astrophysical environments. *Publ. Astron. Soc. Austral.*, 16:160, 1999.
- [32] A. Mucke, Ralph Engel, J. P. Rachen, R. J. Protheroe, and Todor Stanev. SOPHIA: Monte Carlo simulations of photohadronic processes in astrophysics. *Comput. Phys. Commun.*, 124:290–314, 2000.
- [33] Kohta Murase. High energy neutrino early afterglows gamma-ray bursts revisited. *Phys. Rev. D*, 76:123001, 2007.
- [34] Charles D. Dermer, Kohta Murase, and Hajime Takami. Variable Gamma-ray Emission Induced by Ultra-High Energy Neutral Beams: Application to 4C +21.35. *Astrophys. J.*, 755:147, 2012.
- [35] Damiano F. G. Fiorillo, Arjen Van Vliet, Stefano Morisi, and Walter Winter. Unified thermal model for photohadronic neutrino production in astrophysical sources. 3 2021.
- [36] S. R. Kelner and F. A. Aharonian. Energy spectra of gamma-rays, electrons and neutrinos produced at interactions of relativistic protons with low energy radiation. *Phys. Rev. D*, 78:034013, 2008. [Erratum: *Phys.Rev.D* 82, 099901 (2010)].
- [37] Markus Ahlers and Francis Halzen. Opening a New Window onto the Universe with IceCube. *Prog. Part. Nucl. Phys.*, 102:73–88, 2018.
- [38] Francis Halzen, Ali Kheirandish, Thomas Weisgarber, and Scott P. Wakely. On the Neutrino Flares from the Direction of TXS 0506+056. *Astrophys. J. Lett.*, 874(1):L9, 2019.
- [39] Antonio Capanema, Arman Esmaili, and Kohta Murase. New constraints on the origin of medium-energy neutrinos observed by IceCube. *Phys. Rev. D*, 101(10):103012, 2020.
- [40] Jorg P. Rachen and P. Meszaros. Photohadronic neutrinos from transients in astrophysical sources. *Phys. Rev. D*, 58:123005, 1998.
- [41] Tamar Kashti and Eli Waxman. Flavoring astrophysical neutrinos: Flavor ratios depend on energy. *Phys. Rev. Lett.*, 95:181101, 2005.
- [42] Sandip Pakvasa. Neutrino Flavor Detection at Neutrino Telescopes and Its Uses. 4 2010.
- [43] M. Kachelriess and R. Tomas. High energy neutrino yields from astrophysical sources I: Weakly magnetized sources. *Phys. Rev. D*, 74:063009, 2006.
- [44] M. Kachelriess, S. Ostapchenko, and R. Tomas. High energy neutrino yields from astrophysical sources. 2. Magnetized sources. *Phys. Rev. D*, 77:023007, 2008.
- [45] Evgenii Mikhailovich Lifshitz and Lev Petrovich Pitaevskii. *Physical kinetics*. Butterworth Heinemann, 1981.
- [46] Andreas Shalchi. *Nonlinear cosmic ray diffusion theories*, volume 362. Springer, 2009.
- [47] M. Kachelriess and D. V. Semikoz. Cosmic Ray Models. *Prog. Part. Nucl. Phys.*, 109:103710, 2019.
- [48] VS Berezhinskii, SV Bulanov, VL Ginzburg, VA Dogel, and VS Ptuskin. *Astrophysics of cosmic rays*. Moscow, 1984.

- [49] Kenneth Greisen. End to the cosmic ray spectrum? *Phys. Rev. Lett.*, 16:748–750, 1966.
- [50] G. T. Zatsepin and V. A. Kuzmin. Upper limit of the spectrum of cosmic rays. *JETP Lett.*, 4:78–80, 1966.
- [51] R. C. Gilmore, R. S. Somerville, J. R. Primack, and A. Dominguez. Semi-analytic modeling of the EBL and consequences for extragalactic gamma-ray spectra. *Mon. Not. Roy. Astron. Soc.*, 422:3189, 2012.
- [52] Alberto Franceschini and Giulia Rodighiero. The extragalactic background light revisited and the cosmic photon-photon opacity. *Astron. Astrophys.*, 603:A34, 2017.
- [53] Carlos Blanco. γ -cascade: a simple program to compute cosmological gamma-ray propagation. *JCAP*, 01:013, 2019.
- [54] V. Berezhinsky and O. Kalashev. High energy electromagnetic cascades in extragalactic space: physics and features. *Phys. Rev. D*, 94(2):023007, 2016.
- [55] Marco Cirelli, Gennaro Corcella, Andi Hektor, Gert Hutsi, Mario Kadastik, Paolo Panci, Martti Raidal, Filippo Sala, and Alessandro Strumia. PPPC 4 DM ID: A Poor Particle Physicist Cookbook for Dark Matter Indirect Detection. *JCAP*, 03:051, 2011. [Erratum: *JCAP* 10, E01 (2012)].
- [56] Peter Minkowski. $\mu \rightarrow e\gamma$ at a Rate of One Out of 10^9 Muon Decays? *Phys. Lett. B*, 67:421–428, 1977.
- [57] Murray Gell-Mann, Pierre Ramond, and Richard Slansky. Complex Spinors and Unified Theories. *Conf. Proc. C*, 790927:315–321, 1979.
- [58] Tsutomu Yanagida. Horizontal gauge symmetry and masses of neutrinos. *Conf. Proc. C*, 7902131:95–99, 1979.
- [59] B. Pontecorvo. Inverse beta processes and nonconservation of lepton charge. *Zh. Eksp. Teor. Fiz.*, 34:247, 1957.
- [60] Ziro Maki, Masami Nakagawa, and Shoichi Sakata. Remarks on the unified model of elementary particles. *Prog. Theor. Phys.*, 28:870–880, 1962.
- [61] P.A. Zyla et al. Review of Particle Physics. *PTEP*, 2020(8):083C01, 2020.
- [62] M. Ackermann et al. The spectrum of isotropic diffuse gamma-ray emission between 100 MeV and 820 GeV. *Astrophys. J.*, 799:86, 2015.
- [63] A. A. Abdo et al. The Spectrum of the Isotropic Diffuse Gamma-Ray Emission Derived From First-Year Fermi Large Area Telescope Data. *Phys. Rev. Lett.*, 104:101101, 2010.
- [64] W. B. Atwood et al. The Large Area Telescope on the Fermi Gamma-ray Space Telescope Mission. *Astrophys. J.*, 697:1071–1102, 2009.
- [65] P. Sreekumar et al. EGRET observations of the extragalactic gamma-ray emission. *Astrophys. J.*, 494:523–534, 1998.
- [66] A. W. Strong, I. V. Moskalenko, and O. Reimer. A new determination of the extragalactic diffuse gamma-ray background from egret data. *Astrophys. J.*, 613:956–961, 2004.

- [67] C. E. Fichtel, G. A. Simpson, and D. J. Thompson. Diffuse gamma radiation. *Astrophys. J.*, 222:833–849, June 1978.
- [68] P. Sreekumar, D. L. Bertsch, B. L. Dingus, J. A. Esposito, C. E. Fichtel, R. C. Hartman, S. D. Hunter, G. Kanbach, D. A. Kniffen, Y. C. Lin, H. A. Mayer-Hasselwander, P. F. Michelson, C. von Montigny, A. Mücke, R. Mukherjee, P. L. Nolan, M. Pohl, O. Reimer, E. Schneid, J. G. Stacy, F. W. Stecker, D. J. Thompson, and T. D. Willis. EGRET Observations of the Extragalactic Gamma-Ray Emission. *Astrophys. J.*, 494(2):523–534, February 1998.
- [69] M. Ajello et al. The Origin of the Extragalactic Gamma-Ray Background and Implications for Dark-Matter Annihilation. *Astrophys. J. Lett.*, 800(2):L27, 2015.
- [70] W. Benbow. The H.E.S.S. experiment. *AIP Conf. Proc.*, 842(1):998–1000, 2006.
- [71] Nahee Park. Performance of the VERITAS experiment. *PoS*, ICRC2015:771, 2016.
- [72] J. Aleksic et al. Performance of the MAGIC stereo system obtained with Crab Nebula data. *Astropart. Phys.*, 35:435–448, 2012.
- [73] B. S. Acharya et al. *Science with the Cherenkov Telescope Array*. WSP, 11 2018.
- [74] A. U. Abeysekara et al. The 2HWC HAWC Observatory Gamma Ray Catalog. *Astrophys. J.*, 843(1):40, 2017.
- [75] Maurizio Spurio. *Probes of Multimessenger Astrophysics: Charged cosmic rays, neutrinos, γ -rays and gravitational waves*. Springer, 2018.
- [76] E. Andres et al. The AMANDA neutrino telescope: Principle of operation and first results. *Astropart. Phys.*, 13:1–20, 2000.
- [77] M. G. Aartsen et al. The IceCube Neutrino Observatory: Instrumentation and Online Systems. *JINST*, 12(03):P03012, 2017.
- [78] R. Abbasi et al. The Design and Performance of IceCube DeepCore. *Astropart. Phys.*, 35:615–624, 2012.
- [79] M. Ageron et al. ANTARES: the first undersea neutrino telescope. *Nucl. Instrum. Meth. A*, 656:11–38, 2011.
- [80] S. Adrian-Martinez et al. Letter of intent for KM3NeT 2.0. *J. Phys. G*, 43(8):084001, 2016.
- [81] I. A. Belolaptikov et al. The Baikal underwater neutrino telescope: Design, performance and first results. *Astropart. Phys.*, 7:263–282, 1997.
- [82] M. G. Aartsen et al. IceCube-Gen2 - The Next Generation Neutrino Observatory at the South Pole: Contributions to ICRC 2015. 10 2015.
- [83] Shirley Weishi Li, Mauricio Bustamante, and John F. Beacom. Echo Technique to Distinguish Flavors of Astrophysical Neutrinos. *Phys. Rev. Lett.*, 122(15):151101, 2019.
- [84] R. Abbasi et al. Measurement of Astrophysical Tau Neutrinos in IceCube’s High-Energy Starting Events. 11 2020.
- [85] M. G. Aartsen et al. Evidence for High-Energy Extraterrestrial Neutrinos at the IceCube Detector. *Science*, 342:1242856, 2013.

- [86] R. Abbasi et al. The IceCube high-energy starting event sample: Description and flux characterization with 7.5 years of data. 11 2020.
- [87] M. G. Aartsen et al. A combined maximum-likelihood analysis of the high-energy astrophysical neutrino flux measured with IceCube. *Astrophys. J.*, 809(1):98, 2015.
- [88] M. G. Aartsen et al. Measurements using the inelasticity distribution of multi-TeV neutrino interactions in IceCube. *Phys. Rev. D*, 99(3):032004, 2019.
- [89] M. G. Aartsen et al. Detection of a particle shower at the Glashow resonance with IceCube. *Nature*, 591(7849):220–224, 2021.
- [90] J. Stettner. Measurement of the Diffuse Astrophysical Muon-Neutrino Spectrum with Ten Years of IceCube Data. *PoS, ICRC2019:1017*, 2020.
- [91] M. G. Aartsen et al. Characteristics of the diffuse astrophysical electron and tau neutrino flux with six years of IceCube high energy cascade data. *Phys. Rev. Lett.*, 125(12):121104, 2020.
- [92] Gurgen A Askaryan. Excess negative charge of an electron-photon shower and the coherent radio emission from it. *Zhur. Eksptl'. i Teoret. Fiz.*, 41, 1961.
- [93] GA Askar'yan. Coherent radio-emission from cosmic ray showers in the air and in dense media. LIBRARY OF CONGRESS WASHINGTON DC AEROSPACE TECHNOLOGY DIV, 1965.
- [94] J.A. Aguilar et al. Design and Sensitivity of the Radio Neutrino Observatory in Greenland (RNO-G). 10 2020.
- [95] M.G. Aartsen et al. Neutrino astronomy with the next generation IceCube Neutrino Observatory. 11 2019.
- [96] M.G. Aartsen et al. IceCube-Gen2: The Window to the Extreme Universe. 8 2020.
- [97] Jaime Álvarez-Muñiz et al. The Giant Radio Array for Neutrino Detection (GRAND): Science and Design. *Sci. China Phys. Mech. Astron.*, 63(1):219501, 2020.
- [98] K.S. Capelle, J.W. Cronin, G. Parente, and E. Zas. On the detection of ultrahigh-energy neutrinos with the Auger Observatory. *Astropart. Phys.*, 8:321–328, 1998.
- [99] F. Halzen and D. Saltzberg. Tau-neutrino appearance with a 1000 megaparsec baseline. *Phys. Rev. Lett.*, 81:4305–4308, 1998.
- [100] Daniele Fargion, Andrea Aiello, and Roberto Conversano. Horizontal tau air showers from mountains in deep valley: Traces of UHECR neutrino tau. In *26th International Cosmic Ray Conference*, volume 2, page 396, 6 1999.
- [101] Daniele Fargion. Discovering Ultra High Energy Neutrinos by Horizontal and Upward tau Air-Showers: Evidences in Terrestrial Gamma Flashes? *Astrophys. J.*, 570:909–925, 2002.
- [102] F. Becattini and S. Bottai. Extreme energy neutrino(tau) propagation through the Earth. *Astropart. Phys.*, 15:323–328, 2001.
- [103] S.Iyer Dutta, M.H. Reno, I. Sarcevic, and D. Seckel. Propagation of muons and taus at high-energies. *Phys. Rev. D*, 63:094020, 2001.

- [104] John F. Beacom, Patrick Crotty, and Edward W. Kolb. Enhanced Signal of Astrophysical Tau Neutrinos Propagating through Earth. *Phys. Rev. D*, 66:021302, 2002.
- [105] Sharada Iyer Dutta, Mary Hall Reno, and Ina Sarcevic. Secondary neutrinos from tau neutrino interactions in earth. *Phys. Rev. D*, 66:077302, 2002.
- [106] S. Bottai and S. Giurgola. UHE and EHE neutrino induced taus inside the Earth. *Astropart. Phys.*, 18:539–549, 2003.
- [107] Alexander Kusenko and Thomas J. Weiler. Neutrino cross-sections at high-energies and the future observations of ultrahigh-energy cosmic rays. *Phys. Rev. Lett.*, 88:161101, 2002.
- [108] Jonathan L. Feng, Peter Fisher, Frank Wilczek, and Terri M. Yu. Observability of earth skimming ultrahigh-energy neutrinos. *Phys. Rev. Lett.*, 88:161102, 2002.
- [109] Xavier Bertou, Pierre Billoir, O. Deligny, C. Lachaud, and A. Letessier-Selvon. Tau neutrinos in the Auger Observatory: A New window to UHECR sources. *Astropart. Phys.*, 17:183–193, 2002.
- [110] C. Aramo, A. Insolia, A. Leonardi, G. Miele, L. Perrone, O. Pisanti, and D. V. Semikoz. Earth-skimming UHE Tau neutrinos at the fluorescence detector of Pierre Auger observatory. *Astropart. Phys.*, 23:65–77, 2005.
- [111] Gennaro Miele, Sergio Pastor, and Ofelia Pisanti. The Aperture for UHE tau neutrinos of the Auger fluorescence detector using a digital elevation map. *Phys. Lett. B*, 634:137–142, 2006.
- [112] Alessandro Cuoco, G. Mangano, G. Miele, S. Pastor, L. Perrone, O. Pisanti, and P.D. Serpico. Ultrahigh Energy Neutrinos in the Mediterranean: Detecting $\nu(\tau)$ and $\nu(\mu)$ with a km³ Telescope. *JCAP*, 02:007, 2007.
- [113] Jaime Alvarez-Muñiz. The sensitivity of the surface detector of the Pierre Auger Observatory to UHE Earth-skimming and down-going neutrinos. In *30th International Cosmic Ray Conference*, volume 4, pages 389–392, 7 2007.
- [114] M. L. Ahnen et al. Limits on the flux of tau neutrinos from 1 PeV to 3 EeV with the MAGIC telescopes. *Astropart. Phys.*, 102:77–88, 2018.
- [115] A. M. Hillas. The Origin of Ultrahigh-Energy Cosmic Rays. *Ann. Rev. Astron. Astrophys.*, 22:425–444, 1984.
- [116] Kumiko Kotera and Angela V. Olinto. The Astrophysics of Ultrahigh Energy Cosmic Rays. *Ann. Rev. Astron. Astrophys.*, 49:119–153, 2011.
- [117] Shigeo S. Kimura, Kohta Murase, and Kenji Toma. Neutrino and Cosmic-Ray Emission and Cumulative Background from Radiatively Inefficient Accretion Flows in Low-Luminosity Active Galactic Nuclei. *Astrophys. J.*, 806:159, 2015.
- [118] J. Becker Tjus, B. Eichmann, F. Halzen, A. Kheirandish, and S. M. Saba. High-energy neutrinos from radio galaxies. *Phys. Rev. D*, 89(12):123005, 2014.
- [119] Eli Waxman and John N. Bahcall. High-energy neutrinos from astrophysical sources: An Upper bound. *Phys. Rev. D*, 59:023002, 1999.

- [120] John N. Bahcall and Eli Waxman. High-energy astrophysical neutrinos: The Upper bound is robust. *Phys. Rev. D*, 64:023002, 2001.
- [121] Kohta Murase, Dafne Guetta, and Markus Ahlers. Hidden Cosmic-Ray Accelerators as an Origin of TeV-PeV Cosmic Neutrinos. *Phys. Rev. Lett.*, 116(7):071101, 2016.
- [122] VL Ginzburg. On the origin of cosmic rays. *Il Nuovo Cimento (1955-1965)*, 8(2):430–439, 1958.
- [123] Pierre Cristofari, Pasquale Blasi, and Elena Amato. The low rate of Galactic pevatrons. *Astroparticle Physics*, 123:102492, December 2020.
- [124] Kohta Murase, Markus Ahlers, and Brian C. Lacki. Testing the Hadronuclear Origin of PeV Neutrinos Observed with IceCube. *Phys. Rev. D*, 88(12):121301, 2013.
- [125] Lyubov G. Sveshnikova. The knee in galactic cosmic ray spectrum and variety in supernovae. *Astron. Astrophys.*, 409:799–808, 2003.
- [126] Irene Tamborra, Shin'ichiro Ando, and Kohta Murase. Star-forming galaxies as the origin of diffuse high-energy backgrounds: Gamma-ray and neutrino connections, and implications for starburst history. *JCAP*, 09:043, 2014.
- [127] Todd A. Thompson, Eliot Quataert, Eli Waxman, Norman Murray, and Crystal L. Martin. Magnetic fields in starburst galaxies and the origin of the fir-radio correlation. *Astrophys. J.*, 645:186–198, 2006.
- [128] V. S. Ptuskin and Vladimir N. Zirakashvili. On the spectrum of high-energy cosmic rays produced by supernova remnants in the presence of strong cosmic-ray streaming instability and wave dissipation. *Astron. Astrophys.*, 429:755–765, 2005.
- [129] Yutaka Ohira, Kohta Murase, and Ryo Yamazaki. Escape-limited Model of Cosmic-ray Acceleration Revisited. *Astron. Astrophys.*, 513:A17, 2010.
- [130] D. Caprioli, E. Amato, and P. Blasi. The contribution of supernova remnants to the galactic cosmic ray spectrum. *Astropart. Phys.*, 33:160–168, 2010.
- [131] Luke O'C. Drury. Escaping the accelerator: how, when and in what numbers do cosmic rays get out of supernova remnants? *Mon. Not. Roy. Astron. Soc.*, 415:1807, 2011.
- [132] M Amenomori, YW Bao, XJ Bi, D Chen, TL Chen, WY Chen, Xu Chen, Y Chen, Cui Cirennima, Ding Danzengluobu, et al. Potential pevatron supernova remnant g106. 3+ 2.7 seen in the highest-energy gamma rays. *Nature Astronomy*, 2021.
- [133] Luke O'C. Drury, F A Aharonian, and H J Volk. The Gamma-ray visibility of supernova remnants: A Test of cosmic ray origin. *Astron. Astrophys.*, 287:959–971, 1994.
- [134] J. Alvarez-Muniz and F. Halzen. Possible high-energy neutrinos from the cosmic accelerator RX J1713.7-3946. *Astrophys. J. Lett.*, 576:L33–L36, 2002.
- [135] F. L. Villante and F. Vissani. How precisely neutrino emission from supernova remnants can be constrained by gamma ray observations? *Phys. Rev. D*, 78:103007, 2008.

- [136] Di Xiao, Peter Mészáros, Kohta Murase, and Zi-gao Dai. Revisiting the Contributions of Supernova and Hypernova Remnants to the Diffuse High-energy Backgrounds: Constraints on Very High Redshift Injection. *Astrophys. J.*, 826(2):133, 2016.
- [137] Kohta Murase. New Prospects for Detecting High-Energy Neutrinos from Nearby Supernovae. *Phys. Rev. D*, 97(8):081301, 2018.
- [138] R. D. Blandford and R. L. Znajek. Electromagnetic extractions of energy from Kerr black holes. *Mon. Not. Roy. Astron. Soc.*, 179:433–456, 1977.
- [139] Kip S Thorne and Douglas Macdonald. Electrodynamics in curved spacetime: 3+ 1 formulation. *Monthly Notices of the Royal Astronomical Society*, 198(2):339–343, 1982.
- [140] D. MacDonald and K. S. Thorne. Black-hole electrodynamics - an absolute-space/universal-time formulation. *Mon. Not. Roy. Astron. Soc.*, 198:345–383, 1982.
- [141] Brian Punsly and Ferdinand V. Coroniti. Relativistic Winds from Pulsar and Black Hole Magnetospheres. *Astrophys. J.*, 350:518, February 1990.
- [142] B. Punsly and F. V. Coroniti. Ergosphere-driven Winds. *Astrophys. J.*, 354:583, May 1990.
- [143] S. S. Komissarov. Electrodynamics of black hole magnetospheres. *Mon. Not. Roy. Astron. Soc.*, 350:407, 2004.
- [144] J. Becker Tjus, B. Eichmann, F. Halzen, A. Kheirandish, and S. M. Saba. High-energy neutrinos from radio galaxies. *Phys. Rev. D*, 89(12):123005, 2014.
- [145] G. Giacinti, M. Kachelrieß, O. Kalashev, A. Neronov, and D. V. Semikoz. Unified model for cosmic rays above 10^{17} eV and the diffuse gamma-ray and neutrino backgrounds. *Phys. Rev. D*, 92(8):083016, 2015.
- [146] Kohta Murase. *Active Galactic Nuclei as High-Energy Neutrino Sources*, pages 15–31. 2017.
- [147] Dan Hooper. A Case for Radio Galaxies as the Sources of IceCube’s Astrophysical Neutrino Flux. *JCAP*, 09:002, 2016.
- [148] Daniel Smith, Dan Hooper, and Abigail Vieregge. Revisiting AGN as the source of IceCube’s diffuse neutrino flux. *JCAP*, 03:031, 2021.
- [149] Mariangela Lisanti, Siddharth Mishra-Sharma, Lina Necib, and Benjamin R. Safdi. Deciphering Contributions to the Extragalactic Gamma-Ray Background from 2 GeV to 2 TeV. *Astrophys. J.*, 832(2):117, 2016.
- [150] Antonio Ambrosone, Marco Chianese, Damiano F. G. Fiorillo, Antonio Marinelli, Gennaro Miele, and Ofelia Pisanti. Starburst galaxies strike back: a multi-messenger analysis with Fermi-LAT and IceCube data. *Mon. Not. Roy. Astron. Soc.*, 503(3):4032–4049, 2021.
- [151] F. W. Stecker and M. H. Salamon. High-energy neutrinos from quasars. *Space Sci. Rev.*, 75:341–355, 1996.
- [152] Armen Atoyan and Charles D. Dermer. High-energy neutrinos from photomeson processes in blazars. *Phys. Rev. Lett.*, 87:221102, 2001.

- [153] Kohta Murase, Yoshiyuki Inoue, and Charles D. Dermer. Diffuse Neutrino Intensity from the Inner Jets of Active Galactic Nuclei: Impacts of External Photon Fields and the Blazar Sequence. *Phys. Rev. D*, 90(2):023007, 2014.
- [154] P. Padovani, E. Resconi, P. Giommi, B. Arsioli, and Y. L. Chang. Extreme blazars as counterparts of IceCube astrophysical neutrinos. *Mon. Not. Roy. Astron. Soc.*, 457(4):3582–3592, 2016.
- [155] Jaime Alvarez-Muniz and Peter Meszaros. High energy neutrinos from radio-quiet AGNs. *Phys. Rev. D*, 70:123001, 2004.
- [156] Asaf Pe’er, Kohta Murase, and Peter Meszaros. Radio Quiet AGNs as Possible Sources of Ultra-high Energy Cosmic Rays. *Phys. Rev. D*, 80:123018, 2009.
- [157] Andrea Palladino, Xavier Rodrigues, Shan Gao, and Walter Winter. Interpretation of the diffuse astrophysical neutrino flux in terms of the blazar sequence. *Astrophys. J.*, 871(1):41, 2019.
- [158] M. G. Aartsen et al. The contribution of Fermi-2LAC blazars to the diffuse TeV-PeV neutrino flux. *Astrophys. J.*, 835(1):45, 2017.
- [159] Andrii Neronov, Dmitri V. Semikoz, and Ksenia Ptitsyna. Strong constraints on hadronic models of blazar activity from Fermi and IceCube stacking analysis. *Astron. Astrophys.*, 603:A135, 2017.
- [160] A. Keivani et al. A Multimessenger Picture of the Flaring Blazar TXS 0506+056: implications for High-Energy Neutrino Emission and Cosmic Ray Acceleration. *Astrophys. J.*, 864(1):84, 2018.
- [161] Shan Gao, Anatoli Fedynitch, Walter Winter, and Martin Pohl. Modelling the coincident observation of a high-energy neutrino and a bright blazar flare. *Nature Astron.*, 3(1):88–92, 2019.
- [162] Peter Meszaros. Gamma-Ray Bursts. *Rept. Prog. Phys.*, 69:2259–2322, 2006.
- [163] Pawan Kumar and Bing Zhang. The physics of gamma-ray bursts & relativistic jets. *Phys. Rept.*, 561:1–109, 2014.
- [164] Eli Waxman. Cosmological gamma-ray bursts and the highest energy cosmic rays. *Phys. Rev. Lett.*, 75:386–389, 1995.
- [165] Mario Vietri. On the acceleration of ultrahigh-energy cosmic rays in gamma-ray bursts. *Astrophys. J.*, 453:883–889, 1995.
- [166] B. Paczynski and G. H. Xu. Neutrino bursts from gamma-ray bursts. *Astrophys. J.*, 427:708–713, 1994.
- [167] Eli Waxman and John N. Bahcall. High-energy neutrinos from cosmological gamma-ray burst fireballs. *Phys. Rev. Lett.*, 78:2292–2295, 1997.
- [168] Kohta Murase and Shigehiro Nagataki. High energy neutrino emission and neutrino background from gamma-ray bursts in the internal shock model. *Phys. Rev. D*, 73:063002, 2006.

- [169] Philipp Baerwald, Svenja Hummer, and Walter Winter. Magnetic Field and Flavor Effects on the Gamma-Ray Burst Neutrino Flux. *Phys. Rev. D*, 83:067303, 2011.
- [170] Mauricio Bustamante, Kohta Murase, Walter Winter, and Jonas Heinze. Multi-messenger light curves from gamma-ray bursts in the internal shock model. *Astrophys. J.*, 837(1):33, 2017.
- [171] R. Abbasi et al. An absence of neutrinos associated with cosmic-ray acceleration in γ -ray bursts. *Nature*, 484:351–353, 2012.
- [172] M. G. Aartsen et al. Search for Prompt Neutrino Emission from Gamma-Ray Bursts with IceCube. *Astrophys. J. Lett.*, 805(1):L5, 2015.
- [173] Mauricio Bustamante, Philipp Baerwald, Kohta Murase, and Walter Winter. Neutrino and cosmic-ray emission from multiple internal shocks in gamma-ray bursts. *Nature Commun.*, 6:6783, 2015.
- [174] P. Meszaros. Astrophysical Sources of High Energy Neutrinos in the IceCube Era. *Ann. Rev. Nucl. Part. Sci.*, 67:45–67, 2017.
- [175] Philipp Baerwald, Mauricio Bustamante, and Walter Winter. UHECR escape mechanisms for protons and neutrons from GRBs, and the cosmic ray-neutrino connection. *Astrophys. J.*, 768:186, 2013.
- [176] Noemie Globus, Denis Allard, Robert Mochkovitch, and Etienne Parizot. UHECR acceleration at GRB internal shocks. *Mon. Not. Roy. Astron. Soc.*, 451(1):751–790, 2015.
- [177] Daniel Biehl, Denise Boncioli, Anatoli Fedynitch, and Walter Winter. Cosmic-Ray and Neutrino Emission from Gamma-Ray Bursts with a Nuclear Cascade. *Astron. Astrophys.*, 611:A101, 2018.
- [178] Kohta Murase, Kunihito Ioka, Shigehiro Nagataki, and Takashi Nakamura. High Energy Neutrinos and Cosmic-Rays from Low-Luminosity Gamma-Ray Bursts? *Astrophys. J. Lett.*, 651:L5–L8, 2006.
- [179] Nayantara Gupta and Bing Zhang. Neutrino Spectra from Low and High Luminosity Populations of Gamma Ray Bursts. *Astropart. Phys.*, 27:386–391, 2007.
- [180] Nicholas Senno, Kohta Murase, and Peter Meszaros. Choked Jets and Low-Luminosity Gamma-Ray Bursts as Hidden Neutrino Sources. *Phys. Rev. D*, 93(8):083003, 2016.
- [181] Irene Tamborra and Shin’ichiro Ando. Inspecting the supernova–gamma-ray-burst connection with high-energy neutrinos. *Phys. Rev. D*, 93(5):053010, 2016.
- [182] Kohta Murase, Kunihito Ioka, Shigehiro Nagataki, and Takashi Nakamura. High-energy cosmic-ray nuclei from high- and low-luminosity gamma-ray bursts and implications for multi-messenger astronomy. *Phys. Rev. D*, 78:023005, 2008.
- [183] B. Theodore Zhang, Kohta Murase, Shigeo S. Kimura, Shunsaku Horiuchi, and Peter Mészáros. Low-luminosity gamma-ray bursts as the sources of ultrahigh-energy cosmic ray nuclei. *Phys. Rev. D*, 97(8):083010, 2018.
- [184] Denise Boncioli, Daniel Biehl, and Walter Winter. On the common origin of cosmic rays across the ankle and diffuse neutrinos at the highest energies from low-luminosity Gamma-Ray Bursts. *Astrophys. J.*, 872(1):110, 2019.

- [185] B. Theodore Zhang and Kohta Murase. Ultrahigh-energy cosmic-ray nuclei and neutrinos from engine-driven supernovae. *Phys. Rev. D*, 100(10):103004, 2019.
- [186] D. N. Burrows et al. Discovery of the Onset of Rapid Accretion by a Dormant Massive Black Hole. *Nature*, 476:421, 2011.
- [187] Glennys R. Farrar and Andrei Gruzinov. Giant AGN Flares and Cosmic Ray Bursts. *Astrophys. J.*, 693:329–332, 2009.
- [188] Kohta Murase. Astrophysical high-energy neutrinos and gamma-ray bursts. *AIP Conf. Proc.*, 1065(1):201–206, 2008.
- [189] Xiang-Yu Wang, Ruo-Yu Liu, Zi-Gao Dai, and K. S. Cheng. Probing the tidal disruption flares of massive black holes with high-energy neutrinos. *Phys. Rev. D*, 84:081301, 2011.
- [190] Lixin Dai and Ke Fang. Can tidal disruption events produce the IceCube neutrinos? *Mon. Not. Roy. Astron. Soc.*, 469(2):1354–1359, 2017.
- [191] Nicholas Senno, Kohta Murase, and Peter Meszaros. High-energy Neutrino Flares from X-Ray Bright and Dark Tidal Disruption Events. *Astrophys. J.*, 838(1):3, 2017.
- [192] Cecilia Lunardini and Walter Winter. High Energy Neutrinos from the Tidal Disruption of Stars. *Phys. Rev. D*, 95(12):123001, 2017.
- [193] B. Theodore Zhang, Kohta Murase, Foteini Oikonomou, and Zhuo Li. High-energy cosmic ray nuclei from tidal disruption events: Origin, survival, and implications. *Phys. Rev. D*, 96(6):063007, 2017. [Addendum: *Phys.Rev.D* 96, 069902 (2017)].
- [194] Claire Guépin, Kumiko Kotera, Enrico Barausse, Ke Fang, and Kohta Murase. Ultra-High Energy Cosmic Rays and Neutrinos from Tidal Disruptions by Massive Black Holes. *Astron. Astrophys.*, 616:A179, 2018. [Erratum: *Astron.Astrophys.* 636, C3 (2020)].
- [195] Walter Winter and Cecilia Lunardini. A concordance scenario for the observation of a neutrino from the Tidal Disruption Event AT2019dsg. *Nature Astron.*, 5(5):472–477, 2021.
- [196] Robert Stein. Search for Neutrinos from Populations of Optical Transients. *PoS, ICRC2019:1016*, 2020.
- [197] Kohta Murase, Shigeo S. Kimura, B. Theodore Zhang, Foteini Oikonomou, and Maria Petropoulou. High-Energy Neutrino and Gamma-Ray Emission from Tidal Disruption Events. *Astrophys. J.*, 902(2):108, 2020.
- [198] Abraham Loeb and Eli Waxman. The Cumulative background of high energy neutrinos from starburst galaxies. *JCAP*, 05:003, 2006.
- [199] H. J. Voelk. The correlation between radio and far-infrared emission for disk galaxies : a calorimeter theory. *??jnlA&A*, 218:67–70, July 1989.
- [200] Keith Bechtol, Markus Ahlers, Mattia Di Mauro, Marco Ajello, and Justin Vandenbroucke. Evidence against star-forming galaxies as the dominant source of IceCube neutrinos. *Astrophys. J.*, 836(1):47, 2017.
- [201] M. Ackermann et al. The spectrum of isotropic diffuse gamma-ray emission between 100 MeV and 820 GeV. *Astrophys. J.*, 799:86, 2015.

- [202] Andrea Palladino, Anatoli Fedynitch, Rasmus W. Rasmussen, and Andrew M. Taylor. IceCube Neutrinos from Hadronically Powered Gamma-Ray Galaxies. *JCAP*, 09:004, 2019.
- [203] Enrico Peretti, Pasquale Blasi, Felix Aharonian, and Giovanni Morlino. Cosmic ray transport and radiative processes in nuclei of starburst galaxies. *Mon. Not. Roy. Astron. Soc.*, 487(1):168–180, 2019.
- [204] Enrico Peretti, Pasquale Blasi, Felix Aharonian, Giovanni Morlino, and Pierre Cristofari. Contribution of starburst nuclei to the diffuse gamma-ray and neutrino flux. *Mon. Not. Roy. Astron. Soc.*, 493(4), 2020.
- [205] H. J. Volk, F. A. Aharonian, and D. Breitschwerdt. The nonthermal energy content and gamma-ray emission of starburst galaxies and clusters of galaxies. *Space Sci. Rev.*, 75:279–297, 1996.
- [206] V. S. Berezhinsky, P. Blasi, and V. S. Ptuskin. Clusters of Galaxies as a Storage Room for Cosmic Rays. *Astrophys. J.*, 487:529–535, 1997.
- [207] Abraham Loeb and Eli Waxman. Gamma-ray background from structure formation in the intergalactic medium. *Nature*, 405:156, 2000.
- [208] Uri Keshet, Eli Waxman, Abraham Loeb, Volker Springel, and Lars Hernquist. Gamma-rays from intergalactic shocks. *Astrophys. J.*, 585:128–150, 2003.
- [209] Colin A. Norman, Donald B. Melrose, and Abraham Achterberg. The Origin of Cosmic Rays above $10^{18.5}$ eV. *Astrophys. J.*, 454:60, November 1995.
- [210] Susumu Inoue, Felix A. Aharonian, and Naoshi Sugiyama. Hard x-ray and gamma-ray emission induced by ultra-high energy protons in cluster accretion shocks. *Astrophys. J. Lett.*, 628:L9–L12, 2005.
- [211] Fabio Zandanel, Irene Tamborra, Stefano Gabici, and Shin’ichiro Ando. High-energy gamma-ray and neutrino backgrounds from clusters of galaxies and radio constraints. *Astron. Astrophys.*, 578:A32, 2015.
- [212] Kohta Murase, Susumu Inoue, and Shigehiro Nagataki. Cosmic Rays Above the Second Knee from Clusters of Galaxies and Associated High-Energy Neutrino Emission. *Astrophys. J. Lett.*, 689:L105, 2008.
- [213] F. W. Stecker. Diffuse Fluxes of Cosmic High-Energy Neutrinos. *Astrophys. J.*, 228:919–927, 1979.
- [214] G. Domokos, B. Elliott, and S. Kovesi-Domokos. Cosmic neutrino production in the Milky Way. *J. Phys. G*, 19:899–912, 1993.
- [215] V. S. Berezhinsky, T. K. Gaisser, F. Halzen, and Todor Stanev. Diffuse radiation from cosmic ray interactions in the galaxy. *Astropart. Phys.*, 1:281–288, 1993.
- [216] G. Ingelman and M. Thunman. Particle production in the interstellar medium. 3 1996.
- [217] Carmelo Evoli, Dario Grasso, and Luca Maccione. Diffuse Neutrino and Gamma-ray Emissions of the Galaxy above the TeV. *JCAP*, 06:003, 2007.

- [218] M. Ackermann et al. Fermi-LAT Observations of the Diffuse Gamma-Ray Emission: Implications for Cosmic Rays and the Interstellar Medium. *Astrophys. J.*, 750:3, 2012.
- [219] F. Acero et al. Development of the Model of Galactic Interstellar Emission for Standard Point-Source Analysis of Fermi Large Area Telescope Data. *Astrophys. J. Suppl.*, 223(2):26, 2016.
- [220] Markus Ahlers and Kohta Murase. Probing the Galactic Origin of the IceCube Excess with Gamma-Rays. *Phys. Rev. D*, 90(2):023010, 2014.
- [221] Jagdish C. Joshi, Walter Winter, and Nayantara Gupta. How Many of the Observed Neutrino Events Can Be Described by Cosmic Ray Interactions in the Milky Way? *Mon. Not. Roy. Astron. Soc.*, 439(4):3414–3419, 2014. [Erratum: *Mon. Not. Roy. Astron. Soc.* 446, 892 (2014)].
- [222] M. Kachelriess and S. Ostapchenko. Neutrino yield from Galactic cosmic rays. *Phys. Rev. D*, 90(8):083002, 2014.
- [223] Andrey E. Vladimirov, Seth W. Digel, Gudlaugur Johannesson, Peter F. Michelson, Igor V. Moskalenko, Patrick L. Nolan, Elena Orlando, Troy A. Porter, and Andrew W. Strong. GALPROP WebRun: an internet-based service for calculating galactic cosmic ray propagation and associated photon emissions. *Comput. Phys. Commun.*, 182:1156–1161, 2011.
- [224] Daniele Gaggero, Alfredo Urbano, Mauro Valli, and Piero Ullio. Gamma-ray sky points to radial gradients in cosmic-ray transport. *Phys. Rev. D*, 91(8):083012, 2015.
- [225] Daniele Gaggero, Dario Grasso, Antonio Marinelli, Alfredo Urbano, and Mauro Valli. The gamma-ray and neutrino sky: A consistent picture of Fermi-LAT, Milagro, and IceCube results. *Astrophys. J. Lett.*, 815(2):L25, 2015.
- [226] D. Gaggero, D. Grasso, A. Marinelli, M. Taoso, and A. Urbano. Diffuse cosmic rays shining in the Galactic center: A novel interpretation of H.E.S.S. and Fermi-LAT γ -ray data. *Phys. Rev. Lett.*, 119(3):031101, 2017.
- [227] Markus Ahlers, Yang Bai, Vernon Barger, and Ran Lu. Galactic neutrinos in the TeV to PeV range. *Phys. Rev. D*, 93(1):013009, 2016.
- [228] A. Albert et al. New constraints on all flavor Galactic diffuse neutrino emission with the ANTARES telescope. *Phys. Rev. D*, 96(6):062001, 2017.
- [229] M. G. Aartsen et al. Constraints on Galactic Neutrino Emission with Seven Years of IceCube Data. *Astrophys. J.*, 849(1):67, 2017.
- [230] A. Albert et al. Joint Constraints on Galactic Diffuse Neutrino Emission from the ANTARES and IceCube Neutrino Telescopes. *Astrophys. J. Lett.*, 868(2):L20, 2018.
- [231] M. Amenomori et al. First Detection of sub-PeV Diffuse Gamma Rays from the Galactic Disk: Evidence for Ubiquitous Galactic Cosmic Rays beyond PeV Energies. *Phys. Rev. Lett.*, 126(14):141101, 2021.
- [232] Ke Fang and Kohta Murase. Multi-messenger Implications of Sub-PeV Diffuse Galactic Gamma-Ray Emission. 4 2021.
- [233] M. G. Aartsen et al. First observation of PeV-energy neutrinos with IceCube. *Phys. Rev. Lett.*, 111:021103, 2013.

- [234] Pedro Abreu et al. Ultrahigh Energy Neutrinos at the Pierre Auger Observatory. *Adv. High Energy Phys.*, 2013:708680, 2013.
- [235] Roberto Aloisio, Pasquale Blasi, Ivan De Mitri, and Sergio Petrer. *Selected Topics in Cosmic Ray Physics*. 7 2017.
- [236] V. S. Berezinsky and G. T. Zatsepin. Cosmic rays at ultrahigh-energies (neutrino?). *Phys. Lett. B*, 28:423–424, 1969.
- [237] Veniamin Berezinsky, Pasquale Blasi, and Alexander Vilenkin. Ultrahigh-energy gamma-rays as signature of topological defects. *Phys. Rev. D*, 58:103515, 1998.
- [238] M. Nagano and Alan A. Watson. Observations and implications of the ultrahigh-energy cosmic rays. *Rev. Mod. Phys.*, 72:689–732, 2000.
- [239] Ralph Engel, David Seckel, and Todor Stanev. Neutrinos from propagation of ultrahigh-energy protons. *Phys. Rev. D*, 64:093010, 2001.
- [240] Luis Anchordoqui, Thomas Cantzon Paul, Stephen Reucroft, and John Swain. Ultrahigh-energy cosmic rays: The State of the art before the Auger Observatory. *Int. J. Mod. Phys. A*, 18:2229–2366, 2003.
- [241] Z. Fodor, S.D. Katz, and A. Ringwald. Relic neutrino masses and the highest energy cosmic rays. *JHEP*, 06:046, 2002.
- [242] Oleg E. Kalashev, Vadim A. Kuzmin, Dmitry V. Semikoz, and Gunter Sigl. Ultrahigh-energy neutrino fluxes and their constraints. *Phys. Rev. D*, 66:063004, 2002.
- [243] Dmitry V. Semikoz and Gunter Sigl. Ultrahigh-energy neutrino fluxes: New constraints and implications. *JCAP*, 04:003, 2004.
- [244] Z. Fodor, S.D. Katz, A. Ringwald, and H. Tu. Bounds on the cosmogenic neutrino flux. *JCAP*, 11:015, 2003.
- [245] Maximo Ave, N. Busca, Angela V. Olinto, Alan A. Watson, and T. Yamamoto. Cosmogenic neutrinos from ultra-high energy nuclei. *Astropart. Phys.*, 23:19–29, 2005.
- [246] David Seckel and Todor Stanev. Neutrinos: The Key to UHE cosmic rays. *Phys. Rev. Lett.*, 95:141101, 2005.
- [247] Daniel De Marco, Todor Stanev, and F.W. Stecker. Cosmogenic neutrinos from cosmic ray interactions with extragalactic infrared photons. *Phys. Rev. D*, 73:043003, 2006.
- [248] Denis Allard, M. Ave, N. Busca, M.A. Malkan, A.V. Olinto, E. Parizot, F.W. Stecker, and T. Yamamoto. Cosmogenic Neutrinos from the propagation of Ultrahigh Energy Nuclei. *JCAP*, 09:005, 2006.
- [249] Julia K. Becker. High-energy neutrinos in the context of multimessenger physics. *Phys. Rept.*, 458:173–246, 2008.
- [250] Luis A. Anchordoqui, Haim Goldberg, Dan Hooper, Subir Sarkar, and Andrew M. Taylor. Predictions for the Cosmogenic Neutrino Flux in Light of New Data from the Pierre Auger Observatory. *Phys. Rev. D*, 76:123008, 2007.

- [251] V. Berezhinsky, A. Gazizov, M. Kachelriess, and S. Ostapchenko. Restricting UHECRs and cosmogenic neutrinos with Fermi-LAT. *Phys. Lett. B*, 695:13–18, 2011.
- [252] M. Ahlers, L.A. Anchordoqui, M.C. Gonzalez-Garcia, F. Halzen, and S. Sarkar. GZK Neutrinos after the Fermi-LAT Diffuse Photon Flux Measurement. *Astropart. Phys.*, 34:106–115, 2010.
- [253] U.F. Katz and Ch. Spiering. High-Energy Neutrino Astrophysics: Status and Perspectives. *Prog. Part. Nucl. Phys.*, 67:651–704, 2012.
- [254] Graciela B. Gelmini, Oleg Kalashev, and Dmitri V. Semikoz. Gamma-Ray Constraints on Maximum Cosmogenic Neutrino Fluxes and UHECR Source Evolution Models. *JCAP*, 01:044, 2012.
- [255] Kenny C. Y. Ng and John F. Beacom. Cosmic neutrino cascades from secret neutrino interactions. *Phys. Rev. D*, 90(6):065035, 2014. [Erratum: Phys.Rev.D 90, 089904 (2014)].
- [256] Kohta Murase. On the Origin of High-Energy Cosmic Neutrinos. *AIP Conf. Proc.*, 1666(1):040006, 2015.
- [257] Jonas Heinze, Denise Boncioli, Mauricio Bustamante, and Walter Winter. Cosmogenic Neutrinos Challenge the Cosmic Ray Proton Dip Model. *Astrophys. J.*, 825(2):122, 2016.
- [258] R. Aloisio, D. Boncioli, A di Matteo, A.F. Grillo, S. Petrer, and F. Salamida. Cosmogenic neutrinos and ultra-high energy cosmic ray models. *JCAP*, 10:006, 2015.
- [259] Francis Halzen. High-energy neutrino astrophysics. *Nature Phys.*, 13(3):232–238, 2016.
- [260] John F. Cherry and Ian M. Shoemaker. Sterile neutrino origin for the upward directed cosmic ray showers detected by ANITA. *Phys. Rev. D*, 99(6):063016, 2019.
- [261] M. Ajello, M. Di Mauro, V.S. Paliya, and S. Garrappa. The γ -ray Emission of Star-Forming Galaxies. *Astrophys. J.*, 894(2):88, 2020.
- [262] Andrea Palladino and Walter Winter. A multi-component model for observed astrophysical neutrinos. *Astron. Astrophys.*, 615:A168, 2018.
- [263] Timothy A. D. Paglione, Alan P. Marscher, James M. Jackson, and David L. Bertsch. Diffuse Gamma-Ray Emission from the Starburst Galaxy NGC 253. *Astrophys. J.*, 460:295, March 1996.
- [264] Diego F. Torres. Theoretical modelling of the diffuse emission of gamma-rays from extreme regions of star formation. The Case of Arp 220. *Astrophys. J.*, 617:966–986, 2004.
- [265] M. Persic, Y. Rephaeli, and Y. Arieli. Vhe emission from m82. 2008.
- [266] Y. Rephaeli, Y. Arieli, and M. Persic. High Energy Emission from the Starburst Galaxy NGC253. *Mon. Not. Roy. Astron. Soc.*, 401:423, 2010.
- [267] Brian C. Lacki and Todd A. Thompson. Diffuse Hard X-ray Emission in Starburst Galaxies as Synchrotron from Very High Energy Electrons. *Astrophys. J.*, 762:29, 2013.
- [268] Tova M. Yoast-Hull, John E. Everett, J.S. Gallagher, and Ellen G. Zweibel. Winds, Clumps, and Interacting Cosmic Rays in M82. *Astrophys. J.*, 768:53, 2013.

- [269] Xilu Wang and Brian D. Fields. Are Starburst Galaxies Proton Calorimeters? *Mon. Not. Roy. Astron. Soc.*, 474(3):4073–4088, 2018.
- [270] Mark R. Krumholz, Roland M. Crocker, Siyao Xu, A. Lazarian, M.T. Rosevear, and Jasper Bedwell-Wilson. Cosmic ray transport in starburst galaxies. *Mon. Not. Roy. Astron. Soc.*, 493(2):2817–2833, 2020.
- [271] Ji-Hoon Ha, Dongsu Ryu, and Hyesung Kang. Modeling of Cosmic-Ray Production and Transport and Estimation of Gamma-Ray and Neutrino Emissions in Starburst Galaxies. 8 2020.
- [272] Eduardo M. Gutiérrez, Gustavo E. Romero, and Florencia L. Vieyro. Cosmic rays from the nearby starburst galaxy NGC 253: the effect of a low luminosity active galactic nucleus. *Mon. Not. Roy. Astron. Soc.*, 494(2):2109–2116, 2020.
- [273] Robert H. Kraichnan. Inertial-Range Spectrum of Hydromagnetic Turbulence. *Phys. Fluids*, 8:1385–1387, 1965.
- [274] Vladimir N. Zirakashvili and F. Aharonian. Analytical solutions for energy spectra of electrons accelerated by nonrelativistic shock-waves in shell type supernova remnants. *Astron. Astrophys.*, 465:695–702, 2007.
- [275] Pasquale Blasi. Shock acceleration of electrons in the presence of synchrotron losses: I. test particle theory. *Mon. Not. Roy. Astron. Soc.*, 402:2807, 2010.
- [276] Franceschini, Alberto and Rodighiero, Giulia. The extragalactic background light revisited and the cosmic photon-photon opacity (corrigendum). *A&A*, 614:C1, 2018.
- [277] S. Abdollahi et al. *Fermi* Large Area Telescope Fourth Source Catalog. *Astrophys. J. Suppl.*, 247(1):33, 2020.
- [278] C. Gruppioni et al. The Herschel PEP/HerMES Luminosity Function. I: Probing the Evolution of PACS selected Galaxies to z 4. *Mon. Not. Roy. Astron. Soc.*, 432:23, 2013.
- [279] I. Delvecchio et al. Tracing the cosmic growth of supermassive black holes to $z \sim 3$ with Herschel. *Mon. Not. Roy. Astron. Soc.*, 439(3):2736–2754, 2014.
- [280] Jr. Kennicutt, Robert C. Star formation in galaxies along the Hubble sequence. *Ann. Rev. Astron. Astrophys.*, 36:189–231, 1998.
- [281] Jr. Kennicutt, Robert C. The Global Schmidt law in star forming galaxies. *Astrophys. J.*, 498:541, 1998.
- [282] M. Ackermann et al. Resolving the Extragalactic γ -Ray Background above 50 GeV with the *Fermi* Large Area Telescope. *Phys. Rev. Lett.*, 116(15):151105, 2016.
- [283] Austin Schneider. Characterization of the Astrophysical Diffuse Neutrino Flux with IceCube High-Energy Starting Events. *PoS, ICRC2019:1004*, 2020.
- [284] M.G. Aartsen et al. Characteristics of the diffuse astrophysical electron and tau neutrino flux with six years of IceCube high energy cascade data. *Phys. Rev. Lett.*, 125:121104, 2020.
- [285] G. Ghisellini, C. Righi, L. Costamante, and F. Tavecchio. The *Fermi* blazar sequence. *Mon. Not. Roy. Astron. Soc.*, 469(1):255–266, 2017.

- [286] B. Theodore Zhang and Zhuo Li. Constraints on cosmic ray loading and PeV neutrino production in blazars. *JCAP*, 03:024, 2017.
- [287] M.G. Aartsen et al. The contribution of Fermi-2LAC blazars to the diffuse TeV-PeV neutrino flux. *Astrophys. J.*, 835(1):45, 2017.
- [288] Yoshiyuki Inoue. Contribution of the Gamma-ray Loud Radio Galaxies Core Emissions to the Cosmic MeV and GeV Gamma-Ray Background Radiation. *Astrophys. J.*, 733:66, 2011.
- [289] M. Di Mauro, F. Calore, F. Donato, M. Ajello, and L. Latronico. Diffuse γ -ray emission from misaligned active galactic nuclei. *Astrophys. J.*, 780:161, 2014.
- [290] Carlos Blanco and Dan Hooper. High-Energy Gamma Rays and Neutrinos from Nearby Radio Galaxies. *JCAP*, 12:017, 2017.
- [291] Nissim Fraija and Antonio Marinelli. Neutrino, Γ -ray, and Cosmic-ray Fluxes From the Core of the Closest Radio Galaxies. *Astrophys. J.*, 830(2):81, 2016.
- [292] Antonio Capanema, Arman Esmaili, and Pasquale Dario Serpico. Where do IceCube neutrinos come from? Hints from the diffuse gamma-ray flux. 7 2020.
- [293] M. G. Aartsen et al. Evidence for High-Energy Extraterrestrial Neutrinos at the IceCube Detector. *Science*, 342:1242856, 2013.
- [294] Luis A. Anchordoqui, Thomas C. Paul, Luiz H. M. da Silva, Diego F. Torres, and Brian J. Vlcek. What IceCube data tell us about neutrino emission from star-forming galaxies (so far). *Phys. Rev. D*, 89(12):127304, 2014.
- [295] Kimberly Emig, Cecilia Lunardini, and Rogier Windhorst. Do high energy astrophysical neutrinos trace star formation? *JCAP*, 12:029, 2015.
- [296] Reetanjali Moharana and Soebur Razzaque. Angular correlation between IceCube high-energy starting events and starburst sources. *JCAP*, 12:021, 2016.
- [297] M.G. Aartsen et al. Search for steady point-like sources in the astrophysical muon neutrino flux with 8 years of IceCube data. *Eur. Phys. J. C*, 79(3):234, 2019.
- [298] Cecilia Lunardini, Gregory S. Vance, Kimberly L. Emig, and Rogier A. Windhorst. Are starburst galaxies a common source of high energy neutrinos and cosmic rays? *JCAP*, 10:073, 2019.
- [299] Walter Winter. Interpretation of neutrino flux limits from neutrino telescopes on the Hillas plot. *Phys. Rev. D*, 85:023013, 2012.
- [300] Walter Winter. Photohadronic Origin of the TeV-PeV Neutrinos Observed in IceCube. *Phys. Rev. D*, 88:083007, 2013.
- [301] Claire Guépin and Kumiko Kotera. Can we observe neutrino flares in coincidence with explosive transients? *Astron. Astrophys.*, 603:A76, 2017.
- [302] Philipp Baerwald, Svenja Hummer, and Walter Winter. Systematics in the Interpretation of Aggregated Neutrino Flux Limits and Flavor Ratios from Gamma-Ray Bursts. *Astropart. Phys.*, 35:508–529, 2012.

- [303] Svenja Hummer, Philipp Baerwald, and Walter Winter. Neutrino Emission from Gamma-Ray Burst Fireballs, Revised. *Phys. Rev. Lett.*, 108:231101, 2012.
- [304] Shan Gao, Martin Pohl, and Walter Winter. On the direct correlation between gamma-rays and PeV neutrinos from blazars. *Astrophys. J.*, 843(2):109, 2017.
- [305] Olaf Schulz. The IceCube DeepCore. *AIP Conf. Proc.*, 1085(1):783–786, 2009.
- [306] A. Kappes. KM3NeT: A Next Generation Neutrino Telescope in the Mediterranean Sea. 11 2007.
- [307] Erik Blaufuss, C. Kopper, and C. Haack. The IceCube-Gen2 High Energy Array. *PoS, ICRC2015:1146*, 2016.
- [308] Ningqiang Song, Shirley Weishi Li, Carlos A. Argüelles, Mauricio Bustamante, and Aaron C. Vincent. The Future of High-Energy Astrophysical Neutrino Flavor Measurements. *JCAP*, 04:054, 2021.
- [309] Gary J. Feldman and Robert D. Cousins. A Unified approach to the classical statistical analysis of small signals. *Phys. Rev. D*, 57:3873–3889, 1998.
- [310] F. Zwicky. On the Masses of Nebulae and of Clusters of Nebulae. *Astrophys. J.*, 86:217–246, 1937.
- [311] Vera C. Rubin and W. Kent Ford, Jr. Rotation of the Andromeda Nebula from a Spectroscopic Survey of Emission Regions. *Astrophys. J.*, 159:379–403, 1970.
- [312] Gianfranco Bertone and Dan Hooper. History of dark matter. *Rev. Mod. Phys.*, 90(4):045002, 2018.
- [313] W. D. Apel et al. KASCADE-Grande Limits on the Isotropic Diffuse Gamma-Ray Flux between 100 TeV and 1 EeV. *Astrophys. J.*, 848(1):1, 2017.
- [314] M. C. Chantell, C. E. Covault, J. W. Cronin, B. E. Fick, L. F. Fortson, J. W. Fowler, K. D. Green, B. J. Newport, R. A. Ong, S. Oser, M. A. Catanese, M. A. K. Glasmacher, J. Matthews, D. F. Nitz, D. Sinclair, J. C. van der Velde, and D. B. Kieda. Limits on the isotropic diffuse flux of ultrahigh energy γ radiation. *Phys. Rev. Lett.*, 79:1805–1808, Sep 1997.
- [315] M. Cassidy, L. F. Fortson, J. W. Fowler, C. H. Jui, D. B. Kieda, E. C. Loh, R. A. Ong, and P. Sommers. CASA BLANCA: A Large nonimaging Cherenkov detector at CASA-MIA. 7 1997.
- [316] P. Picozza et al. PAMELA: A Payload for Antimatter Matter Exploration and Light-nuclei Astrophysics. *Astropart. Phys.*, 27:296–315, 2007.
- [317] M. Aguilar et al. Antiproton Flux, Antiproton-to-Proton Flux Ratio, and Properties of Elementary Particle Fluxes in Primary Cosmic Rays Measured with the Alpha Magnetic Spectrometer on the International Space Station. *Phys. Rev. Lett.*, 117(9):091103, 2016.
- [318] M. Aguilar et al. Towards Understanding the Origin of Cosmic-Ray Positrons. *Phys. Rev. Lett.*, 122(4):041102, 2019.
- [319] H. Kawai et al. Telescope array experiment. *Nucl. Phys. B Proc. Suppl.*, 175-176:221–226, 2008.

- [320] D. Kang et al. Latest results from the KASCADE-Grande data analysis. *PoS, ICRC2019*:306, 2021.
- [321] J. Abraham, P. Abreu, M. Aglietta, E.J. Ahn, D. Allard, J. Allen, J. Alvarez-Muñiz, M. Ambrosio, L. Anchordoqui, S. Andringa, and et al. Measurement of the energy spectrum of cosmic rays above 1018 ev using the pierre auger observatory. *Physics Letters B*, 685(4-5):239–246, Mar 2010.
- [322] Kohta Murase and John F. Beacom. Constraining Very Heavy Dark Matter Using Diffuse Backgrounds of Neutrinos and Cascaded Gamma Rays. *JCAP*, 10:043, 2012.
- [323] Arman Esmaili, Alejandro Ibarra, and Orlando L.G. Peres. Probing the stability of superheavy dark matter particles with high-energy neutrinos. *JCAP*, 11:034, 2012.
- [324] Brian Feldstein, Alexander Kusenko, Shigeki Matsumoto, and Tsutomu T. Yanagida. Neutrinos at IceCube from Heavy Decaying Dark Matter. *Phys. Rev. D*, 88(1):015004, 2013.
- [325] Arman Esmaili and Pasquale Dario Serpico. Are IceCube neutrinos unveiling PeV-scale decaying dark matter? *JCAP*, 11:054, 2013.
- [326] Carsten Rott, Kazunori Kohri, and Seong Chan Park. Superheavy dark matter and IceCube neutrino signals: Bounds on decaying dark matter. *Phys. Rev. D*, 92(2):023529, 2015.
- [327] Sofiane M. Boucenna, Marco Chianese, Gianpiero Mangano, Gennaro Miele, Stefano Morisi, Ofelia Pisanti, and Edoardo Vitagliano. Decaying Leptophilic Dark Matter at IceCube. *JCAP*, 12:055, 2015.
- [328] Arman Esmaili and Pasquale Dario Serpico. Gamma-ray bounds from EAS detectors and heavy decaying dark matter constraints. *JCAP*, 10:014, 2015.
- [329] Kohta Murase, Ranjan Laha, Shin'ichiro Ando, and Markus Ahlers. Testing the Dark Matter Scenario for PeV Neutrinos Observed in IceCube. *Phys. Rev. Lett.*, 115(7):071301, 2015.
- [330] Timothy Cohen, Kohta Murase, Nicholas L. Rodd, Benjamin R. Safdi, and Yotam Soreq. γ -ray Constraints on Decaying Dark Matter and Implications for IceCube. *Phys. Rev. Lett.*, 119(2):021102, 2017.
- [331] M. G. Aartsen et al. Search for neutrinos from decaying dark matter with IceCube. *Eur. Phys. J. C*, 78(10):831, 2018.
- [332] M. Kachelriess, O. E. Kalashev, and M. Yu. Kuznetsov. Heavy decaying dark matter and IceCube high energy neutrinos. *Phys. Rev. D*, 98(8):083016, 2018.
- [333] Ye Xu. Direct detection of Ultra-High Energy WIMPs with a satellite detector like JEM-EUSO. *Astrophys. J.*, 876(1):14, 2019.
- [334] Atri Bhattacharya, Arman Esmaili, Sergio Palomares-Ruiz, and Ina Sarcevic. Update on decaying and annihilating heavy dark matter with the 6-year IceCube HESE data. *JCAP*, 05:051, 2019.
- [335] Marco Chianese, Damiano F.G. Fiorillo, Gennaro Miele, Stefano Morisi, and Ofelia Pisanti. Decaying dark matter at IceCube and its signature on High Energy gamma experiments. *JCAP*, 11:046, 2019.

- [336] Ariane Dekker, Marco Chianese, and Shin'ichiro Ando. Probing dark matter signals in neutrino telescopes through angular power spectrum. *JCAP*, 09:007, 2020.
- [337] Koji Ishiwata, Oscar Macias, Shin'ichiro Ando, and Makoto Arimoto. Probing heavy dark matter decays with multi-messenger astrophysical data. *JCAP*, 01:003, 2020.
- [338] Carlos A. Argüelles and Hrvoje Dujmovic. Searches for Connections Between Dark Matter and Neutrinos with the IceCube High-Energy Starting Event Sample. *PoS, ICRC2019:839*, 2020.
- [339] Carlos A. Argüelles, Alejandro Diaz, Ali Kheirandish, Andrés Olivares-Del-Campo, Ibrahim Safa, and Aaron C. Vincent. Dark matter annihilation to neutrinos. *Rev. Mod. Phys.*, 93(3):035007, 2021.
- [340] Oleg Kalashev, Mikhail Kuznetsov, and Yana Zhezher. Constraining superheavy decaying dark matter with ultra-high-energy gamma rays from dwarf spheroidal galaxies. 5 2020.
- [341] Marco Chianese, Damiano F. G. Fiorillo, Rasmi Hajjar, Gennaro Miele, Stefano Morisi, and Ninetta Saviano. Heavy decaying dark matter at future neutrino radio telescopes. *JCAP*, 05:074, 2021.
- [342] Marco Chianese, Damiano F. G. Fiorillo, Rasmi Hajjar, Gennaro Miele, and Ninetta Saviano. Constraints on heavy decaying dark matter with current gamma-ray measurements. 8 2021.
- [343] Kim Griest and Marc Kamionkowski. Unitarity Limits on the Mass and Radius of Dark Matter Particles. *Phys. Rev. Lett.*, 64:615, 1990.
- [344] Jesús Zavala. Galactic PeV neutrinos from dark matter annihilation. *Phys. Rev. D*, 89(12):123516, 2014.
- [345] Paolo Ciafaloni, Denis Comelli, Antonio Riotto, Filippo Sala, Alessandro Strumia, and Alfredo Urbano. Weak Corrections are Relevant for Dark Matter Indirect Detection. *JCAP*, 03:019, 2011.
- [346] Christian W. Bauer, Nicholas L. Rodd, and Bryan R. Webber. Dark Matter Spectra from the Electroweak to the Planck Scale. 7 2020.
- [347] Julio F. Navarro, Carlos S. Frenk, and Simon D. M. White. The Structure of cold dark matter halos. *Astrophys. J.*, 462:563–575, 1996.
- [348] Jatan Buch, Marco Cirelli, Gaëlle Giesen, and Marco Taoso. PPPC 4 DM secondary: A Poor Particle Physicist Cookbook for secondary radiation from Dark Matter. *JCAP*, 09:037, 2015.
- [349] Sergio Palomares-Ruiz, Aaron C. Vincent, and Olga Mena. Spectral analysis of the high-energy IceCube neutrinos. *Phys. Rev. D*, 91(10):103008, 2015.
- [350] Giacomo D'Amico. Flavor and energy inference for the high-energy IceCube neutrinos. *Astropart. Phys.*, 101:8–16, 2018.
- [351] A. Palladino, G. Pagliaroli, F. L. Villante, and F. Vissani. What is the Flavor of the Cosmic Neutrinos Seen by IceCube? *Phys. Rev. Lett.*, 114(17):171101, 2015.
- [352] Raj Gandhi, Chris Quigg, Mary Hall Reno, and Ina Sarcevic. Neutrino interactions at ultrahigh-energies. *Phys. Rev. D*, 58:093009, 1998.

- [353] S. S. Wilks. The Large-Sample Distribution of the Likelihood Ratio for Testing Composite Hypotheses. *Annals Math. Statist.*, 9(1):60–62, 1938.
- [354] M. C. Chantell et al. Limits on the isotropic diffuse flux of ultrahigh-energy gamma radiation. *Phys. Rev. Lett.*, 79:1805–1808, 1997.
- [355] G. Schatz et al. Search for extremely high energy gamma rays with the KASCADE experiment. In *28th International Cosmic Ray Conference*, pages 2293–2296, 9 2003.
- [356] Maria Benito, Alessandro Cuoco, and Fabio Iocco. Handling the Uncertainties in the Galactic Dark Matter Distribution for Particle Dark Matter Searches. *JCAP*, 03:033, 2019.
- [357] Maria Benito, Fabio Iocco, and Alessandro Cuoco. Uncertainties in the Galactic dark matter distribution: an update. 9 2020.
- [358] R. Abbasi et al. The IceCube high-energy starting event sample: Description and flux characterization with 7.5 years of data. 11 2020.
- [359] Xavier Rodrigues, Jonas Heinze, Andrea Palladino, Arjen van Vliet, and Walter Winter. Blazar origin of the UHECRs and perspectives for the detection of astrophysical source neutrinos at EeV energies. 3 2020.
- [360] C. Righi, A. Palladino, F. Tavecchio, and F. Vissani. EeV astrophysical neutrinos from flat spectrum radio quasars. *Astron. Astrophys.*, 642:A92, 2020.
- [361] Ke Fang and Kohta Murase. Linking High-Energy Cosmic Particles by Black Hole Jets Embedded in Large-Scale Structures. *Nature Phys.*, 14(4):396–398, 2018.
- [362] Ke Fang, Kumiko Kotera, Kohta Murase, and Angela V. Olinto. Testing the Newborn Pulsar Origin of Ultrahigh Energy Cosmic Rays with EeV Neutrinos. *Phys. Rev. D*, 90(10):103005, 2014. [Erratum: *Phys.Rev.D* 92, 129901 (2015)].
- [363] Glen Cowan, Kyle Cranmer, Eilam Gross, and Ofer Vitells. Asymptotic formulae for likelihood-based tests of new physics. *Eur. Phys. J. C*, 71:1554, 2011. [Erratum: *Eur.Phys.J.C* 73, 2501 (2013)].
- [364] J. Billard, L. Strigari, and E. Figueroa-Feliciano. Implication of neutrino backgrounds on the reach of next generation dark matter direct detection experiments. *Phys. Rev. D*, 89(2):023524, 2014.
- [365] M. Fukugita and T. Yanagida. Baryogenesis Without Grand Unification. *Phys. Lett. B*, 174:45–47, 1986.
- [366] A. Aguilar-Arevalo et al. Evidence for neutrino oscillations from the observation of $\bar{\nu}_e$ appearance in a $\bar{\nu}_\mu$ beam. *Phys. Rev. D*, 64:112007, 2001.
- [367] A. A. Aguilar-Arevalo et al. Significant Excess of ElectronLike Events in the MiniBooNE Short-Baseline Neutrino Experiment. *Phys. Rev. Lett.*, 121(22):221801, 2018.
- [368] Edward W. Kolb and Michael S. Turner. Supernova SN 1987a and the Secret Interactions of Neutrinos. *Phys. Rev. D*, 36:2895, 1987.
- [369] N. Fornengo, M. Maltoni, R. Tomas, and J. W. F. Valle. Probing neutrino nonstandard interactions with atmospheric neutrino data. *Phys. Rev. D*, 65:013010, 2002.

- [370] Patrick Huber and J. W. F. Valle. Nonstandard interactions: Atmospheric versus neutrino factory experiments. *Phys. Lett. B*, 523:151–160, 2001.
- [371] S. Davidson, C. Pena-Garay, N. Rius, and A. Santamaria. Present and future bounds on nonstandard neutrino interactions. *JHEP*, 03:011, 2003.
- [372] J. Barranco, O. G. Miranda, C. A. Moura, and J. W. F. Valle. Constraining non-standard interactions in $\nu(e)e$ or $\bar{\nu}(e)e$ scattering. *Phys. Rev. D*, 73:113001, 2006.
- [373] Gianpiero Mangano, Gennaro Miele, Sergio Pastor, Teguyco Pinto, Ofelia Pisanti, and Pasquale D. Serpico. Effects of non-standard neutrino-electron interactions on relic neutrino decoupling. *Nucl. Phys. B*, 756:100–116, 2006.
- [374] N. C. Ribeiro, H. Minakata, H. Nunokawa, S. Uchinami, and R. Zukanovich-Funchal. Probing Non-Standard Neutrino Interactions with Neutrino Factories. *JHEP*, 12:002, 2007.
- [375] Stefan Antusch, Jochen P. Baumann, and Enrique Fernandez-Martinez. Non-Standard Neutrino Interactions with Matter from Physics Beyond the Standard Model. *Nucl. Phys. B*, 810:369–388, 2009.
- [376] D. V. Forero, S. Morisi, M. Tortola, and J. W. F. Valle. Lepton flavor violation and non-unitary lepton mixing in low-scale type-I seesaw. *JHEP*, 09:142, 2011.
- [377] Maria Archidiacono and Steen Hannestad. Updated constraints on non-standard neutrino interactions from Planck. *JCAP*, 07:046, 2014.
- [378] Ranjan Laha, Basudeb Dasgupta, and John F. Beacom. Constraints on New Neutrino Interactions via Light Abelian Vector Bosons. *Phys. Rev. D*, 89(9):093025, 2014.
- [379] Pilar Coloma. Non-Standard Interactions in propagation at the Deep Underground Neutrino Experiment. *JHEP*, 03:016, 2016.
- [380] André de Gouvêa and Kevin J. Kelly. Non-standard Neutrino Interactions at DUNE. *Nucl. Phys. B*, 908:318–335, 2016.
- [381] Y. Farzan and M. Tortola. Neutrino oscillations and Non-Standard Interactions. *Front. in Phys.*, 6:10, 2018.
- [382] P. Bakhti, Y. Farzan, and M. Rajaei. Secret interactions of neutrinos with light gauge boson at the DUNE near detector. *Phys. Rev. D*, 99(5):055019, 2019.
- [383] Francesco Forastieri, Massimiliano Lattanzi, and Paolo Natoli. Cosmological constraints on neutrino self-interactions with a light mediator. *Phys. Rev. D*, 100(10):103526, 2019.
- [384] K. S. Babu, Garv Chauhan, and P. S. Bhupal Dev. Neutrino nonstandard interactions via light scalars in the Earth, Sun, supernovae, and the early Universe. *Phys. Rev. D*, 101(9):095029, 2020.
- [385] H. Athar, M. Jezabek, and O. Yasuda. Effects of neutrino mixing on high-energy cosmic neutrino flux. *Phys. Rev. D*, 62:103007, 2000.
- [386] Sharada Iyer Dutta, Mary Hall Reno, and Ina Sarcevic. High-energy neutrino signals of four neutrino mixing. *Phys. Rev. D*, 64:113015, 2001.

- [387] Ram Lal Awasthi and Sandhya Choubey. Confusing sterile neutrinos with deviation from tribimaximal mixing at neutrino telescopes. *Phys. Rev. D*, 76:113002, 2007.
- [388] Andrea Donini and Osamu Yasuda. Signatures of sterile neutrino mixing in high-energy cosmic neutrino flux. 6 2008.
- [389] Vedran Brdar, Joachim Kopp, and Xiao-Ping Wang. Sterile Neutrinos and Flavor Ratios in IceCube. *JCAP*, 01:026, 2017.
- [390] Rasmus W. Rasmussen, Lukas Lechner, Markus Ackermann, Marek Kowalski, and Walter Winter. Astrophysical neutrinos flavored with Beyond the Standard Model physics. *Phys. Rev. D*, 96(8):083018, 2017.
- [391] Carlos A. Argüelles, Kareem Farrag, Teppei Katori, Rishabh Khandelwal, Shivesh Mandalia, and Jordi Salvado. Sterile neutrinos in astrophysical neutrino flavor. *JCAP*, 02:015, 2020.
- [392] Markus Ahlers, Mauricio Bustamante, and Niels Gustav Nortvig Willesen. Flavors of Astrophysical Neutrinos with Active-Sterile Mixing. 9 2020.
- [393] Kunihto Ioka and Kohta Murase. IceCube PeV–EeV neutrinos and secret interactions of neutrinos. *PTEP*, 2014(6):061E01, 2014.
- [394] Masahiro Ibe and Kunio Kaneta. Cosmic neutrino background absorption line in the neutrino spectrum at IceCube. *Phys. Rev. D*, 90(5):053011, 2014.
- [395] Kfir Blum, Anson Hook, and Kohta Murase. High energy neutrino telescopes as a probe of the neutrino mass mechanism. 8 2014.
- [396] Ayuki Kamada and Hai-Bo Yu. Coherent Propagation of PeV Neutrinos and the Dip in the Neutrino Spectrum at IceCube. *Phys. Rev. D*, 92(11):113004, 2015.
- [397] Anthony DiFranzo and Dan Hooper. Searching for MeV-Scale Gauge Bosons with IceCube. *Phys. Rev. D*, 92(9):095007, 2015.
- [398] Kohta Murase and Ian M. Shoemaker. Neutrino Echoes from Multimessenger Transient Sources. *Phys. Rev. Lett.*, 123(24):241102, 2019.
- [399] Mauricio Bustamante, Charlotte Rosenstrøm, Shashank Shalgar, and Irene Tamborra. Bounds on secret neutrino interactions from high-energy astrophysical neutrinos. *Phys. Rev. D*, 101(12):123024, 2020.
- [400] Ivan Esteban, Sujata Pandey, Vedran Brdar, and John F. Beacom. Probing Secret Interactions of Astrophysical Neutrinos in the High-Statistics Era. 7 2021.
- [401] K. S. Babu and I. Z. Rothstein. Relaxing nucleosynthesis bounds on sterile-neutrinos. *Phys. Lett. B*, 275:112–118, 1992.
- [402] Ian M. Shoemaker and Kohta Murase. Probing BSM Neutrino Physics with Flavor and Spectral Distortions: Prospects for Future High-Energy Neutrino Telescopes. *Phys. Rev. D*, 93(8):085004, 2016.
- [403] Damiano F. G. Fiorillo, Gennaro Miele, Stefano Morisi, and Ninetta Saviano. Cosmogenic neutrino fluxes under the effect of active-sterile secret interactions. *Phys. Rev. D*, 101(8):083024, 2020.

- [404] Damiano F. G. Fiorillo, Stefano Morisi, Gennaro Miele, and Ninetta Saviano. Observable features in ultrahigh energy neutrinos due to active-sterile secret interactions. *Phys. Rev. D*, 102(8):083014, 2020.
- [405] Jeffrey M. Berryman, André De Gouvêa, Kevin J. Kelly, and Yue Zhang. Lepton-Number-Charged Scalars and Neutrino Beamstrahlung. *Phys. Rev. D*, 97(7):075030, 2018.
- [406] Leonardo Mastrototaro, Alessandro Mirizzi, Pasquale Dario Serpico, and Arman Esmaili. Heavy sterile neutrino emission in core-collapse supernovae: Constraints and signatures. *JCAP*, 01:010, 2020.
- [407] Shashank Shalgar, Irene Tamborra, and Mauricio Bustamante. Core-collapse supernovae stymie secret neutrino interactions. 12 2019.
- [408] Dawn R. Williams. Recent Results from IceCube. *Int. J. Mod. Phys. Conf. Ser.*, 46:1860048, 2018.
- [409] Andrew M. Hopkins and John F. Beacom. On the normalisation of the cosmic star formation history. *Astrophys. J.*, 651:142–154, 2006.
- [410] Markus Ahlers and Francis Halzen. Minimal Cosmogenic Neutrinos. *Phys. Rev. D*, 86:083010, 2012.
- [411] Ivan Esteban, M.C. Gonzalez-Garcia, Michele Maltoni, Ivan Martinez-Soler, and Thomas Schwetz. Updated fit to three neutrino mixing: exploring the accelerator-reactor complementarity. *JHEP*, 01:087, 2017.
- [412] M. Bustamante and M. Ahlers. Inferring the flavor of high-energy astrophysical neutrinos at their sources. *Phys. Rev. Lett.*, 122(24):241101, 2019.
- [413] Alexander Aab et al. Probing the origin of ultra-high-energy cosmic rays with neutrinos in the EeV energy range using the Pierre Auger Observatory. *JCAP*, 10:022, 2019.
- [414] Steven W. Barwick. Progress in the Development of Radio-Cherenkov Neutrino Detectors. *PoS, ICRC2015:027*, 2016.
- [415] T.A. Wagner, S. Schlamminger, J.H. Gundlach, and E.G. Adelberger. Torsion-balance tests of the weak equivalence principle. *Class. Quant. Grav.*, 29:184002, 2012.
- [416] J. Overduin, J. Mitcham, and Z. Warecki. Expanded solar-system limits on violations of the equivalence principle. *Class. Quant. Grav.*, 31:015001, 2014.
- [417] M.A. Hohensee, N. Leefler, D. Budker, C. Harabati, V.A. Dzuba, and V.V. Flambaum. Limits on Violations of Lorentz Symmetry and the Einstein Equivalence Principle using Radio-Frequency Spectroscopy of Atomic Dysprosium. *Phys. Rev. Lett.*, 111:050401, 2013.
- [418] T. Damour and G. Schaefer. New tests of the strong equivalence principle using binary pulsar data. *Phys. Rev. Lett.*, 66:2549–2552, 1991.
- [419] R. Horvat. Pulsar velocities due to a violation of the equivalence principle by neutrinos. *Mod. Phys. Lett. A*, 13:2379–2384, 1998.
- [420] M. Barkovich, H. Casini, J.C. D’Olivo, and R. Montemayor. Pulsar motions from neutrino oscillations induced by a violation of the equivalence principle. *Phys. Lett. B*, 506:20–26, 2001.

- [421] J.T. Pantaleone, A. Halprin, and C.N. Leung. Neutrino mixing due to a violation of the equivalence principle. *Phys. Rev. D*, 47:4199–4202, 1993.
- [422] M.N. Butler, S. Nozawa, R.A. Malaney, and A.I. Boothroyd. Gravitationally induced neutrino oscillations. *Phys. Rev. D*, 47:2615–2618, 1993.
- [423] John N. Bahcall, P.I. Krastev, and C.N. Leung. Solar neutrinos and the principle of equivalence. *Phys. Rev. D*, 52:1770–1779, 1995.
- [424] A. Halprin, C.N. Leung, and J.T. Pantaleone. A Possible violation of the equivalence principle by neutrinos. *Phys. Rev. D*, 53:5365–5376, 1996.
- [425] J.R. Mureika and Robert B. Mann. Mass or gravitationally induced neutrino oscillations?: A Comparison of B-8 neutrino flux spectra in a three generation framework. *Phys. Lett. B*, 368:112–118, 1996.
- [426] J.R. Mureika and Robert B. Mann. Three flavor gravitationally induced neutrino oscillations and the solar neutrino problem. *Phys. Rev. D*, 54:2761–2778, 1996.
- [427] J.R. Mureika. An Investigation of equivalence principle violations using solar neutrino oscillations in a constant gravitational potential. *Phys. Rev. D*, 56:2408–2418, 1997.
- [428] S.W. Mansour and Tzee-Ke Kuo. Solar neutrinos and the violation of equivalence principle. *Phys. Rev. D*, 60:097301, 1999.
- [429] A.M. Gago, H. Nunokawa, and R. Zukanovich Funchal. The Solar neutrino problem and gravitationally induced long wavelength neutrino oscillation. *Phys. Rev. Lett.*, 84:4035–4038, 2000.
- [430] H. Casini, J.C. D’Olivo, and R. Montemayor. VEP oscillation solutions to the solar neutrino problem. *Phys. Rev. D*, 61:105004, 2000.
- [431] D. Majumdar, A. Raychaudhuri, and A. Sil. Solar neutrino results and violation of the equivalence principle: An Analysis of the existing data and predictions for SNO. *Phys. Rev. D*, 63:073014, 2001.
- [432] M. Gasperini. Testing the Principle of Equivalence with Neutrino Oscillations. *Phys. Rev. D*, 38:2635–2637, 1988.
- [433] M. Gasperini. Experimental Constraints on a Minimal and Nonminimal Violation of the Equivalence Principle in the Oscillations of Massive Neutrinos. *Phys. Rev. D*, 39:3606–3611, 1989.
- [434] H. Minakata and H. Nunokawa. Testing the principle of equivalence by solar neutrinos. *Phys. Rev. D*, 51:6625–6634, 1995.
- [435] G.A. Valdivieso, M.M. Guzzo, and P.C. de Holanda. Probing new limits for the Violation of the Equivalence Principle in the solar–reactor neutrino sector as a next to leading order effect. *Phys. Lett. B*, 701:240–247, 2011.
- [436] R. Foot, R.R. Volkas, and O. Yasuda. Up - down atmospheric neutrino flux asymmetry predictions for various neutrino oscillation scenarios. *Phys. Lett. B*, 421:245–249, 1998.

- [437] R. Foot, R.R. Volkas, and O. Yasuda. Confronting solutions to the atmospheric neutrino anomaly involving large angle $\mu \rightarrow e$ oscillations with Super-Kamiokande and CHOOZ. *Phys. Lett. B*, 433:82–87, 1998.
- [438] G.L. Fogli, E. Lisi, A. Marrone, and G. Scioscia. Testing violations of special and general relativity through the energy dependence of μ -neutrino \leftrightarrow τ -neutrino oscillations in the Super-Kamiokande atmospheric neutrino experiment. *Phys. Rev. D*, 60:053006, 1999.
- [439] M.C. Gonzalez-Garcia and M. Maltoni. Status of global analysis of neutrino oscillation data. In *5th Workshop on Neutrino Oscillations and their Origin (NOON2004)*, pages 115–124, 6 2004.
- [440] M.C. Gonzalez-Garcia, F. Halzen, and M. Maltoni. Physics reach of high-energy and high-statistics icecube atmospheric neutrino data. *Phys. Rev. D*, 71:093010, 2005.
- [441] G. Battistoni et al. Search for a Lorentz invariance violation contribution in atmospheric neutrino oscillations using MACRO data. *Phys. Lett. B*, 615:14–18, 2005.
- [442] D. Morgan, E. Winstanley, Lee F. Thompson, J. Brunner, and Lee F. Thompson. Neutrino telescope modelling of Lorentz invariance violation in oscillations of atmospheric neutrinos. *Astropart. Phys.*, 29:345–354, 2008.
- [443] R. Abbasi et al. Determination of the Atmospheric Neutrino Flux and Searches for New Physics with AMANDA-II. *Phys. Rev. D*, 79:102005, 2009.
- [444] S. Pakvasa, W.A. Simmons, and T.J. Weiler. Test of Equivalence Principle for Neutrinos and Anti-neutrinos. *Phys. Rev. D*, 39:1761, 1989.
- [445] M.M. Guzzo, H. Nunokawa, and R. Tomas. Testing the principle of equivalence by supernova neutrinos. *Astropart. Phys.*, 18:277–286, 2002.
- [446] H. Minakata and A.Yu. Smirnov. High-energy cosmic neutrinos and the equivalence principle. *Phys. Rev. D*, 54:3698–3705, 1996.
- [447] K. Iida, H. Minakata, and O. Yasuda. A Test of the equivalence principle by long baseline neutrino oscillation experiments. *Mod. Phys. Lett. A*, 8:1037–1046, 1993.
- [448] R.B. Mann and U. Sarkar. Test of the equivalence principle from neutrino oscillation experiments. *Phys. Rev. Lett.*, 76:865–868, 1996.
- [449] A. Esmaili, D.R. Gratieri, M.M. Guzzo, P.C. de Holanda, O.L.G. Peres, and G.A. Valdivieso. Constraining the violation of the equivalence principle with IceCube atmospheric neutrino data. *Phys. Rev. D*, 89(11):113003, 2014.
- [450] F.N. Díaz, J. Hoefken, and A.M. Gago. Effects of the Violation of the Equivalence Principle at DUNE. *Phys. Rev. D*, 102(5):055020, 2020.
- [451] C. Giunti. Coherence and wave packets in neutrino oscillations. *Found. Phys. Lett.*, 17:103–124, 2004.
- [452] Carlo Giunti and Chung W. Kim. *Fundamentals of Neutrino Physics and Astrophysics*. 2007.
- [453] Richard Phillips Feynman, Robert B. Leighton, and Matthew Sands. *The Feynman Lectures on Physics*. 1963.

- [454] I. R. Kenyon. A Recalculation of the Gravitational Mass Difference Between the K^0 and \bar{K}^0 Mesons. *Phys. Lett. B*, 237:274–277, 1990.
- [455] M.G. Aartsen et al. All-sky Search for Time-integrated Neutrino Emission from Astrophysical Sources with 7 yr of IceCube Data. *Astrophys. J.*, 835(2):151, 2017.
- [456] R. Abbasi et al. IceCube Data for Neutrino Point-Source Searches Years 2008-2018. 1 2021.
- [457] M. Honda, T. Kajita, K. Kasahara, S. Midorikawa, and T. Sanuki. Calculation of atmospheric neutrino flux using the interaction model calibrated with atmospheric muon data. *Phys. Rev. D*, 75:043006, 2007.
- [458] R. Enberg and I. Reno, M.H.and Sarcevic. Prompt neutrino fluxes from atmospheric charm. *Phys. Rev. D*, 78:043005, 2008.
- [459] Marco Chianese, Damiano F. G. Fiorillo, Gianpiero Mangano, Gennaro Miele, Stefano Morisi, and Ofelia Pisanti. Sensitivity of KM3NeT to Violation of Equivalence Principle. *Symmetry*, 13:1353, 2021.
- [460] Arman Esmaili. Violation of Equivalence Principle in Neutrino Sector: Probing the Extended Parameter Space. 5 2021.
- [461] R. Abbasi et al. Measurement of Astrophysical Tau Neutrinos in IceCube’s High-Energy Starting Events. 11 2020.
- [462] Carlos A. Argüelles, Teppei Katori, and Jordi Salvado. New Physics in Astrophysical Neutrino Flavor. *Phys. Rev. Lett.*, 115:161303, 2015.
- [463] Markus Ahlers, Mauricio Bustamante, and Siqiao Mu. Unitarity Bounds of Astrophysical Neutrinos. *Phys. Rev. D*, 98(12):123023, 2018.
- [464] L. Oc. Drury. An introduction to the theory of diffusive shock acceleration of energetic particles in tenuous plasmas. *Rept. Prog. Phys.*, 46:973–1027, 1983.